


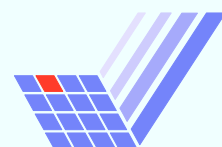
ICHSF 2006

2nd International Conference on High Speed Forming

Proceedings

March 20th - 21st, 2006
Dortmund, Germany

 **Institute of Forming
Technology and
Lightweight Construction**
Universität Dortmund



HIGH SPEED FORMING 2006

PROCEEDINGS OF THE 2nd INTERNATIONAL CONFERENCE

MARCH 20 - 21, 2006
DORTMUND, GERMANY

Edited by:

Prof. Dr.-Ing. M. Kleiner
Institut für Umformtechnik und Leichtbau,
Universität Dortmund

In corporation with:

DFG



Scientific Committee:

T. Altan	Ohio State University (USA)
N. Asnafi	Volvo Body Car Components (Sweden)
Y. Batygin	National Technical University, Kharkov (Ukraine)
G. S. Daehn	Ohio State University (USA)
J.-C. Gelin	University of Franche-Comté (France)
S. Golovashchenko	Ford (USA)
H. Hoffmann	Technical University of Munich (Germany)
F. Hollmann	DFG German Research Foundation (Germany)
M. Kleiner	Universität Dortmund (Germany)
A. Kost	Brandenburg Technical University of Cottbus (Germany)
E. Lugscheider	RWTH Aachen University (Germany)
L. W. Meyer	Technical University of Chemnitz (Germany)
E. El-Magd	RWTH Aachen (Germany)
R. Neugebauer	Technical University of Chemnitz (Germany)
K. Roll	DaimlerChrysler (Germany)
A. E. Tekkaya	ATILIM University, Ankara (Turkey)
F. Vollertsen	University of Bremen (Germany)

© 2006, Organizing committee of the 2nd International Conference on High Speed Forming, March 20th – 21st 2006, Universität Dortmund, Faculty of Mechanical Engineering, Institute of Forming Technology and Lightweight Construction.

All rights reserved, No part of this publication may be reproduced, stored in a retrieval system or transmitted in any form by any means, electronic, mechanical, photocopying, recording or otherwise, without the written prior permission of the authors/publisher.

The articles, diagrams, captions and photographs in this publication have been supplied by the contributors or delegates of the Conference. While every effort has been made to ensure accuracy, the editors, the organizing committee and the University of Dortmund do not under any circumstances accept responsibility for errors, omissions or infringements.

INSTITUT FÜR UMFORMTECHNIK UND LEICHTBAU
Universität Dortmund
Baroper Str. 301
D-44227 Dortmund
Germany

Edited by:



Institute of Forming Technology and Lightweight Construction
Universität Dortmund
Prof. Dr.-Ing. M. Kleiner

ISBN 3-00-018432-5

Table of Contents

	Preface	xi
Session 1:	Materials: Behavior & Testing	1
J. M. Imbert, M. J. Worswick, S. Golovashchenko	Contributing Factors to the Increased Formability Observed in Electromagnetically Formed Aluminum Alloy Sheet	3
N. Herzig, L. W. Meyer	Material Characterization at High Strain Rates with Special Emphasis on Miniaturization and Size Dependencies	13
J. Unger, M. Stiemer, L. Walden, F. Bach, H. Blum, B. Svendsen	On the Effect of Current Pulses on the Material Behavior during Electromagnetic Metal Forming	23
O. Gafri, A. Izhar, Y. Livshitz, V. Shribman	Magnetic Pulse Acceleration	33
L. W. Meyer, S. Abdel-Malek	Deformation and Ductile Fracture of a Low Alloy Steel under High Strain Rate Loading	41
L. Xin, L. Xiangping, G. Changgang	Materials Characterization at High Speed by Dynamic Tensile Tests	49
Session 2:	Modeling & Simulation	61
M. Stiemer, J. Unger, H. Blum, B. Svendsen	Fully-coupled 3D Simulation of Electromagnetic Forming	63

Ph. Conraux, M. Pignol, V. Robin, J. M. Bergheau	3D Finite Element Modeling of Electromagnetic Forming Processes	73
M. Schwarze, A. Brosius, S. Reese, M. Kleiner	Efficient Finite Element and Contact Procedures for the Simulation of High Speed Sheet Metal Forming Processes	83
A. Vovk, V. Vovk, V. Sabelkin, V. Taran	Mathematical Modeling of Impulsive Forming Processes Using Various Energy Sources and Transmitting Medium	95
Session 3:	Process Technology	105
P. Barreiro, V. Schulze, D. Löhe, M. Marré, C. Beerwald, W. Homberg, M. Kleiner	Strength of Tubular Joints Made by Electromagnetic Compression at Quasi-static and Cyclic Loading	107
V. Psyk, C. Beerwald, W. Homberg, M. Kleiner, M. Beerwald, A. Henselek	Investigation of the Process Chain Bending-Electromagnetic Compression-Hydroforming on the Basis of an Industrial Demonstrator Part	117
R. Neugebauer, M. Putz, T. Koch, G. Laux, F. Löschmann	A Production-oriented Approach in Electromagnetic Forming of Metal Sheets	129
S. Golovashchenko, N. Bessonov, R. Davies	Design and Testing of Coils for Pulsed Electromagnetic Forming	141

E. Iriondo, B. Gonzalez, M. Gutierrez, V. Vohnout, G. Daehn, B. Hayes	Electromagnetic Springback Reshaping	153
M. Weber, M. Hermes, A. Brosius, C. Beerwald, G. Gersteyn, H. Olivier, M. Kleiner, F.-W. Bach	Process Investigation of Tube Expansion by Gas Detonation	161
P. Jimbert, A. Arroyo I. Eguia, J.I. Fernandez, E. Silveira, I. Garuz, G. S. Daehn	Efficiency Improvement and Analysis of Changes in Microstructure Associated to a Uniform Pressure Actuator	175
Session 4:	Tools & Equipment	187
D. Risch, E. Vogli, C. Beerwald, A. Brosius, W. Tillmann, M. Kleiner	Aspects of Die Design for the Electromagnetic Sheet Metal Forming Process	189
S. Golovashchenko	Electromagnetic Forming and Joining for Automotive Applications	201
P. Werdelmann, D. Peier	Purposive Design of a Magnetic Sheet Metal Forming Facility	207
M. Kamal, V. Cheng, J. Bradley, S. Hatkevich, G. S. Daehn	Design, Construction and Applications of the Uniform Pressure Electromagnetic Actuator	217

W. Hartman, M. Römheld, A. Donner	A 100kJ Pulse Unit for Electromagnetic Forming of Large Area Sheet Metals	227
A. Welleman, W. Fleischmann	High Power Semiconductor Devices and Solid State Switches for Pulsed Discharge Applications	239

Preface

Forming materials of low ductility, like e.g. aluminum alloys relevant for light weight construction, not only requires an optimisation of conventional methods, but also the invention and further development of alternative forming processes.

The implementation of high speed forming processes, including electromagnetic forming in particular, represents an exceptionally promising approach.

The Second International Conference on High Speed Forming (ICHSF 2006) at the Universität Dortmund will serve as a forum for the presentation of the current research and development status and for an intensive professional exchange.

Research results regarding subjects as workpiece and material behavior, modelling and simulation as well as process design will be presented and discussed in a range of selected scientific lectures.

Dortmund, March 2006

Matthias Kleiner

SESSION 1

MATERIALS: BEHAVIOR & TESTING

Contributing Factors to the Increased Formability Observed in Electromagnetically Formed Aluminum Alloy Sheet^{*}

J.M. Imbert¹, M.J. Worswick¹, S. Golovashchenko²

¹ Dept. of Mech. Engineering, University of Waterloo, Waterloo, Ontario, Canada

² Ford Motor Company, Scientific Research Laboratory, Dearborn, MI

Abstract

This paper summarizes the results of an experimental and numerical program carried out to study the formability of aluminum alloy sheet formed using electromagnetic forming (EMF). Free-formed and conical samples of AA5754 aluminum alloy sheet were studied. The experiments showed significant increases in formability for the conical samples, but no significant increase for the free-formed parts. It was found that relatively little damage growth occurred and that the failure modes of the materials changed from those observed in quasi-static forming to those observed in high hydrostatic stress environments. Numerical simulations were performed using the explicit finite element code LS-DYNA with an analytical EM force distribution. The numerical models revealed that a complex stress state is generated when the sheet interacts with the tool, which is characterized by high hydrostatic stresses that create a stress state favourable to damage suppression increasing ductility. Shear stresses and strains are also produced at impact with the die which help the material achieve additional deformation. The predicted peak strain rates for the free formed parts were on the order of 1000 s^{-1} and for the conical parts the rates are on the order of $10,000\text{ s}^{-1}$. Although aluminum is typically considered to be strain-rate insensitive, the strain rates predicted could be playing a role in the increased formability. The predicted strain paths for the conical samples were highly non-linear. The results from this study indicate that there is an increase in formability for AA5754 when the alloy is formed into a die using EMF. This increase in formability is due to a combination of high hydrostatic stresses, shear stresses, high strain rates, and non-linear strain paths.

Keywords:

Electromagnetic sheet metal forming, Formability, Aluminum alloy sheet, AA5754

^{*} Financial support from the Ontario Research and Development Challenge Fund and Ford Motor Co. is gratefully acknowledged. The authors thank V. Dmitriev.

1 Introduction

Interest in electromagnetic forming (EMF) has increased recently due to the potential formability increases that high speed forming can offer for low formability materials. The exact nature of the mechanisms that contribute to the increased formability observed remains an open question. Daehn and co-workers [1,2,3] studied the phenomenon and reported that the formability increases were due to inertial suppression of necking and inertial ironing. The present authors have proposed that the increases in formability are due to the complex stress state and strains produced by tool/sheet interaction [4, 5, 6, 7]. The importance of the tool/sheet interaction becomes apparent since no significant increases in formability have been observed by the current authors in free-formed parts where the material does not contact a die. In contrast, significant increases in formability have been observed in parts formed into a conical die. Similar observations have been made by Oliveira [8] and Golovashenko et al [9]. Imbert [7] contains an in-depth review on the available literature on this subject.

This paper summarizes the results of a project whose aim was to determine which factors were affecting the formability of sheet material in EMF. The preliminary findings of the project were presented by the authors in the 1st International Conference on High Speed Forming [6]. Both AA5754 and AA6111 were studied, however, for the sake of brevity only the data for AA5754 will be presented in this paper. The reader is referred to Imbert [7] for the complete findings of the project.

2 Experimental procedure

2.1 Formability experiments

The experiments consisted of forming 1mm AA5754 sheet into free-form and conical dies of 34°, 40°, and 45° side angle, using a spiral coil. The yield stress of the material was 98 MPa. An IAP Magnepress [10] system with a maximum storage capacity of 22.5 kJ at 15 kV was used. Figure 1 shows a schematic of the tooling used in the experiments.

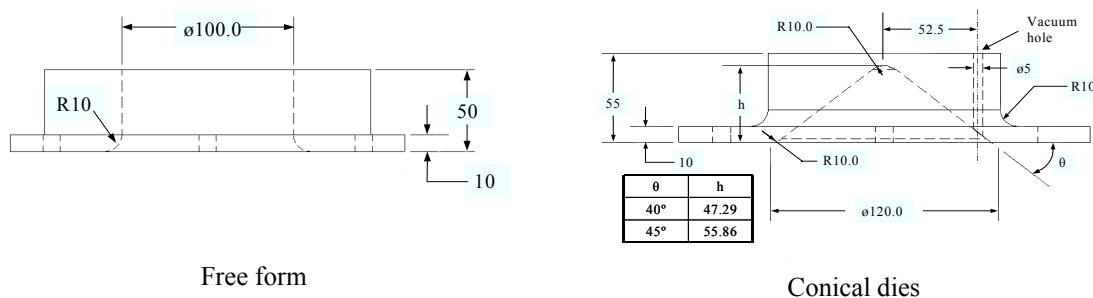


Figure 1: Schematic of the dies used

Circle grids were used to measure the engineering strains in the rolling direction. Metallographic and scanning electron microscopy was carried out to measure the damage levels in the material and to study the failure modes present in the material. A detailed description of the experimental procedures can be found in ref [7].

3 Numerical models

Numerical simulations of the experiments were carried out using the explicit dynamic finite element code LS-Dyna [11]. The EM force was modeled using an analytical pressure distribution. This approach was deemed appropriate since the general behavior of the sheet as it interacts with the tool would not change dramatically with the analytical pressure distribution when compared to the pressure distribution of an actual spiral coil. Constant stress solid elements were used for the sheet in order to capture the trough thickness normal and shear stresses. The die and blank holder were modeled using rigid shell elements.

The EM pressure was modeled with an analytical pressure distribution for an “ideal” spiral coil (i.e. one formed of concentric circles) from Al-Hassani [12]. This results in a radial pressure distribution that does not vary in the circumferential direction. To simplify the load application, no load was applied within a 5 mm radius of the center since the actual loads are very low at this point. A sinusoidal profile was used for the time history of the pressure (Figure 2). The time at which the peak pressure was reached corresponded to the average value observed in the experiments, that is 0.017 ms. The material was modeled using a modified version of the Gurson-Tvergaard-Needleman (GTN) constitutive model [13,14,15]. An in-depth description of the model and its validation is presented in [7].

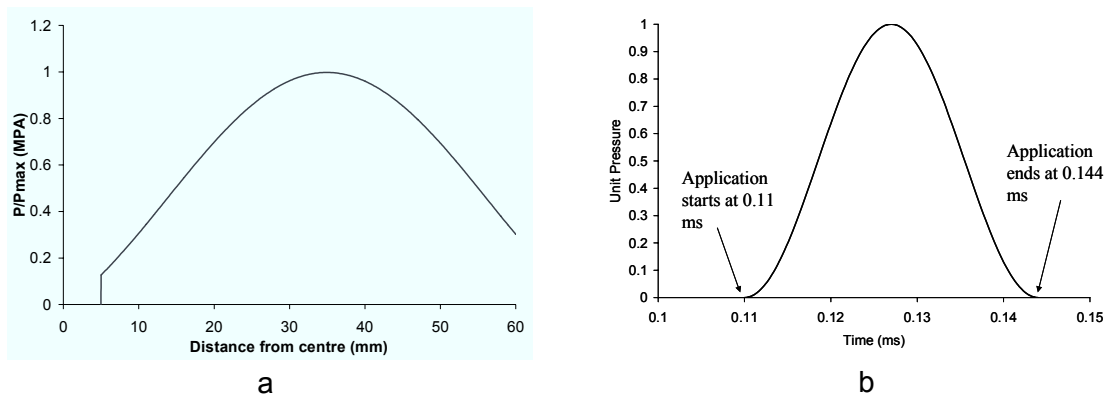


Figure 2: Radial pressure distribution (a) and time history of pressure application (b)

4 Experimental Results

So-called safe parts that did not fracture were produced with the 34° and 40° cone. All the parts formed with the 45° cone fractured. For the purpose of this work, a part that showed no indication of fracture or necking is considered safe; otherwise it is considered to have failed. Figure 3 shows representative free formed and conical parts.

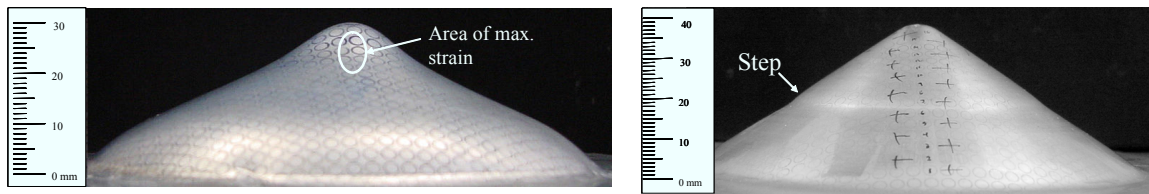


Figure 3: Samples formed using the free form (left) and 34° die (right)

4.1 Formability data

Figure 4 shows the measured strains for the safe and failed conical parts. It can be seen that strains above the conventional forming limit curve (FLC) were achieved. In contrast to the conical die results shown, none of the free-formed samples exhibited measured strains that lay above those obtained using conventional stamping methods [7], indicating that enhanced formability was only observed for the parts formed into conical dies.

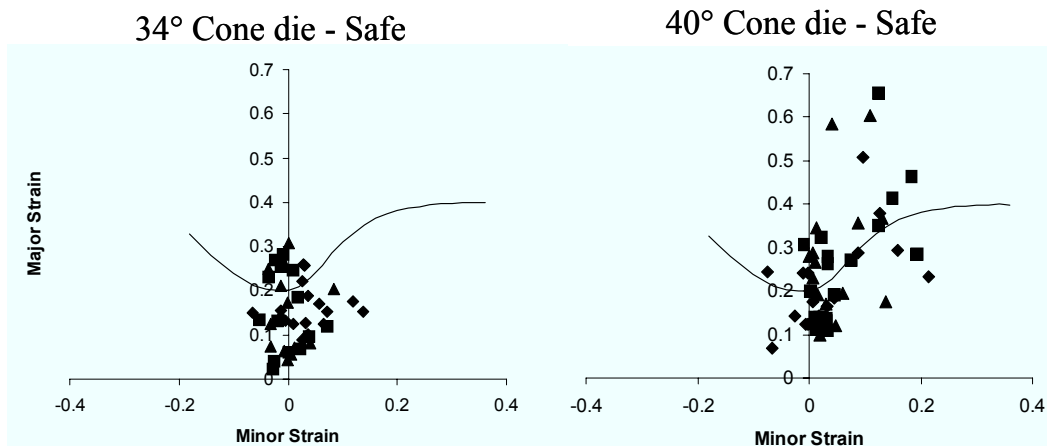


Figure 4: Measured strains for the 34° and 40° conical parts in FLD form. The curve represents a typical FLC for 1.0 mm AA5754 [16]. Each FLD contains the data of three samples

4.2 Damage measurements

In the areas where safe strains beyond the conventional FLD were recorded the material showed little increase in damage relative to the as-received condition of 0.01% void volume fraction. Thus, the data for the conical die experiments showed relatively small increases in damage. Safe areas in the conical parts with strains in the range of 25-30% under near plane strain conditions showed damage levels between 0.01 to 0.02%. Relatively larger increases were measured in the tip area of the 40° sample where 0.067% void volume fraction was measured for major and minor strains of 60% and 10%. The area of the neck has a void volume fraction of 0.15% for similar strains, the higher value is consistent with the localized thinning.

4.3 Observed failure

Micrographs comparing the fractured region of a conical EM formed part to fractures under quasi static and high strain rate tensile loading are shown in Figure 5. It can be

seen that the material formed with EMF thinned considerably before fracture, in a manner more consistent with plastic collapse than with ductile fracture. The amount of thinning is significantly higher than that observed in quasi-static testing and higher than that observed in Hopkinson bar testing at 1500 s^{-1} .

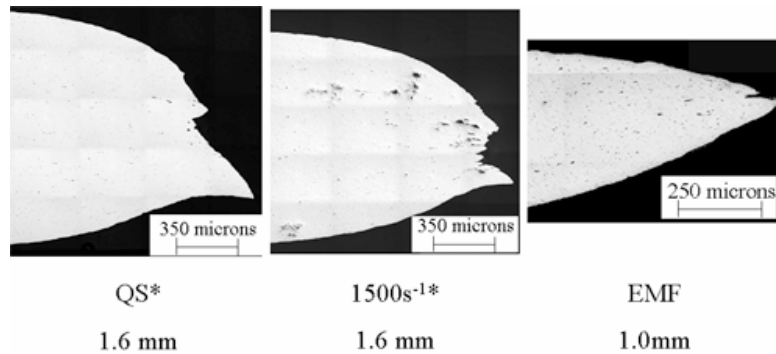


Figure 5: Micrographs of failure of AA5754 for tensile quasi-static (QS), high strain rate Hopkinson bar testing at 1500 s^{-1} , and EM forming, (* Taken from Smerd et al. [17])

Scanning electron microscope images of the EMF failure are shown in Figure 10. There are some areas of dimpling and void sheeting which indicate ductile fracture, with limited areas exhibiting shear fracture. This is non consistent with the quasi-static fractures of the material, which were primarily ductile-shear failures [7]. The dramatic reduction in area and failure modes present in the EMF samples are consistent with damage suppression mechanisms and the presence of large hydrostatic stresses [7].

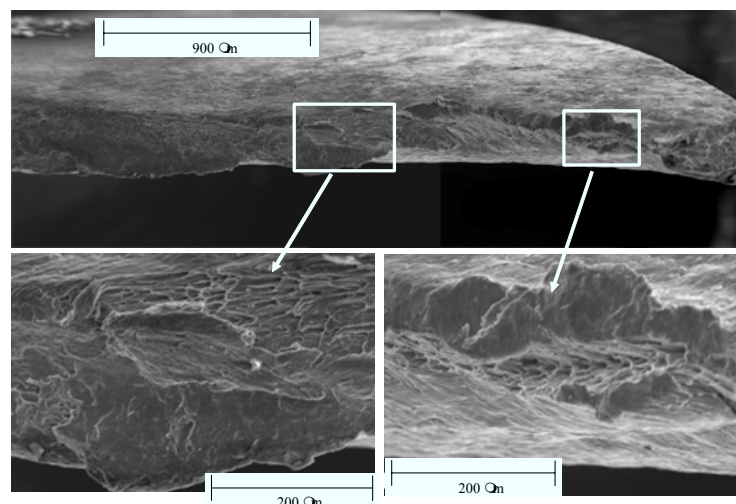


Figure 6: Scanning electron microscope images of the failure of the conical parts. Insets show ductile and shear fracture (bottom right) and shear fracture and void sheeting (bottom left)

5 Numerical results

The numerical analysis yielded considerable insight into the deformation processes of the free-formed and conical parts. In general, the free-formed parts deformed in essentially a

plane-stress manner. Details of this deformation can be seen in [7]. In contrast to the free-formed parts, the forming history of the conical parts was characterized by a complex three dimensional stress and strain state. In region A, the sheet is deforming in plane stress. In region B, the sheet impacts the die, resulting in a complex stress state. Just prior to impact the sheet bends and then straightens as it hits the die. In region C, the sheet is deformed to its final state, but bounces off the wall of the die. The model agrees well with the experimental observations; a more detailed comparison can be seen in [7].

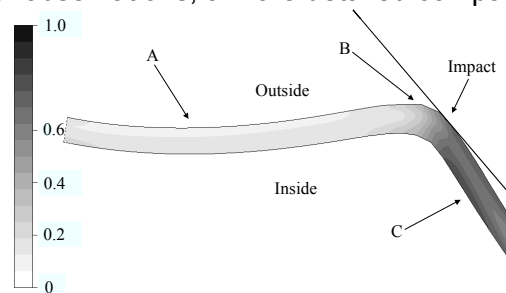


Figure 7: Predicted impact zone. Contours are of true effective plastic strain

5.1 Through thickness stresses

The stress at impact is dominated by large through thickness-stresses. Figure 8 shows the predicted through-thickness stresses and strains for an element on the sheet that makes contact with the die.

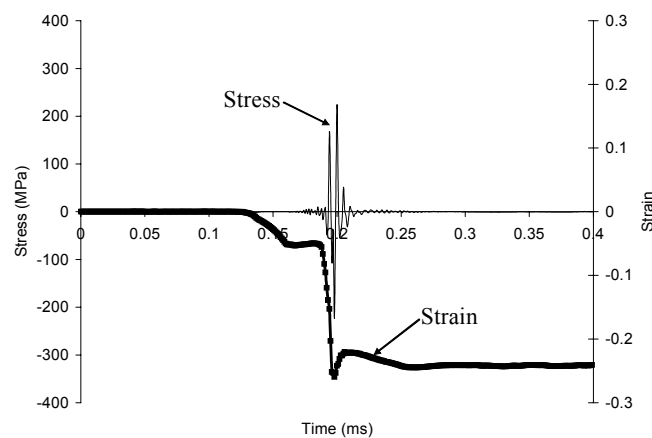


Figure 8: Predicted through-thickness stresses and plastic strains for elements that make contact with the sheet

The through-thickness stresses are very high and contribute to the production of high compressive hydrostatic stresses. The through-thickness stresses vary significantly throughout the thickness of the sheet, being an order of magnitude lower on the inside of the sample. Figure 9 shows a comparison between the triaxiality history predicted for free-formed and conical parts. The triaxiality of the free-formed parts increases relatively monotonically as forming takes place, indicating a plane stress state. The conical part is characterized by a very high negative triaxiality produced by the presence of the through-thickness stresses.

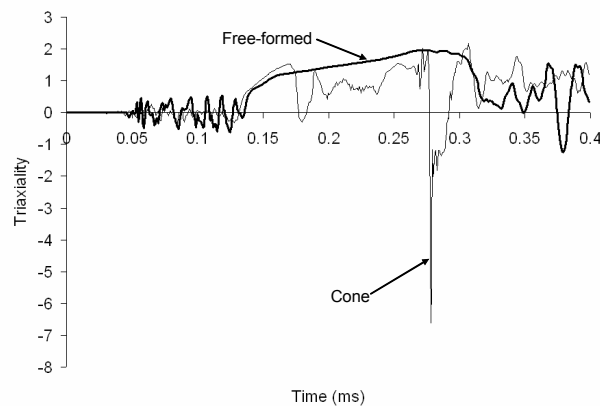


Figure 9: Triaxiality for free-formed and conical part

5.2 Shear stresses

A distinctive feature of the stress state history is the presence of significant shear stresses. Figure 10 shows the predicted shear stress and strain for an element on the outside of the sheet. The maximum predicted shear stresses are on the order of the yield stress of the material. These produce shear strains that contribute to the overall deformation of the material.

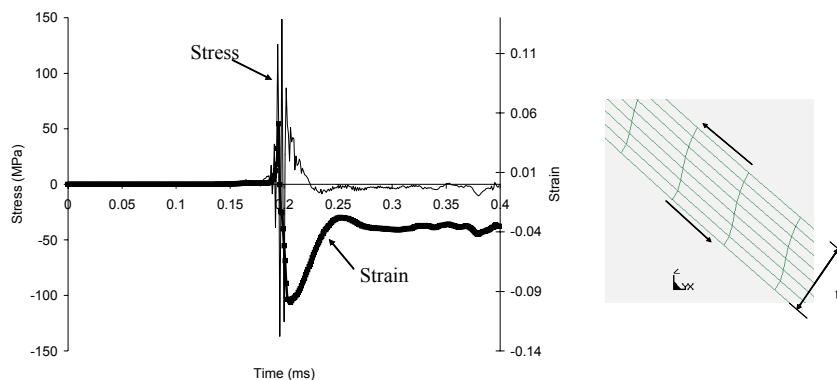


Figure 10: Predicted shear stresses and strains for an outside element. The direction of shear is shown on the left of the figure.

5.3 Strain rates

A careful examination of Figure 7 shows that the majority of the deformation of the sheet happens at impact, the duration of the impact is roughly 10 μs , producing strain rates on the order of $10,000 \text{ s}^{-1}$. This strain rate is very high and no material data are available for AA5754 sheet under these conditions to the authors' knowledge. It is likely that these high rates of strain are affecting the formability, but further work is required to determine any constitutive and thermal effects that might be present. In contrast, for the free-formed samples the predicted strain rates were on the order of $1,000 \text{ s}^{-1}$. It has been shown by Worswick et al [17] that AA5754 experiences some increase in flow stress and increased elongation at strain rates on the order of $1,000 \text{ s}^{-1}$ (Figure 11). If this trend holds for higher strain rates, some of the increased formability observed could be explained.

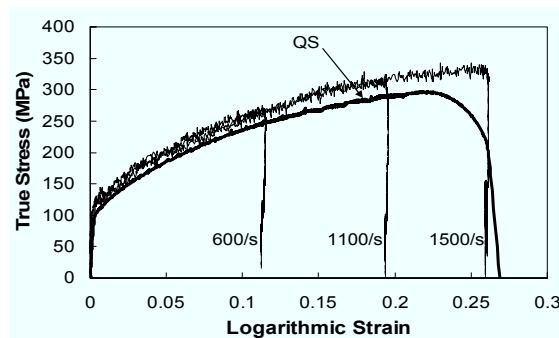


Figure 11: Effect of strain rate on flow stress and elongation for AA5754-O [17]

Strain paths have a significant effect on formability [18,19]. The predicted strain paths for the conical parts are highly non-linear and could also be affecting the formability. More details on the predicted strain paths can be found in [4, 7].

6 Discussion

The experimental evidence suggests that the material formed into conical dies is subject to high hydrostatic stresses that suppress damage and change the failure mode of the material. This is supported by the numerical analysis, which shows that a complex stress state is produced with high through-thickness stresses that lead to high compressive triaxiality. These stress states have been shown to reduce damage and improve ductility. Sheet metal through-thickness stresses have been suggested as a possible mechanism for improving formability, as further discussed by Imbert [7].

The presence of large through-thickness and shear stresses and strains also contributes to the increased levels of deformation observed. For numerical simulations of these processes the shear stresses combined with the through-thickness stresses have significant implications to the choice of elements used. In particular, shell elements should not be used since they do not account for transverse shear stresses.

The effects of the strain rates and strain paths on formability are the subject of ongoing research. Although the available evidence suggests that these may have an effect on formability, data on the properties of the materials studied are not available for the extremely high strain rates encountered in the EMF conical die forming operations.

7 Conclusions

The following conclusions are drawn:

- EM forming of sheet into a die results in non-plane-stress conditions due to the high compressive through-thickness stresses and transverse shear stresses produced.
- Very high strain rates are predicted for which material data are not available for the alloys studied.
- The above mentioned factors combine to produce the increased formability observed.

References

- [1] *Balanethiram, V.S.; Daehn, G.S.*: Hyperplasticity: Increased Forming Limits at High Workpiece Velocity. *Scripta Metall. et Mater.*, 30, 1994 pp. 515-520.
- [2] *Balanethiram, V.S.*: Hyperplasticity: Enhanced Formability of Sheet Metals at High Workpiece Velocities. Ph.D. Thesis, The Ohio State University, 1996.
- [3] *Vohnout, V.S.*: A Hybrid Quasi-Static/Dynamic Process for Forming Large Sheet Metal Parts From Aluminum Alloys. Ph.D. thesis, The Ohio State University, 1998.
- [4] *Imbert, J.; Winkler, S.L.; Worswick, M.J.; Golovashchenko, S.*: Analysis of the Increased Formability of Sheet Metal Formed Using Electromagnetic Forming. *SAE 2005 Transactions J. of Matls. and Mfg*, Paper No. 2005-01-0082, 6-18, 2006.
- [5] *Imbert, J.M.; Winkler, S.L.; Worswick, M.J.; Oliveira, D.A.; Golovashchenko, S.*: The Effect of Tool/Sheet Interaction on Damage Evolution in Electromagnetic Forming of Aluminum Alloy Sheet. *J. Eng. Mats and Tech.*, 127, n.1, 2005, pp. 145152.
- [6] *Imbert, J.M.; Winkler, S.L.; Worswick, M.J.; and Golovashchenko, S.*: Formability and Damage Analysis of Electromagnetically Formed AA5754 and AA6111. *Proceedings of the First International High Speed Forming Conference*, edited by M. Kleiner, 2004, pp. 202-210.
- [7] *Imbert, J.*: Increased Formability and the Effects of the Tool/Sheet Interaction in Electromagnetic Forming of Aluminum Alloy Sheet. Master of Applied Science thesis, 2004. <http://etd.uwaterloo.ca/etd/jmsimber2005.pdf>.
- [8] *Oliveira, D.A.*: Electromagnetic Forming of Aluminum Alloy Sheet: Experiment and Model. Masters of Applied Science thesis, University of Waterloo, 2002.
- [9] *Golovashchenko, S.*: Numerical and Experimental Results on Pulsed Tube Calibration. *Proceedings of the TMS annual meeting "Sheet metal forming technology*, M. Demeri ed., San Diego, Ca., 1999, pp. 117-127.
- [10] IAP Research Inc. 2003. Magnepress System product information. <http://www.iap.com/2col.html>.
- [11] *Hallquist, J.*: *LS-DYNA Theoretical Manual*, Livermore software technology corporation, 1998.
- [12] *Hassani, A.; S.T.S.*: Magnetic Pressure Distributions in Sheet Metal Forming. *Electrical Methods of Machining, Forming and Coating*. Inst. Electr. Eng. Conf. Publ. No. 1975. 1975, pp1-10.
- [13] *Gurson, A.L.*: Continuum Theory of Ductile Rupture by Void Nucleation and Growth: Part 1 – Yield Criteria and Flow Rules for Porous Ductile Media. *J. Eng. Mats and Tech.*, 99, 1977, pp. 2-15.
- [14] *Tvergaard, V.*: Influence of Voids on Shear Band Instabilities Under Plane Strain Conditions. *Int. J. of Fract.*, 37, n.4, 1981, pp. 389-407.
- [15] *Tvergaard, V.; Needleman, A.*: Analysis of the Cup-one Fracture in a Round Tensile Bar. *Acta Metall.*, 32, 1984, pp. 157.
- [16] Data provided by *Alcan International*.
- [17] *Worswick, M.; Smerd, R.; Salisbury, C.P.; Winkler, S.; Lloyd, D.J.*: High Strain Rate Behaviour of Aluminum Alloy Sheet. To be published in the proceedings for the 10th International Conference on Aluminum Alloys, July 9-13, 2006, Vancouver, Canada.
- [18] *Graf, A.; Hosford, W.*: The Influence of strain-path changes on forming limit diagrams of al. 6111 T4. *Int.I J. of Mech. Sci.*, v. 36, n. 10, 1994, pp. 897-910.

- [19] Sang, H.; Lloyd, D.J.: The influence of biaxial prestrain on the tensile properties of three aluminum alloys. *Metall. Trans. A*, 10A, 1979, pp. 1771-1776.

Material Characterization at High Strain Rates with Special Emphasis on Miniaturization and Size Dependencies *

N. Herzig¹, L.W. Meyer¹

¹ Materials and Impact Engineering, Chemnitz University of Technology

Abstract

Within the present work the size-dependent flow stress and failure behaviour of various metallic materials is described. Starting with special issues of testing miniaturized specimens, the influence of manufacturing routes and manufacturing induced geometrical deviations is investigated. The specimen size and time-dependent flow stress behavior of C45E, Ti-6-22-22S, and Al7075T6 is presented. The measured behavior is explained by size-dependent friction effects. Additionally, the influence of size and time scaling on the occurring of failure is investigated. A decrease of compressive deformability with increasing size and strain rate was found. The consideration of a size-dependent thermodynamic process character provides a possible explanation for measured size dependencies.

Keywords:

Material, Strain rate, Miniaturization

1 Introduction

The increased miniaturization of components and processes has led to an increased interest in size effects. They may appear as a not directly predictable change of component or process behaviour, even when scaling is done in correct similarity relations. In material characterization size effects under various loading types and conditions are widely discussed (e.g. [1]-[6]). Nevertheless, less is known about size dependencies at high strain rates.

* This work is part of the DFG priority programme "Process Scaling"; the authors would like to thank the DFG for its financial support.

This study presents experimentally measured size effects on flow stress and failure behavior of different metallic materials within a wide range of strain rates. Special issues of testing miniaturized specimens concerning the influence of manufacturing procedure and geometrical deviations as well as multiple specimen testing are described. Size and time dependencies of flow stress and failure behavior of an unalloyed steel, a titanium, and an aluminum alloy are presented. Possible explanations for the measured behavior result from a size-dependent frictional behavior as well as from size and time dependencies of the thermodynamic state during the deformation process.

2 Special issues of testing miniaturized specimens

2.1 Influence of manufacturing procedure

The characterization of the mechanical behavior of materials starts with the manufacturing of the specimens itself. Especially for testing of miniaturized specimens intensified requirements on accuracy have to be fulfilled.

Preliminary investigations on the influence of different manufacturing routes on the measured material behavior under compressive loading were made by use of the tool steel 40CrMnMo7 [7]. Micro hardness measurements and the determination of residual stresses within the peripheral zone of the specimens lead to different results according to the applied manufacturing procedure, e.g. eroding, grinding, etc. This leads to a significant influence on the measured flow stresses, which were found to be in the order of 50 to 80 MPa. Especially at high strain rates the measured influence of manufacturing routes was increased.

2.2 Influence of geometrical deviations

Due to deviations of guideways and clamping of manufacturing machines as well as oscillations and wear of tools respectively, specimens used in mechanical testing may be flawed by geometrical deviations and roughness of the surface areas. Until now, less is known about the influence of manufacturing induced deviations on the measured material behavior, especially at high loading rates.

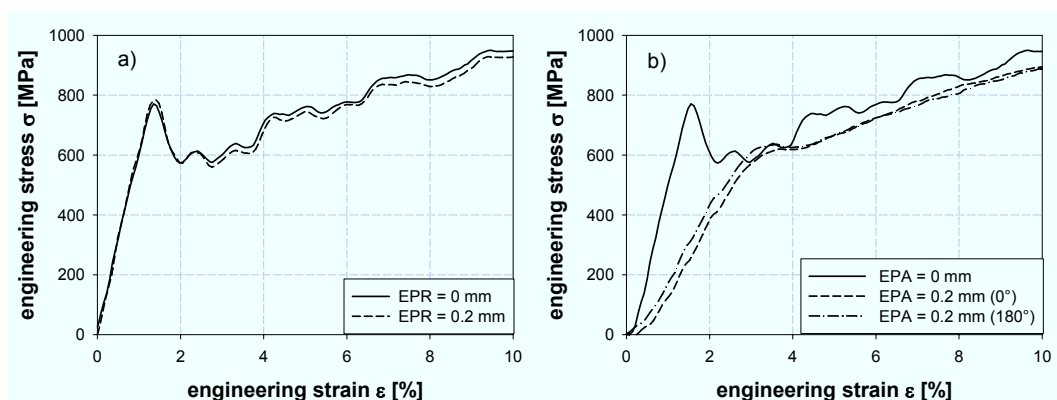


Figure 1: Influence of (a) rectangularity (EPR) and (b) parallelism (EPA) on flow stress of C45E at 200 s^{-1} under compressive loading

Preliminary investigations by use of artificially flawed specimens under compressive loading have shown that e.g. parallelism deviation leads to a distortion of the stress strain distribution and a flattening of the scope in the material's stress-strain-response (Fig. 1,2). Hence, the true flow stress versus plastic strain is underestimated. Although deviations in rectangularity also distort stress and strain distribution, an influence on the measured flow stresses was not found.

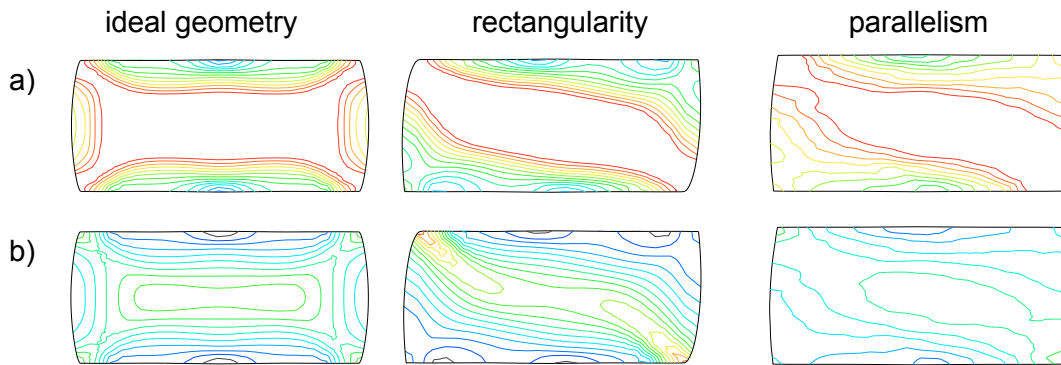


Figure 2: Distribution of (a) von Mises stress and (b) equivalent strain of geometrically deviated cylindrical compression specimens.

Under tensile loading conditions geometrical deviations may also influence the measured stress-strain-response of the material. According to the specimen size and type of deviation, a decrease of the macroscopically measured yield stress as well as a displacement of necking to smaller deformations was found by preliminary FEM simulations (Fig. 3).

Therefore, an accurate specimen manufacturing route with smallest geometrical deviations is required for the testing of miniaturized specimens.

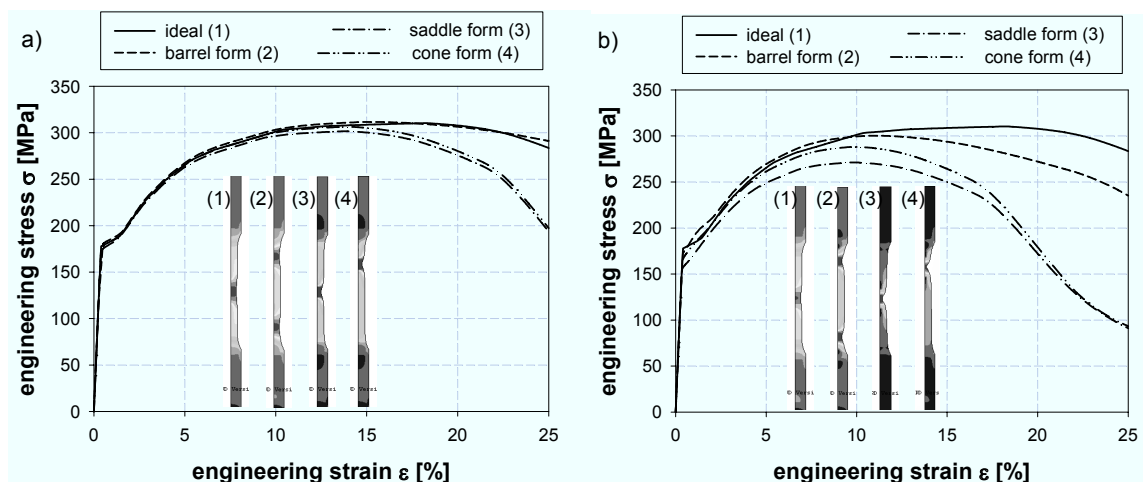


Figure 3: Influence of geometrical deviations under tensile loading: (a) Ø9x45, (b) Ø2x10 calculated by ABAQUS/Standard

2.3 Multiple specimen testing

The determination of the flow stress behavior by use of small specimens requires high accuracy and resolution of force and deformation measuring systems. Preliminary studies have shown that multiple specimen testing improves the signal quality by increasing the total measured forces under compressive as well as under tensile loading conditions. The calculated stresses are nearly identical to single specimen tests, but oscillations in force-time characteristics are reduced significantly (Fig. 4a). Hence, multiple specimen testing is appropriate for the determination of the flow stress behavior of miniaturized specimens.

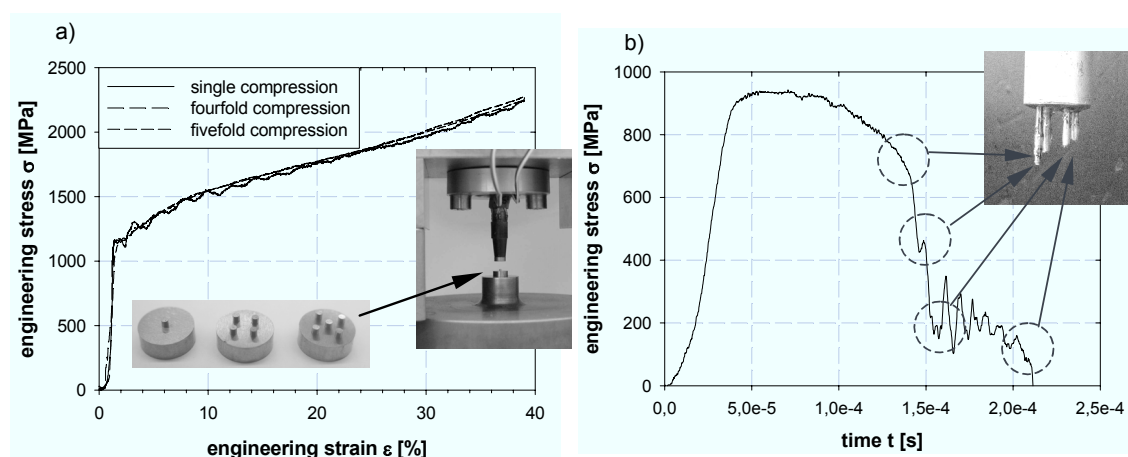


Figure 4: Multiple specimen testing under high loading rates: (a) cylindrical compression test by drop weight device, (b) tensile test by rotating wheel

For the investigation of failure behavior of materials single specimen testing is necessary. Due to the statistical character of initiation and development failure occurs at different times and an unequivocal assignment of failure occurring to a definite stress or strain level is not possible (Fig. 4b).

3 Materials and methods

The experimental investigations on size and time dependencies of flow stress and strengthening were carried out by use of the unalloyed carbon steel C45E in a normalized condition. Additionally, an aluminum and a titanium alloy were used for studying size effects on failure behavior under compressive loading. Their chemical composition is shown in Table 1.

For the experimental investigations under compressive loading both commonly available as well as specially designed testing devices were used. The specimens were scaled in diameter between 1 and 9 mm and in aspect ratio (height to diameter) between 0.5 to 1.5, respectively. Under quasistatic and low dynamic loading conditions mechanical and servo hydraulic universal testing machines were applied. Force was measured by calibrated and adjusted load cells. Deformation was measured by strain gauges and incremental gauges respectively.

<i>Carbon steel C45E</i>							
C	Si	Mn	P	S	Cr	Mo	Ni
0.42-0.5	0-0.4	0.5-0.8	0-0.035	0-0.035	0-0.4	0-0.1	0-0.4

<i>Aluminum alloy Al7075 T6</i>								
Zn	Mg	Cu	Fe	Si	Mn	Ti	Cr	Zr
5.1-6.1	2.1-2.9	1.2-2.0	0.50	0.40	0.30	0.20	0.18-0.28	0.05

<i>Titanium alloy Ti-6-22-22S</i>									
Al	Sn	Zr	Mo	Cr	Si	Fe	O	N	C
5.75	1.96	1.99	2.15	2.10	0.13	0.04	0.082	0.006	0.009

Table 1: Chemical compositions (wt.%)

High dynamic compression tests at strain rates of 10^2 to 10^4 s⁻¹ were carried out by use of drop weight and Hopkinson devices. A detailed description of the test procedure is given in e.g. [8], [9]. In drop weight tests the displacement is measured by incremental gauges. The force is calculated from the elastic deformation of the punch by means of calibrated strain gauges and Hookes law. In Hopkinson tests the stress-strain-response of the material is based on principles of one-dimensional elastic-wave propagation within the pressure bars.

4 Experimental results and discussion

4.1 Flow and strengthening behavior

Fig. 5 shows the size- and time-dependent flow stress and strengthening behavior of C45E, Ti-6-22-22S, and Al7075.

Under quasistatic as well as under dynamic loading conditions a size-dependent flow behavior was measured. The flow stresses of the smaller specimens ($\varnothing 1$ mm) are significantly higher than those of the larger specimens ($\varnothing 9$ mm). The differences are about 50 to 100 MPa. Furthermore, Fig. 5 illustrates the dependency of the flow stress from the logarithmic strain rate. The unalloyed steel and the titanium alloy show a thermal activated flow stress behavior. The flow stress is increased with logarithmic strain rate. Their constitutive behavior can be described by the model of Zerilli-Armstrong [10]. For the aluminum alloy a nearly athermal behavior was found. Its constitutive behavior may be described by the model of Johnson-Cook [11].

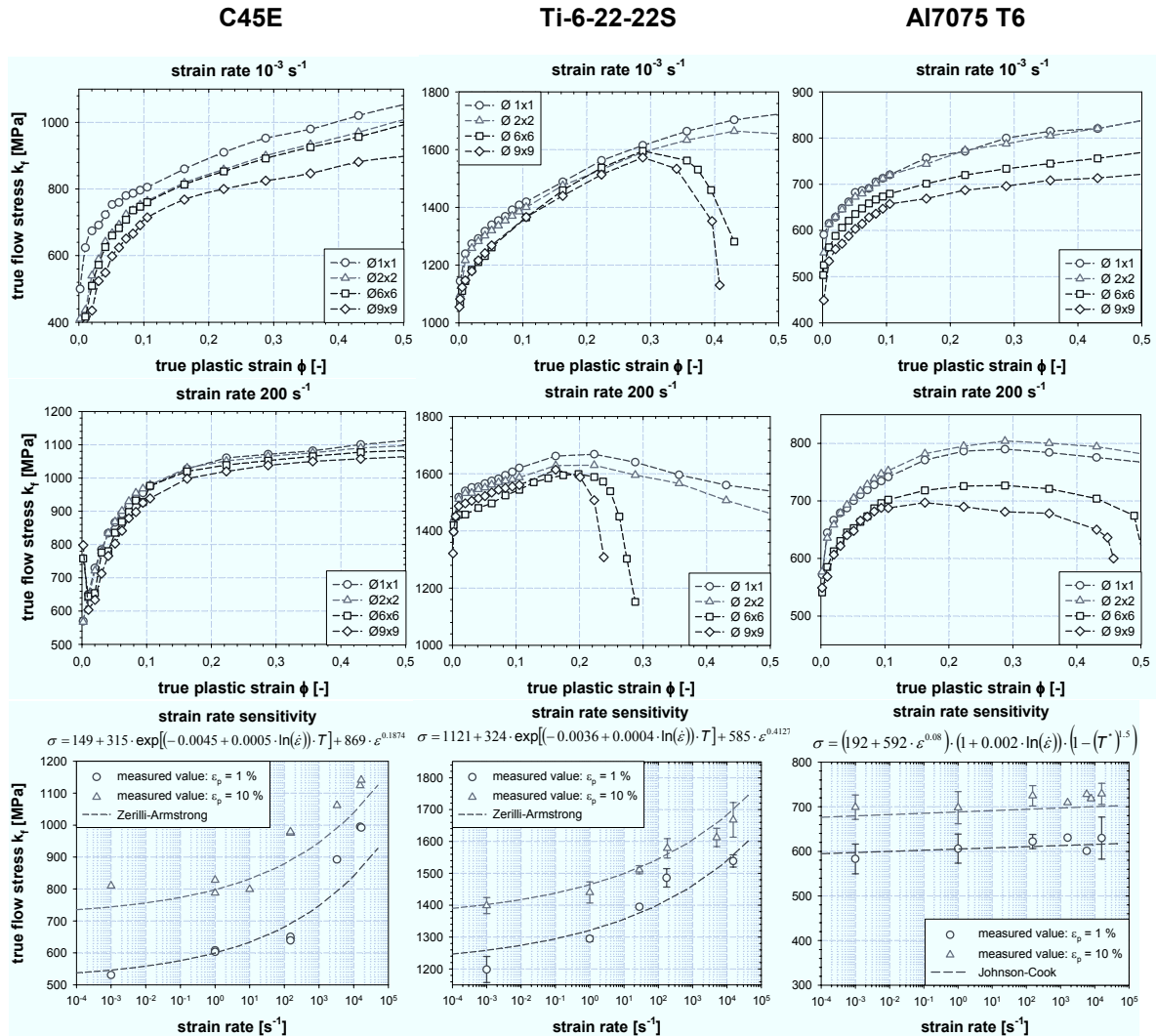


Figure 5: Size-dependent flow and strengthening behavior of C45E, Ti-6-22-22S, and Al7075 under quasistatic and dynamic loading conditions

To explain the measured behaviour, the influence of friction on flow stress was investigated. Due to the disproportionate increase of friction-affected surface relative to specimen volume and the fraction of roughness-affected surface respectively, a size-dependent frictional behavior was expected.

To quantify the effect, cylindrical compression tests until 50 % plastic strain were calculated by ABAQUS/Standard and the friction coefficient μ was varied in a range of 0 and 0.15. The deformed geometry was characterized both by ratio of maximum to minimum diameter as well as by the bulging angle α . Furthermore, quasistatic cylindrical compression tests were realized, whereby the deformed specimen was geometrically characterized in the same way. The results are shown in Fig. 6a. Hence, friction-corrected flow curves are calculated (Fig. 6b), which are nearly identical for the different specimen sizes.

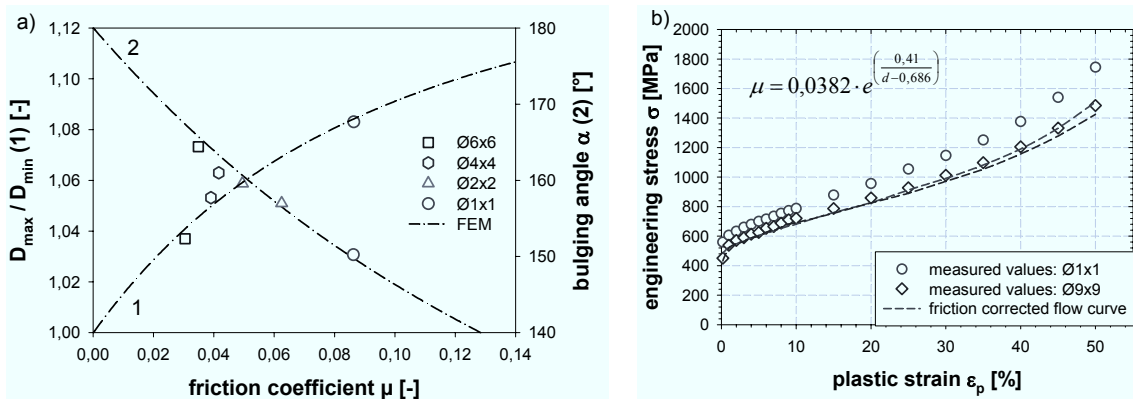


Figure 6: a) Size dependent friction coefficient μ of Al7075 T6 and b) friction-corrected flow curves of Al7075 T6 at a strain rate of 10^{-3} s^{-1}

At high strain rates friction may also play an important role. Additionally, the influence of heat development and heat transfer has to be considered.

4.2 Failure behavior

Investigations on the failure behavior of the titanium and the aluminum alloy yield to a significant size-dependent failure initiation and plastic deformability until fracture. There, the titanium alloy tends to fail even under quasistatic loading conditions, whereas the aluminum alloy only failed at high strain rates. Both materials tend to fail due to adiabatic shear bending at high loading rates. Fig. 7 illustrates the size- and time-dependent failure behavior of both materials. An increase of strain rate as well as an increase of specimen size leads to a decrease of compressive deformability.

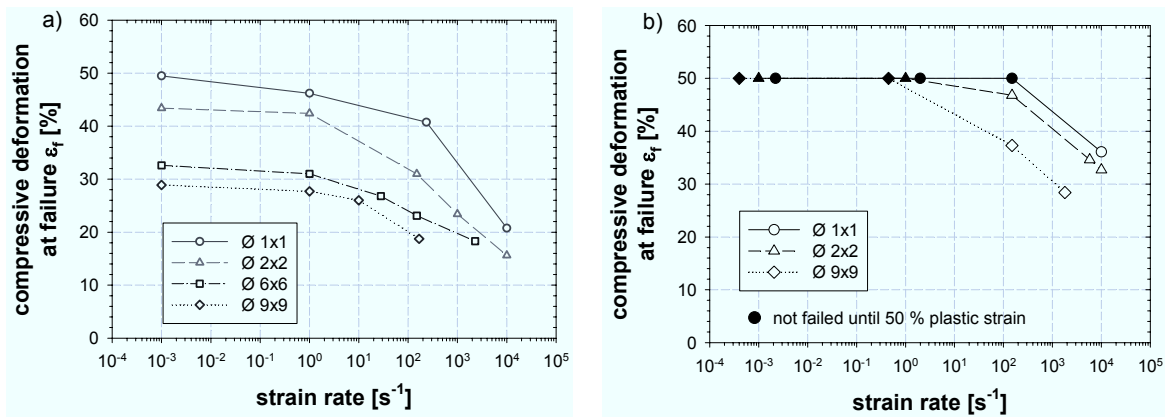


Figure 7: Size- and time-dependent compressive deformability of a) Ti-6-22-22S and b) Al7075 T6.

To investigate the failure process itself, stopped cylindrical compression tests followed by microstructure investigations were performed. Hence, a size dependency was found at the microscopic level (failure initiation) and at the macroscopic level (fracture characteristics). Under quasistatic loading conditions the size-dependent failure behaviour is explained by friction effects [12].

At high strain rates thermodynamic aspects are taken into account. In [13], the transition of isothermal to adiabatic process conditions is described by Fourier number F_0 (Eq. 1). The process time t is substituted by strain ε and strain rate $\dot{\varepsilon}$,

$$F_0 = \frac{\alpha \cdot t}{l^2} = \frac{\alpha \cdot \varepsilon}{\dot{\varepsilon} \cdot l^2} \quad (1)$$

where α is the thermal diffusivity and l the characteristic length.

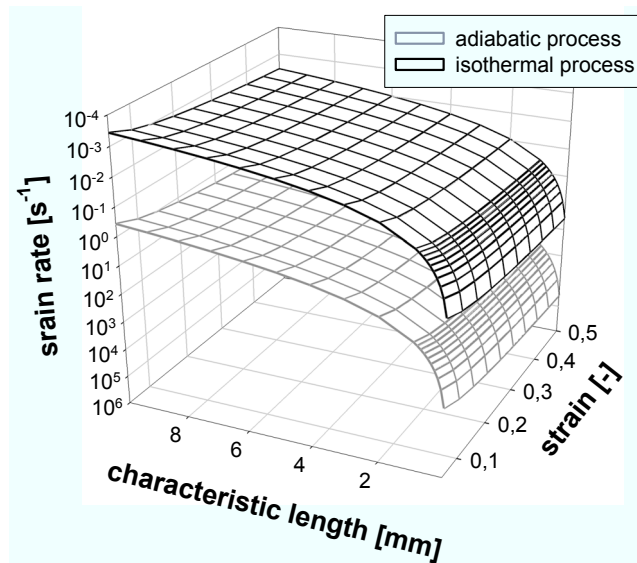


Figure 8: Size-dependent transition of isothermal to adiabatic process conditions for the titanium alloy Ti-6-22-22S

Assuming an adiabatic process for $F_0 < 0,01$ and an isothermal process for $F_0 > 10$, Fig. 8 can be drawn. It illustrates that the transition to adiabatic process conditions is displaced to high strain rates with decreasing size. Hence, testing miniaturized specimens to obtain highest strain rates would lead to an unknown increase of flow stress due to the minor temperature increase and to an underestimation of temperature-induced softening respectively. However, now the question arises: What happens when the thermodynamic state is kept constant ?

To ensure a constant thermodynamic state represented by Fourier number F_0 , the results of stopped cylindrical compression tests for $\varnothing 2$ mm specimens at 250 s^{-1} and $\varnothing 6$ mm specimens at 28 s^{-1} were compared. It was shown that both failure initiation as well as compressive deformability were similar (Fig. 9). The larger flow stress of the $\varnothing 2$ mm specimen is explained by the thermally activated increase of flow stress with increasing strain rate. At loading rates larger than 10^3 s^{-1} this behavior was not confirmed.

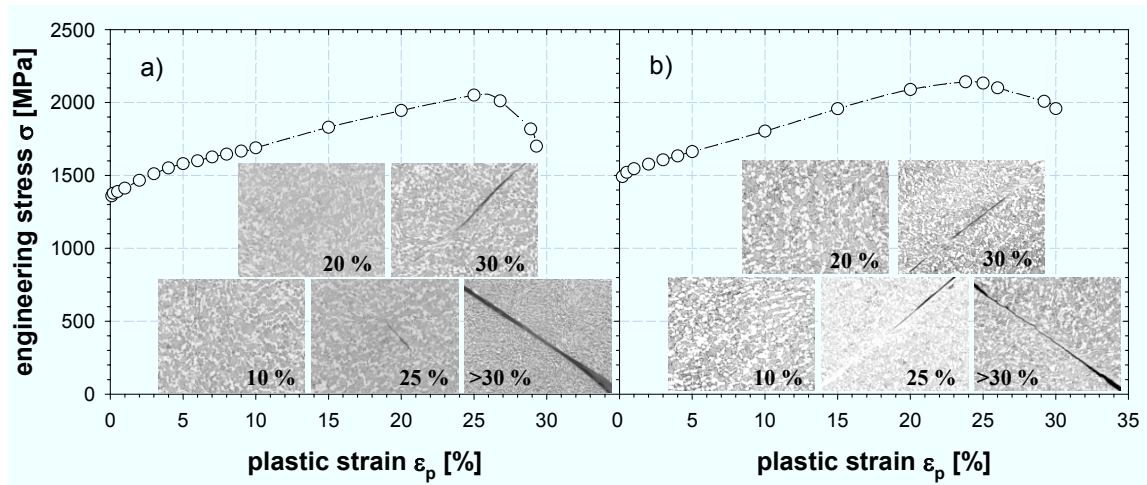


Figure 9: Failure development for Ti-6-22-22S under compressive loading: a) Ø6x6 at 28 s^{-1} and b) Ø2x2 at 250 s^{-1} .

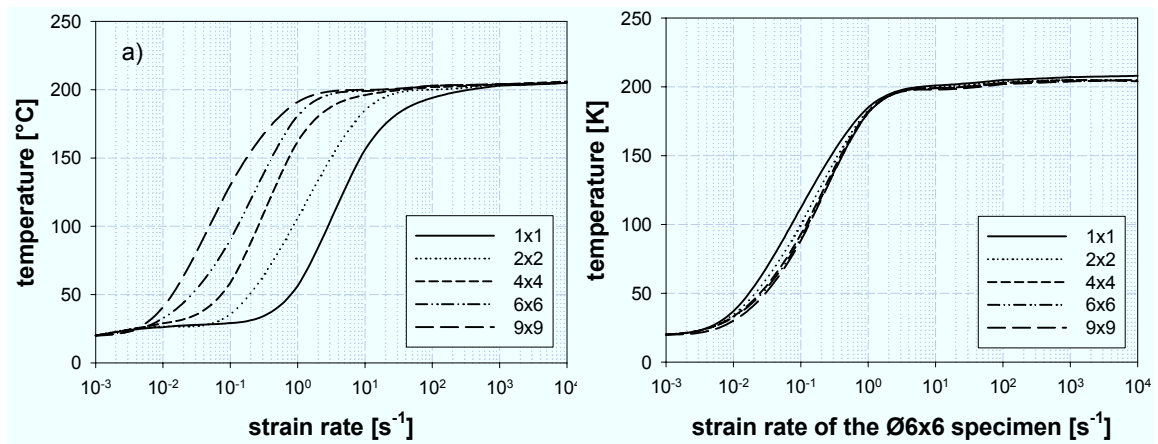


Figure 10: Size- and time-dependent temperature development in the core of a cylindrical compression specimen (30 % strained) calculated by FEM (Deform 2D): a) without and b) with consideration of the displacement of the transition area from an isothermal to an adiabatic process with reducing size (relating to Ø6x6 specimens)

The evaluation of the temperature evolution calculated by FEM led to a size-dependent temperature increase versus strain rate (Fig. 10a). Keeping the thermodynamic state constant by adjusting the strain rate relating to Ø6x6 specimens and by applying Eq. 1, a similar temperature development versus strain rate was found (Fig. 10b). This may give an explanation for the measured behavior. At high strain rates ($>10^3 \text{ s}^{-1}$) the temperature evolution led to a saturation, which may explain that at highest strain rates the approach described above is not applicable.

5 Conclusions

Within this work it was shown that the mechanical testing of miniaturized specimens leads to increasing requirements resulting from the manufacturing procedure, including the development of micro hardness, residual stresses, and geometrical deviations. A size-

and time-dependent flow stress and failure behavior was found for various materials. At quasistatic and low dynamic rates possible explanations are given by increased friction effects with reducing size. Additionally, at high strain rates the thermodynamic state has to be considered. A size- and time-dependent temperature evolution was found, which may cause the macroscopically measured size effect. An adjustment according to Ø6 mm specimens led to a nearly identical behavior. Due to the saturation of temperature development the assumptions made at low and intermediate strain rates up to 10^2 s^{-1} are not directly transferable to describe the material behavior at highest strain rates.

References

- [1] *Armstrong, R.W.*: On size effects in polycrystal plasticity. *J. Mechanics and Physics of Solids*, 9 (1961), 196-199.
- [2] *Gunasekera, J.S.; Havranek, J.; Littlejohn, M.H.*: The effect of specimen size on stress-strain-behaviour in compression. *Trans. ASME*, 104 (1982), 274-279.
- [3] *Gorham, D.A.*: The effect of specimen dimensions on high strain rate compression measurements of copper. *Appl. Physics*, 24 (1991), 1489-1492.
- [4] *Niezgodninski, M.*: Einwirkung der Probengröße auf die Zugfestigkeit plastischer Kupferlegierungen. *Freiberger Forschungshefte* 123, 1967, Seite 79-94.
- [5] *Fleck, N.A.; Muller, G.M.; Ashby, M.F.; Hutchinson, J.W.*: Strain gradient plasticity: theory and experiment. *Acta Materialia et Metallurgica*, 42 (1994), 475-487.
- [6] *Stölken, J.S.; Evans, A.G.*: A microbend test method for measuring the plasticity length scale. *Acta Materialia et Metallurgica*, 46 (1998), 5109-5115.
- [7] *Krüger, L.; Meyer, L.W.; Halle, T.; Herzig, N.*: Size effects on flow stress behaviour of tool steel 40CrMnMo7 at high loading rates. *Proc. 6th Mesomechanics*, 2004, Patras (Greece), 420-425.
- [8] *Meyer, L.W.; Krüger, L.*: Drop-Weight Compression Shear Testing. *ASM Handbook*, Vol. 8, Mechanical Testing and Evaluation, Materials Park, Ohio, 2000, 452-454.
- [9] *Gray, G.T.*: Classic Split-Hopkinson Pressure Bar-Testing. *ASM Handbook*, Vol. 8, Mechanical Testing and Evaluation, Materials Park, Ohio, 2000, 462-476.
- [10] *Zerilli, F.J.; Armstrong, R.W.*: Dislocation-mechanics-based constitutive relations for material dynamic calculations. *Journal of Applied Physics*, 61 (1987), 1816-1825.
- [11] *Johnson, G.R.; Cook, W.H.*: A constitutive model and data for metals subjected to large strain, high strain rates and high temperatures. *Proc. 7th Int. Symposium on Ballistics*, 1983, 541-547.
- [12] *Meyer, L.W.; Herzig, N.*: Größeneinflüsse beim Fließ-, Verfestigungs- und Versagensverhalten metallischer Werkstoffe. *Proc. 2nd Koll. Process Scaling*, 2005, Bremen (Germany), 147-156.
- [13] *Zehnder, A.T.; Babinsky, E.; Palmer, T.*: Hybrid method for determining the fraction of plastic work converted to heat. *Experimental Mechanics*, 38 (1998), 295-302.

On the effect of current pulses on the material behavior during electromagnetic metal forming ^{*}

J. Unger¹, M. Stiemer², L. Walden³, F. Bach³, H. Blum², B. Svendsen¹

¹ Chair of Mechanics, University of Dortmund, Germany

² Chair of Scientific Computing, University of Dortmund, Germany

³ Institute of Material Technology, University of Hannover, Germany

Abstract

Electromagnetic sheet metal forming (EMF) is an example of a high-speed forming process driven by the dynamics of a coupled electromagnetic-mechanical system. Basic physical processes involved in EMF, such as e.g. inelastic and hardening behavior or inertia, have been considered in previous works [1, 2]. The purpose of the current work is the investigation of temperature development during EMF and a possible reduction in the yield stress due to electric currents. While thermoelastic and viscoplastic effects are well-understood in this context [3], the possible influence of electric currents on dislocation motion, generally referred to as the electro-plastic effect [4, 5], is still an unresolved issue. In agreement with previous works [e.g., 6], it is concluded here that such an effect is at most of second-order and can most likely be safely neglected in the modeling and simulation of industrial EMF.

Keywords:

Electromagnetic metal forming, Electroplasticity, Magneto-thermo-inelastic coupling

1 Introduction

In electromagnetic metal forming (EMF) a strong pulsed magnetic field generated in the tool coil adjacent to an electrically-conducting workpiece induces eddy currents in the workpiece, which interact with the magnetic field, inducing, in turn, a Lorentz (body) force (density) in the work-piece which drives the forming process. The entire forming process takes approximately

^{*} This work was carried out in the context of the German Research Foundation (Deutsche Forschungsgemeinschaft (DFG)) Research Group FOR 443. The authors wish to thank the DFG for its financial support.

100-300 μs and achieves strain-rates of up to 10^4 s^{-1} . Compared to other forming methods, it offers increased formability for certain kinds of materials, reduction in wrinkling, the possibility of combining forming and assembly operations, reduced tool-making costs *etc.*. An example of the basic experimental setup for the case of sheet metal forming is shown in Figure 1. The time-dependent current in the tool coil shown on the right in this figure depicts the pulsed nature of this current and, thus, of the resulting magnetic field.

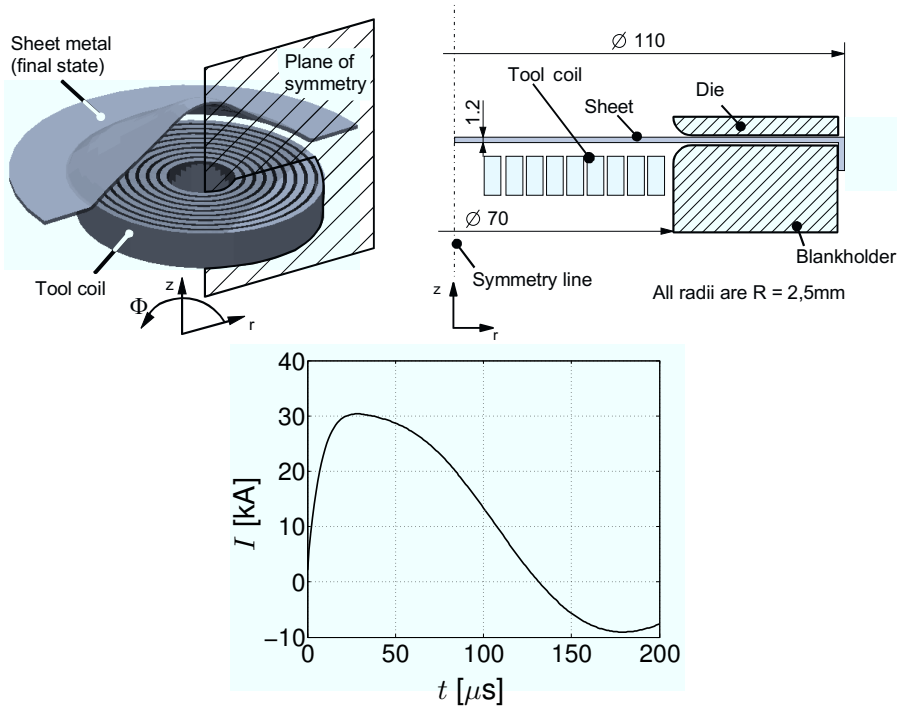


Figure 1: Electromagnetic sheet metal forming setup

The further development of EMF as an industrial forming process depends in particular on the availability and use of reliable simulation tools for the corresponding coupled multifield problem. In particular, these must be able to deal with high strain rates $\dot{\epsilon} \geq 10^4 \text{ s}^{-1}$, large current densities $|j| \geq 10^4 \text{ A/mm}^2$, and strong magnetic fields $|b| \geq 10^0 \text{ T}$. In this context, we examine possible effects in the material such as a reduction in yield stress due to temperature and/or strong electrical currents. In the literature, the electroplastic (EP) effect has been postulated to contribute to the behavior of metals under combined mechanical and electromagnetic loading [7, 8]. Here, the idea is that an interaction between the electric current and dislocations may affect the hardening behavior and, in particular, the yield stress. There has been a considerable debate regarding the significance of such an effect in polycrystal metals [9]. Figure 2 shows the current density and tensile test response of an experiment performed by Okazaki *et al.* [10]. In their experiment, a titanium bar with diameter $d = 0.511 \text{ mm}$ was loaded in simple tension. As shown in Figure 2, the discharge of a capacitor bank at given times during this loading resulted in a sudden increase in the current density and the time-correlated drop in the yield stress. Okazaki *et al.* [10] showed that each of these current-density “jumps” resulted in a temperature rise of about 12.2 K to 99.9 K, depending on the imposed current density. Since a temperature rise of this order of magnitude implies a drop of the yield stress of about 0.4%

and 5.0%, authors favoring the electroplastic effect concluded that the observed drops are due to an interaction of electron movements and the moving dislocations.

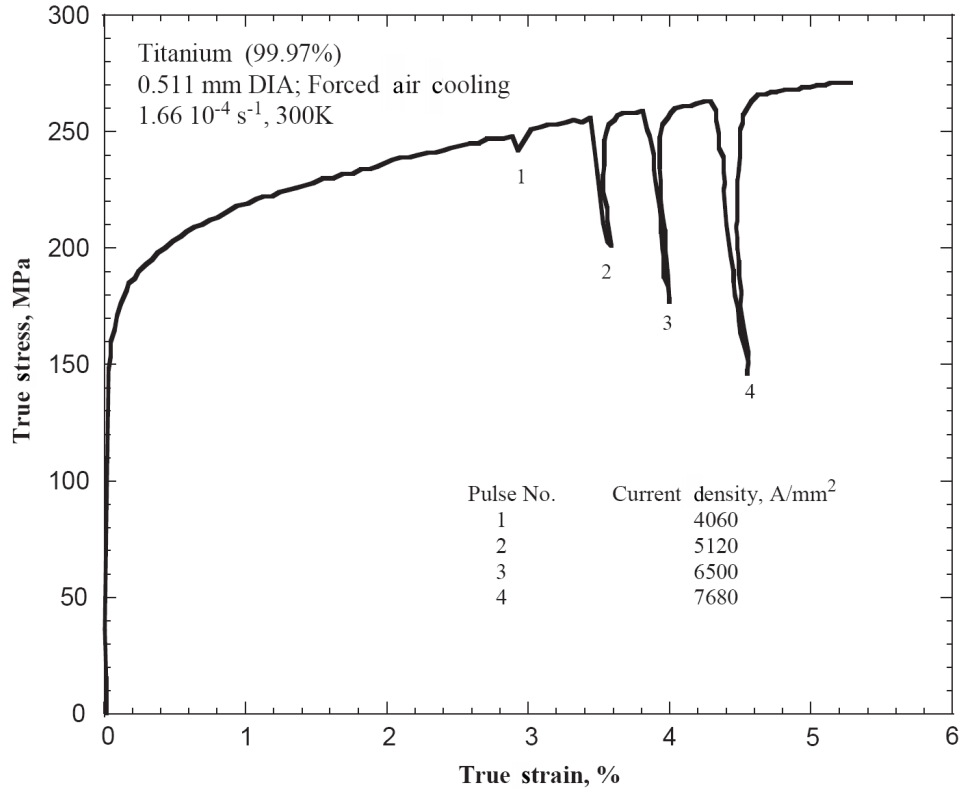


Figure 2: Experimental results of Okazaki *et al.* [10]. During tensile testing of a circular bar an imposed current density results in stress drops. The current density achieved maximum values of 4060 to 7680 A/mm² and lasted for about 60 μs . For pulse no. the 2 tensile stress decreased to about 70% of its original value.

Recently, Bilyk *et al.* [6] showed that the introduction of an EP effect is not necessary to explain the stress drops shown in Figure 2. Bilyk *et al.* [6] concluded that the stress drops can be modeled by an accurate modeling of viscoplastic rate effects during pulsing. The work presented here confirms the view that the stress drops can be explained with the help of conventional effects like Joule heating, thermal expansion, and viscoplasticity. In particular, we focus here on thermal expansion.

2 Thermoelastic, viscoplastic model including Joule heating

The multifield material model used in the current work represents a special case of the general continuum thermodynamic formulation of such models from Svendsen & Chanda [1] to the formulation of models for electromagnetic thermoelastic, viscoplastic solids. In particular, this work provides a framework for the treatment of EMF processes also accounting for the interaction between the electromagnetic and thermomechanical effects at *large* deformation. The case of the simple tension tests mentioned above is somewhat simpler than the one of sheet

metal forming shown in Figure 1 in the sense that the total strain is significantly smaller ($\approx 5\%$). According to Svendsen & Chanda [1], the magnetic field can be modeled as diffusive over the length- and timescales of interest. In this case, Maxwell's equations and Ohm's law yield the diffusive field relation

$$\mathbf{0} = \partial \mathbf{b} - \kappa_{EM} \nabla^2 \mathbf{b} \quad (1)$$

for the spatial magnetic flux density \mathbf{b} . Here, $\kappa_{EM} := \sigma_{EM}^{-1} \mu_{EM}^{-1}$ represents the magnetic diffusivity, μ_{EM} the magnetic permeability, and σ_{EM} the electric permittivity. (Note that all material and modeling data can be found in Tables 2 and 3 as well as in §2). In particular, on a timescale τ , κ_{EM} implies a skin depth (*i.e.* penetration depth of the magnetic field into the material) of $\ell_{EM} = \sqrt{\kappa_{EM} \tau}$. As indicated in Table 1, for the case of titanium the skin depth is significantly larger than the radius of the “bar” (*i.e.*, a wire here). Consequently, the current density is in the wire. For a long wire (*i.e.*, $l/r_0 \gg 1$), (1) can be solved to obtain

$$(b_r, b_\varphi, b_z)(r) = (0, \frac{\sigma_{EM} I r}{2\pi r_0^2}, 0) \quad (2)$$

in cylindrical coordinates (r, φ, z) [11]. Here I represents the imposed current, and r_0 the radius of the wire. In turn, this implies a constant current density

$$(j_r, j_\varphi, j_z)(r) = (0, 0, I/\pi r_0^2) \quad (3)$$

within the cross-section of the wire.

Next, consider the energy balance and temperature evolution in the bar. Here, the characteristic lengthscale is determined as usual by the thermal diffusivity $\kappa_{TM} := k_r / \rho_r c_r$, where k_r represents the thermal conductivity, c_r the specific heat capacity, and ρ_r the mass density at reference temperature θ_r . As usual, on a timescale τ significant thermal conduction will take place on the lengthscale $\ell_{TM} = \sqrt{\kappa_{TM} \tau}$. Since this lengthscale is much smaller than the width of the wire (see Table 1), we are justified in assuming adiabatic conditions over the timescale of the pulses ($\leq 100 \mu\text{s}$). Over longer timescales, of course, this is not the case. Finally, in contrast to EMF we neglect the radially acting Lorentz force for two reasons: firstly, its magnitude is significantly smaller than the applied mechanical loads [6] and, secondly, due to the geometric conditions the structural response is minimal.

	ℓ_{EM}/r_0	ℓ_{TM}/r_0
Al	5.8×10^0	4.0×10^{-1}
Ti	2.2×10^1	1.2×10^{-1}
Assumption	Uniform current density	Adiabatic during pulsing

Table 1: Scaling relations for electromagnetic diffusion and thermal diffusion

With these simplifications the temperature is homogeneous and treated as an internal variable (see (10)₃ below). Consequently, the deformation ξ is the only thermomechanical field, given as usual by the weak form

$$\int_{B_t} \rho_r \ddot{\xi} \cdot \xi_* + \mathbf{K} \cdot \nabla \xi_* = 0 \quad (4)$$

for pure kinematic boundary conditions with respect to the reference configuration B_r for all corresponding test fields ξ_* . Here, \mathbf{K} represents the Kirchhoff stress. As usual, this latter variable, along with the internal variables, is given by a material model. For simplicity, attention is restricted here to the case of (isotropic) thermoelastoviscoplasticity with isotropic hardening. Further, in the case of metals, we have small elastic strain. The relevant internal variables are then the elastic left logarithmic stretch $\ln \mathbf{V}_E$ and the accumulated inelastic strain ϵ_p . On this basis, the thermodynamic formulation being pursued here is based on specific model relations for the referential free energy density ψ as well as on the evolution relations for the internal variables. In particular, assuming for simplicity that the elastic behavior is not affected by inelastic processes such as damage, the split

$$\psi(\theta, \ln \mathbf{V}_E, \epsilon_p) = \psi_E(\theta, \ln \mathbf{V}_E) + \psi_p(\theta, \epsilon_p) \quad (5)$$

of the free energy into thermoelastic and inelastic parts is justified [*e.g.*, 12]. Assuming for simplicity that the specific heat capacity c_r is constant [13] and exploiting the condition of small elastic strain, one obtains the thermoelastic neo-Hooke form

$$\begin{aligned} \psi_E(\theta, \ln \mathbf{V}_E) &= \frac{1}{2} \lambda_r (\mathbf{I} \cdot \ln \mathbf{V}_E)^2 - (3\lambda_r + 2\mu_r) \alpha_r (\theta - \theta_r) (\mathbf{I} \cdot \ln \mathbf{V}_E) + \frac{1}{2} \mu_r (\ln \mathbf{V}_E \cdot \ln \mathbf{V}_E) \\ &+ \varrho_r c_r [\theta - \theta_r - \theta \ln(\theta/\theta_r)] \end{aligned} \quad (6)$$

for ψ_E , where λ_r and μ_r represent Lamé's constants and α_r the thermal heat expansion coefficient. The inelastic part ψ_p is determined empirically with the help of experimental data, as discussed in the next section. Next, consider the evolution of the internal variables and the inelastic behavior. In the metallic polycrystalline materials of interest at low-to-moderate homologous temperature, inelastic deformation processes are controlled predominantly by the activation of dislocation glide on glide systems (*e.g.*, [14]), even at higher strain-rates. As such, higher homologous temperatures are required for other mechanisms such as dislocation climb or even dynamic recrystallization to activate. Resistance to dislocation glide arises due to extended obstacles generating longer-range stress fields related in the phenomenological context to hardening behavior. In addition, such resistance is caused by short-range local obstacles which can be overcome by thermal fluctuation under the action of local effective stress, represented in the current phenomenological context by $|\text{dev}(\mathbf{K})| + \varsigma_p - \sigma_{f0}(\theta)$, where

$$-\varsigma_p := \psi_{,\epsilon_p} \quad (7)$$

represents the static contribution to the flow stress (in shear). On this basis,

$$f_p := \frac{|\text{dev}(\mathbf{K})| + \varsigma_p}{\sigma_p} \quad (8)$$

represents an activation function or non-dimensional overstress in the current rate-dependent context. Here, σ_p represents the dynamic drag contribution to the effective flow stress in the system. On this basis, a power-law approximation of the more exact transition-state-based micromechanical relations for the kinetics of dislocation glide leads to the power-law form

$$\phi = \frac{\gamma_p \sigma_p}{m_p + 1} \langle f_p \rangle^{m_p + 1} \quad (9)$$

upon which the evolution of the internal variables is based. Here, γ_p represents a characteristic strain-rate, $\langle x \rangle := \frac{1}{2} (x + |x|)$ the MaCauley bracket, and m_p the strain-rate exponent. In general, these will be functions of temperature and rate of deformation; here, we treat them for simplicity as constants. This potential determines as usual the forms

$$\begin{aligned} \ln \mathbf{V}_E^* &= -\phi_{,K} &= -\text{sgn}(\text{dev}(\mathbf{K})) \dot{\epsilon}_p \quad (\mathbf{K} \neq \mathbf{0}), \\ \dot{\epsilon}_p &= \phi_{,s_p} &= \gamma_p \langle f_p \rangle^{m_p} \quad (f_p > 0), \\ \dot{\theta} &= \varrho_r^{-1} c_r^{-1} \{ \omega_r + \sigma_{EM}^{-1} \det(\mathbf{F}) \mathbf{j} \cdot \mathbf{j} \} \quad , \end{aligned} \quad (10)$$

for the evolution of the internal variables. Here, ω_r represents the rate of mechanical heating and $\sigma_{EM}^{-1} \mathbf{j} \cdot \mathbf{j}$ the electromotive power.

Now, for the case of incompressible material behavior, we assume that the isotropic forms of the viscoplastic parameters γ_p , σ_p , and m_p are independent of the trace $\mathbf{I} \cdot \mathbf{D}$ of the rate of deformation. In this case, the thermoelastic form

$$\mathbf{K} = \psi_{, \ln \mathbf{V}_E} = \{ \lambda_r (\mathbf{I} \cdot \ln \mathbf{V}_E) - (3\lambda_r + 2\mu_r) \alpha_r (\theta - \theta_r) \} \mathbf{I} + \mu_r \ln \mathbf{V}_E \quad (11)$$

for the Kirchhoff stress holds from (6). In addition,

$$\omega_r = \gamma_p \sigma_p \langle f_p \rangle^{m_p+1} - (3\lambda_r + 2\mu_r) \alpha_r \theta \overline{\ln \det(\mathbf{F})} \quad (12)$$

then follows for the referential form of the mechanical heating rate.

This completes the basic model formulation. The detailed algorithmic formulation and numerical implementation of the finite-element-model has been presented in Stiemer *et al.* [2]. In particular, note that the time-step size for tensile test simulation has to be chosen according to the particular time scale where changes of internal variables are to be expected. During current pulses the time-step size was chosen to be 10^{-6} s. Otherwise, much larger step sizes on the order of 10^0 s were chosen. The time integration of the velocity and acceleration fields was carried out using Newmark's method. Numerical damping was applied during pulsing and afterwards in order to avoid unphysical oscillations.

3 Application to metal bars subject to pulsed currents and simple tension

In this section, the current model is applied to the tensile tests with pulsed electric currents. To this end, we specify the semi-analytical form

$$-s_p = \psi_{, \epsilon_p} = \sigma_{F0} \left(1 + \frac{\epsilon_p}{\epsilon_0} \right)^n - \sigma_{F0} \quad (13)$$

for the strain hardening due to energy storage, with

$$\sigma_{F0} = \sigma_{F0r} (1 - \omega_{TM} (\theta - \theta_r)) \quad (14)$$

of the initial static flow stress, σ_{F0r} being the initial flow stress at reference temperature θ_r . The parameter ω_{TM} mediates the reduction of the initial flow stress due to an increase of the

temperature. Table 2 summarizes the material parameters characterizing the inelastic material behavior. For titanium, the parameters in (13) were obtained from Bilyk *et al.* [6]. In particular, ω_{TM} , γ_P , σ_P , and m_P were fitted to the model data also provided in Bilyk *et al.* [6]. For aluminum, the tensile test data were used for the strain hardening fit. Table 3 lists the remaining material parameter values needed.

	σ_{F0r} MPa	ϵ_0 -	n -	ω_{TM} K ⁻¹	γ_P s ⁻¹	σ_P MPa	m_P -
Al	3.5×10^1	2.0×10^{-3}	1.9×10^{-1}	1.4×10^{-3}	1.0×10^{-4}	5.0×10^0	4.0×10^0
Ti	1.7×10^2	2.0×10^{-3}	1.5×10^{-1}	8.7×10^{-4}	1.0×10^{-4}	4.0×10^0	4.0×10^0

Table 2: Inelastic parameters

	λ_r MPa	μ_r MPa	α_r K ⁻¹	ρ_r kg m ⁻³	c_r m s ⁻² K ⁻¹	k_r J s ⁻¹ m ⁻¹ K ⁻¹
Al	5.0×10^4	2.6×10^4	2.3×10^{-5}	2.7×10^3	9.2×10^8	2.4×10^2
Ti	8.5×10^4	4.4×10^4	8.6×10^{-6}	4.5×10^3	5.2×10^8	2.2×10^1

Table 3: Thermoelastic parameters

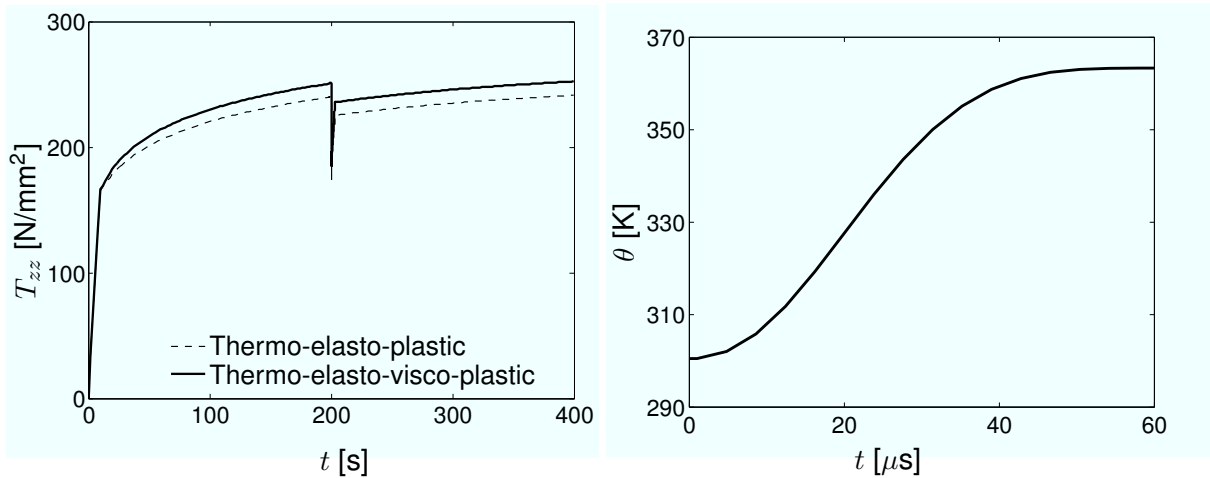


Figure 3: Current pulse applied to a titanium bar undergoing simple tension. Left: Development of the zz -component of the Cauchy stress simulated with a thermoelastic, viscoplastic model (rate-dependent: solid line) and a thermoelastic, elastoplastic model (rate-independent: dashed line). Right: Temperature rise from Joule heating during the current pulse starting at $t = 200$ s

Next, consider the results in Figure 3 for the case of a current pulse applied to a titanium bar undergoing simple tension in the z -direction. At the time of the pulse ($t = 200$ s), Joule heating results in a temperature rise from 301 K to 363 K in 60 μ s. The slight temperature rise of 3 K before the pulse is due to mechanical dissipation. In the left part of Figure 3, the change in the zz -component of the Cauchy stress $T = J^{-1}K$ as a function of time is shown. As can be seen, the current pulse results in a reduction of this component. In addition, both the rate-dependent and rate-independent cases show this change. In contrast to the work of Bilyk *et*

al. [6], we claim that not the rate effect, but rather the thermal expansion effect is crucial to correctly model the observed stress drop.

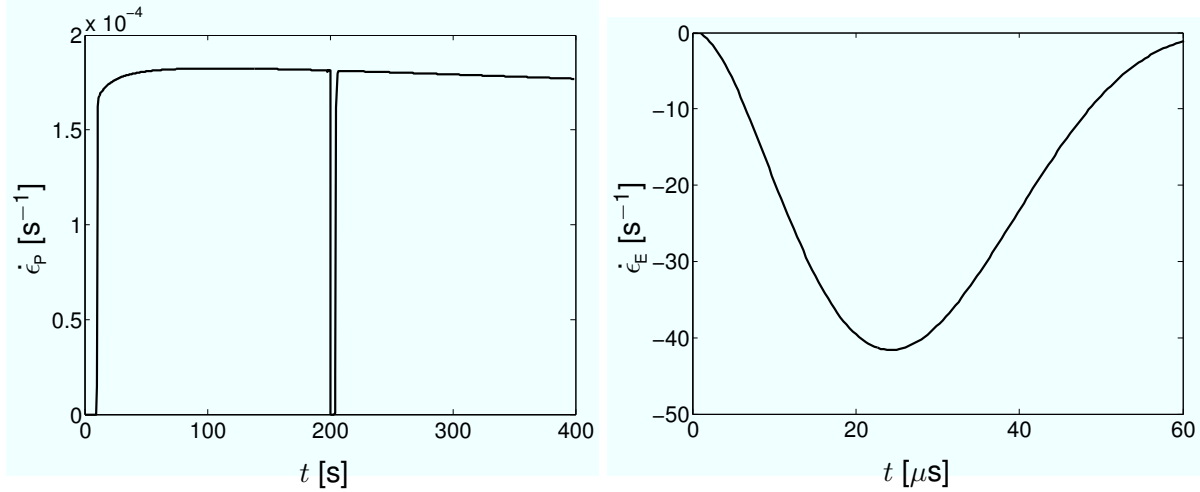


Figure 4: Rate of change of the accumulated inelastic strain as a function of time during pulsing. Left: The current pulse at 200 s forces the stress state below the activation threshold, resulting in $\dot{\epsilon}_p = 0$. Right: Variation in time of $\dot{\epsilon}_E$ starting at $t = 200$ s (note the difference in timescale)

To delve into this in more detail, consider the results in Figure 4 for the rate of the accumulated inelastic strain ϵ_p as well as the rate of $\epsilon_E = |\text{dev}(\ln V_E)|$, representing the norm of the deviatoric part of the left logarithmic stretch tensor. As soon as the temperature rises, the spherical part $\text{sph}(\ln V_E)$ of $\ln V_E$ increases (see (11)). Conversely, the deviatoric part and, hence, ϵ_E decreases. Accordingly, since $|\text{dev}(K)| = 2\mu\epsilon_E$, the activation stress (9) decreases and elastic unloading can be observed. The drop of $\dot{\epsilon}_p$ to zero takes place within 60 μs (see Figure 4 right). Afterwards, the tensile testing machine continues to load the specimen in the elastic domain for several seconds until the inelastic flow is reactivated. As shown, in this range, $\dot{\epsilon}_p = 0$.

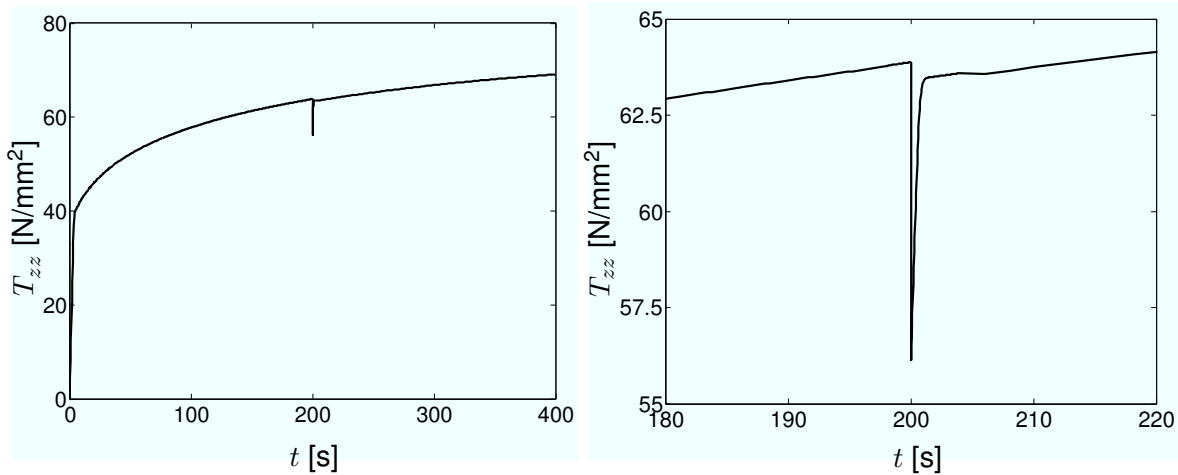


Figure 5: Simulated stress drop in aluminum due to Joule heating during simple tension. Left: Change of T_{zz} with time. Right: Blow-up of the stress drop region in time

Such testing has also been carried out for technically pure aluminum (*e.g.* Al99,5 or AA1000 series). As all experimental conditions are the same as for the tests with titanium, the particular material characteristics of aluminum are the reason for a smaller stress drop. In particular, for the same geometry and imposed current I , j as given by (3) is the same for both materials. Since the contribution to $\dot{\theta}$ from Joule heating is given by $\det(\mathbf{F}) \mathbf{j} \cdot \mathbf{j} / (\rho_r c_r \sigma_{EM})$ from (10)₃ any difference between the two materials is due to the magnitude of $\rho_r c_r \sigma_{EM}$. The parameter values in Table 3 imply that the heat capacity per unit volume $\rho_r c_r$ is comparable in aluminum and titanium. On the other hand, $\sigma_{EM}^{Al} = 3.8 \times 10^7 \text{ Ohm}^{-1} \text{ m}^{-1}$ and $\sigma_{EM}^{Ti} = 2.6 \times 10^6 \text{ Ohm}^{-1} \text{ m}^{-1}$. Consequently, $\sigma_{EM}^{Al} \gg \sigma_{EM}^{Ti}$, and it is clear why the temperature rise in aluminum (6 K) is much smaller than that in titanium (50 K). Via the thermoelastic coupling in (11), then, this difference in temperature increase is reflected in the respective stress drops, *i.e.* 60 MPa for titanium and 6 MPa for aluminum (Figure 5).

4 Conclusions

For the typical timescales, imposed current densities and materials generally relevant for EMF processes load drops during tensile testing are observed. For titanium and aluminum it was shown that the magnitude of the load drops can be modeled without postulating a direct interaction between electron and dislocation movement. The modeling of experimental results indicate that conventional effects such as Joule heating and thermal expansion are able to explain the experimental observations quite well. Such an interaction, if it exists, can be considered to be of second order.

References

- [1] *Svendsen, B. and Chanda, T.*: Continuum thermodynamic formulation of models for electromagnetic thermoelastic materials with application to electromagnetic metal forming. *Cont. Mech. Thermodyn.*, vol. 17 p. 1–16, 2005.
- [2] *Stiemer, M.; Unger, J.; Blum, H. and Svendsen, B.*: Algorithmic formulation and numerical implementation of coupled electromagnetic-inelastic continuum models for electromagnetic metal forming. *Int. J. Numer. Methods Engrg.*, 2006.
- [3] *Lemaitre, J. and Chaboche, J.-L.*: *Mechanics of solid materials*. Cambridge University Press, 1990.
- [4] *Conrad, H. and Sprecher, A. F.*: The electroplastic effect in metals. In F. R. N. Nabarro, editor, *Dislocations in solids*, p. 499–541. Elsevier Science Publishers, 1989.
- [5] *Varma, S. and Cornwell, L. R.*: The Electroplastic Effect in Aluminum. *Scripta Metallurgica*, vol. 13 p. 733–738, 1979.
- [6] *Bilyk, S.; Ramesh, K. and Wright, T.*: Finite deformations of metal cylinders subjected to electromagnetic fields and mechanical forces. *Journal of the Mechanics and Physics of solids*, vol. 53 p. 525–544, 2005.

- [7] *Troitskii, O. A.*: Electromechanical effect in metals. *Zh. Eksp. Teor. Fiz.*, vol. 10(1) p. 18–22, 1969.
- [8] *Molotskii, M.*: Theoretical basis for electro- and magnetoplasticity. *Materials Science & Engineering*, vol. 287 p. 248–258, 2000.
- [9] *Goldman, P. D.; Motowidlo, L. R. and Galligan, J. M.*: The Absence of an Electroplastic Effect in Lead at 4.2 K. *Scripta Metallurgica*, vol. 15 p. 353–356, 1980.
- [10] *Okazaki, K.; Kagawa, M. and Conrad, H.*: Effects of strain rate, temperature and interstitial content on the electroplastic effect in titanium. *Scripta Metallurgica*, vol. 13 p. 473–477, 1979.
- [11] *Jackson, J. D.*: *Classical Electrodynamics*. John Wiley and Sons, 1987.
- [12] *Svendsen, B.*: On the modeling of anisotropic elastic and inelastic material behaviour at large deformation. *Int. J. Solids Structures*, vol. 38 p. 9579–9599, 2001.
- [13] *Rosakis, P.; Rosakis, A. J.; Ravichandran, G. and Hodowany, J.*: A thermodynamic internal variable model for the partition of plastic work into heat and stored energy in metals. *J. Mech. Phys. Solids*, vol. 48 p. 581–607, 2000.
- [14] *Teodosiu, C.*: Dislocation modeling of crystalline plasticity. In C. Teodosiu, editor, *Large plastic deformation of crystalline aggregates*, CISM, p. 21–80. Springer, 1997.

Magnetic Pulse Acceleration

O. Gafri, A. Izhar, Y. Livshitz , V. Shribman

Pulsar Ltd., Yavne, Israel. P.O.B 421, Yavne, Israel

Abstract

The present work is dedicated to describing works in the spheres of simulation, calculation, and experimental results of acceleration by pulsed electromagnetic forces where strain rates of 10,000 - 50,000 s⁻¹ are common. The goal is to design a multidisciplinary model that will overcome the shortcomings of 'normal' simulation methods that solve the EM field and then apply the solution in a mechanical analysis. Improved numeric models for virtual simulation of magnetic pulse processes are detailed, along with the pulse-power equipment and a special measurement system developed to verify these models and to determine material property data. These measure both radial velocity and axial speed (collision-point progression) for tube forming and / or welding processes, while logging the pulse current and magnetic field. The results show good a correlation between test and multiphysics model and provide valuable new insights, as well as an extraction of critical parameters by way of a comparison between calculated and measured data for materials such as aluminum alloys, copper, and steel.

Keywords

Electromagnetic forming, Process modeling, Verification, High speed testing methods

1 Introduction

Magnetic-Pulse Forming and Welding (MPF, MPW) can be useful technologies for industrial fabrication with many benefits compared to conventional welding, stamping, hydroforming, explosive forming/welding, etc. [1-4]. To do that, however, one needs to tailor the velocity field of the flyer (accelerated part) which, in turn, depends both on the shifting magnetic field (time-dependent and variable due to magnetic-mechanical interaction and physical flyer displacement) and on the momentary geometry and properties of the flyer in-flight.

For magnetic pulse processes to enter into industrial use a method had to be derived by which a client's vision or existing application can be quickly and reliably transformed to an optimal MP process with all its major parameters (and parameter tolerance effect) calculated and the proper electrical and physical design recommended. Virtual process modeling is the

best way to view and analyze the process in action, as the short process duration (2 – 20 μ sec) and the nature of the system and process combine to make photography very hard (the part is enclosed and obscured by the coil, die, etc., moves at some 100's m/s, deforms at several km/s, and produces flashes that drown out the picture).

'Normal' methods, such as solving the EM field and then applying the sum body forces as 'pressure' in a mechanical Finite-Element Analysis (FEA), either directly (as pressure-time function in a transient analysis) or using an iterative EM/MEC step (with or without adaptive re-meshing), had several shortcomings, such as difficulty to model an inter-related phenomenon and taking several hours for entering the model geometry, and sometimes days for solving the loosely-coupled magneto-mechanical cycles.

2 Multi-physical model

2.1 Magnetic pulse equipment

The system to be modeled has a Capacitive Pulse-Current-Generator (PCG), connections for pulse currents (terminals, pulse cables, bus-bars, etc.), an optional Current-Augmenting pulse Transformer (CAT)[4,5], a load composed of a flat or cylindrical Coil of 1 or more windings or plates, i.e. Work Coil (WC)[1,2], an optional Flux-Concentrator or Field-Shaper (FS)[2,3], and 1 or more parts inserted in the "business end", i.e. Work-Pieces (WP_#), having a tubular or flat geometry. All these items (except WP) were made in-house and their R/C/L values and $K_{B:l}$ magnetic transference ratio (i.e. magnetic field level and shape for a given driving current) were tested, measured, and entered into a database[4]. Table 1 lists the Pulsar PCG's and their properties.

Energy [kJ]	Rated volts	Rated pulse A	Self R _o	Self L _o	Self C _o	Own S.C. frequency	PCG (e=prototype)
5	10,000	100 kA	6.70	100.0	100 μ F	50.05 kHz	MP5-10-e
7	8,725	200 kA	9.50	82.00	184 μ F	39.92 kHz	MP7-9
10	10,000	400 kA	20.0	79.25	200 μ F	34.57 kHz	MP10-10-e
12	24,500	400 kA	7.20	44.19	40 μ F	119.00	MP12-25
20	25,000	800 kA	26.0	26.80	80 μ F	76.51 kHz	MP20-25-e
20	9,000	800 kA	1.80	29.97	552 μ F	38.84 kHz	MP20-9
25	25,000	400 kA	4.23	46.09	80 μ F	82.56 kHz	MP25-25
25	8,515	1000 kA	1.52	26.39	690 μ F	37.02 kHz	MP25-9
30	6,000	250 kA	3.00	120.0	1.7 mF	10.96 kHz	MP30-6-e
40	9,000	800 kA	8.50	39.07	1.1 mF	16.96 kHz	MP40-9-
100	25,000	1600 kA	1.41	16.46	320 μ F	69.00 kHz	MP100-25

Table 1: Properties of Commercial Pulse Generators

2.2 Modeling

Work was initially carried out using commercial finite-element software (various EM+ME FEA), but the high cost, long solving time, and difficulties in modeling some inter-linked phenomena soon led to the development of a proprietary MP-code. For the issue of tailoring the optimal process for a given application (i.e. optimal magnetic waveform to achieve required impact conditions with minimum charge energy, minimum component heat-up, and no over-stressing of components) two main approaches were used:

2.2.1 Energy-time iteration

In this method, the pulse is calculated as the system step response from the initial energy charge with momentary voltage/current/field strength values re-calculated at each time-step based on remaining electric energy and the new system geometry (as the workpiece, coil and FS deform due to magnetic forces). The geometry for the next time-step is then calculated based on magnetic “pressure”, kinetic energy, and mechanical deformation forces.

2.2.2 Force-translation iteration

This method assumes the magnetic field intensity to act as a simple decaying sine wave and calculates the body forces caused by magnetic repulsion and induction heat. Part acceleration under those forces is calculated, yielding the radial velocity profile along the part.

Both above systems base their calculations on a [client-specified] given geometry and material properties and the database of pulse current generators, coils, and field shapers.

These fast-solving programs sort through the possible combinations, find feasible combinations (those that yield the required impact velocity and angle without exceeding the allowed charge voltage, peak current, coil stress, etc.), sort for the optimum combination (minimum energy), and issue a list of the best combination for sample production.

The same models can then explore the effect of modifying the process parameters (MPF capacitance, coil length, number of winds, workpiece length inside field-shaper, and modification of workpiece diameter or thickness) to issue a list of recommendations as to how to build a suitable commercial system.

2.3 Test design

2 known MPW processes, for which waveforms for current and magnetic field were already measured in the methods listed below, were selected as a test case. The force-time model (fastest) was repeatedly run with changing parameters K_{EFS} , then $\{R,L\}_e$, then σ_d , until the calculated current waveform and magnetic waveform matched exactly to the test waveforms. The extracted K_{EFS} , $\{R,L\}_e$, and σ_d parameters were used for the force-translation model and for an FEA model that served as control group.

The results from both models were similar to those obtained by FEA (figure 5) and solving took only a few minutes, compared to over 3 hours it took the FEA (50x8 elements grid, 64 contact elements, 2-D cylindrical, 2500 time-steps, 1.33MHz IBM PC). The results from both the velocity-versus-time profiles from the commercial FEA and the new algorithms were then compared to those recorded during the actual tests, verifying correctness.

2.3.1 Magnetic pulse equipment

The two processes selected for this test to cover a wide spectrum are listed under Figure 1.

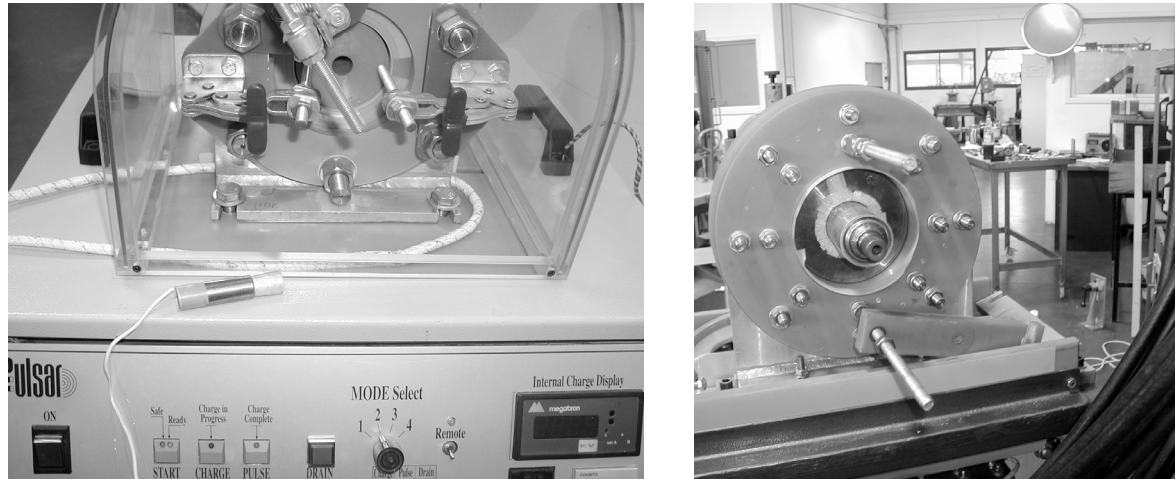


Figure 1. Test samples.

Left: 1mm Al 1000 12.5mm diameter welded to 10mm steel using 2.8kJ on a 5kJ PCG. 6 plate x300° Bitter coil and D=72;X=75 by d=15;z=12 Bronze FS. ~13 TI

Right: 2mm Al 6061-T4 32mm diameter welded to 23mm steel using 40kJ on a 100kJ PCG, 3x270° plate Bitter coil and D=105;X=102 by d=35;z=22 FS. ~32 TI

2.3.2 High-Speed measurement system

To verify the model prediction, measurements were taken of all critical process parameters. Coil current was measured using a “Rogowsky” pickup coil w. RC integrator. Magnetic field and distribution in the work-zone were measured by a thin axial probe (0.2mm thick x 5 or 20 mm wide with one or more 2mm sensor zones, placed between FS and driven part). The system for measuring radial “implosion” velocity is shown below (Figure 2).

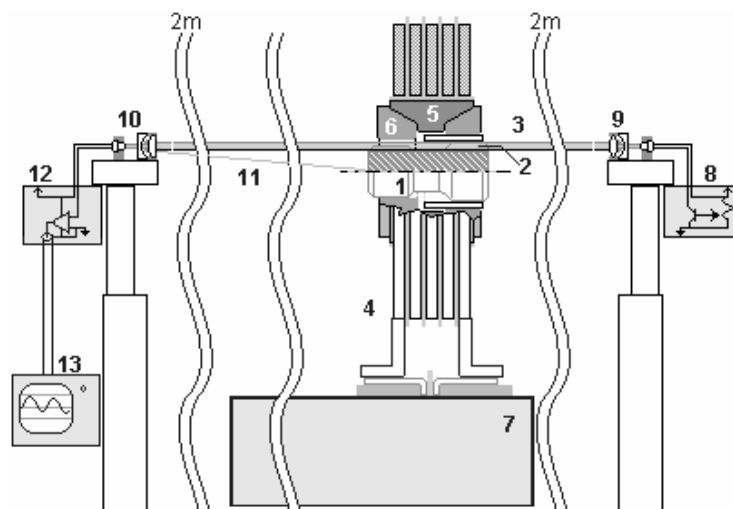


Figure 2: Laser velocimeter for V_r

1) inner workpiece. 2) light slot, the height of the acceleration gap, w. laser through-beam 1mm wide (a partial shadow “dead-zone” occurs near the edge of the driven workpiece #3)

4) work coil 5) flux concentrator/FS 6) insulating part-positioning caps 7) pulse current generator. 8) laser power supply 9) collimator / line-generator optics 10) laser target 11) reflected centering beam 12) 50MHz analog optical sensor 13) data acquisition.

This system measures the % remaining beam power as the beam is being eclipsed by the workpiece imploding, then transforms the beam power record to gap height record, using a pre-calibrated gap:power transfer function to calculate dr/dt , i.e. $V_r(t)$, of the fastest point. To measure the contact progression velocity V_c , a system composed of a flexible adhesive sensor is attached over the inner workpiece, as shown below (Figure 3):

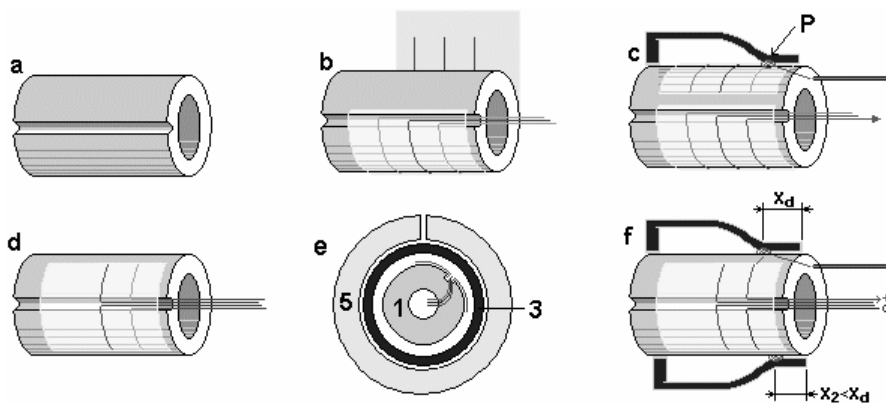


Figure 3: Axial velocity probe

- a) Inner workpiece with stepped groove.
- b) Flexible wrapping with varnish-coated filaments at set intervals (this sensing "Comb" of 360° coverage measures $\text{Max}(V_c)$)
- c) During pulse process, as contact point [P] pass over each electrode, the pinch flattens the filament to crack the insulating coat and shorts the output to ground. Steps in the groove can serve to cut the shorted sense section as P moves further so that each channel generates several on-off signals.
- d) Another variant with left-right 90° coverage, used to measure the effect of field-shaper gap on field uniformity:
 - e) When placed in the shaper so that one "Comb" is under the gap-affected zone, the offset in signals can be measured:
 - f) Due to the drop in field intensity near the gap V_c is lower and contact will only reach position X_2 at the time the unaffected side reach $X_d > X_2$.

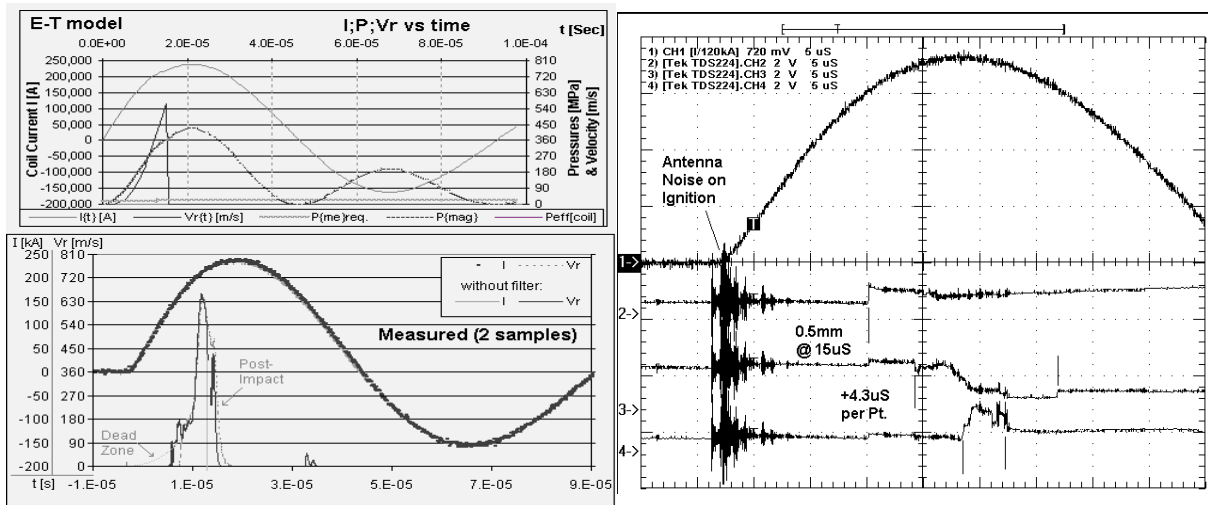


Figure 4: Model results vs. actual I:Vr measured at test and contact point progression from Vc-meter (Current delayed 3.2uS due to acquisition) showing Vc=4mm/4.3uS =930m/S for test geometry #2 (higher impact angle)

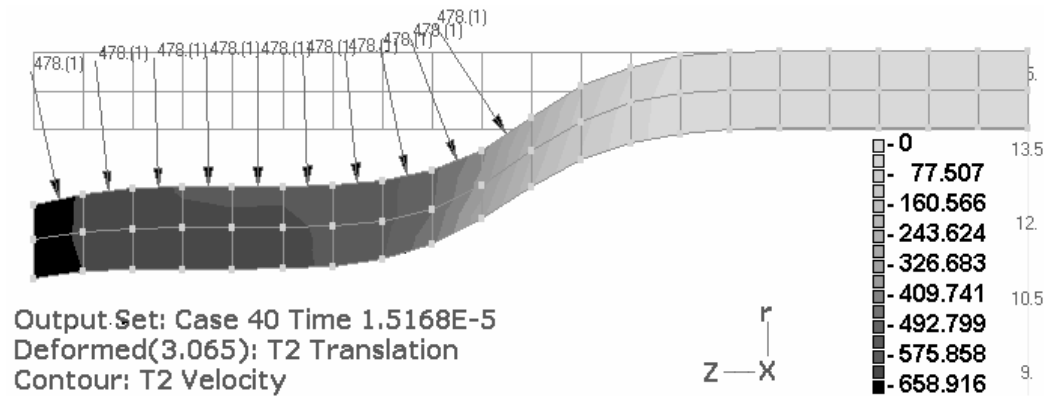


Figure 5: Model verified using conventional Finite-Element Analysis (screen shot Curtsy MSC NASTRAN)

3 Additional insights from the multi-physics model

The inclusion of electric-magnetic-thermal-mechanical to a unified model, stated as sparse-matrix solution with enough computational power to model the entire system, has resulted in some useful new insights into the physical behavior of the MP process itself, such as the compression of the current skin-layer due to dL/dt shift from mechanical deformation, which was later verified by testing, and has major effects on coil / FS design and lifetime [2].

4 Conclusions

For an industry-oriented company, with R&D focusing on improving the efficiency, stability, and durability of pulse-power systems for high magnetic field generation, commercial FEA is best replaced by faster and more physically-accurate computer models.

Researchers in the sphere of EM pulses (and EM forming in particular) can also benefit from employing a multi-physics model with total-system simulation capacity, as these models also give the magnetic, thermal, and stress profile of other major components (the coil, FS, etc.) and can prove to be valuable for designing these parts to withstand repetitive pulses.

Models for simulating and optimizing the electro-magnetic-mechanical coupled process of magnetic pulse acceleration should take into account physical dimensions, electrical and mechanical properties of all materials comprising the system (coil, field shaper, accelerated part, driven part, and impacted part.) The models serve for optimizing the pulse current generator (PCG) design, inductor's system parameters, and the pulse regime itself for any given (industrial) applications.

This paper shows that a low-cost measuring system can be employed for capturing the electrical and mechanical behavior of the electro-magnetic forming process and the model output matched the actual behavior by setting the correct factors (one main benefit of the measurement methods is that it enables the "fine-tuning" of the mathematical models by assembling a database of otherwise unknown parameters, such as material properties at ultra-high deformation rates, exact field distribution ($X_{(x)}$) in FS work-zone, welding conditions for specific bimetallic combination, etc.) This data is automatically generated by converging to the parameters that "force" the model prediction to fit with actual test data.

Electromagnetic and mechanical phenomena regarding the behavior of Field Shapers (FS) and trapezoidal mono-wind coils during core collapse were noted and identified, leading to new improved designs. So far, coils and flux concentrators of 10-30TI (100-300 kGauss) have been designed to withstand several 10,000s pulses at 4PPM repetitive operation, powered by compact pulse current generators with capacitor energy storage (5-100kJ) and 1kA-1.5MA output (or more, using MA-level pulse transformers).

References

- [1] *Livshiz, Y; Gafri, O.:* Technology & equipment for industrial use of pulse magnetic fields. Proceedings of 12th IPPC, Monterey, CA, 1999, p. 475-478.
- [2] *Livshiz, Y; Izhar, A.; Gafri, O.:* One turn coil for industrial use of magnetic pulse processes. Proceedings of 9th Mega-Gauss Conference, 2002, p. 125-131.
- [3] *Livshiz, Y; Izhar, A.; Gafri, O.:* One-turn coil and field-shaper design for industrial use of pulse-power magnetic processes. Proceedings of 14th PPC, 2003, #10397.
- [4] *Izhar, A.; Livshitz, Y.:* Adapting Pulse-Power generators to commercial and laboratory applications. Proceedings of IEE pulsed power seminar, Loughborough UK, 2003. #11.
- [5] *Izhar, A.; Livshitz, Y.:* High-voltage / high-current pulse power for civil, commercial, research & military test applications –Part III– Multi-Mega-Ampere pulse transformers, Proceedings of 15th IEEE Pulse Power Conference, 2005, #10172.

Deformation and Ductile Fracture of a Low Alloy Steel under High Strain Rate Loading

L. W. Meyer¹, S. Abdel-Malek²

¹ Chair Materials and Impact Engineering, Chemnitz University of Technology, Germany

² Nordmetall GmbH Research and Consulting, Burkhardtsdorf, Germany,
www.nordmetall.net

Abstract

Ductile failure of metals always occurs after a specific amount of plastic deformation. Therefore, the investigation and characterization of the deformation behaviour is required to understand the damage process and to describe the failure by a suitable constitutive relation. The effects of temperature and strain rate on the mechanical properties are important for the description of the material behavior in many applications. The MTS model is used here to describe the material behavior of some low alloy steels in a wide range of temperature and strain rates. A new part of stress is added to the MTS model in order to consider the effect of the dynamic strain aging at low strain rate and high temperature.

The determination of material data at high strain and high strain rate is needed to describe the real material behaviour, specially for the simulation of high deformation and fracture. A special technique is used here to stop the deformation of tension specimen at high strain rate in the necking zone to determine the true stress and true strain.

Using FEM computations (LS-DYNA 3D), the stress triaxiality in the necking zone of a tensile specimen is calculated up to the crack initiation. It is shown that the strain hardening characteristics affect the development of stress triaxiality.

Keywords:

High strain rate, High plastic deformation, Ductile failure

1 Introduction

Mechanical testing gives information about material behaviour at different temperatures and strain rates. The results are needed for the numerical analysis and the simulation of high strain rate deformation processes such as automobile crash tests or high speed metal forming processes. For these processes the range of relatively high strains and very

high strain rates is of great interest. In the high strain rate range, the flow stresses are influenced by the temperature increase during the deformation process. The major part of the deformation energy is transformed into heat, leading to a reduction of the flow stress. A precise description of the material behavior does not only need a good agreement of the constitutive model with the experimental results at high strain rates, but also at high deformations. Dynamic strain aging will be active in a limited range of strain rate and temperature and leads to an enhancement of the flow stresses. This must be considered in the material model.

At ductile fractures the material can fail due to the coalescence of voids, which occurs through three mechanisms: 1) squeezing of the matrix between voids, 2) nucleation and growth of secondary voids, and 3) shearing between voids. Factors affecting the ductile failure are: stress state, temperature, strain rate, twin formation, and dynamic strain aging. Understanding these effects allows forecasting how and when failure occurs. This leads to a successful modeling of failure in a numerical simulation.

2 Material model

Accurate modeling of deformation processes of materials over a wide range of strain rates and temperatures requires a reliable constitutive description of the stress-strain behavior. Several physically and empirically based models have been developed for use in computational codes [1]. Most models are use a constant strain hardening exponent n , which leads to higher flow stresses with increasing deformation. The MTS model “Mechanical Threshold Stress”, which was developed by Follansbee et al. [2], is a physically based model. It is considering that the flow stress at a certain temperature and strain rate do not increase above a saturation stress. In the MTS model the flow stress is a sum of three parts: an athermal stress σ_a , a thermal stress σ_i for the interaction of dislocations with interstitial obstacles, and a threshold stress $\hat{\sigma}_\varepsilon$ for the dislocation/dislocation interaction:

$$\frac{\sigma}{\mu} = \frac{\sigma_a}{\mu_0} + S_i(\dot{\varepsilon}, T) \cdot \frac{\sigma_i}{\mu_0} + S_\varepsilon(\dot{\varepsilon}, T) \cdot \frac{\hat{\sigma}_\varepsilon}{\mu_0} \quad (1)$$

μ is the temperature-dependent shear modulus and μ_0 is the shear modulus at 0 K. S_i and S_ε are factors expressing the effect of temperature and strain rate in a general form as:

$$S_{i,\varepsilon} = \left\{ 1 - \left[\frac{kT}{g_{0i,\varepsilon} \mu b^3} \ln \left(\frac{\dot{\varepsilon}_{0i,\varepsilon}}{\dot{\varepsilon}} \right) \right]^{1/q_{i,\varepsilon}} \right\}^{1/p_{i,\varepsilon}} \quad (2)$$

While σ_a and σ_i are taken as constants, the threshold stress $\hat{\sigma}_\varepsilon$ is a state parameter and treated differentially according to:

$$\theta = \frac{d\hat{\sigma}_\varepsilon}{d\varepsilon} = \theta_0(\dot{\varepsilon}) \left(1 - \frac{\tanh\left(\alpha \frac{\hat{\sigma}_\varepsilon}{\hat{\sigma}_{\varepsilon s}(\dot{\varepsilon}, T)}\right)}{\tanh(\alpha)} \right) \quad (3)$$

where θ is the strain hardening and $\hat{\sigma}_{\varepsilon s}$ is the saturation stress. A detailed discussion of MTS model and how to determine the parameter is explained by Follansbee et al. [2-4]. At high temperatures or low strain rates the dynamic strain aging affects the flow stress. In order to consider this effect, we suggest a forth stress part to be added to the MTS model. The equation (1) shall be written as:

$$\frac{\sigma}{\mu} = \frac{\sigma_a}{\mu_0} + S_i(\dot{\varepsilon}, T) \cdot \frac{\sigma_i}{\mu_0} + S_\varepsilon(\dot{\varepsilon}, T) \cdot \frac{\hat{\sigma}_\varepsilon}{\mu_0} + \frac{\sigma_{DSA}}{\mu} \quad (4)$$

where σ_{DSA} is a stress part, which results from the Dynamic Strain Aging. It will be expressed with the following equation so that it is only active in the region of the dynamic strain aging, fig. 1.

$$\frac{\sigma_{DSA}}{\mu} = \frac{\sigma_{D0}}{\mu_0} \cdot \text{sech}[K_1 \cdot S_i(\dot{\varepsilon}, T) - K_2] \quad (5)$$

σ_{D0} , K_1 , and K_2 are constants, which will be determined by using the difference of experimental data σ_{exp} and the σ_{MTS} data calculated with equation (1).

$$\sigma_{DSA} = \sigma_{\text{exp}} - \sigma_{\text{MTS}} \quad (6)$$

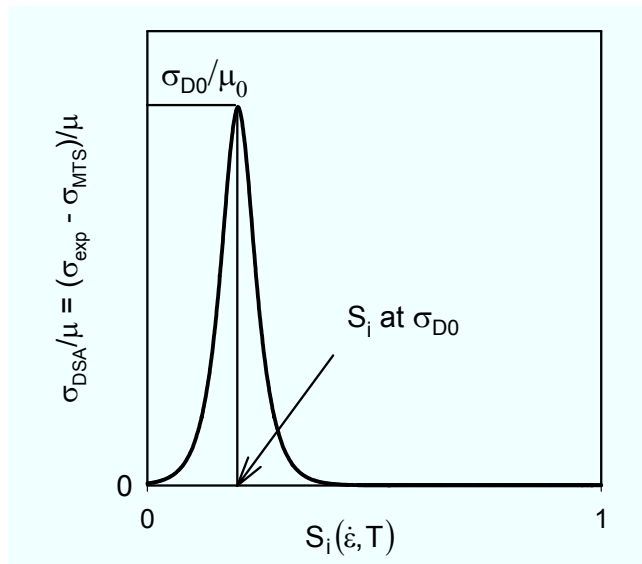


Figure 1: Relationship between σ_{DSA} and $S_i(\dot{\varepsilon}, T)$

3 Experimental procedures

Tension tests were carried out on four high strength low alloyed steels under quasistatic and high rate loading conditions. Tensile tests at low and medium velocities were done with the proved 250 kN hydraulic test machine Instron 8503, which has a large test velocity range of $v = 0.005$ up to 800 mm/s.

Dynamic tensile tests were performed on the rotating wheel machine at different velocities. The rotating wheel machine consists of a flywheel (200 kg) with a claw, which is released at the required test velocity and is impacting a yoke. The yoke pulls the test specimen, which is attached in a specimen holder. The force measurement is applied directly beside the gage length with strain gages. The strain was measured directly with strain gages. Because of the high energy capacity of this apparatus the test velocity is constant up to failure even for high strength, high ductility materials. For more details see Meyer et al. [5].

Only flow stresses up to UTS are used to get the parameter of the MTS model. To verify the material model at high deformations, the high rate tensile test was interrupted in the necking region using a special stopping device. The stress is calculated from the measured force and the actual area of the smallest cross section and corrected to the uniaxial stress state according to Bridgman [6].

A characterization of the ductile failure behavior was performed by using notched specimens, which were tested under tensile loading with three speeds; $v = 0.1$ mm/s, 5 m/s, and 25 m/s. The changes in the minimum diameter at the notch root were used as a criterion to measure the effective strain at failure.

4 Results and discussion

4.1 Modeling the flow stress

The parameters of the MTS model, eq. (1), were determined by using the results of the tension tests up to UTS in the strain rate range 10^{-4} s^{-1} to $5 \cdot 10^3 \text{ s}^{-1}$. For high strain values interrupted dynamic tensile tests were carried out with a test speed of 5 m/s. The required strain value is adjusted with a special device, which guides the deformation process into a secondary specimen, the so-called sacrifice specimen, which fails and leaves the test specimen only deformed with a necking. The flow stress and strain are calculated with the actual force and cross sectional area and corrected to the uniaxial stress state according to Bridgman [6]. An advantage of this method is the consideration of the adiabatic status resulting from the heating of the specimen under dynamic conditions.

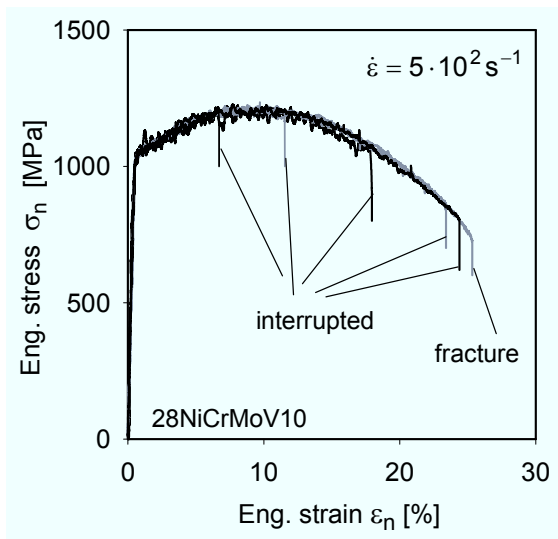


Figure 2: Stress strain diagrams of interrupted tests of low alloyed tool steel

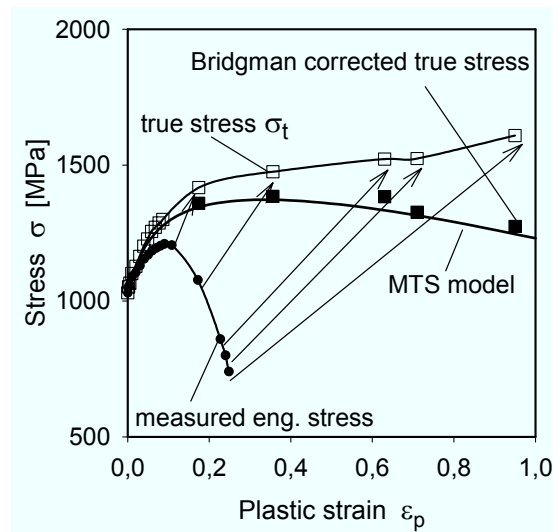


Figure 3: Comparison of experimental data and MTS model

Figure 2 shows the results of interrupted tensile tests of specimens with 10 mm gage length at a strain rate of $5 \cdot 10^2 \text{ s}^{-1}$ with a low scatter between six tests interrupted at certain stages of necking. The true stress was determined from the measured force and the true diameter in the necking zone and corrected for the uniaxial state according to Bridgman [6]. Comparing these results with the calculated curve of the MTS model extrapolated from UTS to the fracture strain, a good agreement was achieved, Figure 3. This offers the important advantage to establish high rate true stress-true strain relations up to the necking strain. This is mostly 10fold to the homogenous strain without friction effects, which disturb results of upsetting tests.

Figure 4 compares the experimental data at different strain rates with the calculated flow curves from the MTS model. Because of the effect of dynamic strain aging the experimental data at the strain rate of 10^{-3} s^{-1} exceeds the flow curve calculated with MTS model eq. (1). Considering the effect of dynamic strain aging by using the modified form of the MTS model eq. (4), a good agreement between the experimental data and the calculated curve (dashed curve) results.

The calculated flow stresses with the modified MTS model eq. (4) are plotted in figure 5 as a function of the temperature at different strain rates. The effect of dynamic strain aging shifts to a higher temperature due to higher strain rates.

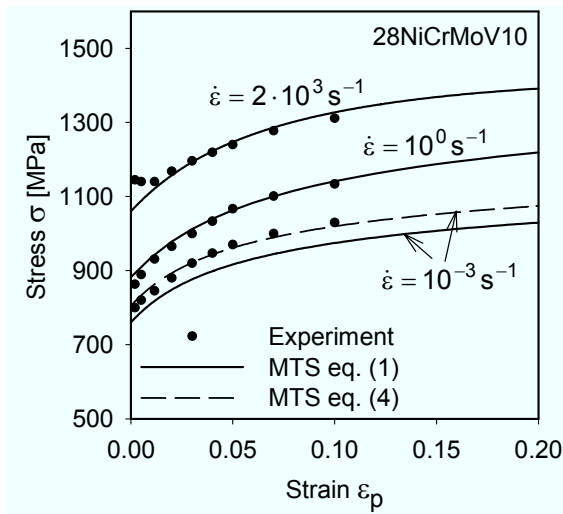


Figure 4: Stress-strain behavior from low to high rates of strain and improvement of the MTS model by dynamic strain aging

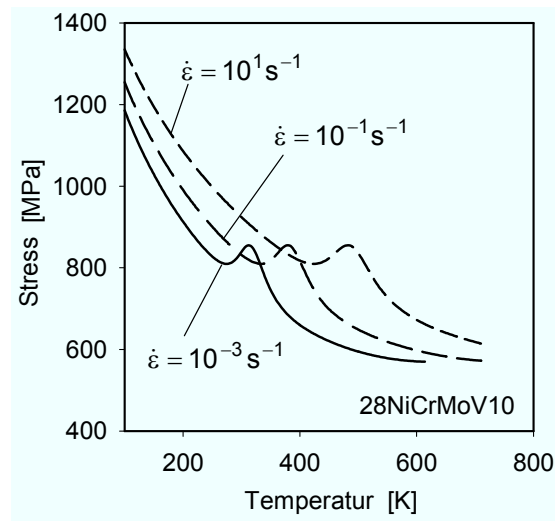


Figure 5: Influence of dynamic strain aging at different temperature and strain rates

4.2 Ductile failure

Notched tensile specimens were used with different stress states in the root section to characterize the ductile failure of the investigated low alloy steel. The stress triaxiality must be determined at the fracture initiation. Therefore, FEM computations were performed to calculate the development of the stress triaxiality σ_m/σ_v . The computations were carried out with LS-DYNA 3D explicit with a striking velocity of 5 m/s and 25 m/s and also as an implicit calculation to simulate the quasistatic loading. A quarter model is used for each notch radius and also for the unnotched specimen. The MTS model was used for the input of the material data.

To show the effect of strain hardening on the development of stress triaxiality, an implicit computation was carried out with a notch radius of 2.5 mm with two different flow curves. The first is an elastic-ideal plastic curve $d\sigma/d\varepsilon = 0$ and the second is an elastic one with a strong linear strain hardening $d\sigma/d\varepsilon = 500$ MPa. The yield stress (elastic limit) for both curves is 500 MPa. The results of these computations show that the high strain hardening yields to smaller stress triaxiality, figure 6.

The computed stress triaxiality of notched and unnotched specimens is represented in dependence of the equivalent strain, figure 7. The arrows represent the experimentally determined effective strain at the fracture initiation under quasistatic loading. It can be noticed that the stress triaxiality affects the failure behavior much more than the strain rate.

The influence of strain rate on the effective fracture strain is shown in figure 8 for the unnotched and notched cases. With increasing strain rate the local fracture strain of unnotched specimens decreases slightly up to $\dot{\varepsilon} \approx 10^1$ s⁻¹, then it increases clearly beyond $\dot{\varepsilon} > 10^3$ s⁻¹. In some metallic materials the so-called strain rate embrittlement was observed [1,8]. At high strain rates the ductility of metals can also increase due to the adiabatic heating resulting from the transformation of the deformation energy into heat.

When the influence of the adiabatic heating is stronger than of the strain rate, then the fracture strain increases at high strain rates. The local fracture strain of the notched specimens decreases only slightly with increasing strain rate. The main influence is due to the stress triaxiality, not due to the strain rate.

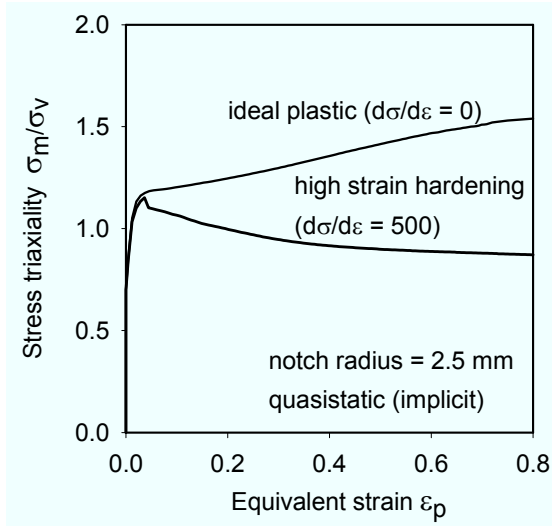


Figure 6: Influence of strain hardening on the stress triaxiality (FEM solution)

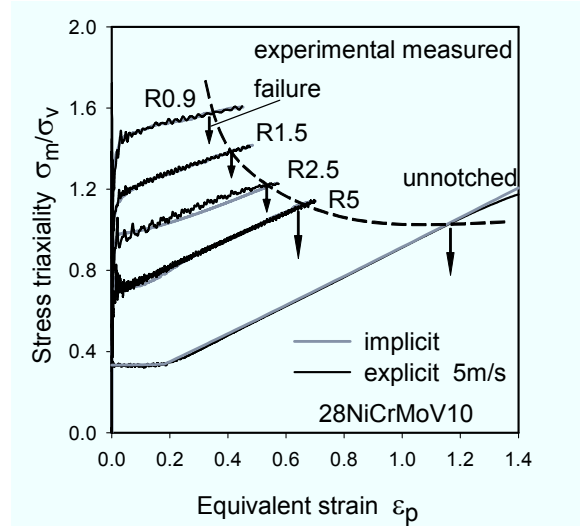


Figure 7: Stress triaxiality of different notch radii under quasistatic and dynamic loading (FEM)

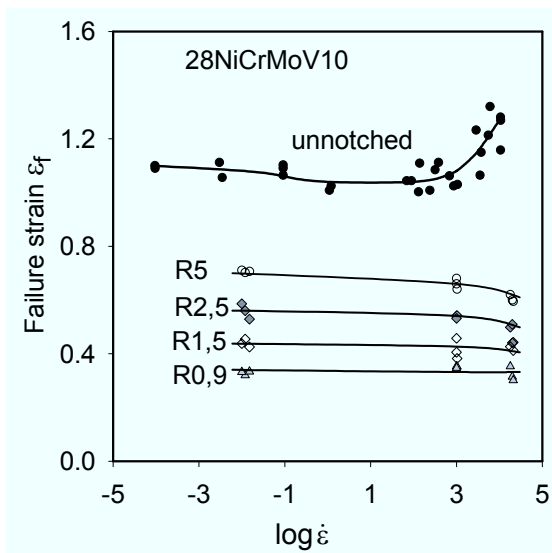


Figure 8: Dependence of the fracture strain on the strain rate

5 Conclusions

The material behavior of a low alloy steel in a wide range of strain rates was described with the MTS model. Adding an extra stress part to the MTS model, the effect of the dynamic strain aging was considered, too.

With stopped tests it was proven that the complete tensile test is usable for evaluating flow stresses with the MTS model, even up to fracture, but without friction influences. This is an important step forward for the simulation community because upsetting tests are never free from unknown friction effects.

The ductile failure depends considerably on the stress triaxiality. The strain rate plays a minor role.

References

- [1] *Meyer, L. W.:* Constitutive equations at high strain rate. In: Shock wave and high strain rate phenomena in materials, Eds.: Meyers, M. A.; Murr, L. E. and Staudhammer, K. P., Marcel Dekker, New Yourk, 1992, p.657-673.
- [2] *Follansbee, P. S.; Kocks, U. F.:* A constitutive description of the deformation of copper based on the use of the mechanical threshold stress as an internal state variable. *Acta Metall.*, 36, 1988, p.81-93.
- [3] *Follansbee, P. S.; Gray, G. T.:* An analysis of the low temperature, low and high strain-rate deformation of Ti-6Al-4V. *Metall. Trans.*, 20A, 1989, p.863-874.
- [4] *Follansbee, P. S.; Huang, J. C.; Gray, G. T.:* Low-temperature and high-strain-rate deformation of Nickel and Nickel-Carbon alloys and analysis of the constitutive behaviour according to an internal state variable model. *Acta Metall.*, 38, 1990, p. 1241-1254.
- [5] *Meyer, L. W.:* Werkstoffverhalten hochfester Stähle unter einsinniger dynamischer Belastung. Dissertation, Universität Dortmund, 1982.
- [6] *Bridgman, P. W.:* The stress distribution at the neck of a tension specimen. *Transactions of the A.S.M.*, 32, 1944, p.553-572.
- [7] *Burgahn, F.:* Einsinniges Verformungsverhalten und Mikrostruktur ausgewählter Stähle in Abhängigkeit von Temperatur und Verformungsgeschwindigkeit. Dissertation, Universität Karlsruhe (TH), 1991.
- [8] *Orava R. N.:* The effect of dynamic strain rates on room temperature ductility. 1. Int. Conf. High Energy Forming, Estes Park, Denver, Col., USA,, 1967.

Materials Characterization at High Speed by Dynamic Tensile Tests^{*}

Lu Xin¹, Li Xiangping², Geng Changgang¹

¹ Beijing Research Institute of Mechanical and Electric Technology, China

² Fiat Research Center, Italy

Abstract

In this paper, the dynamic deformation behaviors of 2 aluminum alloys (AA6016, AA5182) and 2 steels (v 1158, FeP04) are investigated. Firstly, the test method, an improved Hopkinson pressure bar test, is introduced. Then, the test results are presented and analyzed. The strain rate range used in this study is between 290 s^{-1} and 1750 s^{-1} . The test results show that the yield stresses of all four tested materials increase along with the increase of strain rate, but the ductility does not. An interesting finding is that the tested Al alloys demonstrated larger elongation than those of steels. In conventional tensile tests, as it is well known, the tensile elongation of low carbon steels is usually much higher than the one of Al alloys. So, it can be predicted that the aluminum alloys could have better formability than the steels in high speed forming processes, though the underlying mechanism is not fully understood.

Key Words:

High speed, Material test, Aluminum alloy, Steel

1 Introduction

In recent years, the automotive industry has been facing three major challenges: 1) the increasingly strict legislations on environment protection; 2) higher safety standards; 3) more sophisticated customer demands and, therefore, more product segmentations. To meet these challenges, the automotive makers have been in continuous pursuit of new

^{*} The authors would like to thank Ministry of Science and Technology of the People's Republic of China and National Natural Science Foundation of China (NSFC) for their the financial support (2002DFG00036 and 50375016).

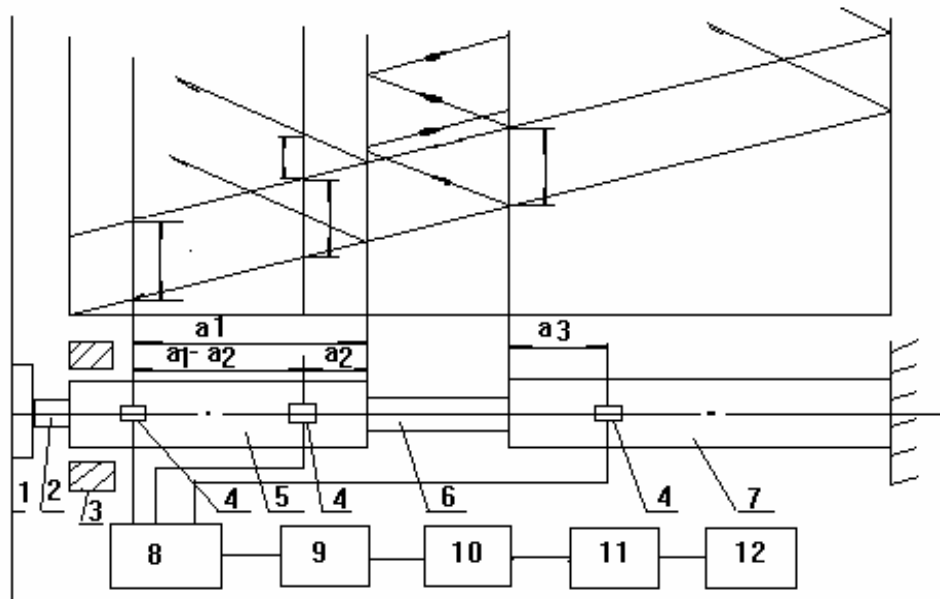
materials and new manufacturing technologies in order to be able to provide lighter and safer cars with lower costs by using lightweight materials like aluminum alloys and more flexible manufacturing processes. In this context, innovative processes such as electromagnetic forming (EMF) and electrohydraulic forming (EHF) received more attention and have become the subject of many research projects. EMF and EHF technologies are based on high-voltage discharge of capacitors: through the conductive coil or the electrodes in water the large pulsing energy discharged from the capacitor banks can generate high pressure and deform the workpiece in very high velocity. The advantages of these technologies include low investment in one sided dies [1], increased formability [2], reduced wrinkling and springback [3]. Strain rates in these forming processes are usually in the range of 10^2 - 10^3 s⁻¹, much higher than the strain rates in which the conventional tensile tests are carried out (10^{-4} to 10^{-2} s⁻¹). For the design and analysis of high speed forming processes the characteristics and deformation behaviors of workpiece materials must be known. However, today there exist only limited dynamic material test data. On the other hand, the need for vehicle crashworthiness design and optimization poses further demands for systematic materials testing under dynamic conditions. The combined needs make the investigation of material dynamic characteristics more imperative.

The actual high speed material testing techniques include dropweight machines [4, 5], split hopkinson pressure bars (SHPBs) [6, 7], Taylor impact [8], and shockloading by plate impact [9]. These testing methods have a common problem related to the disturbed wave by mechanical oscillation. In this paper, a new method based on “rotating disk indirect bar-bar tensile impact apparatus (RSHTB)” is presented. The novelty of the RSHTB method consists in the fact that a destructive short metal bar is used to solve the problem of the mechanical oscillation, using its fracture to filter the oscillation wave. As a result, the reliability of the acquired data is significantly improved.

In this paper, the dynamic deformation behaviors of 2 aluminum alloys (AA6016, AA5182) and 2 steel (V1158, FeP04) materials are investigated by means of the RSHTB dynamic tensile test method.

2 Experimental procedure

The schematic drawing of a RSHTB device is shown in Figure 1. The novelty with the RSHTB device is the introduction of a mechanical filter. When the mass 1 is impacted by hammer 3 on the rotating disk the produced rectangular impulse tensile stress wave is transmitted to input metal stick 5 from the destructive short metal stick 2. The short metal stick 2 is deformed until fracture occurs. So, an incident wave is generated by impact between 2 and 5, other than between 3 and 1. In this way, the incident rectangular wave reached at the input metal stick 5 is mechanically filtered, hence it is clean and stable with a very little disturbed wave. This is very important for obtaining reliable test results. In addition, the height and width of the incident rectangular wave can be adjusted easily with this kind of device to obtain the strain rate range 10^1 - 3.5×10^3 s⁻¹. The test sample's shape, dimension, and the clamping method are illustrated in Figure 2.



1-mass; 2-the destructive short metal stick; 3-hammer; 4-strain cage; 5-input stick; 6-sample; 7-output stick; 8-supper dynamic strain meter; 9-TCL wave shape recorder; 10-connect switch; 11-computer; 12-printer.

Figure 1: Apparatuses *t* for RSHTB

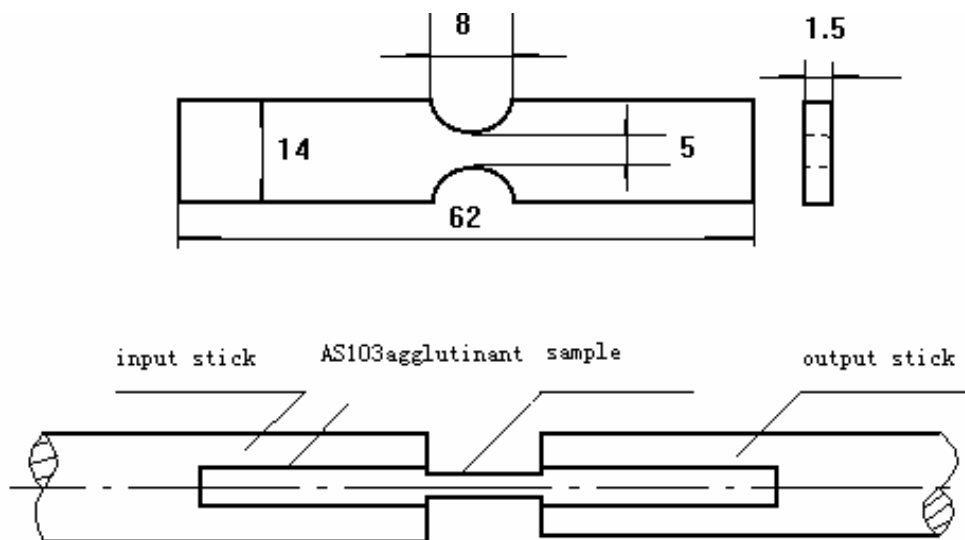


Figure 2: Dimension of test sample and its linking type

From the theory of one-way stress wave the force and the displacement in the two ends of test sample are expressed as follows:

$$P_1(t) = E_1 A_1 [\varepsilon_i(t) + \varepsilon_r(t)] \quad (1)$$

$$P_2(t) = E_2 A_2 \varepsilon_t(t) \quad (2)$$

$$u_1(t) = C_{01} \int_0^t [\varepsilon_i(\tau) - \varepsilon_r(\tau)] d\tau \quad (3)$$

$$u_2(t) = C_{02} \int_0^t \varepsilon_t(\tau) d\tau \quad (4)$$

The E_1 , A_1 , C_{01} and E_2 , A_2 , C_{02} are the elasticity modulus, cross section area, and longitudinal wave speed of elasticity respectively for the end surfaces of both the input stick and output stick. The $\varepsilon_i(t)$, $\varepsilon_r(t)$, $\varepsilon_t(t)$ are the strain signals of the incident wave, the reflective wave, and the transmission wave respectively.

It is supposed that the stress and strain are uniform in the sample without cracks, thus in the uniaxial tension sample, the stress, strain, and strain rate are the following:

$$\sigma_s(t) = \frac{1}{2A_s} [P_1(t) + P_2(t)] = \frac{1}{2A_s} [E_1 A_1 \varepsilon_i(t) + E_2 A_2 \varepsilon_t(t)] \quad (5)$$

$$\varepsilon_s(t) = \frac{1}{l_s} [u_1(t) - u_2(t)] = \frac{1}{l_s} \left\{ C_{01} \int_0^t [\varepsilon_i(\tau) - \varepsilon_r(\tau)] d\tau - C_{02} \int_0^t \varepsilon_t(\tau) d\tau \right\} \quad (6)$$

$$\varepsilon_s(t) = \frac{1}{l_s} [C_{01} (\varepsilon_i(t) - \varepsilon_r(t)) - C_{02} \varepsilon_t(t)] \quad (7)$$

where A_s and l_s are the cross-area and length of the gauge. When the diameters of input stick and output stick are same we have:

$$E_1 = E_2 = E, A_1 = A_2 = A, C_{01} = C_{02} = C_0$$

,thus

$$\varepsilon_i(t) + \varepsilon_r(t) = \varepsilon_t(t) \quad (8)$$

$$\sigma_s(t) = \frac{EA}{2A_s} [\varepsilon_i(t) + \varepsilon_r(t) + \varepsilon_t(t)] = \frac{EA}{A_s} \varepsilon_i(t) \quad (9)$$

$$\varepsilon_s(t) = \frac{C_0}{l_s} \int_0^t [\varepsilon_i(\tau) - \varepsilon_r(\tau) - \varepsilon_t(\tau)] d\tau = \frac{2C_0}{l_s} \int_0^t [\varepsilon_i(\tau) - \varepsilon_t(\tau)] d\tau \quad (10)$$

$$\varepsilon_s(t) = \frac{C_0}{l_s} [\varepsilon_i(t) - \varepsilon_r(t) - \varepsilon_t(t)] = \frac{2C_0}{l_s} [\varepsilon_i(t) - \varepsilon_t(t)] \quad (11)$$

From equation (8) to (11), the stress, stain, and strain rate of the test sample can be obtained at anytime so long as strain signals of input stick and output stick are measured precisely. With the dynamic tensile test device and the test specimen described above the largest reachable strain rate is about $2.2 \times 10^3 \text{s}^{-1}$.

3 Results and discussions

The engineering stress – engineering strain curves of AA6016 and AA5182 are shown in Figure 3 and Figure 4 respectively. And in Figure 5 and Figure 6 the curves of engineering stress vs. engineering strain for two steels V1158 and Fep04 are shown. It can be clearly seen that for all four materials the yield stress increases with strain rate, but the ductility showed a complex picture. The increase of yield stress of steels is much more evident than that of Al alloys, the ductility of Al-alloy is even higher than that of the steel. A comparison between all 4 materials under similar strain rate conditions is shown in Figure 7.

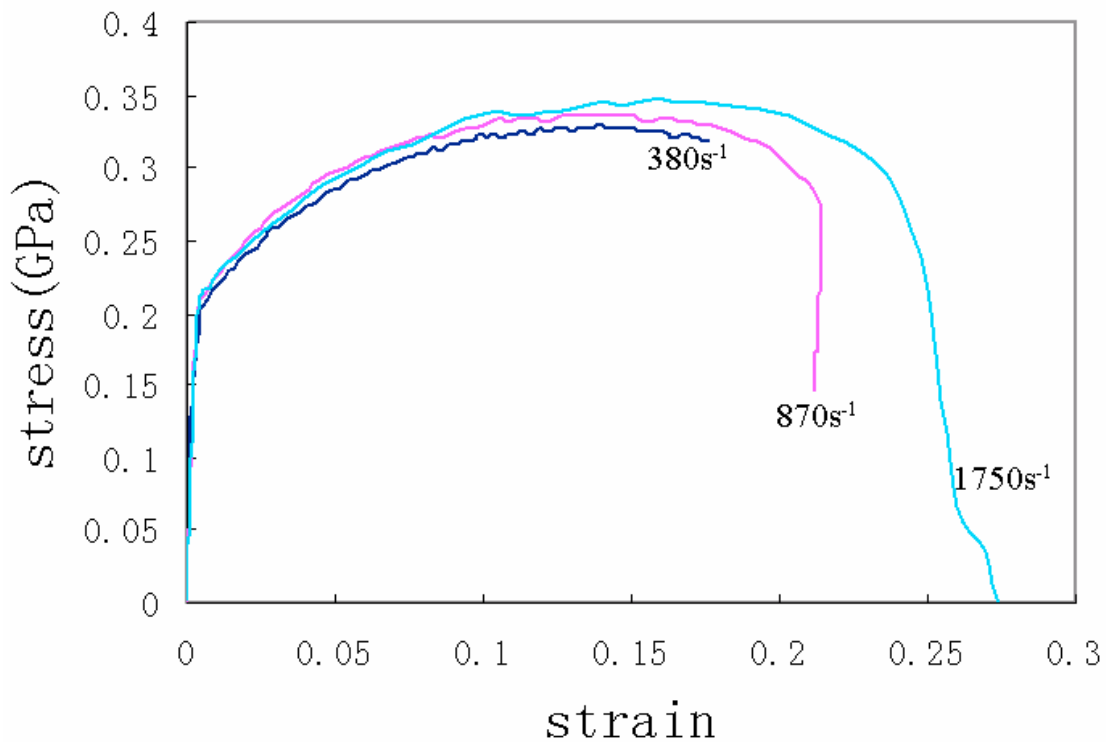


Figure 3: Engineering stress vs. engineering strain of AA6016 alloy

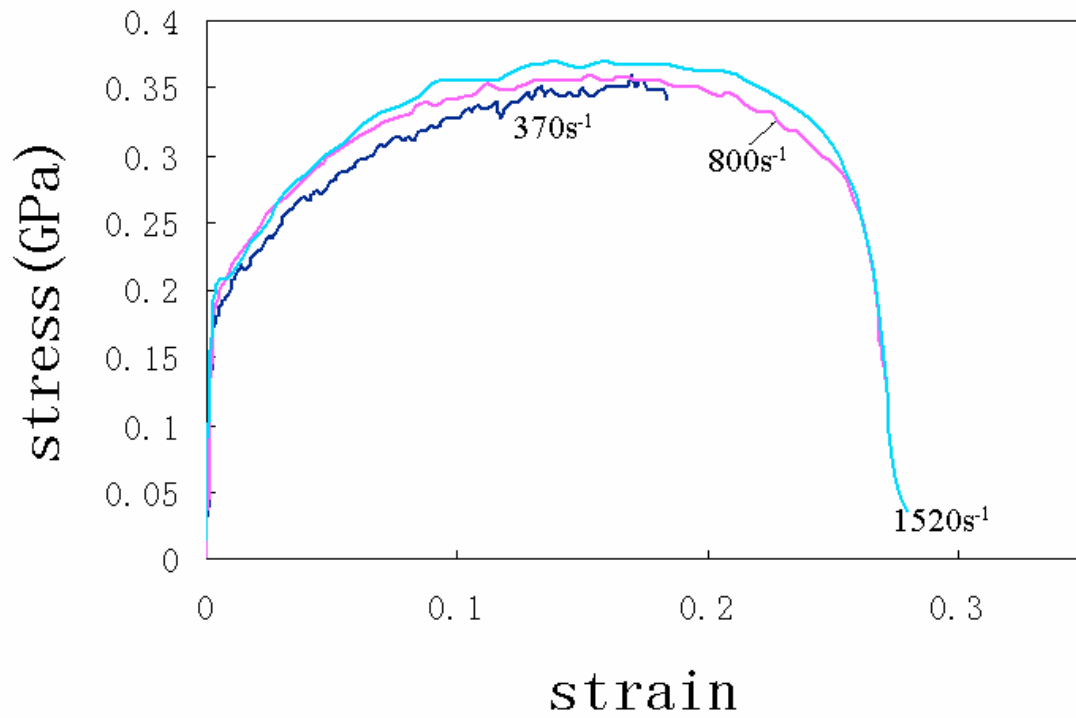


Figure 4: Engineering stress vs. engineering strain of AA5182 alloy

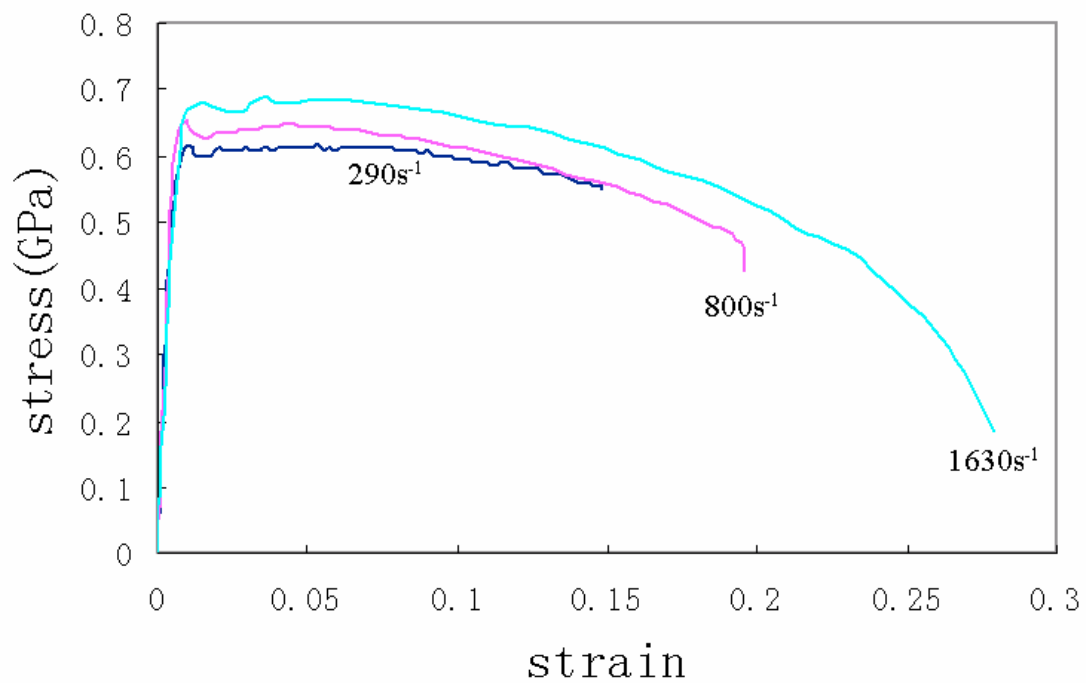


Figure 5: Engineering stress vs. engineering strain plot of V1158 steel

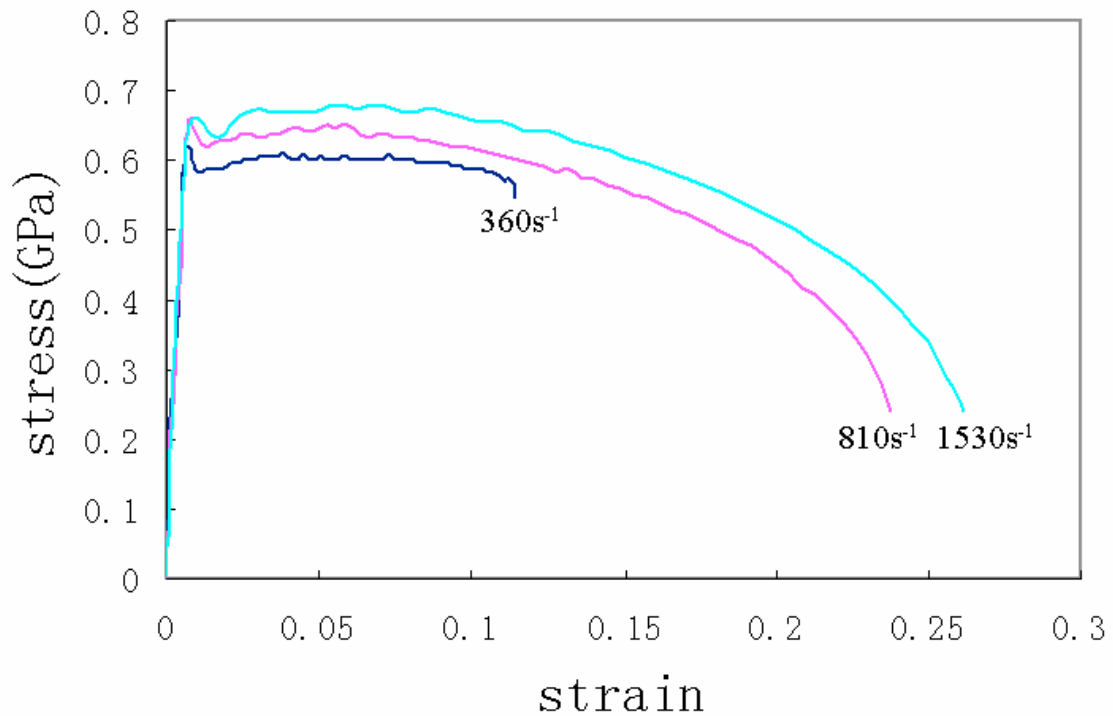


Figure 6: Engineering stress vs. engineering strain plot for FeP04 steel

In conventional quasi static tests, as it is well known, the ductility of low carbon steels is much better than that of aluminum alloys. For example, the total elongation of FeP04 steel sheet can be as high as 45% in conventional quasi static tensile tests (see Figure 8).

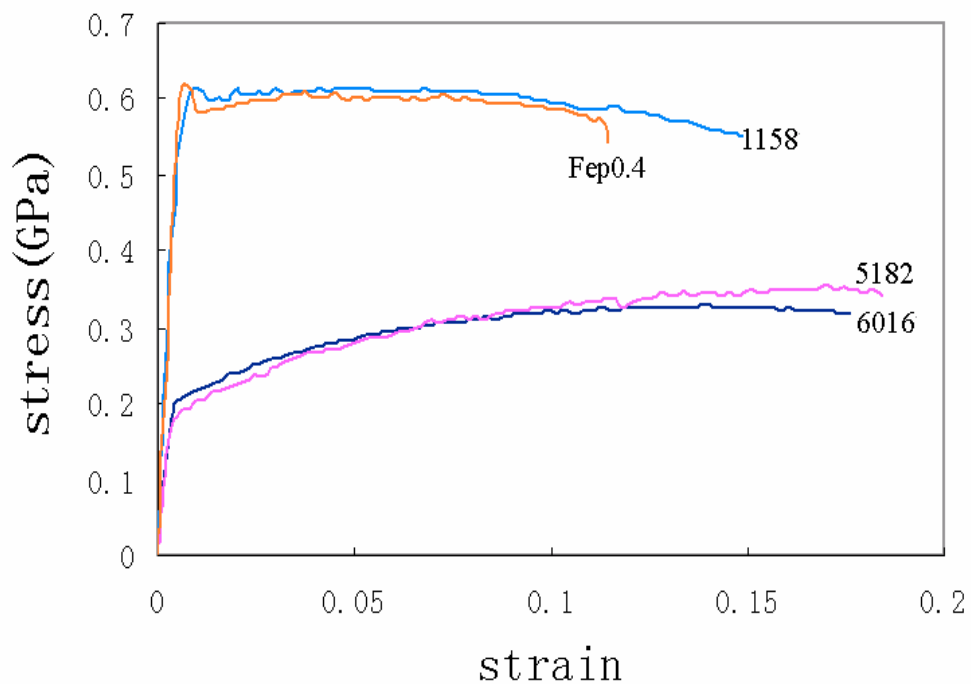


Figure 7: Engineering stress vs. engineering strain plot for all 4 materials under different deformation strain rates: 6016(380 S^{-1}), 5182(370 S^{-1}), 1158(290 S^{-1}) and Fep0.4(390 S^{-1})

For 5000 and 6000 series aluminum alloys the total tensile elongations are usually less than 25%. However, it is interesting to note that the dynamic test results showed the contrary trend. The aluminum alloys demonstrated a higher total elongation than that in quasi static test, although the gain is not large. On the other hand, the steel materials reached a much lower total elongation than that obtained in conventional tests, unexpectedly lower than that of aluminum alloys tested in this investigation. This observation is contrary to the results of some previous studies, which stated that the fracture strain of bcc-steels often was enhanced by 20 to 50% at strain rates about 10^3s^{-1} [10] and attributed the possible reasons to twinning and adiabatic heating [11]. The increase in ductility of aluminum alloys is in agreement with the results obtained in other studies [12].

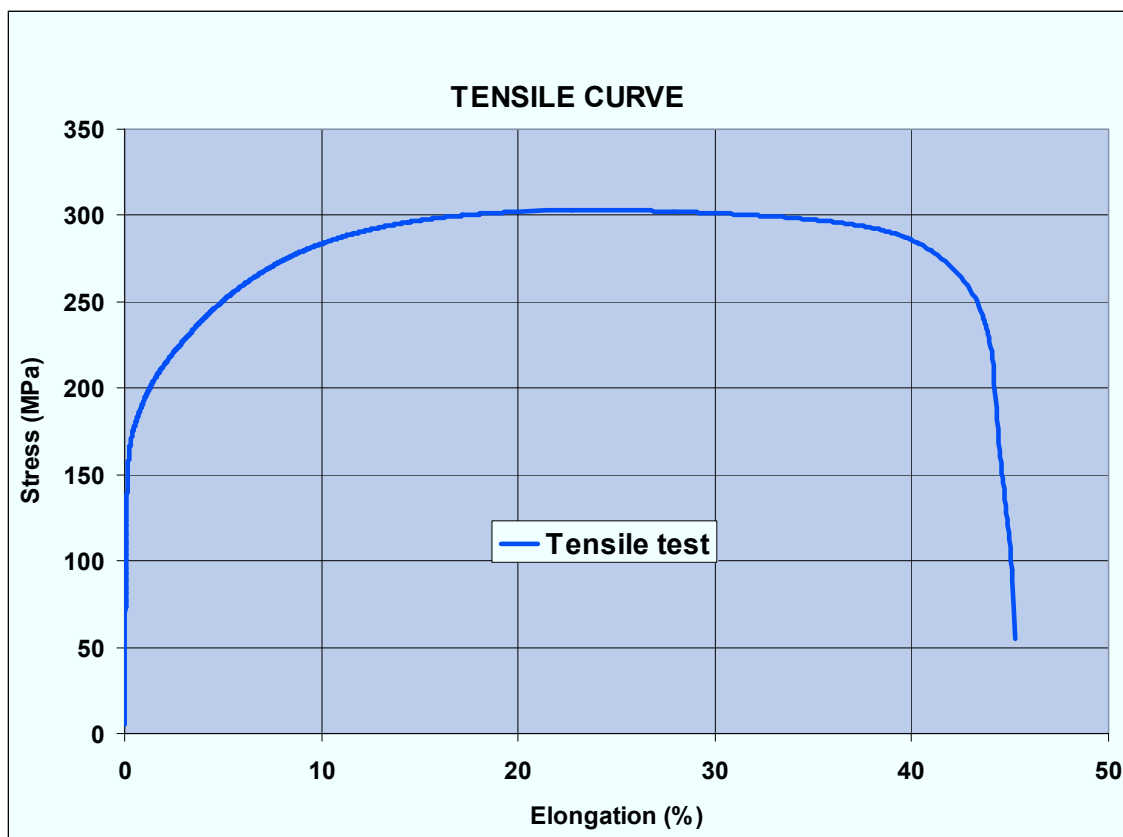


Figure 8: Engineering stress vs. engineering strain curve of FeP04 obtained with conventional quasi static tensile tests

In order to understand the experimental phenomena observed in this study, an analysis on the constitutive stress – strain relationship will be helpful. The strain hardening exponent and strain rate sensitivity are important parameters for the explanation of material flow behavior. Since the data presented above are in engineering stress and engineering strain, true stress and true strain data are needed to get the strain hardening exponent n and the strain rate sensitivity value m . True stress and true strain are calculated according to the following equations:

$$\sigma = s \cdot (1 + e) \quad (12)$$

$$\varepsilon = \log_e(1 + e) \quad (13)$$

where

- e** is the engineering strain
- ε** is the true strain
- S** is the engineering stress
- σ** is the true stress

The n and m values are then calculated according to the slope method. The n values are obtained from log-log plot of true stress and true strain, the selected strain range is between 0.05 and 0.10. For each material the strain hardening exponent at each strain rate is calculated and the results are included in Table 1. Similarly, for each material the m value is obtained from log-log plot of true stress and strain rate, the true stress values corresponding to true strain 0.15 were taken. The results are given in Table 2.

Materials	n-values (at true strain 0.05 – 0.10) in different strain rates		
AA6016	0.118 (380s ⁻¹)	0.203 (870s ⁻¹)	0.195 (1750s ⁻¹)
AA5182	0.225 (370s ⁻¹)	0.197 (800s ⁻¹)	0.235 (1520s ⁻¹)
V1158	0.0014 (290s ⁻¹)	0.0015 (800s ⁻¹)	0.0026 (1630s ⁻¹)
FeP04	0.0021 (360s ⁻¹)	0.0032 (810s ⁻¹)	0.0048 (1530s ⁻¹)

Table 1: Strain hardening exponent (corresponding to strain range 0.05 – 0.10)

Material	AA5182	AA6016	V1158	FeP04
m-value	0.0350	0.0377	0.0624	0.0717

Table 2: Strain rate sensitivity value m (calculated at true strain 0.15)

In metal forming, particularly in stretching and bending deformations, the strain hardening exponent is an indicator of the formability of the material. A higher level of this exponent is desirable since it results in a better distribution of the strain. In conventional tensile tests at room temperature the n values for FeP04 range between 0.23 and 0.25. From table 1 it can be seen that while for the Al alloys the strain hardening exponents are still close to 0.20, those for steels, however, approach to zero. Without strain hardening the steels continuously lose the ability to sustain a stable deformation and, as a result, the total elongations are quite low. As to strain rate sensitivity, for engineering metals at room temperature the m values are in the range of -0.005 to 0.015. The m value is the measure of a material to resist necking and is particularly important for superplastic deformation at high temperatures, but considered less important in quasi static deformation at room temperature. From Table 2 it can be noted that the two steel materials possess much

higher m values than the two aluminum alloys. That is why in the steels a significant increase in yielding strength is observed.

The above mentioned analysis can explain why the steels investigated in the present study demonstrated lower ductility at high speed deformation, but the reason why the aluminum alloys showed better ductility is not understood. For the purpose of EMF and EHF, the results described above reveal that aluminum alloys are ideal materials for high speed forming processes because of their lower strain rate sensitivity and high ductility properties under dynamic conditions, in addition to the advantage of good conductivity which is useful for EMF processes. On the other hand, the high strain rate sensitivity of steels in high speed deformation is a great advantage for automotive applications since this can contribute to the improvement of crashworthiness.

4 Conclusions

The rotating disk indirect bar-bar tensile impact apparatus is proved to be one of the best methods for high speed dynamic material tensile tests. According to the test results, under dynamic conditions the aluminum alloys showed better ductility than in conventional quasi static tests and at the same time there is a noticeable increase in yield strength. The two steel materials investigated in this paper demonstrated quite high strain rate sensitivity in high speed tensile deformation with a significant increase in yield strength in comparison to quasi static conditions. The ductility of the two steels is found to be lower than that obtained in conventional quasi static tensile tests due to close-to-zero strain hardening exponents. These mechanical properties mean that aluminum alloys are very suitable for high speed forming applications, while the high strain rate sensitivity of steels can bring about big advantages in automotive applications in terms of crashworthiness.

References

- [1] *Wilson, F. W.*: High Velocity Forming of Metals. ed. American Society of Tool and Manufacturing Engineers. Prentice-Hall, Inc, Englewood Cliffs, N.J. 1964
- [2] *Golovashchenko, S.; Mamutov, V.; Dmitriev, V.; Sherman, A.*: Formability of sheet metal with pulsed electromagnetic and electrohydraulic technologies. Proceedings of TMS symposium "Aluminum-2003," San-Diego, 2003, p.99-110.
- [3] *Golovashchenko S.*: Numerical and experimental results on pulsed tubes calibration, Proceedings of a 1999 TMS Symposium "Sheet Metal Forming Technology", San-Diego, 1999, p.117-127.
- [4] *Radford, D. D.; Walley, S.M.; Church, P.; Field, J.E.*: Dynamic upsetting and failure of metal cylinders: Experiments and analysis. J. Phys. IV France 110(2003)263-268.
- [5] *Swallowe, G. M.; Lee, S.F.*: A study of the mechanical properties of PMMA and PS at strain rates of 10⁻⁴ to 10³ s⁻¹ over the temperature range 293-363K. J. Phys. IV France 110(2003) 33-38.
- [6] *Albertini, C.; Cadoni, E.; Labibes, K.*: Study of the mechanical properties of plain concrete under dynamic loading. Exper. Mech. 39 (1999) 137-141.
- [7] *Gorham, D.A.*: Measurement of stress-strain properties of strong metals at very high strain rates. Inst. Phys. Conf. Ser. 47 (1980) 16-24.

- [8] *Couque, H.; Walley, S.; Lichtenberger, A.; Chartagnac, P.; Dormeival, R.; Petit, J.:* Test recommendation: Dynamic compression testing using the Talor test, publ. DYMAT, Arcueil, France (2001)
- [9] See the website www.dymat.org.
- [10] *Hartmann, K.-H.; Kunze, H.-D.; Meyer, L.W.:* Metallurgical Effects of Impact Materials. In: Shock Waves and High Strain Rate Phenomena in metals. Hrsg.M.A. Meyers and L.E.Murr, Plenum Press, New York 1981, S. 325-337.
- [11] *Reinders, B.-O.; Kunze, H.-D.:* Influence of Mechanical Twinning on the Deformation Behavior of Armco Iron. In: Shock Waves and High-Strain-Rate Phenomena in Materials Eds. M.A. Meyers, L.E.Murr, K.P. Staudhammer, M. Dekker, 1990, S. 127-136.
- [12] *Xin, L.; Zhongren, W.; Jintao, H.:* A Comparison of Mesomechanism of Dynamic Deformation between Copper and Aluminum. Journal of Materials Processing Technology 70 (1997)228-230.

Acknowledgement:

The research and experimental activities were partially carried out in the context of the Fifth Framework Project of the European Unione "Electromagnetic Forming of Tube and Sheet Metal for Automotive Parts (Acronym: EMF; Project Number: GRD2-2001-50057; Contract Number: G3RD-CT-2002-00798). The authors want to thank European Community for the financial support through the European Commision "GROWTH" Programme.

SESSION 2

MODELING & SIMULATION

Fully-coupled 3D Simulation of Electromagnetic Forming*

M. Stiemer¹, J. Unger², H. Blum¹, B. Svendsen²

¹Chair of Scientific Computing, University of Dortmund

²Chair of Mechanics, University of Dortmund

Abstract

Electromagnetic metal forming is a contact-free high-speed forming process in which strain rates of more than 10^3 s^{-1} are achieved. The deformation of the workpiece is driven by a material body force, the Lorentz force, that results from the interaction of a pulsed magnetic field with eddy currents induced in the workpiece by the magnetic field itself. The purpose of this work is to present a fully-coupled 3D simulation of the process. For the mechanical structure a thermoelastic, viscoplastic, electromagnetic material model is relevant, which is incorporated in a large-deformation dynamic formulation. The evolution of the electromagnetic fields is governed by Maxwell's equations under quasistatic conditions. Their numerical solution in 3D requires particular arrangements due to a reduced regularity at material interfaces. Hence, Nédélec elements are employed. Coupling between the thermomechanical and electromagnetic subsystems takes the form of the Lorentz force, the electromotive intensity, and the current geometry of the workpiece. A staggered scheme based on a Lagrangian mesh for the workpiece and an ALE formulation for the electromagnetic field is utilized to solve the coupled system, guaranteeing the efficiency and accuracy of the data transfer between the two meshes.

Keywords:

Modeling, Viscoplasticity, Electromagnetic metal forming

1 Introduction

Electromagnetic metal forming (EMF) is a contact-free high-speed forming process in which strain rates of more than 10^3 s^{-1} are achieved. In this process, the deformation of the workpiece

* This work was carried out in the context of the German Research Foundation (Deutsche Forschungsgemeinschaft (DFG)) Research Group FOR 443. The authors would like to thank the DFG for its financial support.

is driven by a material body force, the Lorentz force, that results from the interaction of a pulsed magnetic field with eddy currents induced in the workpiece by the magnetic field itself. The magnetic field is triggered by a tool coil adjacent to the workpiece, which is excited by the discharging current of a capacitor bank. Fig. 1 displays a typical device for sheet metal forming.

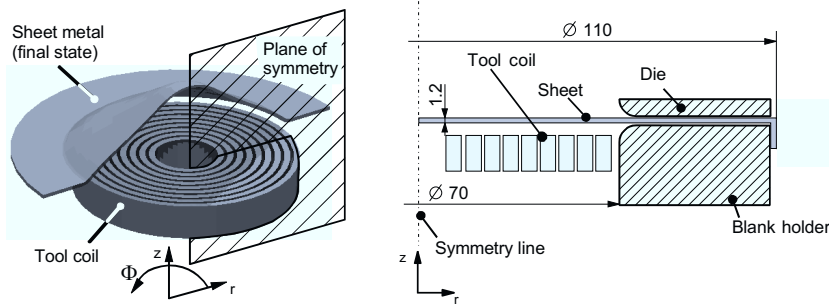


Figure 1: A typical device for electromagnetic sheet metal forming

EMF offers certain advantages over other forming methods such as an increased formability, a reduction in wrinkling, reduced tool making costs, the opportunity to combine forming and assembly operations, the avoidance of contact, and many more. However, the highly dynamic nature of this process inhibits its monitoring and control. Consequently, its industrial use has been limited to joining tubular semi-finished materials, while e.g. electromagnetic sheet metal forming is not ready for a profitable application yet. This emphasizes the significance of reliable simulations of this process to identify relevant process parameters and to optimize them.

Since the introduction of high speed computers in the 1980s, several attempts at the numerical simulation of EMF have been undertaken, including [1, 2, 3, 4]. More recently, [5, 6] and [7] utilized commercial programs like ABAQUS or MARC for the simulation of the process. However, in all approaches reported on above emphasis is placed on the modeling and simulation of the coupling between the electromagnetic and the mechanical model, while the employed material models were not adapted to the particular requirements of the process. These include first of all a consideration of the rate-dependence, which is typical of the behavior of metallic materials at high forming rates such as those achieved during EMF. This is connected to the fact that the mechanical dissipation may result in a possibly significant temperature increase in this nearly adiabatic process. A relevant thermodynamically-consistent electromagnetic thermoelastic multifield model has been developed in [8, 9] and implemented in [10], based on a Lagrangian formulation for the mechanical system and an Eulerian formulation on a fixed mesh for the electromagnetic system within an axisymmetric context.

A further drawback of the numerical schemes reported on above is their restriction to two-dimensional or axisymmetric situations. However, practical forming devices often significantly deviate from axisymmetry. Beside the much larger number of unknowns that dramatically increase the numerical expenses necessary to solve the problem and that require much more sophistication to avoid unacceptably long computing times, three-dimensional electromagnetic simulations demand a particular numerical treatment due to the lack of smoothness solutions to Maxwell's equations typically exhibit at material interfaces: A standard approach based on finite elements that enforce continuity of the approximation leads to a poor approximation of the jumps of the normal component of the electromagnetic field at material interfaces. There are several methods to cope with this difficulty, including penalty or least square methods. In this

work, Nédélec elements [11, 12] are applied, which imitate the regularity of the electromagnetic field. Instead of values in the vertices of the cells of the finite elements discretization, integral mean values over the edges represent the degrees of freedom of these elements. Nédélec elements have also been chosen in [13] to simulate three-dimensional coupled electromagnetic mechanical systems, where emphasis is laid on a fast solution of the coupled system via a multigrid solver. However, these results do not apply for EMF since the mechanical system is restricted to linear elasticity. A further difficulty arises from the fact that a Coulomb gauge condition, which is always satisfied in plane or axisymmetric situations, is not automatically fulfilled and has to be cared for. In this work, a novel non-isoparametric version of Nédélec elements is presented working with trial functions with zero divergence such that the Coulomb gauge condition is automatically fulfilled without any further requirements. This simplifies the system equations to be discretized significantly.

There are several coupling mechanisms between the thermomechanical and the electromagnetic subsystem. On the one hand, the Lorentz force computed from the electromagnetic simulation serves as load term in the mechanical impulse balance. On the other hand, the conductivity distribution entering the electromagnetic simulation via the diffusivity is determined by the current position of the structure. Further, the electromotive intensity represents an additional coupling term. The most natural way to discretize the field equations in the context of their usual formulation is to employ a fixed Eulerian mesh for the electromagnetic field and to use a moving Lagrangian mesh for the mechanical structure. However, there are problems inherent to this approach since the character of the electromagnetic field equation in a certain point of the electromagnetic mesh changes from one instant to another when the structure moves over it: As long as it is not covered by the mechanical structure, the field equations are elliptic (instantaneous assumption of the equilibrium field) and they become parabolic (diffusion process) as soon as the point is covered by the structure. This leads to a sudden change in the local discretizations since in the first case there is no explicit dependency on values of the preceding instant, while in the second case there is. Methods that rely on this Euler-Lagrange approach are sometimes called *fictitious boundary method* and are also applied to simulate liquid-structure interaction in computational fluid dynamics (e.g. [14, 15]). They are known to produce bad approximations to the forces exerted on the mechanical structure since oscillations are inevitable as long as the discretization in the (moving) transition zone between the structure and the air is not resolved very finely. However, averaged quantities are quite good approximated with this approach, even with relatively coarse discretizations. In [10], the deformation of the structure could be computed in good accuracy since the determination of the deformation field canonically includes temporal and spatial averaging of the forces applied.

However, if a good approximation to the forces is required an ALE-based method is more promising. Here, the position of the electromagnetic mesh is adapted to the current position of the structure such that the character of the electromagnetic field equations as well as the local discretizations never change. In the approach presented here, this is done in such a way that the combinatorial structure of the mesh can be maintained during the simulation, which allows the use of effective methods like fast multigrid solvers for the solution of the resulting linear system of equations.

2 Coupled model for conducting, thermoelastic viscoplastic metals

The multifield material model applied in this work is derived from a general continuum thermodynamic approach [8, 9] to the formulation of models for electromagnetic thermoelastic solids. For all structural problems of interest the frequencies of relevance (i.e. less than 10 MHz) correspond to electromagnetic wave lengths which are much larger than the structures of interest. Hence, the wave character of the electromagnetic fields is insignificant and can be neglected for such structural problems. This represents the so-called quasistatic approximation [16, §2.2 and §8.2]. In this case, it is shown in [9] that Maxwell's relations together with Ohm's law and the Coulomb gauge condition $\text{div}_s \mathbf{a} = 0$ (e.g. [17], §6.5) result in the weak forms*

$$\begin{aligned} \int_R \mathbf{a}^* \cdot \mathbf{a}_* + \{\zeta \mathbf{I} + \kappa_{EM} \nabla_s \mathbf{a}\} \cdot \nabla_s \mathbf{a}_* &= \int_{\partial R} \{\zeta \mathbf{I} + \kappa_{EM} \nabla_s \mathbf{a}\} \mathbf{n} \cdot \mathbf{a}_* \\ \int_R \nabla_s \chi \cdot \nabla_s \chi_* &= \int_{\partial R} (\nabla_s \chi \cdot \mathbf{n}) \chi_* \end{aligned} \quad (1)$$

for all test fields \mathbf{a}_* and χ_* with respect to a domain R containing the workpiece, the tool coil, and a large area of air around the tool coil and the workpiece. As usual, the test fields vanish on those parts of ∂R where \mathbf{a} and χ are specified. Here, χ denotes the electric scalar potential, \mathbf{a} the magnetic vector potential, connected to the flux density \mathbf{b} via $\mathbf{b} = \text{curl}_s \mathbf{a}$, $\zeta := \chi - \mathbf{a} \cdot \mathbf{v}$ a Euclidean frame-indifferent form of the scalar potential, \mathbf{I} a second order unit tensor, $\mathbf{a}^* := \partial \mathbf{a} + (\nabla_s \mathbf{a})\mathbf{v} + (\nabla_s \mathbf{v})^T \mathbf{a}$ the objective time-derivative of \mathbf{a} , and $\kappa_{EM} = \sigma_{EM}^{-1} \mu_{EM}^{-1}$ the magnetic diffusivity computed from the electric conductivity σ_{EM} and the permeability μ_{EM} . For the materials involved ferro-magnetic effects are not relevant and μ_{EM} can be constantly set to the value of the permeability of the vacuum. The conductivity σ_{EM} equals zero outside the tool coil and the workpiece, resulting in an infinite diffusivity there. This means that the equilibrium distribution of the magnetic vector potential depending on its current values on the interface to the tool coil and to the workpiece is instantaneously assumed in each time step. Finally, ∇_s represents the usual nabla-operator in the spatial variables. Note that the Coulomb gauge condition does not automatically hold for three-dimensional problems such that it has to be considered explicitly. On the timescale $\tau_{Exp} \sim 10^{-4}$ s relevant to EMF the typical order of magnitude $\kappa_{EM} \sim 10^{-1} \text{ m}^2 \text{ s}^{-1}$ implies that magnetic diffusion will be important in the process since it takes place over lengthscales of $\sqrt{\kappa_{EM} \tau_{Exp}} \sim 10$ cm, which are significantly larger than the smallest dimension of interest (e.g. sheet metal thickness ~ 1 mm). Turning next to the mechanical part of the coupled model, the weak momentum balance for the deformation field ξ is given by

$$\int_{B_r} (\varrho_r \ddot{\xi} - \mathbf{f}) \cdot \xi_* + \mathbf{P} \cdot \nabla_r \xi_* = \int_{\partial B_r} |\text{cof}(\mathbf{F}) \mathbf{n}_r| \mathbf{t}_c \cdot \xi_* \quad (2)$$

with respect to the referential configuration $B_r \subset R$ of the workpiece for all corresponding test fields ξ_* vanishing on those parts of the current boundary ∂B_c where ξ is specified. Here, $\mathbf{f} = \det(\mathbf{F}) \mathbf{j} \times \mathbf{b}$ represents the Lorentz (body) force (density), \mathbf{P} the first Piola-Kirchhoff stress, $\mathbf{F} := \nabla_r \xi$ the deformation gradient, and \mathbf{t}_c the current boundary traction. The mechanical model

*For notational simplicity the volume dv and surface da elements are dispensed with in the corresponding integrals.

relations are completed by the specification of the material model. For a given thermodynamic state of the mechanical structure P can, as usual, be computed from the free Helmholtz-energy stored in the material. The evolution of its density ψ_r is determined by the evolution of certain inner variables, which are in this case the accumulated inelastic strain, the elastic left Cauchy Green tensor, and the temperature. Characteristic for the viscoplastic material model here is a power law approximation to the inelastic potential determining the inelastic part of ψ_r . Hence, the projection onto the yield surface typical of rate independent J2-plasticity is replaced by a power-law function, penalizing over-stresses. See [8, 9] for a detailed discussion.

3 An ALE approach to the coupled problem

In the above formulation the mechanical field is given in a Lagrangian formulation, while the electromagnetic field is given in an Eulerian formulation. The most natural discretization of the field equations leads to a moving mesh for the mechanical system, representing its current configuration and a fixed Eulerian mesh for the electromagnetic field. The whole coupled system is then solved via a staggered solution algorithm. However, this approach implicates serious difficulties in the data transfer between the two meshes: In those areas of the electromagnetic mesh currently covered by the moving structure a diffusive process with a positive finite diffusivity takes place, while outside this region the diffusivity is infinite such that the equilibrium state of the field is immediately assumed. As shown in Figure 2, whenever the structure moves those points of the electromagnetic mesh in which a finite diffusivity arises change.

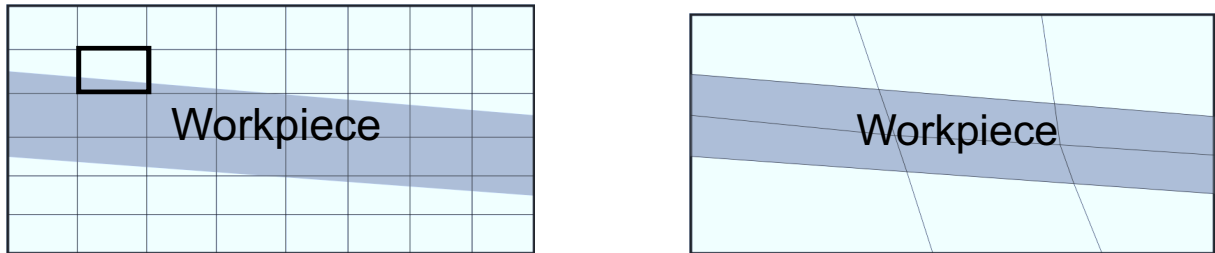


Figure 2: Comparison of a fictitious boundary method (Euler-Lagrange-approach, on the left) and an ALE-approach (Lagrange-ALE, on the right).

Such a change alters the local discretization dramatically since a contribution to the mass matrix arises as soon as a point is covered by the structure and it disappears when it is uncovered again. Particularly, for those points of the electromagnetic mesh covered by the mechanical structure values of the last time step are relevant, while the values in the other points do not depend explicitly on those of the preceding time step. It has turned out that this change of the discretization in a certain point of the electromagnetic mesh causes oscillations in the time derivative $\partial \mathbf{a}$ of the vector potential and, thus, in the Lorentz force via the contribution $\sigma_{EM} \partial \mathbf{a} \times \text{curl}_s \mathbf{a}$. These oscillations can be moderated by a very fine discretization of that part of the electromagnetic mesh lying in the interface region of the structure and the surrounding air. To avoid an inadequate fine discretization of the whole structure, adaptive techniques are necessary for a sufficiently fine resolution of the interface region. On the other hand, it is well known that averaged quantities can be determined sufficiently accurate with this approach,

which is sometimes called* *fictitious boundary method*. In [10], it was successfully applied to compute the deformation of a mechanical structure even with relatively coarse discretizations. By the integration of Lorentz forces and due to the time stepping algorithm the above mentioned oscillations are smoothed out. However, as soon as a good and efficient approximation of the forces applied on the mechanical structure is required, a fictitious boundary method is not adequate. In this case, an arbitrary Lagrangian Eulerian (ALE) formulation leads to much better results. In this approach, the electromagnetic mesh is adapted to the moving structure such that always the same elements are covered by the moving mechanical structure (see Fig. 2). Consequently, the character of the discretization in a particular element does never change, which avoids those jumps of $\partial\mathbf{a}$ that are typical for the fictitious boundary method. The movement of the electromagnetic mesh is arbitrary in the sense that the position of the discretizing mesh is not determined by requirements of the electromagnetic field equations themselves, but by accompanying conditions. To obtain a high quality mesh for the electromagnetic system with hexahedra elements that deviate as little as possible from the shape of a parallelepiped and that matches the mesh for the mechanical structure, the following algorithm is applied. Before a new time step is started each component of the deformation increment $d\xi = \xi_{n+1} - \xi_n$ is considered as the boundary value of a one-dimensional Dirichlet problem $\Delta u_k = 0$ in the air around tool coil and workpiece (i.e. in those parts of R that are outside the workpiece and outside the tool coil) with boundary values $u_k = d\xi_k$, $k = 1, \dots, 3$, on the interface between workpiece and air as well as $u_k = 0$ on the interface between tool coil and air and on the *outer boundary* ∂R (i.e. the mesh nodes are held fixed there). The solution of these problems (all possessing the same stiffness matrix) is added to the current positions of the electromagnetic mesh in the air-region around tool coil and workpiece to obtain a mesh for the next time step. To get an impression of the quality of the arising meshes, one can consider the transformation from the old to the new mesh as an elastic deformation with no transversal contraction and with elasticity module 1. This deformation is conducted by the boundary values on the interface to the tool coil, on the workpiece, and on the outer boundary since no forces are assumed to be present. In contrast to remeshing strategies, this approach preserves the combinatorial structure of the mesh, which allows an effective solution of the arising huge systems of linear equations.

The discrete field equations on the electromagnetic mesh have to be reformulated such that the movement of the mesh is correctly considered. Surprisingly, the resulting field equations simplify. Instead of working with the partial time derivative $\partial\mathbf{a}$, it is convenient in this case to employ the material time derivative $\dot{\mathbf{a}} = \partial\mathbf{a} + (\nabla_{\mathbf{s}}\mathbf{a})\mathbf{v}$ since its discretization is a function of the vertices of the moving mesh inside the mechanical structure rather than of spatial points. Thus, no interpolation is necessary to link past data to current data. Inside the fixed tool coil $\dot{\mathbf{a}} = \partial\mathbf{a}$ applies and in the air surrounding the tool coil and the workpiece the field assumes an equilibrium position instantaneously, which is explicitly neither depending on values of $\partial\mathbf{a}$ nor on values of \mathbf{a} from a preceding time step. The weak form for the electromagnetic problem – still under the assumption that a Coulomb gauge is provided for (see the next section) – then

* *The approaches discussed here are also used to simulate fluid-structure interaction in computational fluid dynamics.*

takes the form

$$\begin{aligned} \int_R \kappa_{EM}^{-1} \{ \dot{\mathbf{a}} + \nabla_s \chi - (\nabla_s \mathbf{a})^T \mathbf{v} \} \cdot \mathbf{a}_* + \nabla_s \mathbf{a} \cdot \nabla_s \mathbf{a}_* &= 0, \\ \int_R \nabla_s \chi \cdot \nabla_s \chi_* &= 0, \end{aligned} \quad (3)$$

with the additional approximation $\mathbf{a} = \mathbf{0}$ and $\chi = 0$ on ∂R , which has been chosen to be a large box containing the tool coil, the workpiece, and a large area of air surrounding them. This approximation is well founded due to the asymptotic decay of the vector and of the scalar potential of a dipole field like $O(|x|^{-2})$, $|x| \rightarrow \infty$. At interfaces between different materials further transition conditions have to be considered (see e.g. [13]).

4 Divergence-free discretization of the electromagnetic system

Next, the weak form for the electromagnetic system and for the mechanical system have to be spatially discretized. In the context of the finite-element method, standard eight-node elements are used in the latter case, while Nédélec elements [11, 12] are employed for the vector potential equation in the first case. Nédélec elements represent one of several methods to overcome the problem that finite elements enforcing continuity, as standard nodal finite elements, provide a very poor approximation to \mathbf{a} at material interfaces where the normal components of this field possess discontinuities. Moreover, a new non-isoparametric divergence-free use of Nédélec's elements has been developed here that guarantees a Coloumb gauge condition without any further requirements.

The discretization of the Lagrangian formulation of the mechanical system is based, as usual, on a spatial discretization of the mechanical structure with eight-node brick elements, each of which is the image of a reference cube under transformations that form an isoparametric family. All integrations necessary to compute the local contributions of these elements to the stiffness matrix are pulled back to the referential cube. The same strategy is applied to solve the equation for the electro-magnetic scalar potential. In case of the vector potential equation, however, no transformation on a referential cube is performed, but in each element of the discretization $R \approx \bigcup_e R^e$ of R into a finite number of hexahedra R^e a local basis of the test and trial space is constructed as follows: To each edge Γ_i of a hexahedron R^e , $1 \leq i \leq 12$, a basis function b_k of the form

$$b_k(x) = \begin{pmatrix} a_{11}^{(k)} + a_{12}^{(k)}x_2 + a_{13}^{(k)}x_3 + a_{14}^{(k)}x_2x_3 \\ a_{21}^{(k)}x_1 + a_{22}^{(k)} + a_{23}^{(k)}x_3 + a_{24}^{(k)}x_1x_3 \\ a_{31}^{(k)}x_1 + a_{32}^{(k)}x_2 + a_{33}^{(k)} + a_{34}^{(k)}x_1x_2 \end{pmatrix} \quad (4)$$

is assigned with

$$\int_{\Gamma_i} b_k \cdot t_i = \delta_{ki}, \quad (5)$$

where t_i represents a tangential vector to Γ_i of unit length and δ_{ki} is defined by $\delta_{ii} = 1$, $1 \leq i \leq 12$, and $\delta_{ki} = 0$ for $k \neq i$ respectively. Algorithmically, the determination of the b_k leads to the solution of 12 systems, each of which consists of 12 equations, in any element R^e of the

finite-element discretization. The necessary numerical efforts remain acceptably small since all 12 systems to be solved in a certain element possess the same system matrix and, e.g. MATLAB, solves 100,000 sets of 12 systems of this type within a CPU time of 5.36 s on a 2394 Mhz Opteron machine.

One easily deduces that all b_k are divergence-free and such is the local approximation to the electromagnetic field being a linear combination of these basis functions. The method presented here deviates from the usual employment of Nédélec elements (of first order) where a local basis obeying the above approach (4) is only constructed for a referential cube and then transformed by a family of isoparametric transformations on the *physical* elements such that integrals over the edges of the form (5) remain invariant. However, the local test and trial spaces obtained from this process are no longer divergence-free such that the Coulomb gauge condition is not satisfied. Hence, the weak forms for the scalar and for the vector potential to be discretized contain further terms and are more complicated. Another drawback of an isoparametric family of Nédélec elements results from further approximations that are usually undertaken in the practical implementation of the method: Certain second order terms that are dropped may become significantly large when the shape of the elements deviates too much from a parallelepiped, which may happen, if large deformations occur in the ALE context.

With the shape function matrix $\mathbf{N} \in \mathbb{R}^{12 \times 12}$ at hand constructed in the usual fashion from the basis functions b_k , one obtains

$$\mathbf{a}_e = \mathbf{N} \mathbf{a}^e$$

for the vector potential field at the element level \mathbf{a}_e . Here, $\mathbf{a}^e \in \mathbb{R}^{12}$ represents the vector of integral means (5) over the edges of R^e . This implies

$$\nabla_s^e \mathbf{a}_e = (\nabla_s^e \mathbf{N})^s \mathbf{a}^e$$

for the corresponding gradient. On this basis, one obtains the spatially-discretized form

$$\mathbf{A}^s \mathbf{a}^s + \kappa_{EM}^{-1} \mathbf{B}^s \dot{\mathbf{a}}^s = \mathbf{c}^s \quad (6)$$

for the vector \mathbf{a}^s of time-dependent integral means of the form (5) over all edges of the discretization of R . The stiffness matrix \mathbf{A}^s , the mass matrix \mathbf{B}^s , and the source vector \mathbf{c}^s are assembled from the local contributions

$$\mathbf{A}^e := \int_{R^e} (\nabla_s^e \mathbf{N})^{sT} (\nabla_s^e \mathbf{N})^s,$$

$$\mathbf{B}^e := \int_{R^e \cap W} \mathbf{N}^T \mathbf{N},$$

and

$$\mathbf{c}^e := \int_{R^e \cap W} \mathbf{N}^T \nabla_s \chi$$

of the single elements as usual. The entries of the source vector are computed from the solution χ of the electro-static equation. For simplicity, it has not been indicated in the notation that only a finite-element approximation to χ is available. According to the degenerate parabolic character of the underlying boundary value problem, equation (6) represents an ordinary differential-algebraic system of equations, yielding a purely algebraic relation for those degrees of freedom

lying in the area of infinite diffusivity.

For the simulation of the transient process time stepping algorithms have to be chosen. To solve the dynamic second order equation for the mechanical system, Newmark's method is employed. For the degenerate parabolic electromagnetic equations the generalized trapezoidal rule is utilized. With optimal parameters both methods provide an accuracy of $O(\Delta t^2)$, $\Delta t \rightarrow 0$, where Δt denotes the size of the time step.

The coupling may be realized explicitly or implicitly. In an explicit coupling scheme the electromagnetic field of the $(n + 1)$ th time step is computed from the position of the structure in the n th time step and the position of the structure in the $(n + 1)$ th time step is then computed according to this field distribution. Hence, in any time step the electromagnetic and the deformation field are only computed once. In an implicit scheme, however, the electromagnetic field is several times recalculated in each time step according to the position of the altered structure and the structure is altered several times according to the changed electromagnetic field. The latter method is more stable and allows for larger time steps. However, if the numbers of unknowns is large an explicit method may be more efficient.

5 Conclusions

A fully-coupled three-dimensional simulation of EMF has been presented based on a thermoelastic, viscoplastic, electromagnetic material model incorporated in a large-deformation dynamic Lagrangian formulation and Maxwell's equations under quasistatic conditions. To compute the applied Lorentz forces in high accuracy, an ALE approach for the electromagnetic fields has been chosen. The adaption of the electromagnetic mesh to the moving structure avoids, on the one hand, unphysical oscillations of the computed forces and simplifies, on the other hand, the field equations. In contrast to remeshing strategies this approach preserves the combinatorial structure of the mesh, which allows an effective solution of the arising huge systems of linear equations. To discretize the electromagnetic system, a novel, non-isoparametric version of Nédélec elements is employed. This formulation guarantees a Coulomb gauge, which simplifies the field relations, avoids a bad approximation at material interfaces due to the discontinuity of the normal component of the vector potential, and, finally, avoids further deviations in case of large mesh deformation, which would arise in an isoparametric context. A comparison of simulations based on the methods presented here to experimental data represents work in progress.

References

- [1] *Gourdin, W. H.*: Analysis and assessment of electromagnetic ring expansion as a high-strain rate test. *J. Appl. Phys.*, volume 65: p. 411, 1989.
- [2] *Gourdin, W. H.; Weinland, S. L.; and Boling, R. M.*: Development of the electromagnetically-launched expanding ring as a high strain-rate test. *Rev. Sci. Instrum.*, volume 60: p. 427, 1989.
- [3] *Takata, N.; Kato, M.; Sato, K.; and Tobe, T.*: High-speed forming of metal sheets by

- electromagnetic forces. *Japan Soc. Mech. Eng. Int. J.*, volume 31: p. 142, 1988.
- [4] *Fenton, G. and Daehn, G. S.*: Modeling of electromagnetically formed sheet metal. *J. Mat. Process. Tech.*, volume 75: pp. 6–16, 1998.
- [5] *Beerwald, C.; Brosius, A.; Homberg, W.; Kleiner, M.; and Wellendorf, A.*: New aspects of electromagnetic forming. In *Proceedings of the 6th International Conference on the Technology of Plasticity*, volume III, pp. 2471–2476. 1999.
- [6] *Beerwald, C.; Brosius, A.; and Kleiner, M.*: Determination of flow stress at very high strain-rates by a combination of magnetic forming and FEM calculation. In *Proceedings of the International Workshop on Friction and Flow Stress in Cutting and Forming (CIRP)*. EN-SAM - Paris, 2000.
- [7] *Brosius, A.; Chanda, T.; Kleiner, M.; and Svendsen, T.*: Finite-element modeling and simulation of material behavior during electromagnetic metal forming. In *Proceedings of the 6th International ESAFORM Conference on Material Forming 28.-30. April 2003, Italy*, pp. 971–974. ESAFORM 2003, 2003.
- [8] *Svendsen, B. and Chanda, T.*: Continuum thermodynamic modeling and simulation of electromagnetic forming. *Technische Mechanik*, volume 23: pp. 103–112, 2003.
- [9] *Svendsen, B. and Chanda, T.*: Continuum thermodynamic formulation of models for electromagnetic thermoelastic materials with application to electromagnetic metal forming. *Cont. Mech. Thermodyn.*, volume 17: pp. 1–16, 2005.
- [10] *Stiemer, M.; Unger, J.; Blum, H.; and Svendsen, B.*: Algorithmic formulation and numerical implementation of coupled multifield models for electromagnetic metal forming simulations. *Int. J. Numerical Methods in Engineering*, 2006. Accepted.
- [11] *Nédélec, J. C.*: Mixed Finite Elements in \mathbb{R}^3 . *Numerische Mathematik*, volume 35: pp. 315–341, 1980.
- [12] *Nédélec, J. C.*: A New Family of Mixed Finite Elements in \mathbb{R}^3 . *Numerische Mathematik*, volume 50: pp. 57–81, 1986.
- [13] *Schinnerl, M.; Schöberl, J.; Kaltenbacher, M.; and Lerch, R.*: Multigrid Methods for the 3D Simulation of Nonlinear Magneto-Mechanical Systems. *IEEE transactions magnetics*, volume 38: pp. 1497–1511, 2002.
- [14] *Wan and Turek, S.*: Numerical Simulation of Coupled Fluid–Solid Systems by Fictitious Boundary and Grid Deformation Methods. Technical report, FB Mathematik, Universität Dortmund, 2005. *Ergebnisberichte des Instituts für Angewandte Mathematik*, 305.
- [15] *Wan, D. and Turek, S.*: Fictitious Boundary and Moving Mesh Methods for the Numerical Simulation of Rigid Particulate Flows. Technical report, FB Mathematik, Universität Dortmund, 2006. *Ergebnisberichte des Instituts für Angewandte Mathematik*, 310.
- [16] *Moon, F.*: *Magnetic interactions in solids*. Springer-Verlag, 1980.
- [17] *Jackson, J. D.*: *Classical Electrodynamics*. John Wiley and Sons, 1987.

3D Finite Element Modeling of Electromagnetic Forming Processes^{*}

Ph. Conraux¹, M. Pignol², V. Robin², J.M. Bergheau³

¹ ESI Group, Lyon, France

² ESI France, Lyon, France

³ LTDS, UMR 5513, CNRS/ECL/ENISE, St Etienne, France

Abstract

In the electromagnetic forming process (EMF, also known as magnetic pulse forming) the metal is deformed by applying a pressure generated by an intense, transient magnetic field. A great deal of research and investigation efforts are needed for gaining better understanding on the deformation mechanism in order to develop a suitable forming strategy and equipment. One way to reach this target is to employ suitable FE software to model the process. This investigation was partly conducted in the framework of a European project called EMF (G3RD-CT-2002-00798).

The first part of the paper presents the relevant physical phenomena which govern the EMF process and their interactions. The physical coupling principle as well as the required numerical models are also established. In the second section some cases for which the so developed code can be used for virtual testing is presented for validation. Finally, numerical results are compared with experiments on a 3D model, highlighting the interest of numerical modeling for process improvements.

Keywords:

Finite element method (FEM), Electromagnetic forming, Process modeling

1 Introduction

Electromagnetic forming requires the generation of a high and transient magnetic field by using an appropriate electrical device bringing energy of about hundreds of kJ [1]. This

^{*} *This work was partly performed within the framework of the European project called EMF (G3RD-CT-2002-00798); the authors would like to thank the European Commission for its financial support*

field is developed in the surrounding of the forming coil and the metallic object to be formed. Like any other forming process, a die might be necessary to give the workpiece the required final geometry. The high current pulse passing through the coil produces eddy currents in the opposite direction to the process current that causes repulsive forces between the two components due to Lorentz forces. Modeling such a forming process requires the coupling of multiphysical phenomena, as described in Figure 1.

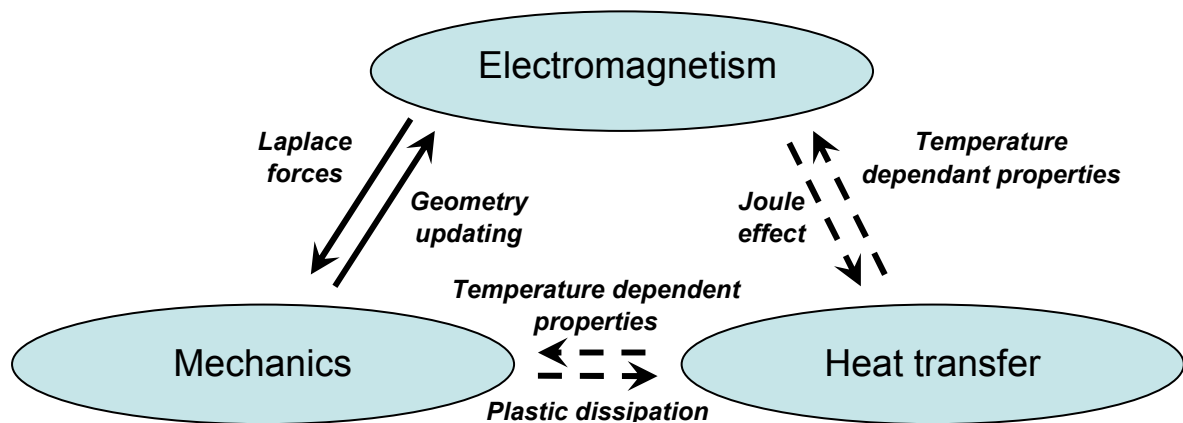


Figure 1: Interaction between involved physical phenomena

The effect of temperature variations was considered to be negligible for the simulation of the stamping process unlike some other approaches [2]. Indeed, temperature effects are very localized. Eddy currents generate a high thermal power density in a very short time so that heat transfer cannot affect the complete workpiece. The plastic work is distributed in the whole plastically deformed part of the component and does not need to be considered for more than classical stamping process.

ESI group's commercial finite element software solution is designed to model such a complex process. SYSMAGNA [3] can especially solve the electromagnetic part. PAMSTAMP code [4], dedicated to the stamping process simulation, is chosen for the structural analysis. In order to realize 3D simulations, some developments were performed in this software. The first part of the paper details the constitutive equations that govern electromagnetism and introduces the formulation of the 3D magnetodynamic problem.

The second part of the paper deals with some examples of application like tube compression test and plates, for which virtual testing is very efficient in order to optimize coil geometry or process parameters. A 3D non-rotationally symmetric component has been designed and its modeling finally demonstrates the now accomplished feasibility of 3D simulation of electromagnetic forming processes.

2 Electromagnetism finite element modeling

2.1 Maxwell equations

The electromagnetism phenomena are governed by Maxwell's equations. For sinusoidal currents whose frequency is in the order of 10^{12} Hz, displacement currents can be neglected and so the equations to be solved reduce to

$$\text{curl}H = J \quad (1)$$

$$\text{curl}E = -\frac{\partial B}{\partial t} \quad (2)$$

$$\text{div}B = 0 \quad (3)$$

where \mathbf{H} is the magnetic field, \mathbf{B} is the magnetic induction or magnetic flux density vector, \mathbf{E} is the electric field, and \mathbf{J} is the current density.

Constitutive material behavior laws relate these quantities together such as the magnetization law (4) and the Ohm's law (5).

$$B = \mu(\|H\|, \theta) \cdot (H) \quad (4)$$

where μ is the magnetic permeability that can depend considerably on temperature (Curie point) and on $\|H\|$.

$$J = \sigma(\theta)E \quad (5)$$

where σ is the electric conductivity which depends on temperature.

In order to solve this system of equations, the magnetic vector potential \mathbf{A} is introduced from equation (3)

$$B = \text{curl}A \quad (6)$$

To ensure the uniqueness of \mathbf{A} , a gauge condition (7) is mandatory (Coulomb's gauge):

$$\text{div}A = 0 \quad (7)$$

Equation (2) with relation (6) gives

$$E = -\frac{\partial A}{\partial t} - \text{grad}V \quad (8)$$

In equation (8), \mathbf{E} is not uniquely defined because it depends on the electric scalar potential \mathbf{V} that leads to an introduction of the conservation of current density (9) from equation (1).

$$\operatorname{div}(J) = 0 \quad (9)$$

2.2 Partial differential problem

Finally, the system of equations to be solved is the following:

$$\sigma \left(\frac{\partial A}{\partial t} + \operatorname{grad} V \right) + \operatorname{curl}(\nu \operatorname{curl} A) = 0 \quad (10)$$

$$\operatorname{div} \left(\sigma \left(\frac{\partial A}{\partial t} + \operatorname{grad} V \right) \right) = 0 \quad (11)$$

$$\operatorname{div} A = 0 \quad (12)$$

where $\nu = \frac{1}{\mu}$ is the magnetic reluctivity.

The different boundary conditions possible in a bounded domain Ω with boundary $\partial\Omega = \partial\Omega_A \cup \partial\Omega_H = \partial\Omega_V \cup \partial\Omega_j$ are:

- Prescribed magnetic vector potential that can depend on time

$$A(t) = A^d(t) \text{ on } \mathcal{A}\Omega_A \quad (13)$$

- Prescribed electric potential

$$V(t) = V^d(t) \text{ on } \mathcal{A}\Omega_V \quad (14)$$

- Prescribed tangential magnetic field (with n being the outward unit normal to the surface)

$$H(t) \times n = H^d(t) \text{ on } \mathcal{A}\Omega_H \quad (15)$$

- Prescribed surface current density

$$-J \cdot n = \sigma \left(\frac{\partial A}{\partial t} + \operatorname{grad} V \right) \cdot n = j^d \text{ on } \mathcal{A}\Omega_j \quad (16)$$

2.3 Finite element formulation

The variational problem consists in finding A and V such as:

$$\forall \mathbf{A}^*, \mathbf{A}^* = 0 \text{ on } \mathcal{A}\Omega_A \text{ and } \forall V^*, V^* = 0 \text{ on } \mathcal{A}\Omega_V$$

$$\int_{\Omega} A^* \cdot \sigma \left(\frac{\partial A}{\partial t} + \operatorname{grad} V \right) dv + \int_{\Omega} \operatorname{curl} A^* \cdot \nu \operatorname{curl} A dv + \alpha \int_{\Omega} \operatorname{div} A^* \cdot \operatorname{div} A dv - \int_{\mathcal{A}\Omega_H} A^* \cdot H^d ds = 0 \quad (17)$$

$$\int_{\Omega} \text{grad}V^* \cdot \sigma \left(\frac{\partial A}{\partial t} + \text{grad}V \right) dv - \int_{\partial\Omega_j} V^* \cdot j^d ds = 0 \quad (18)$$

This formulation leads to the following first order partial differential system of equations.

$$\begin{Bmatrix} \Psi_A(\mathbf{A}, V) \\ \Psi_V(\mathbf{A}, V) \end{Bmatrix} = \begin{Bmatrix} \mathbf{R}_A(\mathbf{A}, V) \\ \mathbf{R}_V(\mathbf{A}, V) \end{Bmatrix} - \begin{bmatrix} \mathbf{C}_{AA} & 0 \\ \mathbf{C}_{VA} & 0 \end{bmatrix} \cdot \begin{Bmatrix} \dot{\mathbf{A}} \\ \dot{V} \end{Bmatrix} = \begin{Bmatrix} 0 \\ 0 \end{Bmatrix} \quad (19)$$

with

$$\begin{aligned} \{\mathbf{R}_A\} &= \mathbf{A}_{\text{elements}} \{\mathbf{R}_A^e\} & \{\mathbf{R}_V\} &= \mathbf{A}_{\text{elements}} \{\mathbf{R}_V^e\} \\ [\mathbf{C}_{AA}] &= \mathbf{A}_{\text{elements}} [\mathbf{C}_{AA}^e] & [\mathbf{C}_{VA}] &= \mathbf{A}_{\text{elements}} [\mathbf{C}_{VA}^e] \end{aligned} \quad (20)$$

$$\begin{aligned} \{\mathbf{R}_A^e\} &= \int_{\partial\Omega^e \cap \partial\Omega_H} [N^e]^T H^d ds \\ &- \int_{\Omega^e} [\text{curl}N^e]^T \cdot \nu \text{curl}A dv - \alpha \int_{\Omega^e} [\text{div}N^e]^T \text{div}A dv \\ &- \int_{\Omega^e} [N^e]^T \cdot \sigma \cdot \text{grad}V dv \end{aligned}$$

$$\begin{aligned} \{\mathbf{R}_V^e\} &= \int_{\partial\Omega^e \cap \partial\Omega_j} [N^e]^T j^d ds \\ &- \int_{\Omega^e} [\text{grad}N^e]^T \cdot \sigma \cdot \text{grad}V dv \end{aligned}$$

$$[\mathbf{C}_{AA}^e] = \int_{\Omega^e} [N^e]^T \cdot \sigma [N^e] dv \quad [\mathbf{C}_{VA}^e] = \int_{\Omega^e} [\text{grad}N^e]^T \cdot \sigma [N^e] dv$$

In the equations above, $\begin{Bmatrix} \mathbf{A} \\ V \end{Bmatrix}$ gather all degrees of freedom (dof) of the problem. 4 dof

(A_x, A_y, A_z, V) are related to each node of the mesh. $\mathbf{A}_{\text{elements}}$ is the assembling operator of the elements. $[N^e]$ represents the shape functions of the element, $[\text{grad}N^e]$, the shape function gradient, and $[\text{curl}N^e]$ the shape function curl in such a way that inside each element $A = [N^e]\{\mathbf{A}\}$, $V = [N^e]\{V\}$, $\text{grad}V = [\text{grad}N^e]\{V\}$, and $\text{curl}A = [\text{curl}N^e]\{\mathbf{A}\}$.

Equations (19) are solved step by step in time using an implicit backward Euler method. At each time step the solution is obtained through a Newton-Raphson procedure.

3 Validation examples

3.1 Mechanical behavior law

The sheet and tube specimens used for validation are aluminum alloys AA5754, AA5182, and AA6016. Their flow behavior needs to take into account high strain rates and the so-called Johnson-Cook model (21) is then used [5]. The model can also consider the influence of temperature, but this term is neglected for the simulation.

$$\sigma = \left(A + B(\varepsilon_{eq}^p)^n \right) \left(1 + C \ln \dot{\varepsilon}_{eq}^* \right) \left(1 - T^{*m} \right) \quad (21)$$

with

$$\dot{\varepsilon}_{eq}^* = \frac{\dot{\varepsilon}_{eq}}{\dot{\varepsilon}_0} \quad \text{and} \quad T^* = \frac{\theta - T_{ref}}{T_{melt} - T_{ref}}$$

$\dot{\varepsilon}_{eq}^*$ is the strain rate without dimension with $\dot{\varepsilon}_0$ usually set to $1.0s^{-1}$. T_{melt} , T_{ref} , and θ respectively represent the fusion temperature, a reference temperature as room temperature, and the media temperature.

The parameters of the Johnson-Cook material behavior law has been identified at the Department of Material Engineering of the University of Trento in Italy.

3.2 Virtual testing

The experiments have been conducted at the Department of Forming Technology at the University of Dortmund in Germany. The experimental results are compared to the ones obtained by calculation. The isotropic plastic behavior of the workpiece is governed by the Johnson-Cook law. The electromagnetic behavior is also isotropic. No material non-linearity is considered for the electromagnetism simulation.

3.2.1 Tube compression tests

The geometry and the mesh are presented in Figures 2a and 2b. The surrounding air is meshed in order to propagate the magnetic field generated by the coil. The tube is made of AA5754 aluminum alloy. The charging energy is about 500J. The current applied to the coils becomes null after 200 μ s and, thus, the coupling between electromagnetism calculation and mechanical analysis is carried out each 2 μ s.

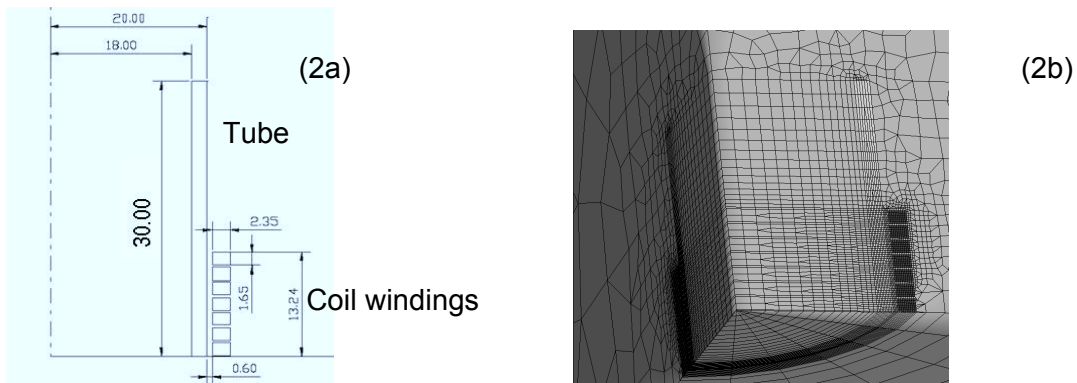


Figure 2: Tube test geometry description (2a) and related 3D mesh (2b)

Figure 3 gives the maximal diameter reduction versus time. Experiments are compared to the numerical results and both are really in good agreement.

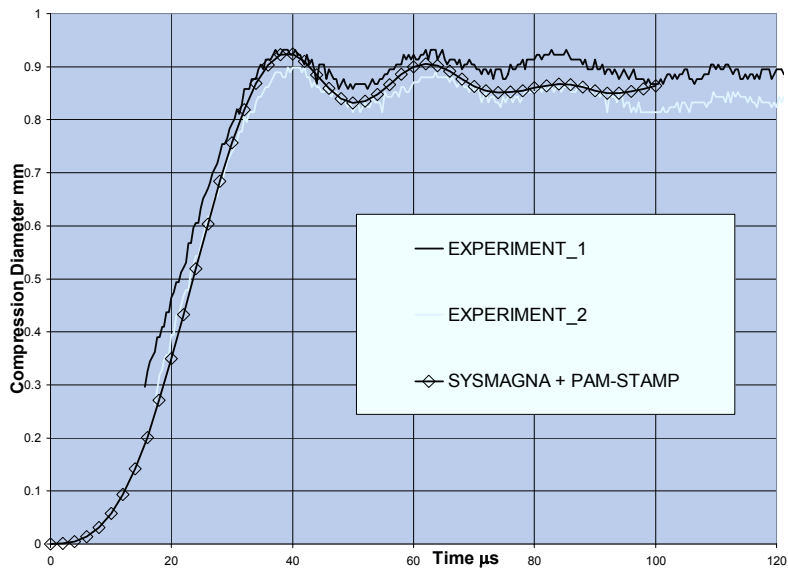


Figure 3: Diameter reduction as a function of time

3.2.2 Plate tests

The geometry of the plate test specimen is shown in Figure 4.

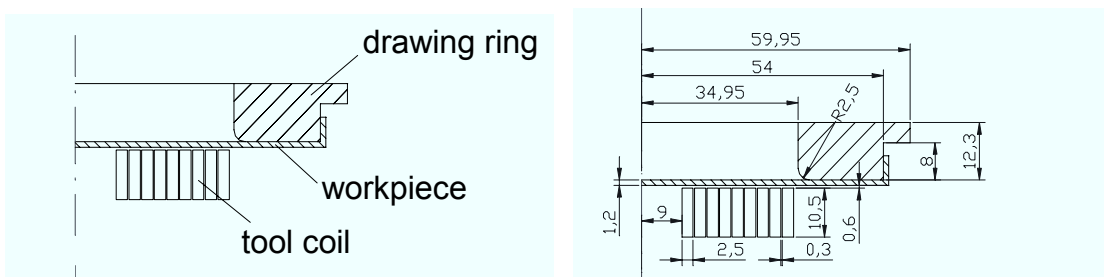


Figure 4: Geometry description of the plate test specimen

The sheet is made of AA5182 aluminum alloy. The charging energy is about 1200J. The coupling time step is $2\mu\text{s}$. For this simulation contact conditions need to be considered between the plate and the drawing ring as it influences the way the workpiece is deforming.

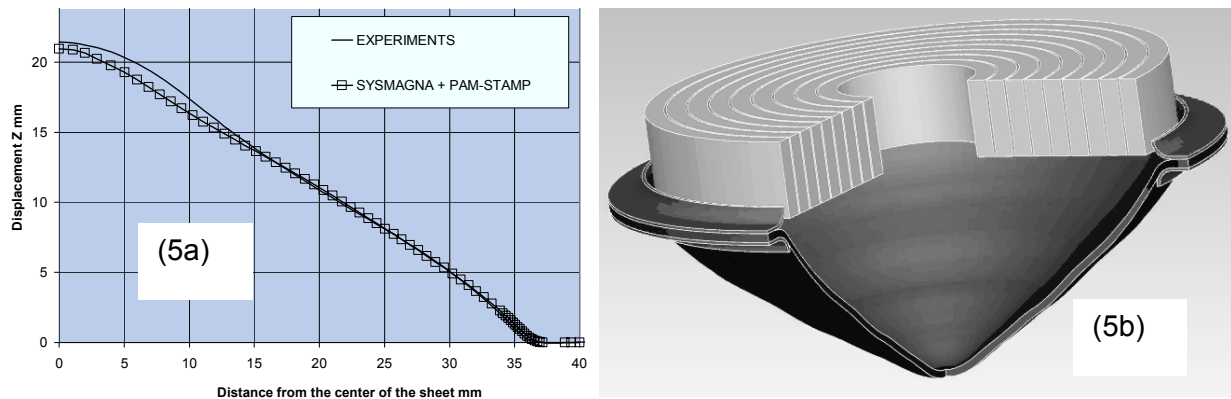


Figure 5: Deformation at the end of the process

Figures 5a and 5b give the displacements of the outer surface of the plate according to the distance from its centre and the deformed shape at the end of the process respectively. Experimental results and calculated displacements are very close to each other.

3.3 Industrial validation

This paragraph highlights all the technical functionalities of the software used to model the electromagnetic forming process. Indeed, the proposed validation of the industrial example is non-rotationally symmetric and a die is required to accurately obtain the final deformed shape. The die is oval, as shown in Figure 6, and the coil is designed according this shape.

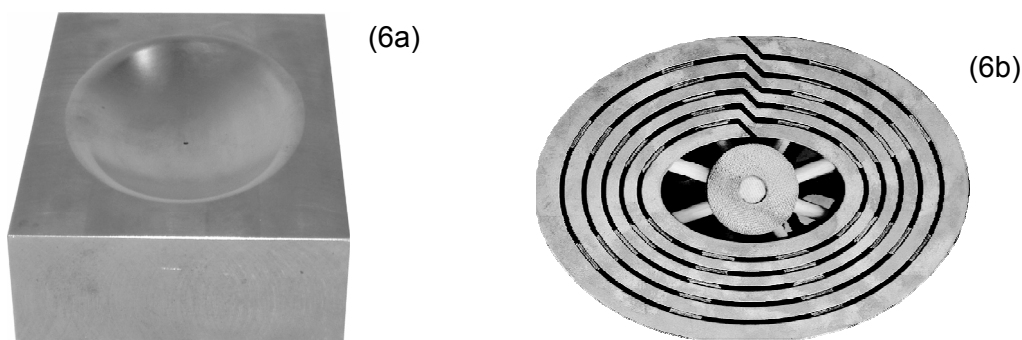


Figure 6: Die (6a) and coil (6b) geometries

The sheet is made of AA6016 aluminum alloy. Two charging energies were tested for this component. With a charging energy of about 2100J the required deformed shape is not obtained. So, the comparison between experiments and calculations focuses on the

process performed with the highest energy. Experimentally, the final geometry does not fit the die. Numerically, the results emphasize the same phenomena, as shown in Figure 7a along the major axis and 7b along the minor one.

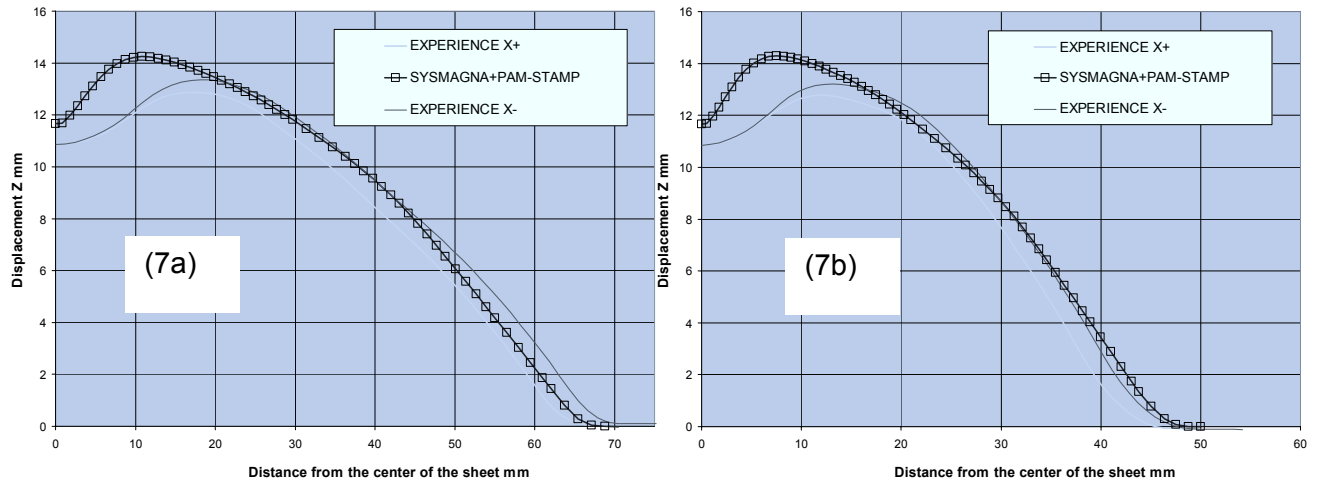


Figure 7: Displacement at the end of the process along the major axis (7a) and the minor axis (7b)

4 Conclusions

The efficiency of the fully 3D coupled numerical modeling of an electroforming process for virtual testing has been demonstrated. Indeed, experiments and computations correlate with each other, which validates the assumption made on temperature effects. Another approach should consist in combining the finite element method and boundary element method in order to get rid of the difficulty of meshing. Modeling movable parts involves to take care of the mesh density of the surrounding air. Sometimes, remeshing cannot be prevented. If the boundary element method makes the work easier in this case, it generally also leads to higher CPU costs directly related to the number of nodes on the boundary. For tube or sheet virtual testing CPU time is less than one hour using a personal computer (Pentium 4 and 2GHz) when the air is meshed. The required RAM is about 500Mbytes. Finally, concerning the tube compression test, the advantage of 3D analyses compared to 2D ones is the capability to predict the wrinkling effect due to a local reduction of the thickness of the tube or a non-perfect round tube. The highly dynamic nature of deformations involved during electroforming processes has the ability to improve the formability of aluminum more than conventional forming. Nevertheless, the alloy can exceed its forming limit and fracture. This other kind of defect can also be numerically predicted by including fracture mechanics to detect a crack initiation and the way it propagates [6].

References

- [1] *Psyk, V.; Beerwald, C.; Kleiner, M; Beerwald, M; Henselek, A:* Use of electromagnetic forming in process combination for the production of automotive part. Proceedings of the 2nd European Pulser Power Symposium, Hamburg, September 2005.
- [2] *Karch, C.; Roll, C.:* Transient simulation of electromagnetic forming of aluminium tubes. Proceedings of the 11th International Conference on Sheet Metal, Nürnberg, April 2005.
- [3] SYSWELD®, User's manual, ESI Group, 2005.
- [4] PAM-STAMP®, User's manual, ESI Group, 2005.
- [5] *Johnson, G.R.; Cook, W.H.:* A constitutive model and data for metals subjected to large strains, high strain rates and high temperature. Proceedings of the 7th International Symposium on Ballistic, 1983, p. 541.
- [6] *Kamoulakos, A.; Culiere, P.; Araki, T:* Prediction of ductile metal rupture with the E-W model in PAM-CRASH. Proceedings of the International Body Engineering Conference, Chiba, October 2003.

Efficient Finite Element and Contact Procedures for the Simulation of High Speed Sheet Metal Forming Processes*

M. Schwarze¹, A. Brosius², S. Reese¹, M. Kleiner²

¹Institute of Solid Mechanics, University Carolo-Wilhelmina at Braunschweig, Germany

²Institute of Forming Technology and Lightweight Construction, University of Dortmund, Germany

Abstract

A large variety of forming processes is used in industrial manufacturing processes. The numerical simulation of such processes puts high demands on the finite element technology. Usually first order isoparametric elements are preferred because of their robustness and numerical efficiency. Unfortunately, these elements tend to undesired numerical effects like "locking", predominant in situations characterized by plastic incompressibility or pure bending. To overcome this problem, several authors [1, 2, 4] propose finite element formulations based on the concept of reduced integration with hourglass stabilization by applying the "enhanced strain method". The main advantage of the proposed new isoparametric solid-shell formulation with linear ansatz functions is the fact that the undesirable effects of locking are eliminated.

The previously described element technique can be applied to analyze specific problems of high speed forming into a cavity: Working with contact surfaces discretized by first order finite elements leads to discontinuities of the normal patch vector and, subsequently, to non-smooth sliding [5]. In quasi-static forming processes these discontinuities will not influence the contact forces noticeably. However, in dynamic investigations the sudden change of contact forces due to the rough surface description leads to a very high acceleration of the contact nodes. To avoid this effect, a smoothing algorithm will be described.

Keywords:

Sheet metal forming, Solid-shell formulation, Contact formulation

*This work is based on the results of the research group FOR 443. The authors wish to thank the German Research Foundation – DFG for its financial support.

1 Introduction

In mechanical engineering, e.g. in car industries, the development and optimization of forming tools and their parameters according to the desired forming result is a cost and time intensive factor of the production process. In order to reduce expensive try-out processes, numerical tools, especially the finite element method, are applied before setting up the forming tools. The numerical simulation of forming processes makes high demands on the finite element technology. Finite element formulations with low order ansatz functions are preferred due to their numerical efficiency and robustness. Furthermore, they prove to be advantageous when automatic meshing tools are applied.

During the forming process the structure underlies extreme bending. Furthermore, the material shows nearly incompressible behavior during plastification. By using the standard finite element formulation with linear ansatz functions (Q1) the undesirable effect of locking can be observed. It leads to an overestimation of the stresses and an underestimation of the deformation. One possibility to overcome locking is the use of element formulations with high ansatz order. However, then one can not profit from the advantages described before. In the field of element technology modifications of classical low order finite element formulations are derived to avoid the non-physical effect of locking. A possible strategy is the method of incompatible modes. It is the basis of the enhanced assumed strain (EAS) concept [16]. Based on a mixed variational principle additional "enhanced" strains are introduced to avoid the non-physical constraint caused by the low order ansatz functions. In problems under compression numerical instabilities might arise [17]. A second concept in finite element technology is the method of reduced integration. The integration over a smaller number of integration points eventually leads to non-physical zero-modes (hourglassing). For this reason an hourglass stabilization is necessary. Several authors (e.g. [17, 1, 18] and [4]) have worked on reduced integration with hourglass stabilization in combination with the EAS concept. The results are simple, robust, and efficient element formulations. For the special context of sheet metal forming processes a so-called solid-shell formulation with reduced integration and hourglass stabilization by means of the EAS concept is derived. It only has displacement degrees-of-freedom and takes the element thickness correctly into account.

In forming processes contact between work tools and workpiece occur. The treatment of contact problems is an important aspect in the finite element analysis of forming processes. In the context of the computational modeling we differentiate between deformable-to-deformable contact (including self contact) and deformable-to-rigid contact. In the first case the description of all contact surfaces depends on the discretized domain. Due to the use of modern and efficient element formulations only a relative coarse mesh is necessary. By using finite element formulations with linear ansatz functions contact surfaces are modeled as being piecewise linear. This leads to a non-smooth normal patch vector and to non-smooth sliding. We observe sudden changes of contact forces and jumps in the velocity field. Furthermore, using an implicit time integration a divergence of the Newton-Raphson scheme and numerical instabilities might arise.

To avoid these non-physical effects, various approaches to smoothen the contact surface are developed. For two-dimensional cases in [5, 8] the interpolation polynomials are defined at the midpoints of neighbored element edges, whereas in [7, 9] the element nodes themselves are

used. In the first case the contact interface lies inside the discretized domain and in the second case it is modeled at the outside. Three-dimensional smoothing procedures are formulated by [10, 12].

The contact formulation presented here follows geometrically the smoothing strategy of [5] for the two-dimensional case. The contact interpolation is carried out by cubic Hermite ansatz functions. The new aspect in this approach is the smoothing of slave surface and master surface as well. This leads to a quasi-segment-to-segment approach with six nodes per contact element (three for the slave segment and three for the master segment). The contact interface can be correctly taken into account by using a gauss integration over the slave surface.

2 Solid-shell formulation

The basic equation set of continuum mechanics will be given here for the dynamic case without damping

$$\text{Div } \mathbf{P} + \rho_0 (\mathbf{b}_v - \ddot{\mathbf{u}}) = \mathbf{0} \quad (1)$$

$$\mathbf{P} - \frac{\partial W}{\partial \mathbf{H}} = \mathbf{0} \quad (2)$$

$$\mathbf{H} - \text{Grad } \mathbf{u} = \mathbf{H}_{enh} = \mathbf{0} \quad (3)$$

Equation 1 denotes the balance of linear momentum, in which ρ_0 is the reference mass density and $\rho_0 \mathbf{b}_v$ the vector of volume forces, e.g. the gravity. In the constitutive equation (Equation 2) $W = W(\mathbf{H}, \mathbf{X})$ defines the strain energy function as a function of the total strain \mathbf{H} and the vector of internal variables \mathbf{X} . \mathbf{P}^h is the first Piola-Kirchhoff stress tensor. The total strain \mathbf{H} is additively decomposed into the compatible strain $\text{Grad } \mathbf{u}$ and the enhanced part \mathbf{H}_{enh} , compare Equation 3. The index h denotes the finite element discretization of the domain. Starting point of the solid-shell formulation is the two-field functional

$$g_1(\mathbf{u}^h, \mathbf{H}_{enh}^h) = \int_{B_0^h} \tilde{\mathbf{P}}(\mathbf{H}^h) : \text{Grad } \delta \mathbf{u}^h dV + \int_{B_0^h} \rho_0 \ddot{\mathbf{u}} \delta \mathbf{u}^h dV - g_{ext} = 0 \quad (4)$$

$$g_2(\mathbf{u}^h, \mathbf{H}_{enh}^h) = \int_{B_0^h} \tilde{\mathbf{P}}(\mathbf{H}^h) : \delta \mathbf{H}_{enh}^h dV = 0 \quad (5)$$

in which the displacement vector \mathbf{u}^h and the tensor of enhanced strains \mathbf{H}_{enh}^h are the independent variables. The term g_{ext} includes the virtual work of the external forces. In the following all values are given in matrix notation. The interpolation of \mathbf{H}^h does not differ from the one chosen for the hexahedral element formulation proposed by [14]:

$$\mathbf{H}^h = \underbrace{(\mathbf{B}_{lin} + (\mathbf{j}_0^1 \mathbf{L}_{hg}^1 + \mathbf{j}_0^2 \mathbf{L}_{hg}^2) \mathbf{M}_{hg}) \mathbf{U}_e}_{:= \mathbf{H}_{comp}^h = \mathbf{H}_{lin}^h + \mathbf{H}_{hg}^h} + \underbrace{\mathbf{j}_0^1 \mathbf{L}_{enh}^1 \mathbf{W}_e}_{:= \mathbf{H}_{enh}^h} \quad (6)$$

It is well known that the hourglass part \mathbf{H}_{hg}^h of the compatible strain tensor \mathbf{H}_{comp}^h includes the locking behavior, whereas the linear part \mathbf{H}_{lin}^h does not include any constraints which lead to locking. For the definition of variables used above, see [3]. In contrast to classical finite element formulations the Jacobian matrix is always evaluated in the center of the element. Further modifications avoid volumetric locking [15].

At the present point of the derivation the formulation does not differ majorly from [15]. However, the analysis of thin structures with only one element over the thickness is the main target of the development of the formulation from the numerical point of view. So the main question is how to transfer the three-dimensional formulation into a solid-shell concept. A good description of the stress state over the thickness is very important. The first Piola-Kirchhoff stress tensor has to be non-linear in thickness direction. For this reason a Taylor expansion is carried out with respect to the point $\xi_*^T = \{0, 0, \xi\}$, see Figure 1. In this way the non-linear dependence on ζ is retained in the constitutive qualities, namely the stress \mathbf{P}_*^h and the tangent \mathbf{A}_* . This leads to the split

$$\mathbf{P}^h \approx \mathbf{P}^h \Big|_{\xi=\xi_*} + \frac{\partial \mathbf{P}^h}{\partial \xi} \Big|_{\xi=\xi_*} (\xi - 0) + \frac{\partial \mathbf{P}^h}{\partial \eta} \Big|_{\xi=\xi_*} (\eta - 0) \quad (7)$$

$$= \mathbf{P}_*^h + \mathbf{A}_*^h \left((\mathbf{j}_0^1 \mathbf{L}_{hg*}^1 + \mathbf{j}_0^2 \mathbf{L}_{hg*}^2) \mathbf{M}_{hg} \mathbf{U}_e + \mathbf{j}_0^1 \mathbf{L}_{enh*} \mathbf{W}_e \right) \quad (8)$$

of the stress tensor. \mathbf{P}_*^h is non-linear in the thickness direction ζ and independent of ξ and η .

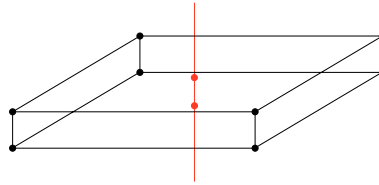


Figure 1: Solid-shell element

The second term is non-linear in ζ and linear in ξ and η . The stresses are therefore non-linear in thickness direction and linear in the shell plane. \mathbf{A}_*^h denotes the derivative of $\tilde{\mathbf{P}}(\mathbf{H}^h)$ with respect to the total strain \mathbf{H}^h (consistent tangent). At the element level the following steps are executed: The identification of the thickness direction will be performed by a coordinate transformation. Furthermore, the analysis of the enhanced degrees-of-freedom is necessary. Using Equation 8, they are determined by the non-linear equation

$$\mathbf{R}_w = \int_{\zeta=-1}^{\zeta=+1} \hat{\mathbf{L}}^{\zeta T} \mathbf{j}_0^{1T} \mathbf{P}_*^h d\zeta 4J_0 \quad (9)$$

for \mathbf{W}_e^ζ and the linear equation

$$\mathbf{W}_e^{\xi\eta} = -\mathbf{K}_{ww} \mathbf{K}_{wu} \mathbf{U}_e \quad (10)$$

for $\mathbf{W}_e^{\xi\eta}$. Due to the linearity of Equation 10 only a reduced number of enhanced degrees-of-freedom, namely the three values \mathbf{W}_e^ζ , have to be saved as history variables.

The differential equation

$$\mathbf{R}_{uG}(\mathbf{U}) + \mathbf{K}_{stab,G} \mathbf{U} + \mathbf{M}_G \ddot{\mathbf{U}} - \mathbf{F}_{ext} = \mathbf{0} \quad (11)$$

which finally results from the weak form, has to be analyzed in every time step. In comparison to the classical form, the product of the stabilization matrix $\mathbf{K}_{stab,G}$ and the global displacement vector \mathbf{U} is added. The element stabilization matrix $\mathbf{K}_{stab,e}$ has the form

$$\mathbf{K}_{stab,e} = \int_{\square} \mathbf{B}_{def}^T \mathbf{A}_* \mathbf{B}_{def} d\xi d\eta \quad (12)$$

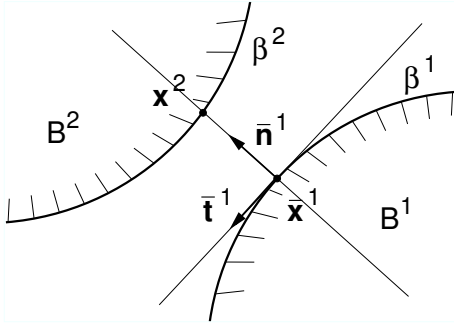


Figure 2: Contact kinematic

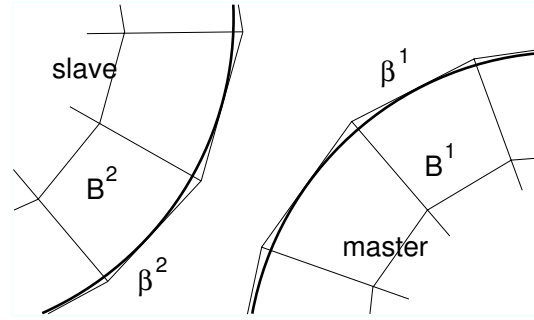


Figure 3: Smoothing concept

point $\bar{\mathbf{x}}^1$ on the master surface β_c^1 has to be found. Assuming a convex surface description of a two-dimensional problem, the minimum distance problem

$$|g_n| = \|\mathbf{x}^2 - \bar{\mathbf{x}}^1\| = \min \|\mathbf{x}^2(\hat{\xi}) - \bar{\mathbf{x}}^1(\bar{\xi})\| \quad (15)$$

has to be investigated. $\mathbf{x}^2(\hat{\xi})$ denotes the current slave node depending on the gauss point coordinate $\hat{\xi}$ and $\bar{\mathbf{x}}^1(\bar{\xi})$ is the master node at the convective solution coordinate $\bar{\xi}$. The unit outward normal vector at the master surface can be defined as

$$\bar{\mathbf{n}}^1(\bar{\xi}) := \frac{\bar{\mathbf{t}}^1(\bar{\xi}) \times \mathbf{e}_3}{\|\bar{\mathbf{t}}^1(\bar{\xi}) \times \mathbf{e}_3\|} \quad (16)$$

in which the cartesian basis vector \mathbf{e}_3 indicates the outward normal vector on the sheet plane. The tangent vector is computed by

$$\bar{\mathbf{t}}^1(\bar{\xi}) = \frac{\partial \bar{\mathbf{x}}^1(\bar{\xi})}{\partial \bar{\xi}} \left\| \frac{\partial \bar{\mathbf{x}}^1(\bar{\xi})}{\partial \bar{\xi}} \right\|^{-1} \quad (17)$$

If non-linear contact surface descriptions are used, Equation 15 leads with

$$[\mathbf{x}^2(\hat{\xi}) - \bar{\mathbf{x}}^1(\bar{\xi})] \cdot \frac{\partial \bar{\mathbf{x}}^1(\bar{\xi})}{\partial \bar{\xi}} = 0 \quad (18)$$

to a non-linear equation system. The gap function

$$g_n = [\mathbf{x}^2(\hat{\xi}) - \bar{\mathbf{x}}^1(\bar{\xi})] \cdot \bar{\mathbf{n}}^1(\bar{\xi}) \quad (19)$$

declares the contact condition between the slave and master node. If $g_n > 0$ no contact holds, for $g_n = 0$ perfect contact, and if $g_n < 0$ penetration occurs.

As depicted in Figure 3 we model the contact smoothing along the element edges in a similar way to [5] and [10]. The starting point \mathbf{x}_a and the end point \mathbf{x}_b of the contact segment are defined by

$$\mathbf{x}_i = \sum_{k=1}^2 N_k(\phi_i) \mathbf{x}_k, \quad i = a, b \quad (20)$$

in which N_k ($k = 1, 2$) denote the classical linear ansatz functions, see Figure 4, and \mathbf{x}_k the nodes of the adjacent element edge. ϕ_a and ϕ_b are user defined convective coordinates. Using a cubic Hermite interpolation, e.g. [11], the contact segment

$$\mathbf{x}(\xi) = H_1(\xi) \mathbf{x}_a + H_2(\xi) \mathbf{x}_b + H_3(\xi) \beta_a l_a \mathbf{t}_a + H_4(\xi) \beta_b l_b \mathbf{t}_b \quad (21)$$

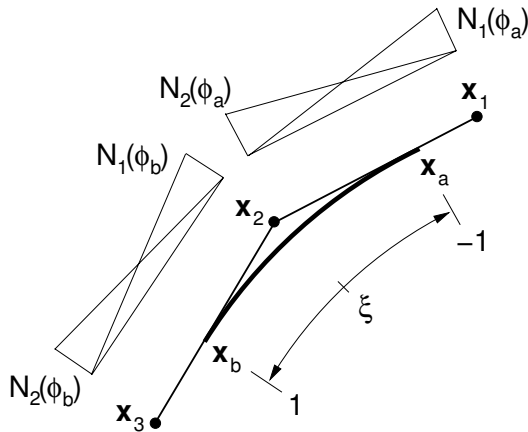


Figure 4: Contact segment definition

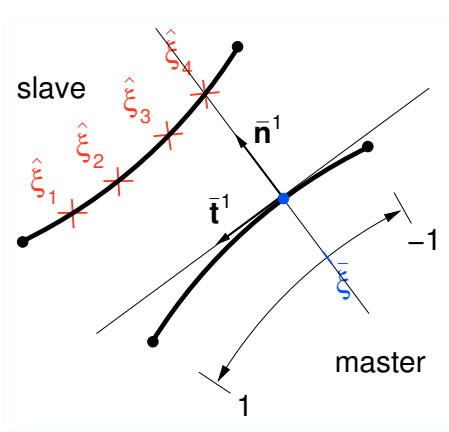


Figure 5: Gauss point integration

with the weighted tangents

$$l_a \mathbf{t}_a = \frac{1}{2} (\mathbf{x}_2 - \mathbf{x}_1) \quad \text{and} \quad l_b \mathbf{t}_b = \frac{1}{2} (\mathbf{x}_3 - \mathbf{x}_2) \quad (22)$$

at the starting point \mathbf{x}_a and the end point \mathbf{x}_b is defined by the Hermite functions

$$\begin{aligned} H_1(\xi) &= \frac{1}{4} (2 - 3\xi + \xi^3), & H_3(\xi) &= \frac{1}{4} (1 - \xi - \xi^2 + \xi^3), \\ H_2(\xi) &= \frac{1}{4} (2 + 3\xi - \xi^3), & H_4(\xi) &= \frac{1}{4} (-1 - \xi + \xi^2 + \xi^3), \end{aligned} \quad (23)$$

the factors β_a and β_b and the element nodes $\mathbf{x}_1, \mathbf{x}_2$ and \mathbf{x}_3 of the discretized domain. For simplification reasons we define $\beta_a = \beta_b = \beta$. In contrast to other authors ([7], [9]) the slave contact surface as well as the master surface is smoothed, see Figures 3 and 5. This leads to a quasi-segment-to-segment approach discretized by a six-node contact element formulation. Using Equation 22 and 23, Equation 21 reduces after rearranging to

$$\mathbf{x}^2(\hat{\xi}) = \sum_{k=1}^3 c_k(\hat{\xi}) \mathbf{x}_k^2 \quad \text{and} \quad \bar{\mathbf{x}}^1(\bar{\xi}) = \sum_{k=1}^3 c_k(\bar{\xi}) \mathbf{x}_k^1 \quad (24)$$

for the current slave node $\mathbf{x}^2(\hat{\xi})$ at the gauss point $\hat{\xi}$ and its master node $\bar{\mathbf{x}}^1(\bar{\xi})$. The coefficients c_k ($k = 1, 2, 3$) include the Hermite ansatz functions as well as the definition of the starting point and the end point of the current segment. A gauss integration over the slave segment allocates the contact constraints over the contact element nodes. The path length between \mathbf{x}_a^2 and \mathbf{x}_b^2 is defined by

$$\int_{s_a^2}^{s_b^2} (\bullet) ds^2 = \int_{\hat{\xi}=-1}^{\hat{\xi}=1} (\bullet) \det J d\hat{\xi} \approx \sum_{k=1}^{n_g} (\bullet)|_{\hat{\xi}} w_k \det J_k \quad (25)$$

in which w_k denotes the weighting factor and n_g the number of gauss points over the slave segment. The determinant of the Jacobian matrix

$$\det J_k = \left\| \frac{\partial \mathbf{x}^2(\hat{\xi})}{\partial \hat{\xi}} \right\| \quad (26)$$

maps between the physical and the convective coordinates.

The classical weak form [13, 5] of the normal contact contributions for the penalty method

$$G_c = \int_{\beta^2} \epsilon_n g_n \delta g_n dA^2 = \int_{\beta^2} \epsilon_n g_n \bar{\mathbf{n}}^1(\bar{\xi}) \cdot [\delta \mathbf{u}^2 - \delta \bar{\mathbf{u}}^1(\bar{\xi})] dA^2 \quad (27)$$

depends on the penalty parameter ϵ_n for the normal contact, the gap function g_n and the variation of the displacement vectors $\delta \mathbf{u}^2$ and $\delta \bar{\mathbf{u}}^1(\bar{\xi})$. Discretizing the contact contribution given in Equation 28 by means of the smooth six-node contact element formulation described above leads to

$$G_c \approx \sum_{j=1}^{n_s} \sum_{k=1}^{n_g} \epsilon_n g_{n,k} \bar{\mathbf{n}}^1(\bar{\xi}_k) \cdot [\delta \mathbf{u}^2(\hat{\xi}_k) - \delta \bar{\mathbf{u}}^1(\bar{\xi}_k)] w_k \det J_k \quad (28)$$

where $\hat{\xi}_k$ denotes the k 'th gauss point coordinate of the j 'th slave segment and $\bar{\xi}_k$ the convective solution coordinate at the contact segment to the given slave node. If contact occurs there exists only one master segment according the current slave node.

The advantages of the given two-dimensional smooth six-node contact element can be summarized as follows:

- The smooth contact surface description approximately re-establishes the natural surface of the bodies coming in contact. It leads to a smooth computation of the normal vector and works independently of the finite element formulation and its ansatz functions.
- In this way artificial jumps in the contact constraints over the iterations are avoided and, consequently, in the displacement field and its derivatives. A better convergence of the Newton-Raphson scheme can be achieved.
- Smoothing the slave surface as well as the master one leads to a quasi-segment-to-segment approach. A correct integration over the contact surface is possible.
- The given contact formulation allows the implementation of contact material laws at the slave surface.

4 Numerical examples

The numerical examples present simulations of an electromagnetic forming process. The geometry of the workpiece is depicted in Figure 6. The material parameters of the aluminum

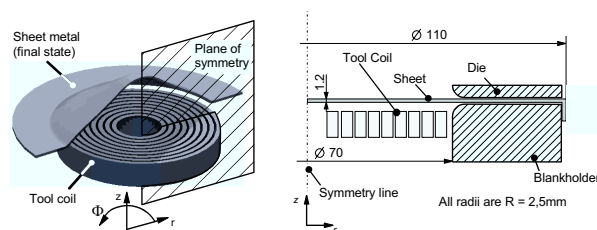


Figure 6: Workpiece, tool coil and die [21]

alloy AC 120 can be found in [19] and [20]. A viscoplastic material model based on a classical overstress formulation is used. To simulate electromagnetic forming, additional terms have to be considered in the balance equations. In the balance of linear momentum so-called Lorentz forces are introduced and in the balance of energy the electromotive power has to be considered. The additional unknown variables are the vector potential and the scalar potential. In the first simulation we analyze the free forming process using the three-dimensional solid-shell formulation described above. The study of convergence in Figure 7 shows that already

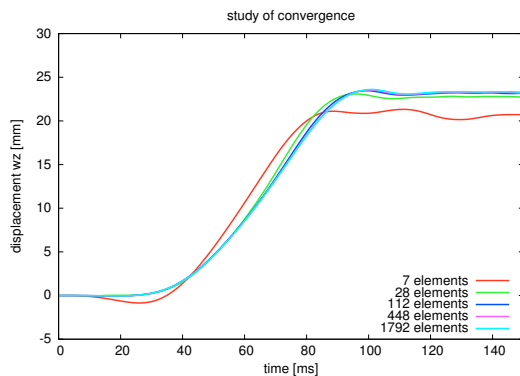


Figure 7: sheet midpoint displacement

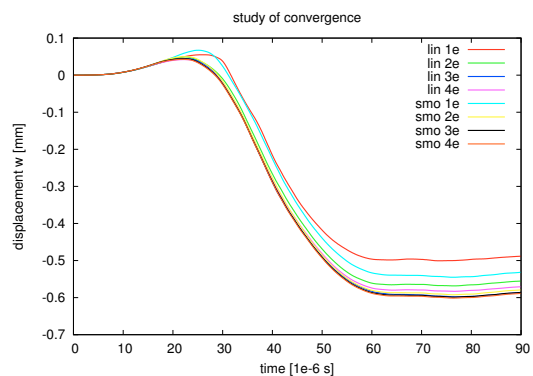


Figure 8: displacement node 81

a mesh with 112 elements (for the quarter structure) leads to a converged result. Depicted is the displacement of the sheet midpoint over time. At the beginning of the forming process the sheet metal is accelerated over the tool coil caused by the Lorentz forces. After that the work of deformation is done by the mass inertia (kinetic energy). In Figures 9 and 10 the Cauchy

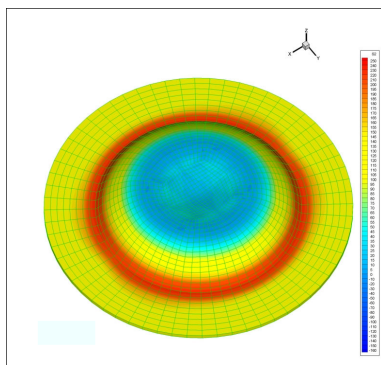


Figure 9: Cauchy stress at $t = 55 \mu s$

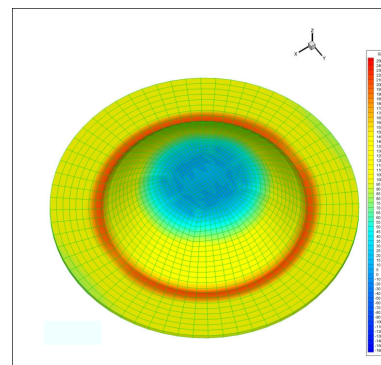


Figure 10: Cauchy stress at $t = 70 \mu s$

stresses at the times $t = 55 \mu s$ and $t = 70 \mu s$ are depicted.

The second simulation uses the same parameters given before. We compute the forming process by using the axisymmetric version of the solid-shell concept. The die restricts the forming geometry by an angle of 35.7 degrees. It is approximated as a rigid surface. We compare a piecewise linear contact description (see Figure 11) and a formulation using cubic Hermite ansatz functions (Figure 12) to discretize a radius of 5 mm of the die. In Figure 13 and 14 different states of deformation are depicted. A study of convergence for the horizontal

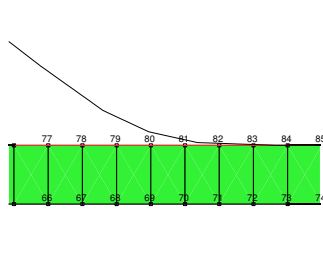


Figure 11: Piecewise linear contact

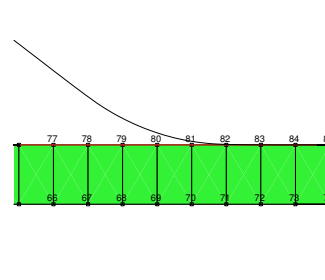
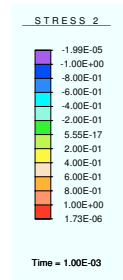


Figure 12: Smooth contact

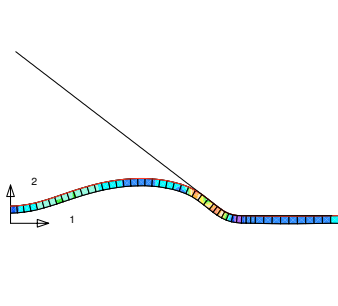
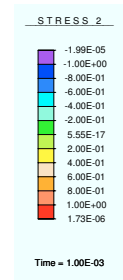


Figure 13: Deformation at $t = 40 \mu s$

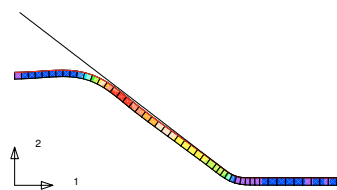
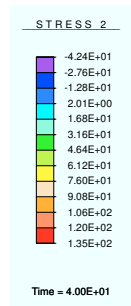
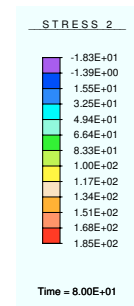


Figure 14: Deformation at $t = 80 \mu s$



displacement of node 81 is given in Figure 8. We start discretizing the radius with one contact segment (lin1e and smo1e). Already two smooth contact segments are necessary to achieve a nearly converged result. In comparison to this using the linear discretizing four segments are necessary. Furthermore, the usage of the Hermite contact formulation leads to a better convergence behavior of the Newton-Raphson scheme during the implicit time integration.

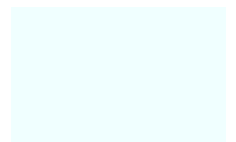
5 Conclusion and Outlook

In the present paper two aspects of modeling high speed forming processes by means of the finite element method are described. The first one enfoldes the formulation of a solid-shell element using a reduced integration schema and a physically oriented stabilization technique. The second aspect deals with a smooth contact formulation suitable for modeling impact processes present at the electromagnetic forming. The element as well as the contact formulation was successfully implemented into a commercial finite element code in order to demonstrate the capability as well as the convergence behavior separately. Future work will be done to combine both beneficial developments into one code in order to simulate the high speed forming process of electromagnetic forming in a time-efficient, robust way without locking effects and numerical oscillations due to contact condition.

References

- [1] *T. Belytschko & L. P. Bindemann.* Assumed strain stabilization of the eight node hexahedral element. *Computer Methods in Applied Mechanics and Engineering*, 105: 225–260, 1993.
- [2] *R. Hauptmann, K. Schweizerhof & S. Doll.* Extension of the 'solid-shell' concept for application to large elastic and large elastoplastic deformations. *International Journal for Numerical Methods in Engineering*, 49:1121–1141, 2000.
- [3] *S. Reese.* On a physically stabilized one point finite element formulation for three-dimensional finite elasto-plasticity. *Computer Methods in Applied Mechanics and Engineering*, 194: 4685–4715, 2005.
- [4] *S. Reese.* A large deformation solid-shell concept based on reduced integration. *International Journal for Numerical Methods in Engineering*, submitted.
- [5] *P. Wriggers, L. Krstulovic-Opara & J. Korelc.* Smooth C^1 -interpolations for two-dimensional frictional contact problems. *International Journal for Numerical Methods in Engineering*, 51:1469–1495, 2001.
- [6] *D. Risch, C. Beerwald, A. Brosius & M. Kleiner.* On the Significance of the Die Design for Electromagnetic Sheet Metal Forming. *Proc. of the ICHSF 2004 - 1st Int. Conference on High Speed Forming, 31.3.-1.4.2004, Dortmund*, 191–200, ISBN 3-00-012970-7.
- [7] *N. El-Abbasi, S. A. Meguid & A. Czekanski.* On the modelling of smooth contact surfaces using cubic splines. *International Journal for Numerical Methods in Engineering*, 50:953–967, 2001.
- [8] *L. Krstulovic-Opara & P. Wriggers.* A two-dimensional C^1 -continuous contact element based on the moving friction cone description. *Fifth World Congress on Computational Mechanics, July 7-12, Vienna, Austria*.
- [9] *M. Stadler, G.A. Holzapfel & J.Korelc.* C^n continuous modelling of smooth contact surfaces using NURBS and application to 2D problems. *International Journal for Numerical Methods in Engineering*, 57:2177–2203, 2003.
- [10] *L. Krstulovic-Opara, P. Wriggers & J.Korelc.* A C^1 -continuous formulation for 3D finite deformation frictional contact. *Computational Mechanics*, 29: 27–42, 2002.
- [11] *G. Dhett, G. Touzot & G. Cantin.* The Finite Element Method Displayed. *John Wiley & Sons*, 1984.
- [12] *M. A. Puso & T. A. Laursen.* A 3D contact smoothing method using Gregory patches. *International Journal for Numerical Methods in Engineering*, 54:1161–1194, 2002.
- [13] *T. A. Laursen & J. C. Simo.* A continuum-based finite element formulation for the implicit solution of multibody, large deformation frictional contact problems. *International Journal for Numerical Methods in Engineering*, 36:3451–3485, 1993.

- [14] *S. Reese, P. Wriggers & B. D. Reddy.* A new locking-free brick element technique for large deformation problems in elasticity. *Computers and Structures*, 75:291–304, 2000.
- [15] *J. C. Simo, F. Armero & R. L. Taylor.* Improved versions of assumed enhanced strain tri-linear elements for 3d finite deformation problems. *Computer Methods in Applied Mechanics and Engineering*, 110:359–386, 1993.
- [16] *J. C. Simo & F. Armero.* Geometrically nonlinear enhanced strain mixed methods and the method of incompatible modes. *International Journal for Numerical Methods in Engineering*, 33:1413–1449, 1992.
- [17] *P. Wriggers & S. Reese.* A note on enhanced strain methods for large deformations. *Computer Methods in Applied Mechanics and Engineering*, 135:201–209, 1996.
- [18] *M. A. Puso.* A highly efficient enhanced assumed strain physically stabilized hexahedral element. *International Journal for Numerical Methods in Engineering*, 49:1029–1064, 2000.
- [19] *C. Beerwald, A. Brosius & M. Kleiner.* Determination of flow stress at very high strain-rates by a combination of magnetic forming and FEM calculation. *Proceeding of the International Workshop of Friction an Flow Stress in Cutting and Forming (CIRP)*, 25.-26.01.2000, ENSAM-Paris.
- [20] *B. Svendsen & T. Chanda.* Continuum thermodynamic formulation of models for electromagnetic thermoelastic solids with application to electromagnetic metal forming. *in press.*
- [21] *M. Badelt, C. Beerwald, A. Brosius, & M. Kleiner.* Process Analysis of Electromagnetic Sheet Metal Forming by Online-Measurement and Finite Element Simulation. *Proc. of the 6th Int. ESAFORM Conf. on Material Forming*, 28.-30. April 2003, Salerno, Italy, p.123-126.



Mathematical Modeling of Impulsive Forming Processes Using Various Energy Sources and Transmitting Medium

A. Vovk¹, V. Vovk¹, V. Sabelkin², V. Taran¹

¹ IFQ, Otto-Von-Guericke University, Universitaetsplatz 2, 39106 Magdeburg, Germany

² IMP, Mexico/USA

Abstract

High-speed forming uses high explosives, gun powder, combustible gas mixes and compressed gases as sources of energy. Special mathematical models are used to take into account specific dynamic properties. Different technological processes of forming have been modeled in the work. They use liquid (water), elastic (polyurethane), and gaseous transmitting medium. The difference between impulse energy transference, load distribution on a blank and tool surface, and also wave propagation is shown for used transmitting medium. The developed procedures allow taking account significant thermal effects at adiabatic compression of the material and heat transference directly from products of explosion. Specially developed modules and mathematical models have allowed the application of standard software products for modeling high-speed forming and sheet metal punching processes.

Keywords:

Sheet metal blank, Explosive forming, Hydro-impulsive forming, Gas detonating forming

1 Introduction

Mathematical modeling of high-speed processes is widely used at the present time. Simulation represents the effective tool to study high energy forming processes. High-speed physical experiments are provided with special expensive engineering and measuring equipment. Therefore, the analysis of complex technological processes on models is cost efficient; it gives more information about the process and allows determining influencing parameters.

The majority of the commercial software products used for modeling of traditional technological processes of sheet metal forming and punching of thin-walled tubes (shells) is inapplicable for calculation of high-speed processes. They do not take into account

specific dynamic effects. Neglect of mass forces, dynamic properties of materials, temperatures, dynamic friction, etc. leads to essential errors in calculations.

2 Mathematical modeling of high-speed forming technological processes

There are some special software products in the field of high pressure, defense and aerospace techniques allowing precisely calculate wave processes, high-speed deformations in material and medium. However, these programs are not adapted for calculation of forming technological processes; therefore, it is necessary to adapt these special programs to solve new technological problems of sheet metal forming.

The commercial software code AUTODYN® of the Center Dynamics has been selected as the base product. The University Otto-Von-Gericke, Magdeburg, has long-term experience regarding to the use of this code for studying the explosion phenomena. Specially developed mathematical models and code modules have allowed to apply the AutoDyn program for modeling of sheet metal high-speed forming and punching processes.

Various sources of energy are used for high-speed forming [1, 2]. The most common of them are:

- High explosives using for explosive forming;
- Compressed gases using for solid body impact forming and
- Combustible gas mixtures using for gas detonation forming.

The listed above sources of energy have different initial density of energy, speed of discharge of the internal energy, developed shock wave peak pressures and temperatures.

In the given work, results of mathematical modeling of different technological processes are submitted. They are explosive forming, forming by solid body impact, and gas detonation forming.

2.1 Modeling of explosive forming processes

Essence of explosive forming consists in transference of explosion energy generated by an impulsive source of energy to a metal preparation (blank) through a transmitting medium. The basic set-up for explosive forming of parts from a flat sheet blank (Figure 1) consists of a basin with a transmitting medium, a die with clamped sheet blank, and a charge of impulsive energy.

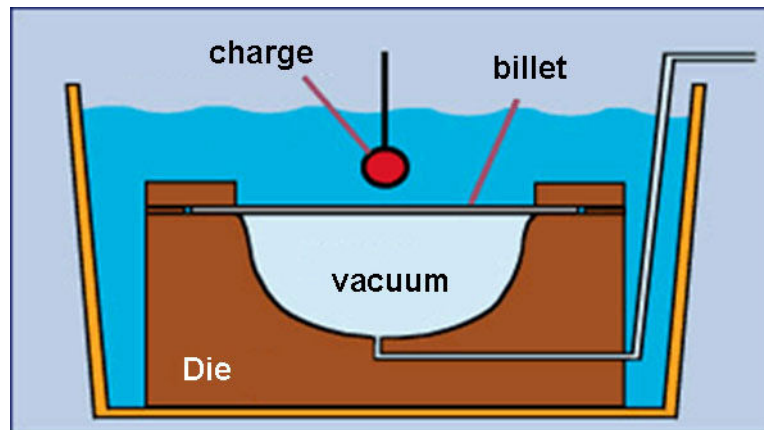


Figure 1: Set-up for explosive forming of sheet metals

Charges of simple forms are used: spherical (Figure 1), cylindrical, or cord type. The transmitting medium as a rule is liquid, gaseous, loose powder, jelly, or elastic. Technical water is used as the liquid medium, humidified sand is used as loose medium. Explosive forming is carried out in stationary, reusable pools or in a destroyed micro-basin.

Results of numerical simulation of explosive forming processes show that the most important factors of the production technology can be modeled using noted special software products. They are:

- Shock waves distribution in transmitting medium (Figure 2a)
- Gas bubble formation during forming process (Figure 2d)
- Die and technological equipment elements presence (Figure 2b, Figure 2c)

Specific feature of explosive forming, in comparison with "classic" methods of forming, is presence of direct and reflected shock waves in the transmitting medium. High pressure shock waves move through the transmitting medium. They move successfully through the continuum, increase on rigid surfaces, but reflect with negative stress from flexible and free boundaries. Therefore in the transmitting medium local zones with negative stress are formed. The transmitting medium (technical water) maintains a low negative stress (some units only). It leads to formation of gas-filled micro-cavities inside the transmitting medium (see Figure 2c, 2d). Properties of these discontinuity ("boiling") zones are very different in comparison with the continuum media.

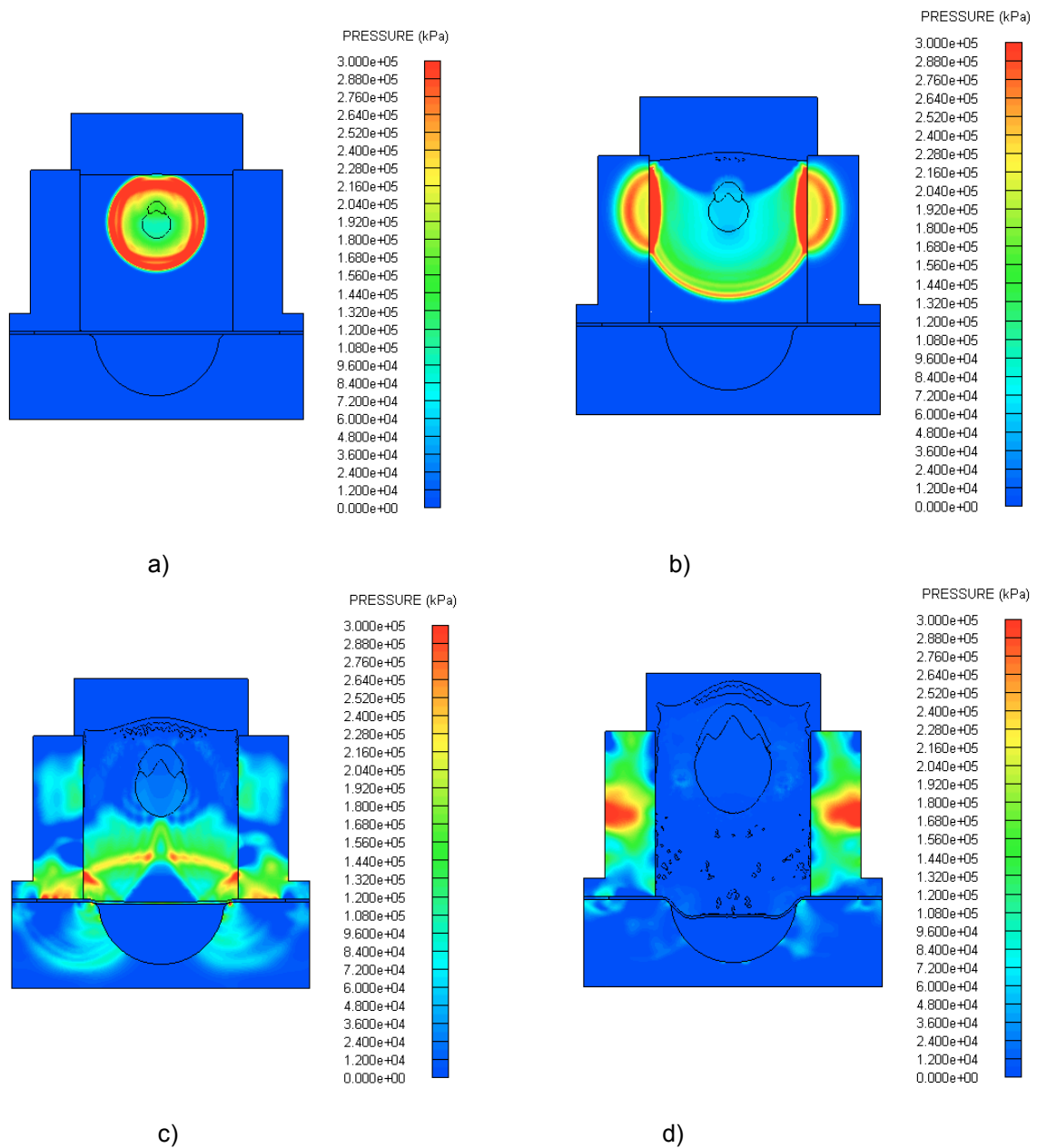


Figure 2: Stages of calculation of explosive forming using a rigid micro-basin

Cavitation essentially affects the pressures generated in the transmitting medium. Hence, numerical modeling of explosive forming has to take into account cavitation effects.

2.2 Simulation of the forming process by solid body impact

A basic set-up for forming using solid body impact energy is shown in Figure 3. A solid cylinder accelerates in the special thick-walled tube by a source of energy. Impact of the noted solid body with the transmitting medium generates shock waves. These shock waves deform the blank to the die cavity.

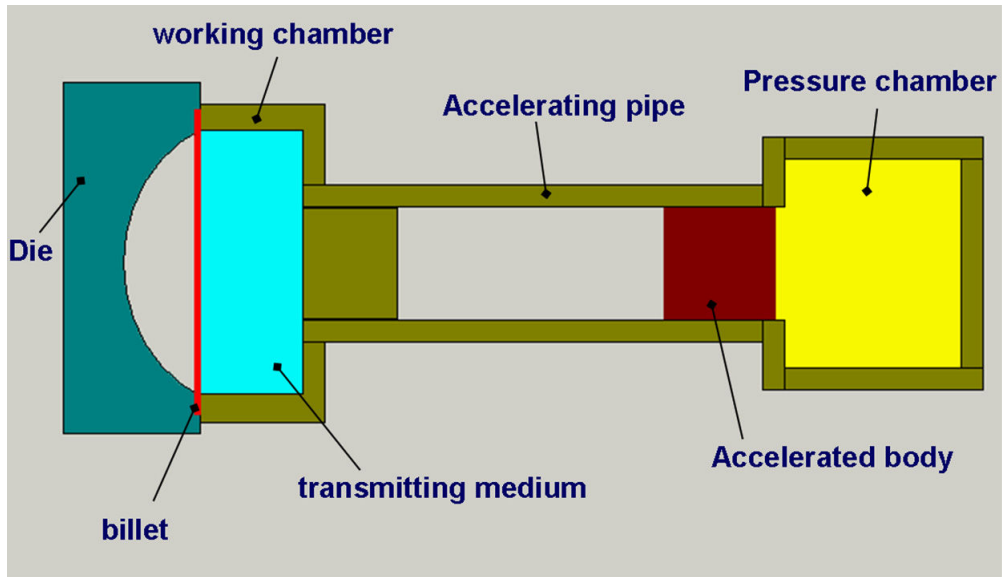
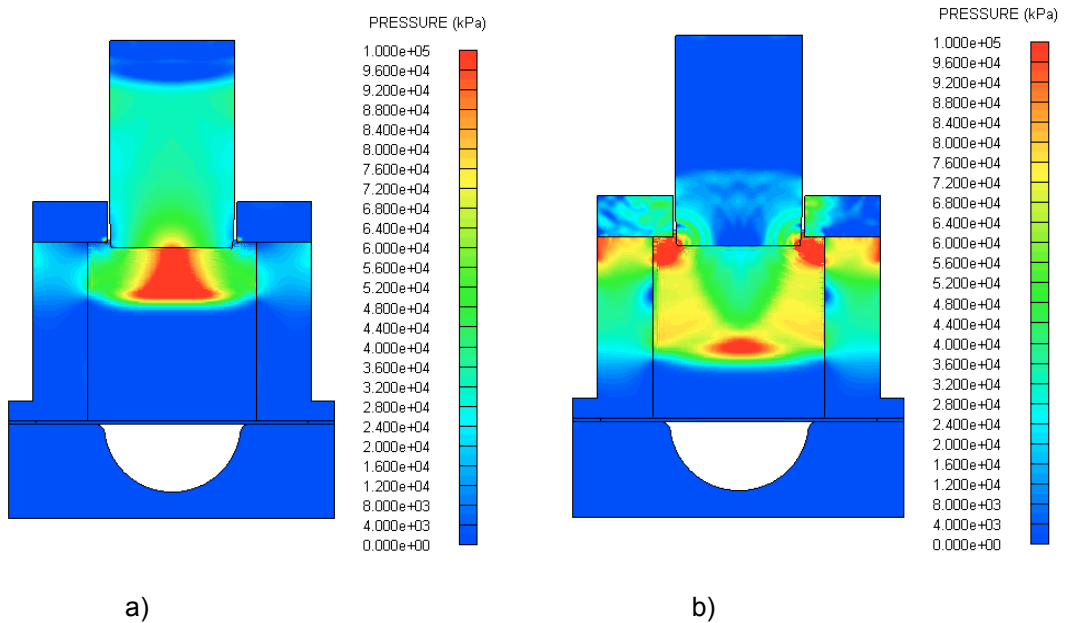


Figure 3: Set-up for thin-walled part forming using an elastic medium

An example for a forming process simulation of a hemispherical part has been provided. The blank was sheet steel (type QStE340) with diameter 200 mm and thickness 1 mm. The transmitting medium was elastic medium (polyurethane). Results of the numerical modeling are submitted in Figure 4.



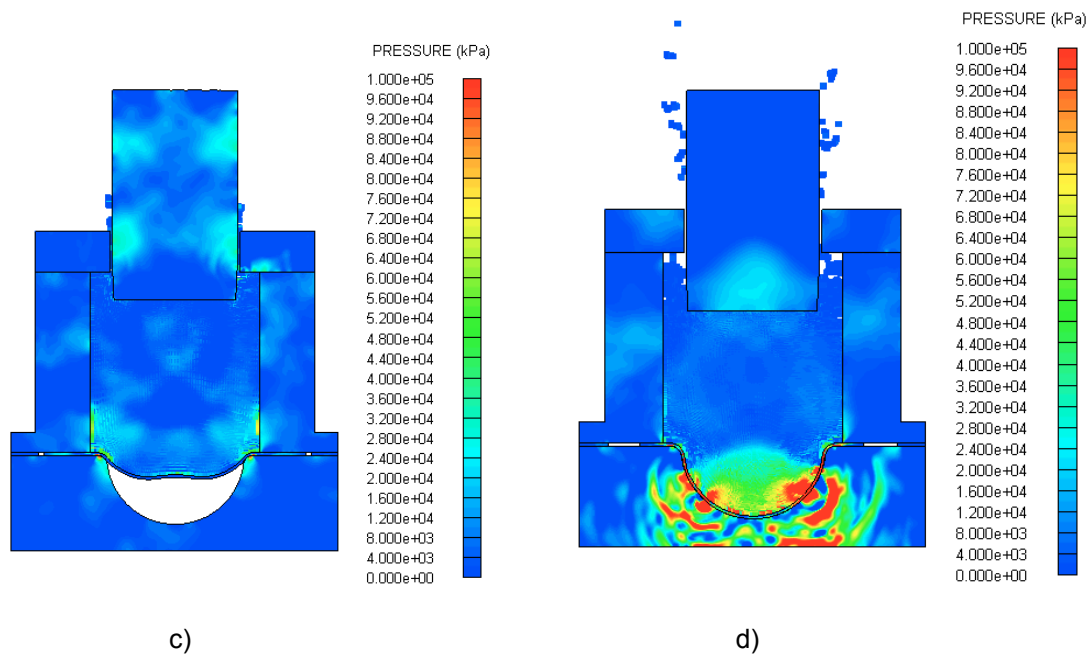


Figure 4: Sheet-metal forming using solid body impacts

Figure 4a shows a solid cylinder impact with the transmitting medium. Shock waves are generated. Figure 4b – Figure 4c shows distribution, reflections, and evolutions of shock waves in the cylinder, die, working chamber, and in the semi-product. The deformation of the workpiece during forming is irregular, as against of static methods. Wavy character of the work piece deformation is caused by plastic waves expanded in the blank during forming.

2.3 Modeling of gas detonation forming

Figure 5 shows a set-up for gas detonation forming.

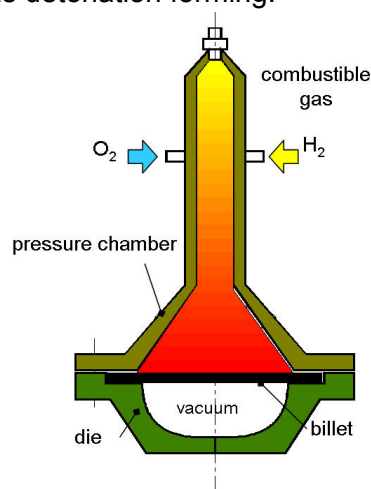


Figure 5: Set-up for gas detonation forming

There is a strong compression of the hydrogen-oxygen mixture in the shock wave at gas detonation forming. The temperature grows sharply and the pressure wave transforms to the detonation wave in the gas mixture. In this method, the energy which is necessary for shaping, is generated by a chemical reaction in the gas mixture. External pressure for forming generates by gas detonation wave. Therefore, the calculation of burning processes in gas and transition from burning to explosion is the important for numerical modeling of forming process.

Figure 6 shows shock waves evolution in the tube at gas detonation. Repeated reflected shock waves are visible. The reflections of shock waves lead to pressure, temperature and speed increase in the shock waves during deformation. This is the reason why to take into account dynamic effects is very important. The factor of reflection has essential influence on the results of forming process numerical simulation.

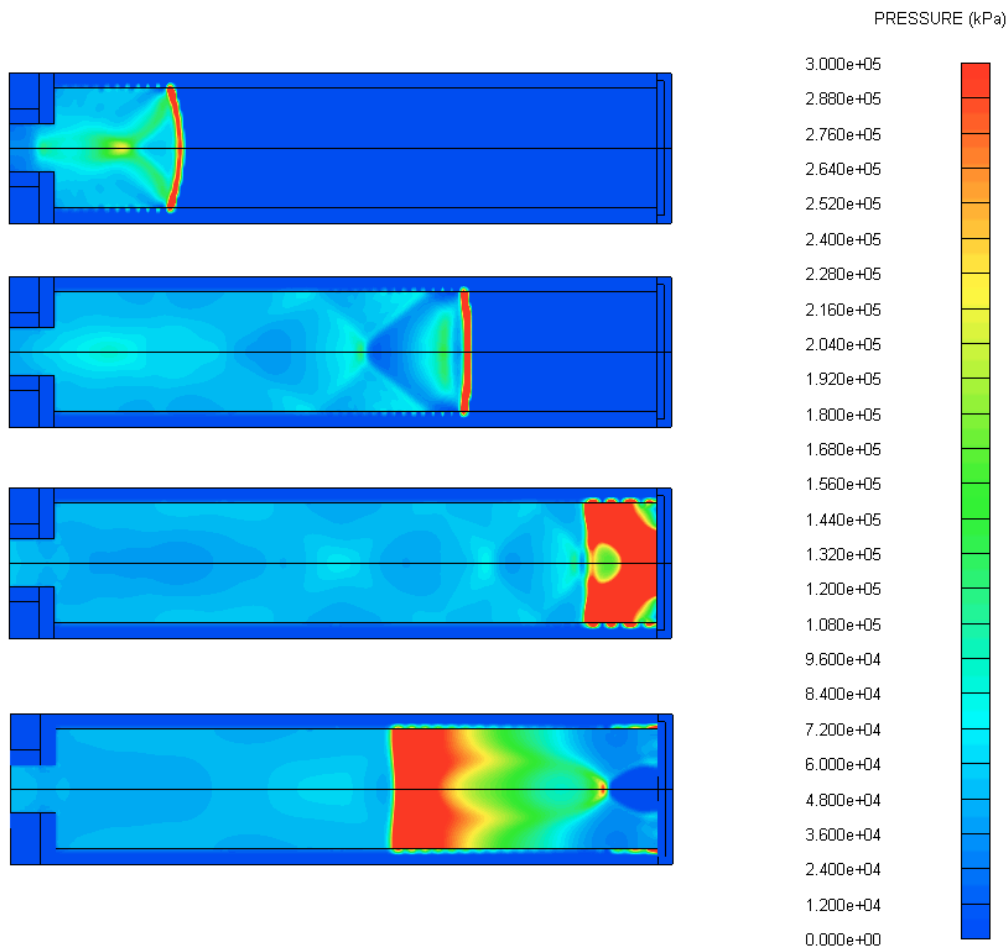


Figure 6: Shock wave evolutions and reflections during tube expansion

3 Technological features of high-speed forming

Some materials at high-speed forming have a higher plasticity. This effect is observed in the limited range of deformation speeds. At designing of new technological processes dynamic properties of materials have been accounted. Loading speed was defined by the amplitude-time characteristics of the impulse. Figure 7 shows how the impulse profile effects the part profile.

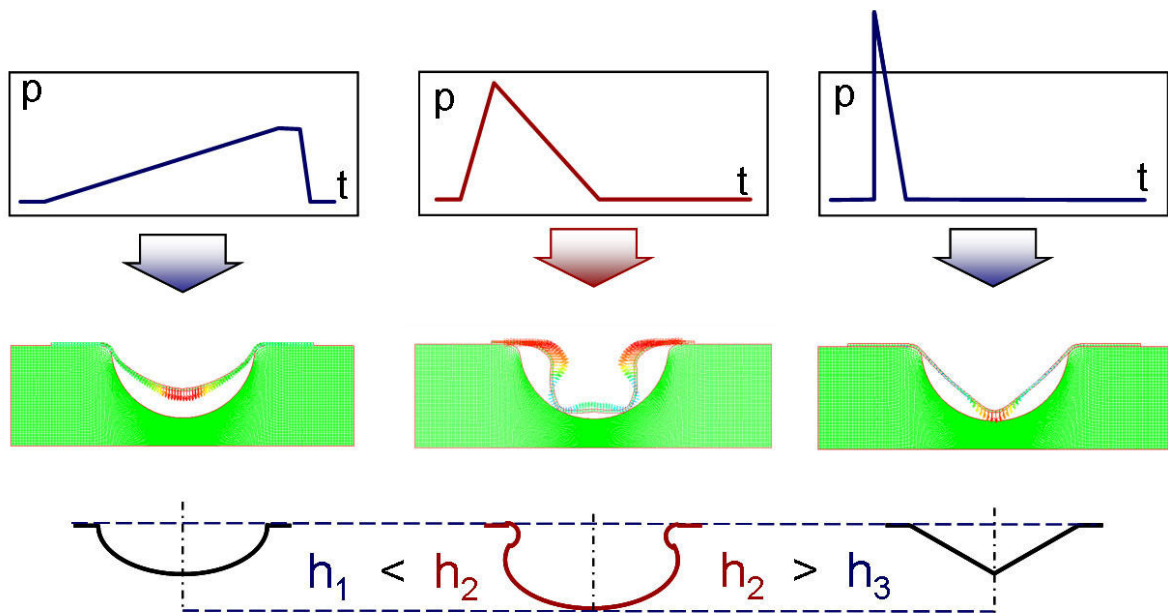


Figure 7: Influence of impulse parameters on the form of preparation

The temperature of the preparation during explosive forming is increased. This is due to adiabatic compression in the elastic - plastic wave moving through the blank. Figure 8 shows areas with such thermal effects. They are located in the bottom of the part and near the drawn-out edge. It has been established that the temperature increase depends on material properties, speed of deformation, and thickness of preparation.

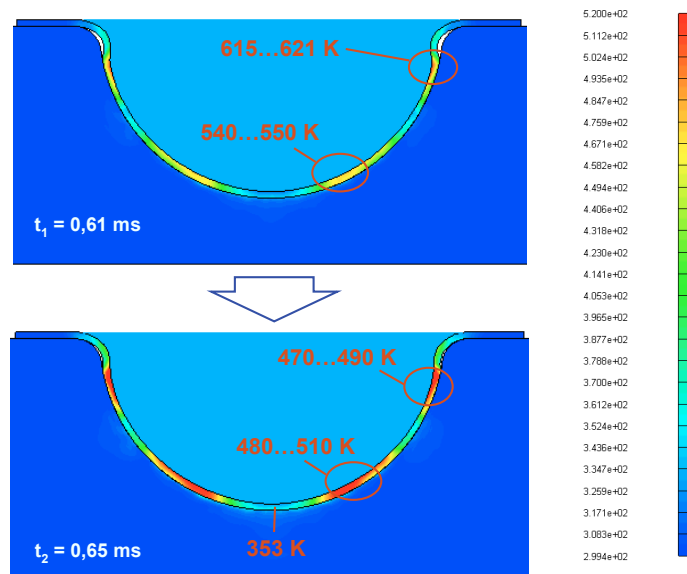


Figure 8: Thermal effects at high-speed forming

Figure 9 shows how mass distributed forces influences on the character of deformation. These forces can be positive and useful increasing the flange displacement at deep drawing. Nevertheless, they can be negative generating corrugations on the flange if excessive value [3,4]. Right impulse value and flange friction after simulation have been received.

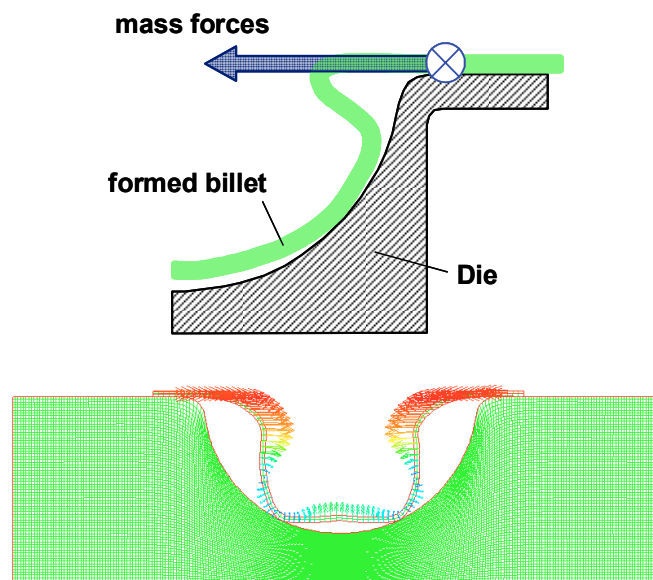


Figure 9: Flange displacements due to mass forces presence

4 Conclusions

In the work, transfer of impulse energy, distribution of loading on a blank and die, and wave processes in various technological methods are shown.

Influence of the form of an impulse and properties of the blank material on the final form of the stamped detail is shown.

The developed models allow taking into account dynamic effects such as cavitation, distribution, reflection and imposing of intensive shock waves to preparation, equipment and the transmitting media.

Calculations are carried out with the account of thermal effects at adiabatic compression of a blank material and direct heat transference from explosion products to the blank.

Optimum selection of amplitude-time characteristics of a pressure impulse provides maximum use of the materials deformation ability.

References

- [1] *Herold, K. P.; Vovk, V.; Taran, V.; Vovk, A.*: Explosive Forming of High-Strength Sheet Material. 10th International Conference on Sheet Metal, Ulster, E; April 14-16, 2003.
- [2] *Sabelkin, V. P.; Krivtsov, V. S.*: Concept of Development of Technological Processes for Aerospace Equipment Parts Manufacture with Application of Impulsive Sources of Energy. - Proc. IV Ukraine-Russia-China Symp. on Space Sci. and Techn., Kiev, Sept. 12-17, 1996, Vol. 2, p.639.
- [3] *Taran, V.; Vovk, V.; Vovk, A.*: Dynamic Forming of Sheet Materials for Parts-Prototypes. Konferenz-Einzelbericht: International Conference IDDRG 2004, Tagung, Sindelfingen, D, 24.05-26.05.2004, 2004.
- [4] *Vovk V.; Taran V.; Vovk A.*: Methods of Increase of Ductility in Explosion Shaping of High-Strength Sheet Material, International Conference on High Speed Forming, Dortmund 2004.

SESSION 3

PROCESS TECHNOLOGY

Strength of Tubular Joints Made by Electromagnetic Compression at Quasi-static and Cyclic Loading *

P. Barreiro¹, V. Schulze¹, D. Löhe¹, M. Marré², C. Beerwald², W. Homberg², M. Kleiner²

¹ Institute of Materials Science and Engineering I, University of Karlsruhe, Kaiserstr. 12, Karlsruhe 76131, Germany

² Institute of Forming Technology and Lightweight Construction, University of Dortmund, Baroper Strasse 301, 44221 Dortmund, Germany

Abstract

Electromagnetic compression of tubular profiles with high electrical conductivity is an innovative joining process for lightweight structures. The components are joined using pulsed magnetic fields which apply radial pressures of up to 200 MPa to tubular workpieces, causing a symmetric reduction of the diameter with typical strain rates of up to 10^4 sec^{-1} . This process avoids any surface damage of the workpiece because there is no contact between component and forming tool.

The strength of electromagnetically formed joints made of aluminum tubes under cyclic loads is essential to establish electromagnetic forming in automotive structures. In the present paper, the quasi-static performance of tubular joints made by electromagnetic compression produced of different mandrel materials will be analyzed as to the influence of process parameters. Therefore, experimental investigations on aluminum tubes (AA6060) joined on mandrels made of different aluminum, copper, and steel alloys were carried out. Furthermore, the behavior of joints with both mandrel and tube made of AA6060 at swelling cyclic loads ($R = \sigma_{\min} / \sigma_{\max} = 0$) has been evaluated.

Keywords:

Assembly, Electromagnetic compression, Cyclic load

* This paper is based on investigations of the Transregional Collaborative Research Centre SFB/TR10, which is kindly supported by the German Research Foundation (DFG).

1 Introduction

The dead weights of car bodies can be significantly reduced by introducing lightweight materials (e.g. aluminum) in the manufacturing of car body components. Therefore, the demand on joining technologies is to produce joints of high strength for the manufacturing of lightweight frame structures. In general, joints could be established by e.g. welding, bonding, and mechanically by dominating form-fit or dominating force-fit. Joining processes like laser-welding, screwing, clinching, riveting, and bonding are established in the manufacturing of lightweight frame structures, but they contain process-related constraints. Exemplary aspects are a complex preparation of the joining area, an accurately guiding during the joining process as well as a long process duration. The mentioned constraints do not have to be considered if joining has been done by compressing cylindrical tubes on mandrels by electromagnetic forming. Besides this, composite materials or two non-weldable alloys can be joined without extensive preparations of the joining area.

Experimental investigations have been done to evaluate both feasibility and capability of joining by forming processes. The influence of process parameters on the performance of the joints is actually in the focus of investigation. On the one hand, it is the joint strength under quasi-static loads, but on the other it is necessary to know the performance and behavior of joints made by electromagnetic compression at cycling loads to establish electromagnetic forming in industrial production [1,2 3,4,5].

2 Process principle and characteristic of force-fit joints

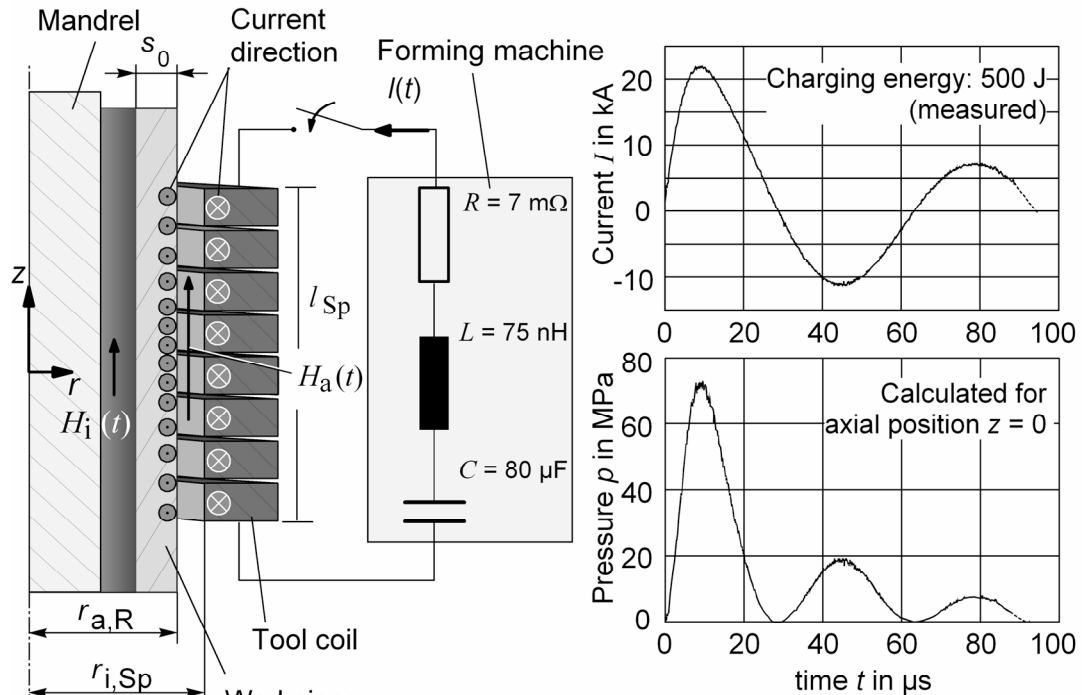
Electromagnetic forming is a high speed process using a pulsed magnetic field to form metals with high electrical conductivity such as aluminum. The energy density of a pulsed magnetic field is used for the contact-less forming of a workpiece. The resulting deformation is closely related to the electromagnetic properties. The process model (Figure 1) can be described as an oscillating circuit which includes the capacitor C , the resistance R , and the inductance L of the pulse generator as well as the consumer load consisting of tool coil and workpiece, here a solenoid and a tube. After the capacitor bank has been charged it is suddenly discharged by closing a high current switch. As a result, a damped oscillating current flows through the coil, generating a corresponding magnetic field. According to Lenz's law, a current in the workpiece will be induced flowing in the opposite direction to its cause. Due to the skin effect the current as well as the magnetic field penetrate the workpiece wall.

The resulting magnetic pressure $p(t,r,z)$ is determined by the energy density of the magnetic field outside H_a and inside H_i of the workpiece and can be calculated on the basis of the measured coil current by [6]

$$p(t,r,z) = \frac{1}{2} \cdot \mu_0 \cdot (H_a^2(t,r,z) - H_i^2(t,r,z))$$

The resulting pressure pulse acts vertically on both the field strength and the induced current [7], i.e. in radial direction on tube and tool coil, as Figure 1 shows. If the yield strength of the tube is exceeded, radial necking occurs. This deformation mode can be used for realizing a joint between a tube and a cylindrical mandrel. During this process the tube is deformed plastically and the mandrel ideally remains elastically. After a decrease

of the forces a corresponding elastic recovery of mandrel and tube proceeds [8]. If a full relaxation of the mandrel is prevented by the tube, a permanent pressure in the joining area in radial direction is established. This pressure is a balanced condition of the mandrel's stress relief, on the one hand, and the resulting reinduced stress (by the elastic recovery of the mandrel) in the tube, on the other hand.



Typical current and pressure pulse for:

Workpiece		Tool coil	
Conductivity	$\kappa = 26.5 \text{ MS/m}$	No. of turns	$n = 14$
Wall thickness	$s_0 = 1.25 \text{ mm}$	Length of the coil	$l_{Sp} = 27 \text{ mm}$
Outer radius	$r_{a,R} = 8.95 \text{ mm}$	Inner radius	$r_{i,Sp} = 9.6 \text{ mm}$

Figure 1: Process principle

In the case of massive shafts, their pure elastic deformation determines the maximum allowable joint pressure in the contact zone to realize an optimum interference pressure. The strength of interference-fits strongly depends on the area of the contact zone, the friction coefficient, and the remaining interference stress in the contact zone. While the first two aspects directly influence the strength of the joint, the last point depends on material parameters like yield point and Young's modulus as well as the geometrical stiffness of the parts to be joined [8, 9, 10, and 11]. In the following, the influence of the tube compressing velocity and the joint material of the inner join partner (mandrel) on the joint quality has been evaluated by quasi-static and exemplarily cyclic-load.

3 Materials and testing method

For the present experimental investigations aluminum tubes were electromagnetically compressed on mandrels made of different materials at the Institute of Forming

Technology and Lightweight Construction, Universität Dortmund (Germany). The material of the tube was AA6060 and its outer diameter was 20 mm along with a wall thickness of 1 mm. The joining process was made with charging energies of 1.1 kJ and 1.5 kJ. In Table 1, yield strength and Young's modulus of the mandrel materials are listed.

ID	Material	Alloy composition	Yield strength [MPa]	Young's modulus [MPa]
A	AA5754	AlMg3	100	70,000
B	AA6060	AlMgSi0,5	160	70,000
C	AA7075	AlZn5,5MgCu	460	70,000
D	C1100P	Cu-ETP	180	116,000
E	CW106C	CuCrZr	470	116,000
F	NSB4	CuNi3Si1	590	116,000
G	S235		235	210,000
H	1.0715	9SMn28k	440	210,000
I	1.0601	C60	580	210,000

Table 1: Typical values of yield strength and Young's modulus of the different mandrel materials, taken from literature [12].

Mandrels of nine different materials were joined in order to study the influence of the mandrel's stiffness and strength on the mechanical properties of the joint. Aluminum alloys, copper alloys and steels were chosen to compare the influence of strength and stiffness. Furthermore, three different alloys of each material with the same Young's modulus were joined to compare the influence of yield strength. The tensile tests were carried out in a 200 kN Zwick machine with a crosshead velocity of 2 mm/min to assure an approximate strain rate ($\dot{\epsilon}$) of $3 \cdot 10^{-3}$ 1/s. Cyclic tests at swelling loads ($R = \sigma_{\min} / \sigma_{\max} = 0$) were carried out in a 63 kN Instron (Fast-Track 8800) servo-hydraulic machine. The test frequency was 2 Hz. The maximum and the middle loads were varied from 2 kN to 12 kN and 1 kN to 6 kN respectively. The quantities measured were the force, the relative displacement of the tubular component, and the complete displacement of the test tube. The relative displacement of the tubular component was measured with a capacitive sensor (small measuring range with high resolution) and the complete displacement of the test tube was measured with an inductive sensor (large measuring range with low resolution). The experiments were stopped either by test tube's failure or by 10^6 cycles.

4 Experimental results

4.1 Influence of the forming velocity and mandrel material on the mechanical properties

In contrast to quasi-static forming and joining procedures, the forming velocity plays a decisive role in the EMF process. The velocity of the tube being compressed as well as its mass determine the kinetic energy at the moment of impact, and therefore the force which takes effect on the mandrel. To investigate the influence of the necking velocity, the radial displacement has been measured during the forming process without a mandrel by the light-shadowing-method, as described in detail in [1, 13, and 14]. A line-shaping laser beam will be shadowed by the smallest cross section of the tube during the compression

progress. The related velocity of the radial displacement at the smallest cross section can be calculated by derivation of the measured and smoothed displacement curve. The characteristic shape of the necking velocity during this high speed process shows a characteristic acceleration and deceleration progression.

A mandrel inside the tube limits the radial displacement. So, the gap a_0 between tube and mandrel is the distance which can be used for tube acceleration. In Figure 2, the influence of this acceleration gap a_0 on the strength of the joints is presented.

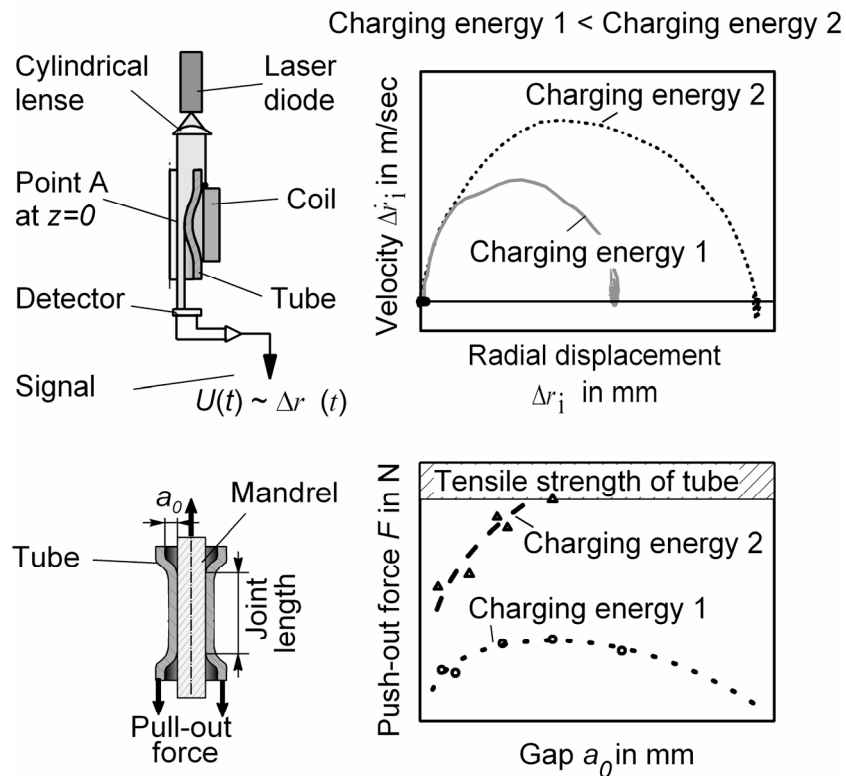


Figure 2: Influence of the compression velocity on the push-out force

On the one hand, it is possible to increase the velocity (and therefore the kinetic energy) of the tube at the moment of impact by increasing the charging energy. On the other hand, the charging energy which is required for a particular velocity at the moment of impact can be reduced by an increase of the gap a_0 .

In former full scale experimental investigations joints were produced with tubes of the alloy AA6060 (with a diameter of 20 mm and a thickness of 1 mm) and with three different mandrel materials [1]. In that work AA6060 and AA2007 were chosen to compare the influence of strength for the same stiffness, and 9SMn28k to compare the influence of stiffness for a comparable strength at different charging energies as well as acceleration gaps. The strength has been evaluated by the required force to separate the inner and outer part by pressing the inner part (mandrel) out of the tube. Failure was defined by means of the force value that refers to the first relative movement between tube and mandrel. As expected, the push-out force increased with an increasing charging energy and the non-linear correlation between the strength of a joint and the gap width a_0 could be observed. This corresponds to the theory that the kinetic energy of the deformed part at the moment of impact with the inner part determines the remaining interference stress

within the contact zone (Figure 2). This is an important aspect in consideration of an efficient design of the joining process because the smaller the gap the higher the required discharge energy.

The results of pull-out tests in Figure 3 indicate that a force-fit without any acceleration gap ($a_0 = 0$ mm) on massive mandrels could not be produced.

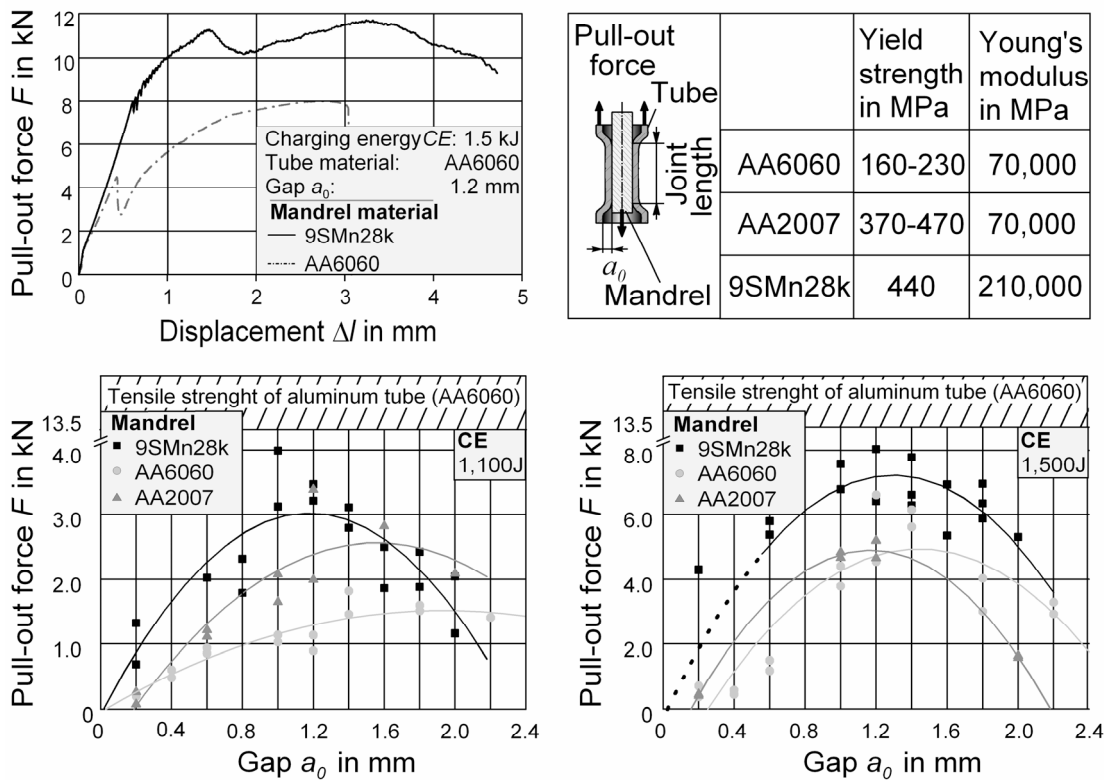


Figure 3: Left: Results of pull-out-tests for a charging energy of 1,100J (AA6060, AA2007 and 9SMn28k). Right: Results of pull-out-tests for a charging energy of 1,500J (AA6060, AA2007, and 9SMn28k) [1]

On the contrary, an increase of the gap width, and therefore an increase of the acceleration distance, causes a reduction of the necessary charging energy. An increase of the charging energy leads to higher levels of pull-out forces. In addition, it was found that by using a mandrel material of both higher strength and stiffness results in higher pull-out loads, too. The pullout loads of test tubes joined with different mandrel materials are presented in Figure 4. All columns show an increase of the pull-out load by increasing the yield strength of the mandrel. Furthermore, the pull-out loads increase if the Young's modulus of the mandrel increases. By comparing the results from a single curve, meaning at constant stiffness, a joint produced with the same charging energy (same impact velocity due to the joining process with the same parameters) seems to cause a higher radial reaction force of the mandrel if the mandrel's strength is higher, too, leading to higher pull-out loads. Furthermore, the different columns, meaning different stiffnesses, show higher pull-out forces in the case of stiffer materials, especially steels. From this point of view, it will be favourable to use a mandrel material of higher strength and

stiffness than the tube material. Basically, joining by EMF provides the opportunity to produce joints which can resist axial forces as high as the yield strength of the tube.

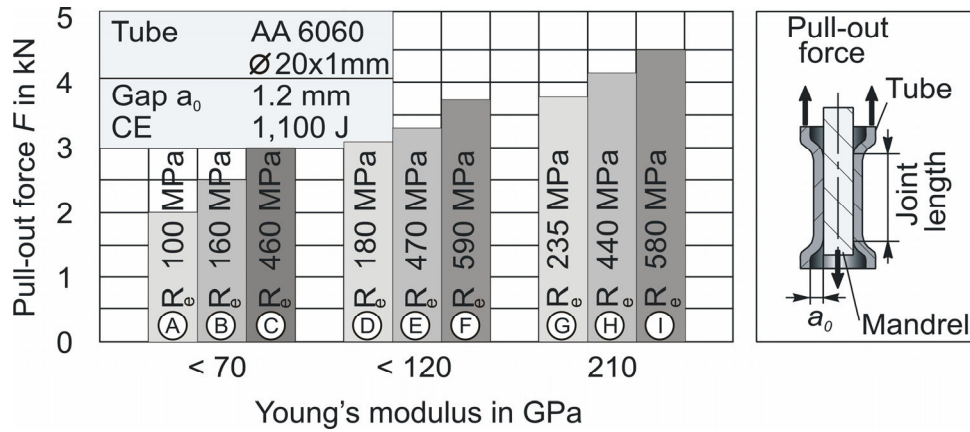


Figure 4: Results of pull-out-tests for different mandrel materials

4.2 Behavior under cyclic load

Though joints with a steel mandrel have higher levels of pull-out loads than joints with an aluminum mandrel [1], cyclic tests were first carried out for reasons of lightweight construction at the specimens mentioned above, Figure 5.

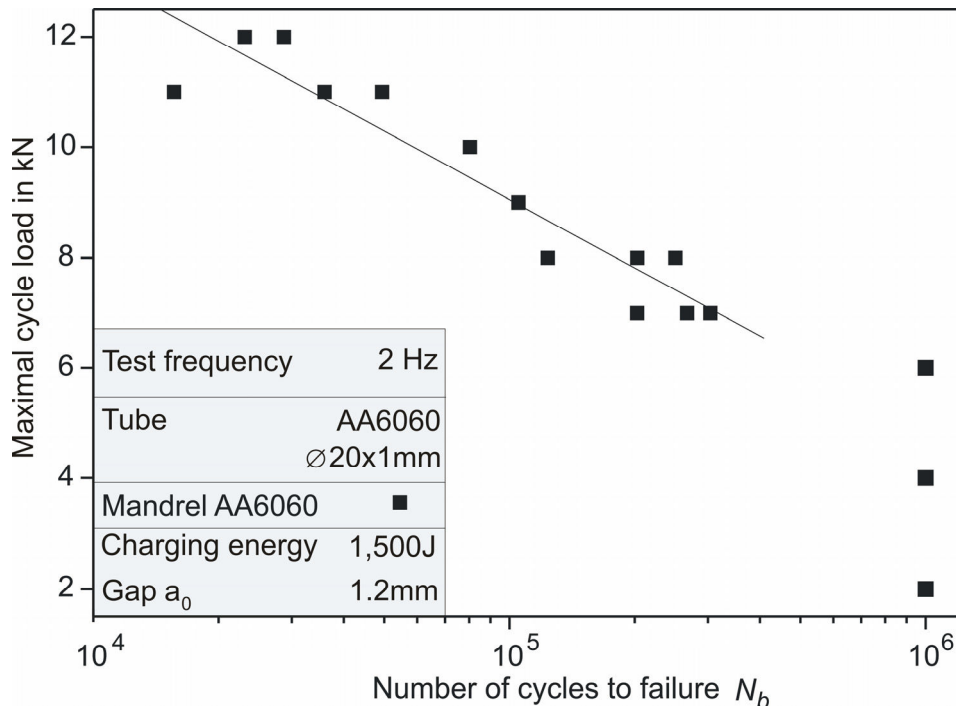
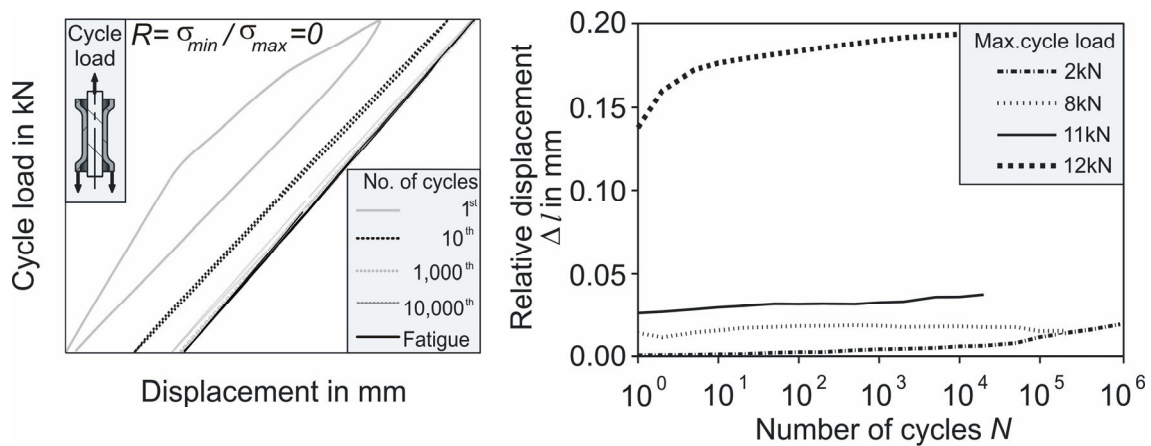


Figure 5: Swelling curve for joints made with an aluminum mandrel

The influence of the mandrel material at cyclic load will be investigated in further studies. Figure 5 shows a linear relationship between the uniform load amplitude and the number of cycles causes failure / separation of the test tube. The fatigue life is about $2 \cdot 10^4$ cycles for a load of 12 kN and it increases up to $5 \cdot 10^5$ cycles for a load of 7 kN. The fatigue limit

for $1 \cdot 10^6$ cycles of these joints is about 6 kN. It can be noticed that all maximal loads are fairly higher than the pull-out and the maximal loads found by [1] in tensile tests. Such a behavior could not be expected since conventional joints can not transmit higher loads than the maximal load in a tensile test for more than one cycle. Figure 6 right shows the relative displacement Δ/l of the tubular component during a cycling test for different maximal loads, and Figure 6 left shows the hysteresis curves from a test with a maximal load of 8 kN of five different cycles. In Figure 6 left it can be seen that the first cycles lead to a shift of the tubular component on the mandrel. This initial displacement becomes bigger the higher the maximal load is, especially for the maximal load of 12 kN (Figure 6 right). After a few cycles the displacement decreases and remains nearly constant. Finally, there is no further glide until test tube's failure. The slipping of the tubular component out of the mandrel was continuous only in the test by a maximal load of 12 kN.



Tube	AA6060	Mandrel	AA6060	Charging energy	1,500J
	$\varnothing 20 \times 1 \text{ mm}$	Gap a_0	1.2 mm	Test frequency	2 Hz

Figure 6: Left: hysteresis curves from a test with a maximal load of 8 kN for five different cycles. Right: Relative displacement of the tubular component during test for different maximal loads

This high displacement of the tubular component at the beginning of the test, which is followed by a small glide until test tube's failure, is evidence for a "hardening process" which takes place in the beginning of the test.

The metallographic examination after test tube's failure points out that the specimen failure always occurs in the transition zone between deformed and undeformed zone of the tubular component, as Figure 7 A shows. Then the crack propagation along the transition area finally causes complete collapse of the tubular component. To investigate this in detail, samples of the mentioned region were cut out and then examined in a Scanning Electron Microscope (SEM). Figure 7 B shows a SEM picture with a magnification of factor 50 of the crack initiation zone. In the lower area of the picture it is possible to identify that a fragment of the tubular component is fused with the mandrel. The fusion between both components is clearly observable in Figure 7 C. Furthermore it can be noticed that the crack propagates in the mandrel, too.

With this observation it is possible to understand the high level of loads that the joint can transmit under swelling cyclic loads (Figure 5). Besides this, the relative displacement of the tubular component (Figure 6) can be explained as follows:

Due to testing there is a relatively high level of friction between both components of the joint. First, this friction clears the oxide layer of both components in the contact points between them. Afterwards, the friction produces a local increment of the temperature which induces diffusion welding. When this happens the further displacement of the tubular component is largely impeded

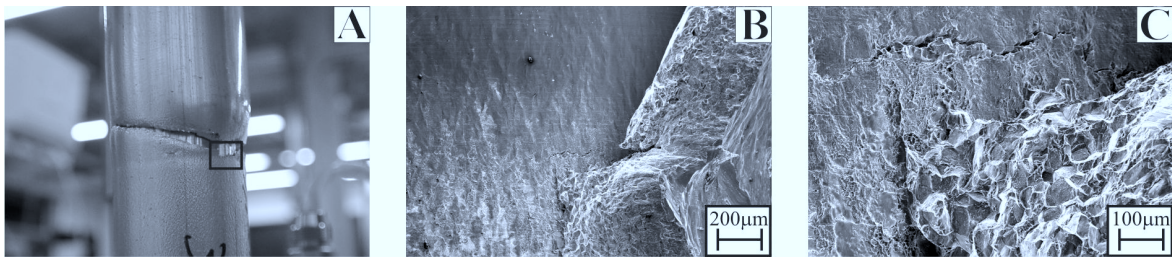


Figure 7: A: Fracture mode by cyclic test B: SEM picture of the crack initiation zone C: Magnification of picture B

5 Conclusions

In the present work, electromagnetically joined tubes of AA 6060 and mandrels of different materials were investigated at quasi-static and cycling loads. The results of tensile tests show that higher levels of pull-out load are achievable by increasing strength or stiffness of the mandrel material by the same impact velocity due to the joining process with the same parameters. This is because the radial reaction force of the mandrel is higher if the mandrel's strength or stiffness is higher as well which, therefore, leads to higher pull-out forces.

The results of cyclic swelling tests indicate that the fatigue life and the fatigue limit of the joints are a multiple factor higher than the pull-out loads found in quasi-static tensile tests. Furthermore, the displacement of the tubular component shows a big slide at the beginning of the test, which is followed by a small continuous glide until test tube's failure. The explanation is that friction during the first cycle may clear the oxide layer of both components in the contact points between them. Subsequently, the friction produces a local increment of the temperature, which induces diffusion welding impeding the further displacement of the tubular component.

References

- [1] *Kleiner, M.; Löhe, D.; Marré, M.; Beerwald, Ch.; Barreiro, P.; Schulze, V.; Homberg, W.:* Investigation of force-fit joints produced by electromagnetic tube compression. Submitted by WGP-Annals.
- [2] *Mamalis, D.; Manolakos, A.; Kladas, A. Koumoutsos:* Electromagnetic forming and powder processing: Trends and developments. Applied Mechanics Reviews (2004) 57, pp. 299-324.
- [3] *Bach, F.; Rossberg, A.; Schäperkötter, M.; Schaper, M.; Walden, L.; Weber J.:* The sheet metal materials aluminum, magnesium, steel and also titanium and their forming properties.
- [4] *Bach, F.; Rossberg, A.; Schäperkötter, M.; Schaper, M.; Walden, L.:* Verhalten von Aluminiumwerkstoffen bei der elektromagnetischen Blechumformung. Proc. 2. Kolloq. Elektromagnetische Umformung, 28. Mai 2003, Dortmund, S. 11–18.
- [5] DIN7190:2001-02: Interference fits – Calculation and design rules. Beuth Verlag GmbH, Berlin 2001.
- [6] *Kleiner, M.; Beerwald, C.; Homberg, W.:* Analysis of Process Parameters and Forming Mechanisms within the Electromagnetic Forming Process. CIRP Annals 2005, Vol.1.
- [7] *Beerwald, C.; Homberg, W.; Marré, M.; Psyk, V.; Kleiner, M.:* Einfluss der Geschwindigkeit beim kraftschlüssigen Fügen rohrförmiger Werkstücke durch elektromagnetische Kompression. Vol. 11 Paderborner Symposium Fügetechnik (2004), pp 162-172.
- [8] DIN7190:2001-02: Interference fits – Calculation and design rules. Beuth Verlag GmbH, Berlin 2001.
- [9] *Eichhorn, A.; Meyer, F.:* Innenhochdruckfügen von Rohren mit Rohrabschnitten, In: FOSTA Forschung für die Praxis P461. Verl. u. Vertriebsges. mbH 2004.
- [10] *Al-Ahmad, N.:* Das Fügen rotationssymmetrischer Formelemente durch Umformen mit Impulsmagnetfeldern. Dissertation Ingenieurhochschule Zwickau 1980.
- [11] DE 199 19 301 A1: Teilbare Einwindungsspule zur Erzeugung starker Magnetfeldimpulse (2000). Beerwald, H.; Beerwald, M.; Henselek, A.
- [12] ASM Metals Handbook 9th ed., vol.9, (1985).
- [13] *Beerwald, C.:* Grundlagen der Prozessauslegung und -gestaltung bei der elektromagnetischen Umformung. Universität Dortmund - IUL, Dr.-Ing. Diss., Reihe Umformtechnik, Shaker Verlag, Aachen 2005, ISBN 3-8322-4421-2.
- [14] *Kleiner, M.; Beerwald, C.; Homberg, W.:* Analysis of Process Parameters and Forming Mechanisms within the Electromagnetic Forming, 55th CIRP General Assembly, 22.-28.8.2005, Antalya (Turkey).

Investigation of the Process Chain Bending- Electromagnetic compression-Hydroforming on the Basis of an Industrial Demonstrator Part*

V. Psyk¹; C. Beerwald²; W. Homberg¹; M. Kleiner¹; M. Beerwald²;
A. Henselek²

¹ Institute of Forming Technology and Lightweight Construction, University of Dortmund,
Germany

² Poynting GmbH, Dortmund, Germany

Abstract

The increasing significance of lightweight construction concepts requires innovative and adapted production technologies and process chains for the manufacturing of complex parts made of typical lightweight materials. The feasibility and potential of such a process chain consisting of the steps Bending - Electromagnetic compression (EMC) – Hydroforming is shown in the present paper on the basis of a demonstrator part similar to a structural component from the automotive industry. Here, special focus is put on the requirements on the production steps and the workpiece properties. Furthermore, the development and testing of EMC-equipment that is optimally adapted to the special forming task is described.

Keywords:

Process chain, Electromagnetic forming, Hydroforming, Extension of forming limits

* The present study has been performed by the authors within the European project "Electromagnetic forming of tube and sheet metal for automotive parts - EMF - G3RD-CT-2002-00798". The conclusions drawn and the views put forward here do only reflect the opinions of the authors and not necessarily those of the rest of the project consortium. The project has been funded by the European Commission and the consortium has the following partners: VolvoCars Body components, Centro Recherche Fiat SCpA, DaimlerChrysler AG, PSA Peugeot- Citroen Automobiles, Alcan Technology & Management Ltd, Beijing Research Institute of Mechanical and Electrical Technology, ESI SA, University of Dortmund, and University of Trento.

1 Introduction

Given the general trend of a growing sense of responsibility for environmental protection, research and development in the automotive industry show an increasing interest in reducing fuel consumption and, thus, diminishing exhaust emissions. An important approach for the realization of this aim is the use of lightweight construction concepts including, among other techniques, the application of typical lightweight materials, as e.g. aluminum alloys and an optimized component design, which usually involves a more complex shape of the part (integral construction concept). This requires innovative and adapted production technologies and process chains suitable for the manufacturing of these parts. An example of such a sequence of processes, consisting of the steps Bending - Electromagnetic compression (EMC) – Hydroforming (compare Figure 1), is investigated within a European project (G3RD-CT-2002-00798).

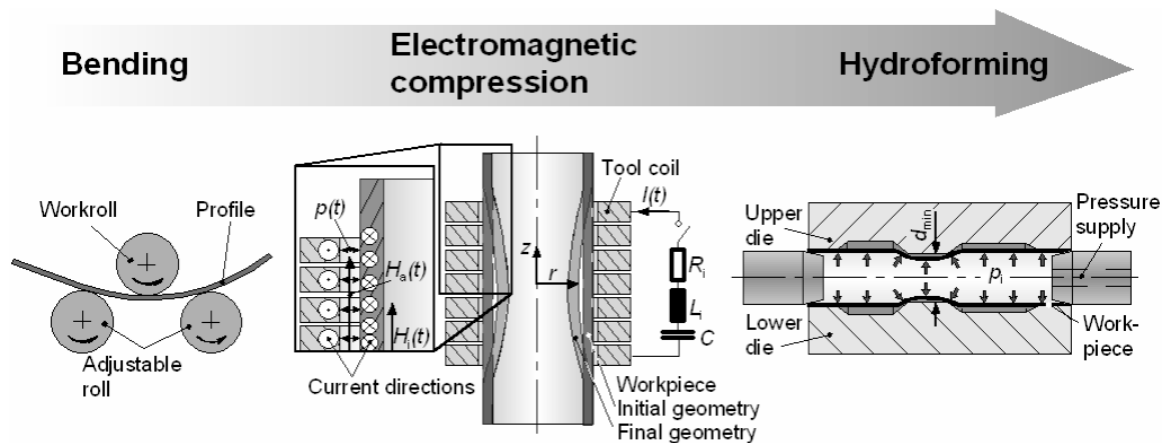


Figure 1: Investigated process chain and industrial demonstrator

The standard tube hydroforming technology offers comprehensive possibilities for the production of complex component shapes [1]-[3], which can be further extended by using appropriately contoured preforms. In the conventional hydroforming process the forming limits are set, on the one hand, by the initial tube diameter, which is usually determined by the smallest local circumference of the finished workpiece geometry, and, on the other hand, by the maximum tangential strain, restricting the maximum achievable circumference of the produced part. The use of contoured semi-finished parts offers the possibility to apply tubes of longer initial diameters, which are locally compressed in those areas where the circumference of the finished part is relatively small so that a wider spectrum of circumferences can be realized within one and the same part.

One possible technology for the production of such contoured preforms is the electromagnetic compression, a high speed forming process using the energy density of pulsed magnetic fields to apply a radial pressure to tubular workpieces with high electrical conductivity, causing a commonly, but not necessarily, symmetric reduction of the diameter. In practical applications a hydroforming process is frequently preceded by a bending step. One important advantage of EMC in comparison to alternative preforming operations, as e.g. spinning, is that it is applicable not only to straight, but even to curved profiles.

2 Influences on the feasibility of the process chain

In a sequence of processes the product of each manufacturing step is the semi-finished material of the subsequent steps. Therefore, each production step defines the requirements on the results of the previous processes. With regard to the investigated forming strategy, this means that especially the two interfaces between the subsequent manufacturing steps are significant for feasibility investigations. From the point of view of EMC, on the one hand, there are requirements made on the result of the workpiece properties after the bending operation and, on the other hand, the achievable workpiece characteristics after the EMC have to fulfill the demands of the hydroforming process.

2.1 Feasibility of the combined electromagnetic compression and hydroforming process

The general feasibility of the combined EMC and hydroforming process could be proved on the basis of different laboratory geometries in [4]. Thereby, the most important requirements of the hydroforming process on the previous steps have been identified as

- sufficient remaining forming capability allowing the calibration of the previously compressed workpiece areas without material failure in the form of cracking, and
- sufficient geometric accuracy of the cross section geometry in order to avoid material failure in the form of wrinkling.

The remaining forming capability of the material strongly depends on the heat treatment and it is reduced by all previous forming operations due to strain hardening effects. According to [5], the strain hardening caused by the electromagnetic compression merely depends on the tangential strain and can not be influenced by an adaptation of the applied pressure pulse. Thus, the tangential strain realized in the preforming operation limits the potential for the deformation and calibration in the subsequent hydroforming step.

Regarding the geometric accuracy of the cross section geometry, it is shown in [5] that the roundness of a tube which has been electromagnetically compressed without a form defining tool (mandrel) decreases with an increasing tangential strain, but it also depends on the course of the applied magnetic pressure. In order to achieve a defined radial deformation, it is possible to apply either a pressure pulse with a longer pressure rise time and a lower pressure maximum or a pressure pulse with a shorter rise time and a higher pressure maximum, whereby the latter leads to a higher forming velocity, related to a better roundness of the specimen. In [4], it could be shown that even a remarkable wrinkling effect can be completely reversed during the subsequent hydroforming process if the shape of the wrinkles is smooth.

In **Figure 2**, an electromagnetically compressed preform and the according workpiece, calibrated by means of hydroforming, is presented. Starting from an aluminum tube ($\varnothing 40 \times 2$ mm), here, a mean tangential strain of approx. 22% was realized in the compression zone while the tangential strain in the expansion area was approx. 8%, a value that was identified to be critical during hydraulic burst tests. With respect to the strong strain hardening effect caused by the EMC, the special potential of this technology to produce preforms of non-rotationally symmetric cross section geometry was exploited

in order to reduce the necessary tangential strain during the hydroforming step in this area. On the basis of this example the potential of the combined electromagnetic compression and hydroforming process could be shown for straight tubes.

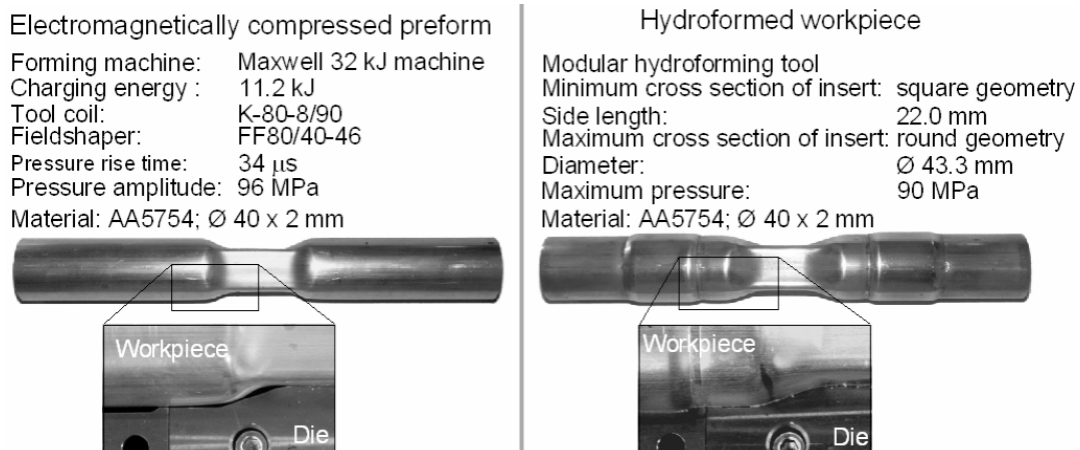


Figure 2: Hydroforming tests of workpiece with square cross section geometry [4]

2.2 Feasibility of the combined bending and electromagnetic compression process

Regarding the feasibility of the combined bending and electromagnetic compression process, investigations using laboratory equipment have shown that, in principle, it is possible to perform an EMC process on curved specimens. Thereby, the influences of the process parameters and the material properties on the roundness of the specimen in the compression area remain the same as in case of straight profiles. Thus, according to [4], the most important requirements on the workpiece characteristics are a good roundness of the tube as well as a homogeneous distribution of the wall thickness and the material properties along the circumference of the tube after the bending process.

Comparative measurements of bent profiles before and after an EMC process have proved a marginal influence of the electromagnetic compression on the contour accuracy. Thereby, a slight tendency to increase the bending radius locally in the compressed area can be detected, while the contour next to the compression area seems to remain unaffected. Nevertheless, depending on the size of the part and the position of the compression zone also, a slight deviation can be problematic with respect to the subsequent hydroforming process so that for processes with high demands on the preform contour an additional adjustment might be necessary.

In order to analyze the reason of this effect, the influence of a non-uniform gap width distribution between tool coil and workpiece was investigated. These tests have shown that, despite of the effect of the gap width on the acting magnetic pressure (compare [10]), even for extremely inhomogeneous gap widths no significant influence on the contour of the workpiece could be detected. This means that a compression process on a curved profile with a curving radius in the dimension of 1000 mm or more can even be performed using a straight tool coil without a remarkable deterioration of the forming result as long as the geometric conditions, as e.g. workpiece diameter, bending radius, and clearance of the compression coil, allow a positioning of the specimen inside the tool coil. On the other

hand, a significant increase of the gap width between tool coil and workpiece in order to extend these possibilities causes an increase of the common inductance of tool coil and workpiece. This influences the course of the discharging current to that effect that amplitude as well as frequency are reduced. Thus, the roundness in the compression zone and the efficiency of the process are declined.

Another possible explanation for the influence of the electromagnetic compression on the contour might be given by residual stresses caused by the preceding bending operation that interfere with the additional stresses caused by EMC. A promising solution to reduce or even avoid this could be the substitution of the bending process by curved profile extrusion, an innovative production technique developed at the Institute of Forming Technology and Lightweight Construction (IUL), University of Dortmund (compare [EP 1 169 146 B1]).

3 Production of an industrial demonstrator part using the process chain Bending-EM-compression-Hydroforming

Based on the previously described fundamental investigations, the feasibility of the complete process chain is analyzed, considering an industrial demonstrator part as an example. The chosen geometry is similar to a structural component from the automotive industry, more precisely to a roof rail, and DaimlerChrysler provides the according hydroforming tool. The part could already be realized successfully for different steel materials by using the process chain Spinning – Bending – Hydroforming (compare [6]) and will now be produced in aluminum in order to reduce weight. Therefore, extruded tube material with a diameter of 76.2 mm and a wall thickness of 2.5 mm made of AA5754 and AA6008 has been used. In Figure 3, the final workpiece as well as the target geometries after each production step, which proved to be suitable for the production of the steel parts, are shown.

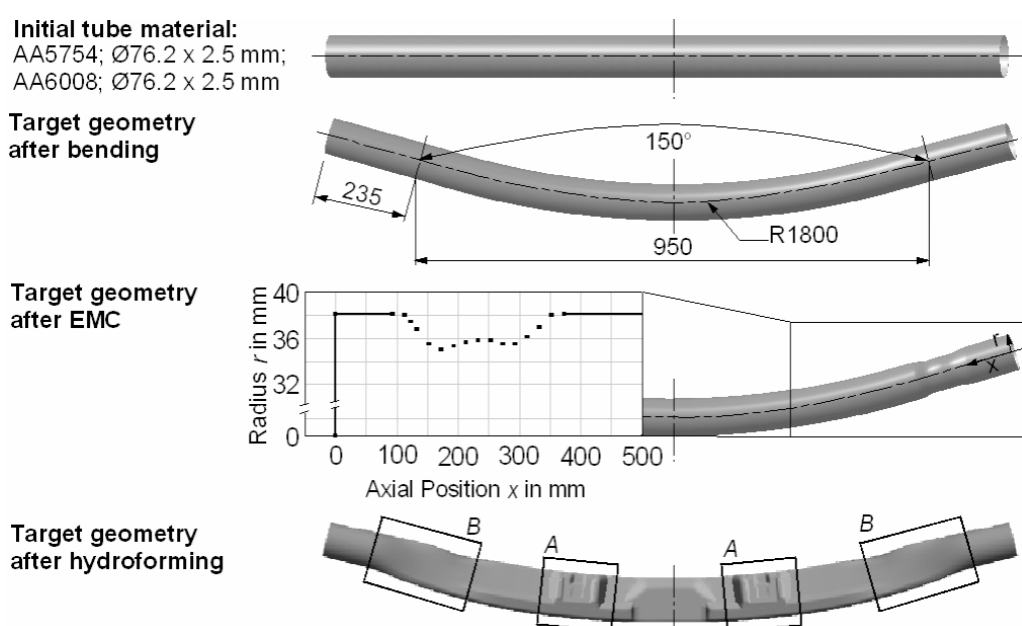


Figure 3: Industrial demonstrator part

The target contour after bending was developed on the basis of the final workpiece geometry and the geometric conditions of the used hydroforming tool. The investigations have shown that, with regard to the subsequent hydroforming process, there are extremely high demands on the contour accuracy in order to avoid any extrusion of the workpiece material into the parting plane during the closing of the hydroforming tool.

The target contour after the electromagnetic compression step was determined on the basis of the local circumferences of the finished part. These have been measured and the corresponding diameters were adapted to the bending line. The maximum strain is located in area *A* where the sunshades are mounted to the roof rail. With regard to the strain at failure of the applied aluminum alloys, an initial tube diameter of at least 76.2 mm and an initial circumference of 239.4 mm respectively is required. In contrast, the local circumferences in the area *B* are shorter than 239.4 mm so that a compression becomes necessary. The length of this compression zone is approx. 250 mm and the distribution of the desired diameters along the bended axis of the tube (as sketched in Figure 3) should not cause any significant tangential strain in the compression area during the subsequent hydroforming step.

3.1 Design of EMF-equipment

Although there are a lot of thinkable preform contours oriented by the circumferences of the final workpiece cross sections, the first proved feasibility should be shown using EMC without any mandrel, the easiest process variant. This results in the already mentioned axis-symmetric preform and requires a tool coil, which has to be optimally adapted in order to realize a suitable pressure distribution. In close cooperation of the IUL and the Poynting, a directly acting compression coil was developed to be used with the 32 kJ Maxwell Magneform machine at the IUL (capacitance $C \approx 960 \mu\text{F}$; inner resistance $R_i \approx 3 \text{ m}\Omega$; inner inductance $L_i \approx 52 \text{ nH}$; short circuit frequency $f_{\text{SC}} \approx 23 \text{ kHz}$).

To allow an easy handling of the partly curved semi-finished part after bending, a usable diameter of 80 mm has been defined, keeping in mind that the inductance has to be as low as possible to realize a short pressure rise time. As described more detailed in [8], for every forming task and forming machine an optimum number of turns exists to achieve an efficient transfer of charging energy into the acting pressure. In this case the optimum requires 8-10 turns. Typically, the construction is on the safer side if one or two turns more than the optimum are used, but in this case the number of turns should be as low as possible within the efficiently reasonable solution due to the mentioned reasons of a low inductance. This small number of turns and the length of the forming zone of approx. 250 mm lead to the idea of a double-winding coil (see Figure 4): This coil consists of two separate windings, which are connected in parallel to the clamping unit of the pulse generator. As indicated in the equivalent diagram in Figure 4, the discharge current runs through the common middle contact plate over both windings to the contact plates at the right and the left ends of the whole coil system. So the width of the turns could be reduced significantly.

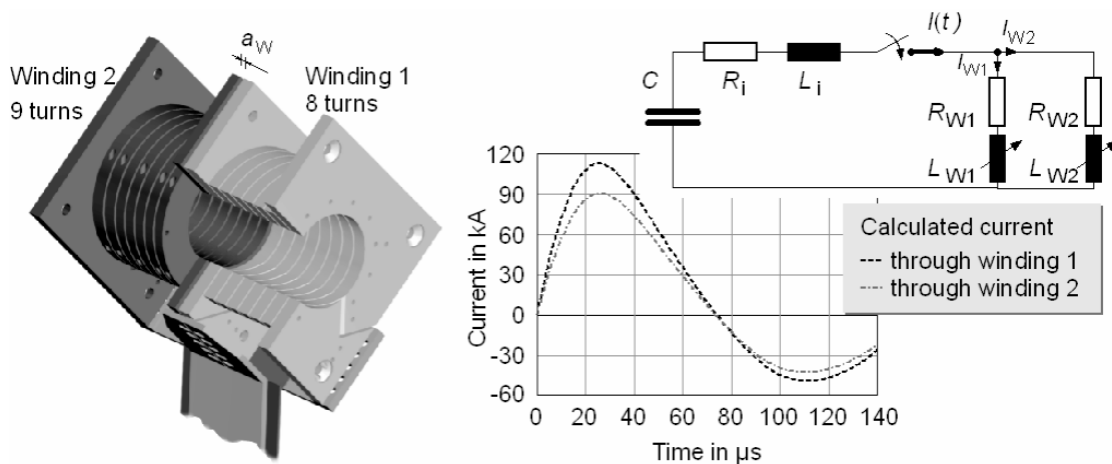


Figure 4: Tool coil developed for the electromagnetic compression of the demonstrator part and according coil current

For a further and more detailed dimensioning, as for example the precise width of every single turn to realize the required pressure distribution, a coupled Finite Element Analysis (FEA) has been used. The numerical modeling is based on the developments of Karch, as described in [7], using the software package ANSYS 8.0. It contains the simultaneous solution of the transient electric circuit (including the pulse generator), the electromagnetic and the structural equations. Since the simulation tool is restricted to 2-dimensional problems the design of the tool coil could only be performed considering straight workpieces and the previous bending step had to be disregarded. Also the used material characteristics are determined by quasistatic tensile tests, neglecting the strain rate terms. Being aware of its inaccuracy, the simulation results are qualitatively good enough to dimension the tool coil especially considering the resulting course of the discharge current as well as the distribution of the magnetic pressure.

As shown in **Figure 5**, the desired workpiece deformation could be approximated best by an asymmetric winding design: one with 8 turns and one with 9 turns and a varying width of 10 to 13 mm. The use of a varying winding density to influence the pressure distribution according to DE 102 07 655 was successfully tested for flat coils (compare [9]) and could now be transferred to compression coils.

According to the different electrical properties of the parallel windings, the current will be distributed, while the measurement detects the sum of both. The simulated current over time curves as well as the resulting pressure distribution at the time of current maximum are shown in Figure 4, too. As an additional feature and with the aim of achieving as much flexibility as possible for slight modifications of the preform contour, both windings can be mounted with different distances a_w between them, adjustable from 0.5 up to 6 mm.

In order to evaluate the numerical coil design and the realized coil as well, compression tests have been carried out using straight workpieces and the resulting contour in the deformation zone was measured. As presented in Figure 5, the comparison of the numerically and experimentally determined contours shows good qualitative agreement.

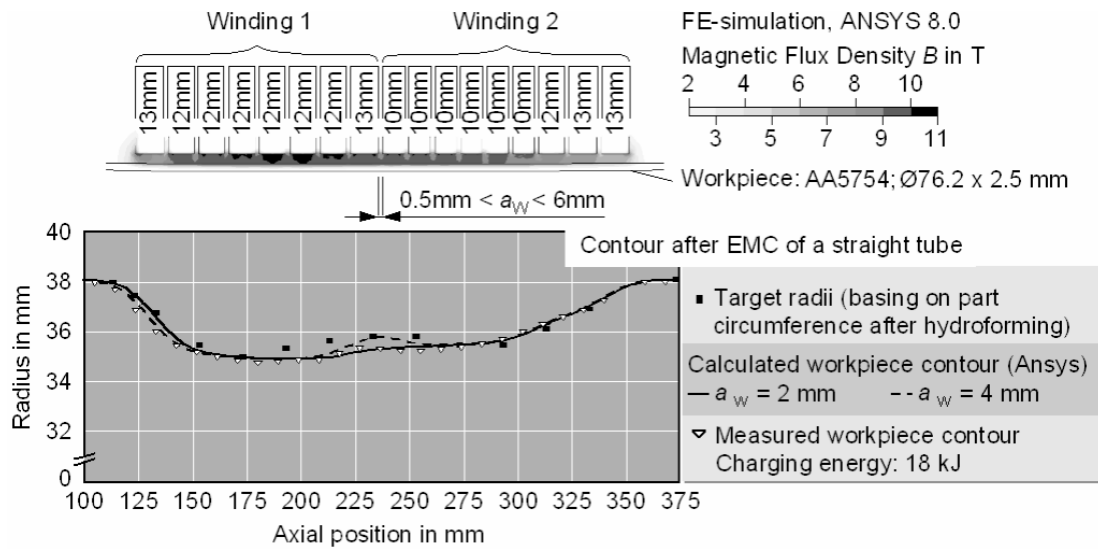


Figure 5: Coil winding and resulting contours of the electromagnetically compressed workpiece

3.2 Electromagnetic compression of bent semi-finished parts

In the next step the compression of previously bent profiles was regarded. The target geometry after the bending step, shown in Figure 3, could be realized with high contour accuracy. The mean deviation from the ideal contour could be reduced to less than 1 mm. Comparative contour measurements after bending and after EMC have proved a small influence of the electromagnetic compression on the contour accuracy (compare **Figure 6**). Thereby, the bending radius in the middle between the two compression areas seems to be largely unaffected, while the angle between the straight end zones of the part is slightly increased.

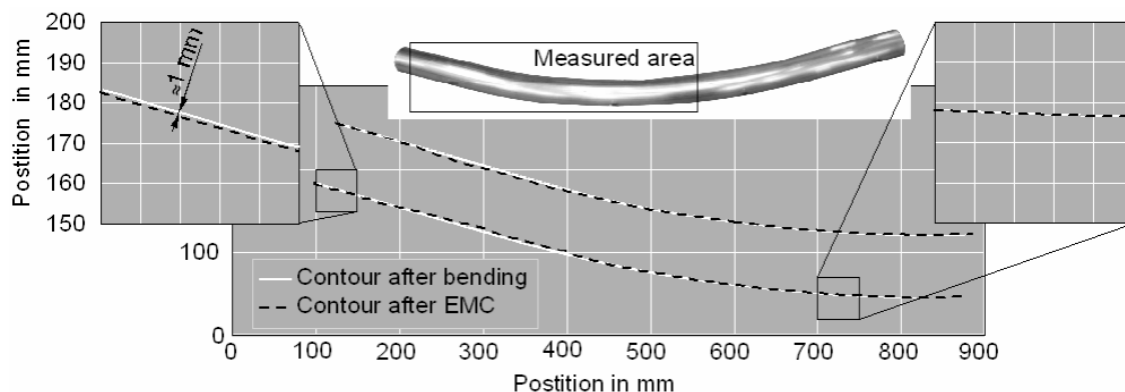


Figure 6: Contour accuracy of the bent and compressed preform

3.3 Testing of the bent and compressed semi-finished parts

In order to evaluate the preforms, hydroforming tests have been carried out in close cooperation between IUL and DaimlerChrysler AG, Hamburg. The parts were formed in a two-stage process consisting of the steps closing of the tool without or with low inner pressure and high pressure calibration of the part. With regard to the motivation of the

investigated process chain, especially the first step is of interest because, here, it can already be seen whether the preforming was successful and the complete closing of the hydroforming tool is possible.

As presented in Figure 7, the testing of bent and compressed preforms has shown that extrusions of the material into the parting plane of the hydroforming tool could nearly be avoided (example (b)). Contrary and as expected, the application of bent semi-finished parts of uniform initial diameter led to significant extrusions (example (a)). These obvious extrusions render the closing of the tool and the successful production of the part impossible. This clearly shows the advantage of the combined forming strategy Bending – Electromagnetic compression – Hydroforming in comparison to the standard hydroforming process.

The subsequent testing of the calibration step has shown that after a successful closing of the tool the part could be formed without cracking, whereby a pressure of up to 2500 bar was applied. For this pressure all deviations on the roundness caused by the EMC using the optimized tool coil described in 3.1 could be reversed (example (d)). So the feasibility and the potential of the complete investigated process chain could be proved. On the other hand, comparative experiments applying a tool coil that is less suitable with regard to this special application have affirmed the importance of adapting the coil parameters to the forming task. As shown in example (c), the preform quality achievable by performing multiple subsequent compression sequences, using a tool coil with the same diameter (80 mm), a shorter length (90 mm), and a longer pressure rise time is not sufficient to avoid irreversible wrinkling.

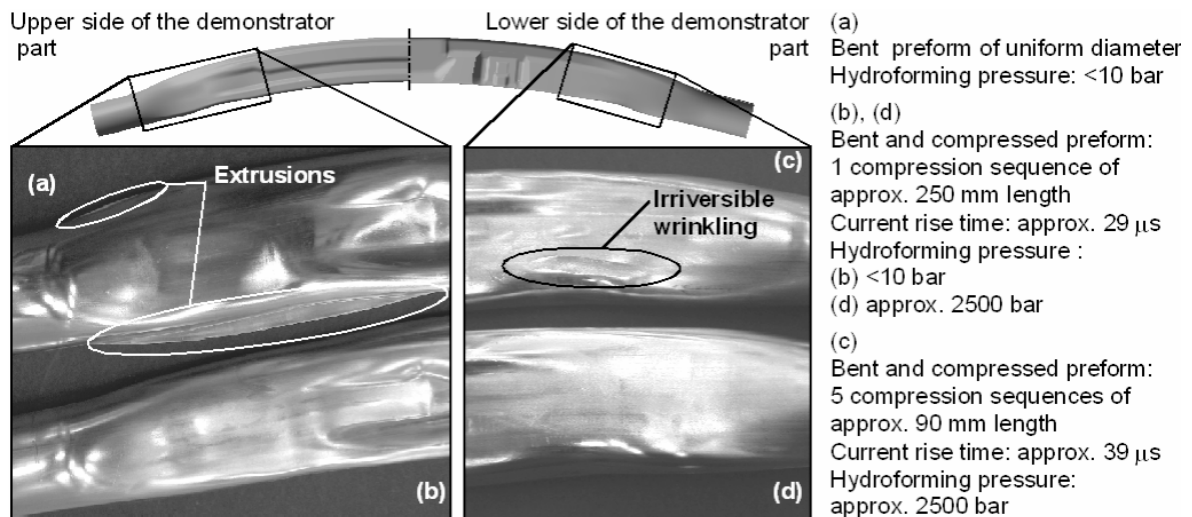


Figure 7: Results of hydroforming tests for compressed tubes and tubes of uniform diameter

4 Summary and Outlook

The increasing significance of lightweight construction concepts requires innovative and adapted production technologies and process chains for the manufacturing of complex parts made of typical lightweight materials. The feasibility of such a process chain consisting of the steps Bending - Electromagnetic compression (EMC) – Hydroforming

could be shown on the basis of a demonstrator part from the automotive industry. In order to realize a suitable preform geometry by means of EMC without applying a mandrel, a tool coil optimized for this special forming task was developed using a coupled 2-dimensional Finite Element Analysis. Thereby, the resulting course of the discharging current, on the one hand, and the distribution of the magnetic pressure causing the resulting workpiece contour, on the other hand, has been considered. In order to evaluate the coil design, compression tests were carried out on straight and bent workpieces, validating the numerically determined workpiece contour. The further processing of the bent and compressed semi-finished parts by means of hydroforming could be realized successfully and the potential of the investigated process chain to extend forming limits of the conventional hydroforming process could clearly be proved.

On the other hand, the experiments have shown an extreme sensitivity of the hydroforming process regarding the bending line and the contour in the compressed area for this special part. Already slight contour deviations caused extrusions into the parting plane during the closing of the tool. In order to render the hydroforming process easier and more reliable numerous possibilities to improve the shape of the preform, e.g. by applying mandrels of different cross section geometries are thinkable. As shown in [4], the adaptation of the cross section geometry causes an inhomogeneous distribution of the tangential strain along the circumference of the part related to an according distribution of wall thickness and strain hardening. Selective variations of the workpiece properties in that way might be used in order to purposefully influence the forming stages during the hydroforming process.

References

- [1] *Birkert, A.*: Herstellung von Strukturbauteilen durch Innenhochdruck-Umformen, Diss., Institute for Metal Forming Technology, University of Stuttgart, 2000.
- [2] *Dohmann, F.; Lange, K. (publisher)*: Innenhochdruckumformen, Umformtechnik - Handbuch für Industrie und Wissenschaft, Volume 4, Springer-Verlag, Berlin/Heidelberg, 1993.
- [3] *Schroeder, M.*: Recent Developments in the Hydroforming of Tubular and Sheet Blanks – Semi Productive and Productive, Proceedings of the International Conference on Hydroforming, Volume 3, Fellbach, 2003, p. 165- 184.
- [4] *Psyk, V.; Beerwald, C.; Homberg, W.; Kleiner, M.*: Extension of Forming Limits by Using a Process Combination of Electromagnetic Forming and Hydroforming, Proceedings of the 8th International Conference on Technology of Plasticity (ICTP), 09.-13.10.2005, Verona (Italy), ISBN 88-87331-74-X.
- [5] *Psyk, V.; Beerwald, C.; Homberg, W.; Kleiner, M.*: Electromagnetic Compression as Preforming Operation for Tubular Hydroforming Parts. ICHSF 2004 - 1st International Conference on High Speed Forming, 31.3.-1.4.2004, Dortmund, Germany, Proceedings pp. 171-180, ISBN 3-00-012970-7
- [6] *Kleiner, M.; Chatti, S.; Ewers, R.; Hermes, M.; Homberg, W.; Shankar, R.*: Process Chain for the Improvement of Hydroforming Processes Using Tailored Semi-Finished Tubes, Production Engineering - Annals of the German Academic Society for Production Engineering (WGP), Volume XIII-1, 2005 (paper accepted).

- [7] *Karch, C.; Roll, K.: Transient simulation of Electromagnetic Forming of Aluminium Tubes, Proceedings of the 11th International Conference on Sheet Metal, 05.-08. April 2005, Erlangen, Germany, Advanced Materials Research Volumes 6-8, pp. 639-646, ISBN 0-87849-972-5.*
- [8] *A. Henselek, M. Beerwald, C. Beerwald: Design and Adaption of EMF Equipment - From Direct Acting Multi-turn Coils to Separable Tool Coils for Electromagnetic Tube Compression, Proceedings of the International Conference on High Speed Forming, Dortmund, 2004.*
- [9] *Psyk, V., Beerwald, C.; Kleiner, M.; Beerwald, M.; Henselek, A.: Use of Electromagnetic Forming in Process Combinations for the Production of Automotive Parts. EPPS 2004 – 2nd European Pulsed Power Symposium, 22.9.2004, Hamburg, Proceedings pp. 82-86, ISBN 3-8322-3217-6*
- [10] *Beerwald, C.: Fundamentals for Process Dimensioning and Design of Electromagnetic Forming (in German), PhD.-Thesis, Dortmund, Germany, 2004.*

A Production-oriented Approach in Electromagnetic Forming of Metal Sheets

R. Neugebauer¹; F. Löschmann²; M. Putz¹; T. Koch¹; G. Laux¹

¹ Fraunhofer-Institute for Machine Tools and Forming Technology, Chemnitz, Germany

² Volkswagen Sachsen GmbH, Zwickau, Germany

Abstract

In recent years, sheet metal forming shows tendencies to process a smaller number of parts per unit. Especially demands of modern lightweight design seem to be hard to satisfy by stretching conventional production methods. Thus, it is necessary to find new approaches. Adapting electromagnetic forming technology for the automotive industry would gain additional benefits like

- *less surface damaging owing to contact-less forming,*
- *the possibility of achieving smaller radii,*
- *focusing on low volume production through minimizing investment costs, and*
- *more manufacturing flexibility.*

An approach to start qualifying this technology under the aspect of production engineering has been attempted by establishing a high speed forming project. The Volkswagen AG, Siemens AG, H&T ProduktionsTechnologie GmbH together with Fraunhofer Institute of Machine Tools and Forming Technology started activities focusing on

- *clarifying the fields of research and development which are not resolved to date,*
- *developing necessary equipment, and*
- *a systematic research on the according technology.*

The analysis of available equipments brought up a number of questions with respect to production engineering requirements. It resulted in a 100 kJ pulse power generator. One of the core components to define the quality of the forming process of flat parts is the flat coil. A coil design is selected to transfer a maximum of stored energy into the sheet metal. A selection of basic and applied experiments had the aim to know the limits of the technique. The paper introduces some representative results of the project. It touches the challenges related to the process of bringing this technology to production

Keywords:

Forming technology; Electrical discharge machining, Production engineering

1 Introduction

Caught between the forces of international competition and an emerging trend towards individualization of customer requirements, today's companies are attempting to assert themselves and/or acquire new market shares by increasing their product range. The consequence is severe upward pressure on costs and production methods used to date are now being called into question. Possible solutions are to increase the efficiency of existing processes and to harness technologies which are new or which have, up until now, been somewhat neglected.

Electromagnetic flat forming is an example of one such technology. The primary field of application for flat forming is in postforming i.e. the process which follows the actual forming procedure in the process chain and in the opportunity for forming ancillary formed elements. However, many of the familiar challenges in this technology segment which have been known for decades have not yet been resolved, even with today's knowledge. New materials and advanced development of the technologies required for magnetic forming nevertheless present obvious possibilities in terms of overcoming the complex obstacles.

In the context of a project sponsored by the investment bank Sächsische Aufbaubank (SAB) and implemented in partnership with Volkswagen AG, Siemens AG, H&T Produktionstechnologie GmbH, and the Fraunhofer Institute for Machine Tools and Forming Technology, research is being carried out in the areas of current impulse equipment, magnetic coils, forming technology, and simulation. This project represents an attempt by the partners to highlight magnetic forming in terms of application-oriented research.

2 Technical installations for electromagnetic flat forming

2.1 The experimental equipment

In order to investigate electromagnetic forming under production engineering conditions, a suitable experimental plant was developed, consisting essentially of an energy storage equipment with appropriate switching technology to provide the energy, a flat forming coil with the necessary connectors and links to transfer the energy to the workpiece, and a tool holder to absorb the forming forces. As is required in forming technology production plants, the individual processes must be capable of being safely controlled and operated as well as important measurement and status parameters must be automatically recorded.

The design project focused on the safe integration of the pulsed current equipment and its connection to the forming coil inside the tool holder. The necessary development work was carried out in close collaboration with our joint venture partner Siemens.

The specifications for the tool holder were defined by the anticipated forces and the degree of flexibility required in accordance with the program of experiments. The objective of the investigations to be performed using the experimental plant is to qualify the technical and technological aspects of the installation for production engineering applications (see Figure 1).

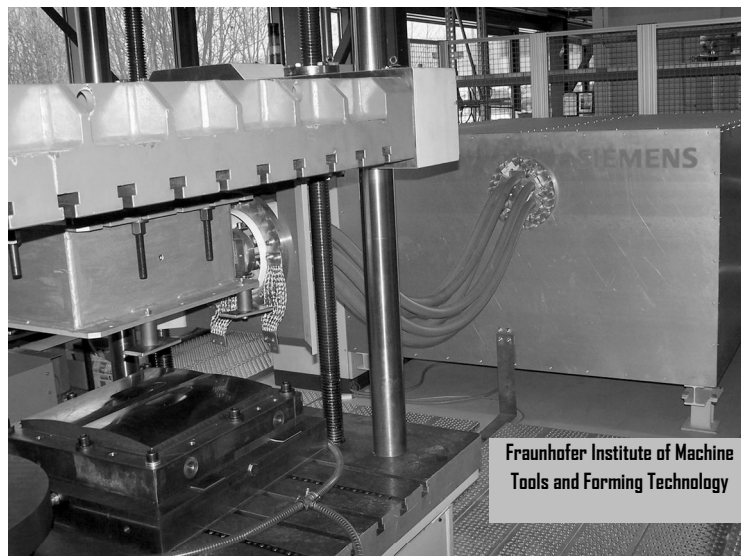


Figure 1: *Experimental electromagnetic forming plant*

The pulse magnetic field required to produce a pressure impulse on a sheet of metal to be formed is generated by a current impulse. Suitable current impulse equipment consists without exception, of a fast bank of capacitors with a charging voltage of some 100 V up to some 10 kV and the associated power circuit breakers. By closing the circuit breaker the energy is discharged from the bank of capacitors via the forming coil. A survey of commercially available pulsed current equipment for use in magnetic forming revealed that the equipment can be classified according to stored energy and that energy stores of up to 80 kJ are used. The selection and dimensioning of the components used is a function of the maximum voltage used, the maximum amount of energy to be stored, the peak currents and maximum increases in current arising in the oscillating circuit, and the mechanical and thermal load. In addition, when estimating the useful life of the equipment as part of the design of the experimental plant the shock load of all the components during the discharge process must be taken into account.

The design of the impulse equipment was essentially underpinned by the idea that the technological investigations into electromagnetic forming of flat components should concentrate initially on smaller structural elements. During the course of the investigations the results obtained were applied to flat geometries of more extensive size. As there is no reliable ratio between the amount of energy required and the area to be formed, taking account of geometric and materials parameters, it was decided - after consulting users and following extensive research in the literature - to specify 100 kJ as the electrical energy storage capability. The experimental plant was designed on the modular principle in order to permit replacement of selected components, if necessary.

In order to keep the capacity of the bank of capacitors low, given a specific energy requirement, and hence to keep the size of the impulse generating equipment to a minimum, the usable voltage level was set at 20 kV. In the voltage range envisaged vacuum switches (spark gaps), ignitrons (gas discharge tubes), and thyristors (semiconductor switches) were used as circuit breakers and high-current switches. Previous current impulse plants have hitherto been produced almost exclusively with vacuum switches or with gas discharge tubes. The use of vacuum switches requires a higher level of maintenance, which ultimately makes them difficult to use in production engineering situations. Ignitrons, on the other hand, require no maintenance. The crucial disadvantage

of ignitrons is that they consist of a liquid mercury cathode. In the event of a disastrous failure of the tube the ambient air may be contaminated with mercury. As this residual risk can not be completely excluded, in some countries the use of these switching elements is subject to the most severe restrictions or is prohibited altogether. Semi-conductor switches, by contrast, require no maintenance, nor do they carry the aforementioned risk. In the past, because their performance parameters were too low, these switching elements were only used for switching at low power levels or for switching processes in which the switching times were not critical. As a result of the development of GCTs (Gate Commutated Thyristors), it was possible to improve the switching characteristics of GTO thyristors (Gate Turn Off thyristors), given comparable load parameters. In addition, the characteristic values required, such as cut-off voltage, current carrier capability, and current rise time, are provided by the switching elements. Therefore the decision was, taken to opt for semi-conductor elements as circuit breakers (see Figure 2).



Figure 2: Arrangement of semi-conductor switches in the pulsed current plant

In order to specify equipment requirements for electromagnetic forming plants in production engineering settings, it is essential to consider the handling of the tools and the workpieces. For this reason, a tool holder was chosen which is fitted with a spindle-driven lifting and tipping unit. After applying the electromagnetic setup approx. 650 mm of travel of the upper mounting plate is left. Since no masses (tools) have to be accelerated during the forming process the position of the working coil and the tool can be chosen arbitrarily. In the case of larger profiles it should be noted that the metal sheet to be formed flexes due to gravity, depending on the geometric and material parameters. This effect is further intensified by evacuating the space between the tool and the profile. This alters the distance between the sheet of metal to be formed and the working coil which, in turn, adversely affects the electromagnetic coupling and, hence, the degree of efficiency. This change in the process parameters must be taken into consideration when constructing the tool, the working coil, and the production plant and appropriate measures must be taken to compensate in certain circumstances.

Investigations into position-dependent process characteristics require a mobile connection to the pulsed current equipment on the tool holder. Therefore, it is important to

analyze the electrical properties such as contact resistances on the connecting elements and self-inductance of the cable and insulating sections. The chosen design fulfils the necessary criteria and can be mounted on both the rigid and the mobile mounting plate, thereby guaranteeing the flexibility in terms of assembly that is absolutely indispensable for the investigations.

In addition to the vertical positioning axis, the tool holder has a tilting axis permitting rotation of the upper plate through 360 degrees. This has proved to be particularly advantageous for installing the working coil on the upper plate. The connecting elements between the working coil and the energy chain must, however, be released manually before each rotation and fixed in place again after each coil change. An automated solution should be provided for the replacement and adjustment of the working coils in order to minimize tooling times.

Besides the availability of the main components such as capacitors and circuit breakers, it is essential to assess whether the selected voltage level and the resulting peak currents can be safely controlled in the installation as a whole. To this end, a safety and grounding plan was devised, based on a risk analysis. In addition to the usual mechanical dangers associated with forming machinery, electromagnetic forming plants carry risks resulting from high voltages and power outputs as well as from impulse magnetic fields. For this reason, the working area was galvanically isolated from the operator area. The power is supplied via a specially dimensioned contact separator. Control data and measurement data are exchanged via fibre optic cable between the autonomously operating control components. The experimental plant is controlled via a central operator console outside the protected zone. In case of an emergency an uninterruptible voltage supply ensures that the safe operational status of the installation as a whole can be restored. For the pulsed current equipment this means a complete discharge of the capacitors via rheostats specially designed for this purpose. All components within the protected zone are centrally grounded.

Measuring the forming process itself is made more difficult by the electromagnetic and mechanical properties of the setup and the expected high forming speeds. As has been shown in comparable applications, here, too, the current path and voltage path across the working coil are measured in order to determine the relationships between stored energy and the forming outcome. Although the measured results only reflect the global relationship between electromagnetics and structural mechanics, they nevertheless serve to verify coupled simulation models. In addition, the data provide information on the loading of the components within the pulsed current equipment. For the above reasons, experimental protocols containing both the measurement data and relevant parameters concerning the equipment are automatically generated.

2.2 Flat coils for magnetic forming

The tool and working coils must be adapted as closely as possible to the eventual form of the workpiece in order to create an efficient energy transfer and, hence, to apply the maximum possible amount of force to the workpiece. In sheet metal forming the working coils are constructed so they are flat (and are therefore also referred to as flat coils). Since all that is needed in the gap is space for the electrical insulation between coil and work piece the gap should be minimized in order to improve efficiency.

The natural frequency and maximum current of the oscillating circuit, consisting of the pulsed current equipment, transmission lines, and working coil, are determined with the electrical properties of the working coil – inductance and resistance. These parameters, in conjunction with the coupling characteristics of the sheet metal to be formed, define the forces between the working coil and the sheet metal. In addition to the definitive axial forces, however, comparable radial forces also occur between the turns. The calculation models drawn up in a joint project with Siemens are used to determine the electrical and mechanical characteristic values, which serve as input quantities for dimensioning and constructing the working coils.

In theory, a working coil consists of a conductor with corresponding connectors, a coil mount, possibly consisting of more than one section, and the power supply elements.

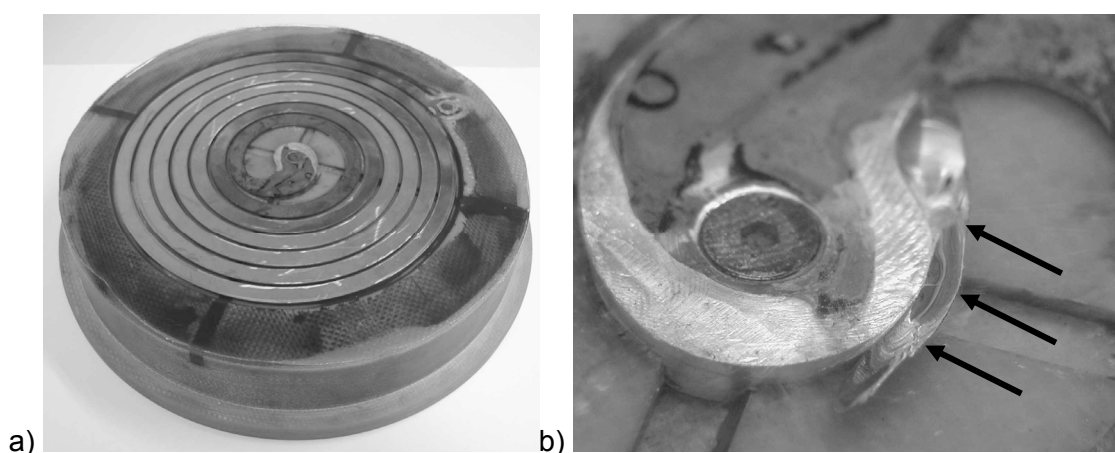


Figure 3: Flat coil with spiral turns a) flat coil after casting, b) crack formation along the turn

If the conductor is shaped in the form of an Archimedes screw (see Figure 3a) special structural measures are required to connect the inner end of the conductor. The coil is incorporated in a coil mount which must be capable of withstanding the high shock loads. If the turns are very tight care must be taken to provide good electrical insulation between them. Depending on the design of the coil, voltage differences can arise corresponding with the maximum useful voltage. If the voltage insulation is provided in the form of a cast resin this will be subjected to the pulse-like radial forces. For this reason, selection of the cast resins must take account of their impact strength, rupture strength, and elongation at fracture. As shown in Figure 3b, an increase in crack formation along the turns was observed when cast resins with a very high E-modulus were used.

Depending on the design, established manufacturing processes such as milling and water jet cutting can be used to produce the working coils. If the current-carrying elements consist of several parts the contact resistance must be minimized. Abutting or arced connections are subject to electrical forces that must be taken into account at the design stage. If the individual components are connected to one another by means of hard-soldered connections, the execution of the joints must be optimized with regard to contact resistance and mechanical stability. The turns are mildly annealed due to the increased application of heat and their strength is thereby reduced. In order to be able to withstand the radial load, the turns must be supported by additional constructional measures, for example the selective choice of casting material.

The load on the working coil is also determined by the position of the sheet metal to be formed in relation to the working coil. If the sheet metal completely covers the coil and at a minimal distance a good coupling should be guaranteed. If the sheet metal is smaller than the coil or is no longer homogeneous (with sections cut out or formed areas) then the initial inductance of the oscillating circuit is determined by the position of the workpiece in relation to the coil. A poorer electromagnetic coupling means an increase in the mechanical load on the coil. It was observed during investigations in connection with this aspect that the coils fail in the vicinity of poor electromagnetic coupling. This must be taken into account in particular where the sheet metal is formed in several stages without adjusting the working coil properly and restoring the coupling. These special operating conditions must be considered during the design process of the working coil.

In addition to the increased mechanical load on the working coil, poor coupling conditions also affect the components inside the pulsed current equipment. The increased inductance accompanying the diminished coupling results in an increase in the load current integral (I^2t). The thermal ageing process triggered as a result reduces the anticipated serviceable life of the components. In order to be able to estimate the load on all the components, it is necessary to calculate the expected current flow. Since under production engineering conditions it is not possible to launch a full-length coupled simulation before every forming process a simplified calculation should be used at this point, based on the initial values and end values for inductance of the working coil. The measuring technology required for this determines the inductance of the coil before and after each forming process, without interrupting or affecting the timing of the process. The measurement results are continuously evaluated and can be used both for technological process control and for ensuring the safety of the installation components. A measurement model of this kind is currently being developed at the Fraunhofer Institute for Machine Tools and Forming Technology.

3 Technological investigations into electromagnetic flat forming

In the trio comprising installation, coil, and technology, all efforts are concentrated on providing optimum conditions for the forming process. This does not mean, however, that any of the aspects carries more weight than the others. On the contrary, a particular feature of electromagnetic forming is the need for mastery of the interaction between all three aspects. In the project, the potential of the technology is analyzed in experimental investigations both on a theoretical level and in applications using real components.

3.1 Basic investigations

The primary aim of the design and implementation of series of experiments on the technological theories is to be able to put forward fundamental propositions regarding the behavior of a blank under the conditions of electromagnetic forming.

The tool geometry used in the investigations already exhibits characteristics of the eventual components and permits a generalized extrapolation of the knowledge acquired from the experiments. Careful consideration of the design of a tool that would meet all these requirements resulted in the dish with a conical body, shown in Figure 4, and the illustrated tool design.

The tool consists of the actual matrix and a universal base plate. Several air ducts are incorporated in the base plate to enable a vacuum to be created via additional ducts in the matrix. The connections for the suction hoses of the pump and various fixing options are also provided in the base plate. The change in depth of the basic form is achieved by means of tool inserts and subsequent mechanical processing is envisaged for the variation in other parameters.

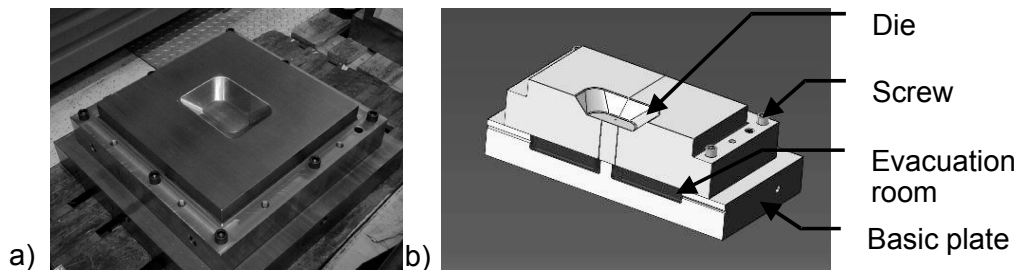


Figure 4: *Experimental tool for basic investigations*
 a) top view b) cross-section through the CAD model

Since the development of an innovative impulse power installation and the basic technological investigations started almost at the same time in this project initial experimental investigations were carried out in collaboration with the University of Applied Science in Zwickau. The variables in these investigations included the energy, the vacuum, the forming depths, and the materials. The coil was positioned centrally.

Figure 5 shows the effect of various different energy quantities. The material used is AA5182 and the forming depth is 15 mm. It is evident that higher energy levels do not necessarily result in better forming results. Two points can be made to summarize this:

- As the amount of energy increases, there is an improvement in the forming of the corner radii,
- and as the energy increases, so does the central “indentation” because the acceleration of the areas subject to applied pressure increases and the inertia of the unaccelerated central areas has greater effect.



Part order	
22,2 KJ	15,24 KJ
18,18 KJ	30,22 KJ

Material: AA5182

Figure 5: *Influence of varying energy levels*

Another important point is the investigation into the effect of the vacuum. The forming process takes place so quickly that air cushions are created if the tool is not adequately evacuated. This has a detrimental effect on the forming result (Figure 6).

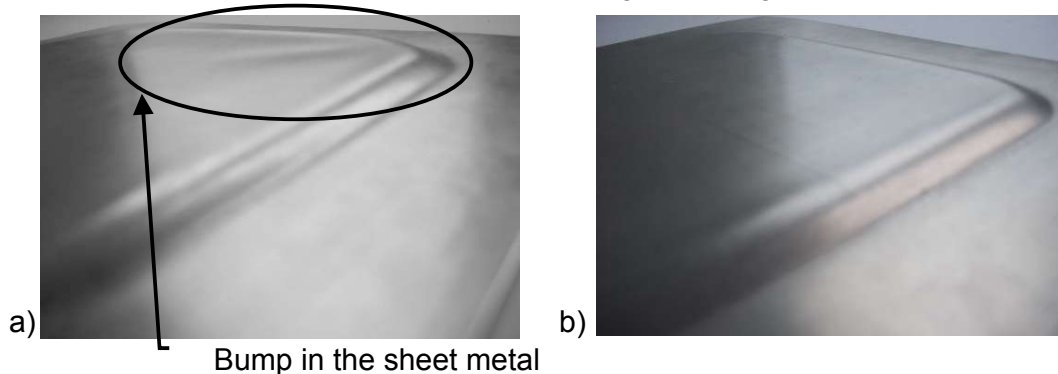


Figure 6: The effect of an inadequate vacuum
 a) vacuum approx. 78.5% b) vacuum approx. 95%

As can be seen from Figure 7a, in magnetic forming the blank is drawn in. In order to achieve greater depths in the component, as envisaged by the investigations, drawing in of the sheet metal is indispensable. The possibilities and the challenges resulting from this knowledge have not yet undergone comprehensive analysis at this stage of the project.

Inclusion of steel materials is also the subject of the investigations. The mechanical and electrical properties are less advantageous compared with those of aluminum. However, it seems sensible to consider the possibility of using steel materials in electromagnetic forming in terms of subsequent forming operations for the manufacture of ancillary formed elements, for example in doors. Differences in the forming of various sheet metal materials are shown for the purpose of illustration in Figure 7b.

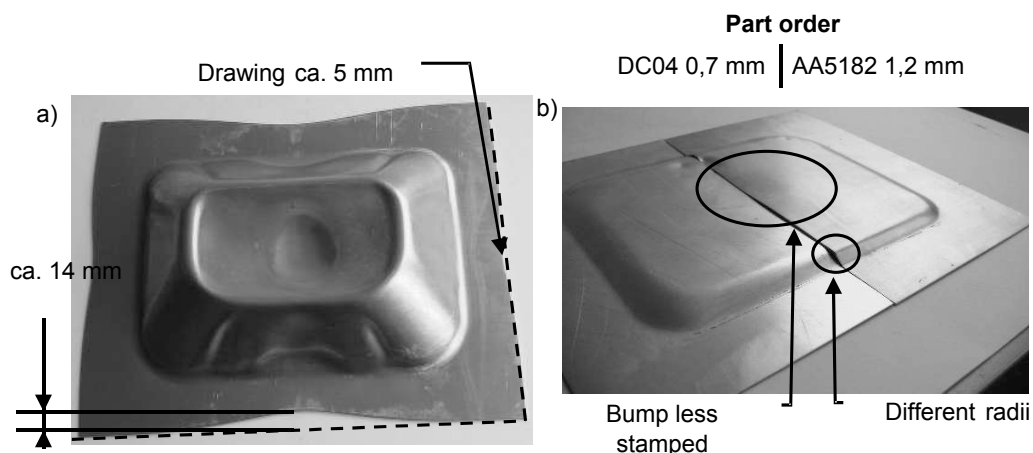


Figure 7: Experimental results from the basic investigations
 a) illustration showing how the blank is drawn in b) comparison of components made from different materials

3.2 Component-related investigations

As the second step in the technological investigations, the knowledge acquired from the basic investigations was applied in the project to a real component. An additional experimental tool was used as an intermediate step in relation to the real part geometry of the depression in a door to accommodate a door handle. This tool contains the geometry of the door handle depression and its immediate vicinity and is intended to enable preliminary investigations to be carried out.

The results of experiments to date are encouraging (Figure 8). The crease that is still present is due to the necessity of repositioning the coil, which is currently too small. The surface damage occurred as a result of persisting inadequacies in the process sequence.

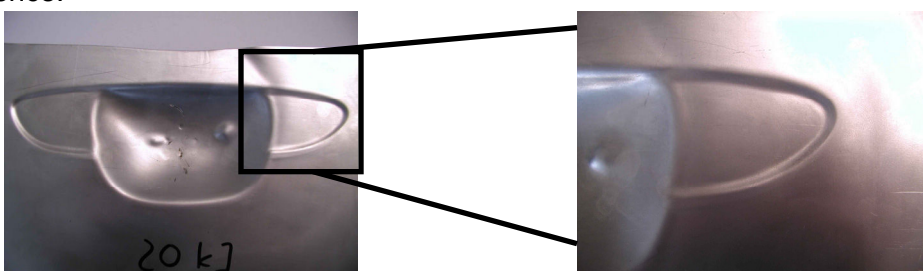


Figure 8: Experimental results from the door handle depression
a) forming with 3 kJ b) forming with 5 kJ

4 Summary and prospects

The experimental installation, which has been developed for the electromagnetic forming of flat components, represents a further step towards qualifying appropriate plant and equipment for production engineering. Rather than focusing primarily on maximizing the known parameters of the equipment, development of the installation was geared to the technical adaptation of the equipment from the point of view of production engineering. The knowledge acquired, in conjunction with the results of technological investigations, will influence the development of future magnetic forming installations.

Overall, interesting aspects have emerged from the basic investigations, which will have a bearing on future investigations. Particularly noteworthy are the following:

- drawing in of the sheet metal at greater drawing depths;
- the theoretical possibility of achieving good results with steel as well as other metals, and
- initial encouraging results from the experimental forming of a depression for a door handle, which was central to this project.

Additional tasks have been identified for inclusion in future investigations, for example optimized process control for greater drawing depths. Similarly, the inclusion of the electromagnetic forming process in process chains and the further improvement in economic viability by means of additional process integration will also play a role in this connection. In the future, too, investigations will continue to focus on practical applications of electromagnetic forming of sheet metals.

References

- [1] *Löschmann, F.*: Technologieflexibilität für Kleinserienkonzepte. Proceedings of The 4th Car Body Colloquium; ISBN 3-937524-33-9, Chemnitz, Germany, 2005, p. 175.
- [2] *Flegel, H. A.*: Herausforderungen für Karosseriekonzepte: „Neue Werkstoffe und Technologien, Flexibilität“. Proceedings of The 4th Car Body Colloquium; ISBN 3-937524-33-9, Chemnitz, Germany, 2005, p 111.

Design and Testing of Coils for Pulsed Electromagnetic Forming

S. Golovashchenko¹, N. Bessonov², R. Davies³

¹ Ford Research & Advanced Engineering, Dearborn, USA

² University of Michigan-Dearborn, Dearborn, USA

³ Pacific Northwest National Laboratory, Richland, Washington, USA

Abstract

Coil design influences the distribution of electromagnetic forces applied to both the blank and the coil. The required energy of the process is usually defined by deformation of the blank. However, the discharge also results in a significant amount of heat being generated and accumulating in the coil. Therefore, EMF process design involves working with three different problems: 1) propagation of an electromagnetic field through the coil-blank system and generation of pulsed electromagnetic pressure in specified areas, 2) high-rate deformation of the blank, and 3) heat accumulation and transfer through the coil with the cooling system. In the current work, propagation of an electromagnetic field in the coil, blank, die and surrounding air was defined using a consistent set of quasi stationary Maxwell equations applying a corresponding set of parameters for each media. Furthermore, a deformation of the blank driven by electromagnetic forces distributed through the volume of the blank was modeled using a solid mechanics equation of motion and the elastic plastic flow theory. During the discharge of capacitors the process was considered to be adiabatic due to the short duration of the pulse, so a heat transfer during the discharge time was neglected. The distribution of electric current density integrated during the discharge process defines the increase of temperature at every element of the coil. The distribution of temperature was calculated as a function of time using the energy conservation law.

Keywords:

Sheet metal forming, Electrical discharge, Tool, Cooling

1 Introduction

Pulsed electromagnetic forming (EMF) uses a coil as tooling, which is employed to generate electromagnetic pressure on the blank during a high-voltage electric discharge of capacitors. Typically, the coil is subjected to the same pressure as the blank. In the

case of a multi-turn coil, additional forces may be generated between the turns of the coil since the clearance between the turns is usually similar to the clearance between the coil and the blank. Typically, the amount of electric energy involved in an EMF process is largely defined by the required deformation of the blank. This electric energy pulse also generates a significant amount of heat after each discharge, which accumulates in the coil over time. In order to implement the EMF technology in high-volume production, an efficient cooling system providing stable temperature of the coil needs to be developed. Therefore, we need to work with three different problems: 1) propagation of electromagnetic field through the coil-blank system and generation of pulsed electromagnetic pressure in specified areas, 2) high-rate deformation of the blank, and 3) heat accumulation and transfer through the coil taking into account the cooling system.

These predictive tools are also a necessary element to design a coil system that would be feasible for high-volume production of automotive panels - specifically of exterior panels with class A surfaces. These predictive numerical models of electromagnetic elastic-plastic forming and heat transfer processes are all important elements for a model that designs a process that works the first time and tolerates high-volume production.

2 Theoretical approach

Propagation of an electromagnetic field within a coil-blank-die-air system can be defined by quasi stationary Maxwell equations:

$$\nabla \times \mathbf{H} = \mathbf{j}, \quad (1)$$

$$\mu_a \frac{\partial \mathbf{H}}{\partial t} = -\nabla \times \mathbf{E}, \quad (2)$$

$$\mathbf{j} = \sigma(\mathbf{E} + \mu_a \mathbf{v} \times \mathbf{H}), \quad (3)$$

Where \mathbf{H} is magnetic field intensity; \mathbf{j} is current density; \mathbf{E} is electric field intensity; σ is electric conductivity; \mathbf{v} is velocity; μ_a is magnetic permeability of the medium under consideration. For short duration processes we assume $\mu_a = 4\pi \times 10^{-7}$, H/m. In EMF processes the coil and die are almost stationary, while the blank is quickly accelerated; therefore, the equation for magnetic field intensity \mathbf{H} can be transformed in Lagrangian form. Based upon equations (1)-(3), the equation for vector \mathbf{H} can be written as:

$$\mu_a \frac{\partial \mathbf{H}}{\partial t} = -\nabla \times \left(\frac{1}{\sigma} \nabla \times \mathbf{H} - \mu_a \mathbf{v} \times \mathbf{H} \right), \quad (4)$$

or transformed in integral form

$$\mu_a \frac{d}{dt} \int_V \mathbf{H} dV - \mu_a \oint_S \mathbf{v} \mathbf{H} \cdot d\mathbf{s} = \oint_S \frac{1}{\sigma} d\mathbf{s} \times (\nabla \times \mathbf{H}). \quad (5)$$

Dynamic elastic-plastic deformation of a solid can be defined by the following equation:

$$\rho \frac{d}{dt} \int_V \mathbf{v} dV = \oint_S \boldsymbol{\sigma} \cdot d\mathbf{s} + \int_V \mathbf{f} dV, \quad (6)$$

where

$$\mathbf{f} = \mathbf{j} \times \mathbf{B} = -\mu_a \mathbf{H} \times \mathbf{j} = -\mu_a \mathbf{H} \times (\nabla \times \mathbf{H}), \quad (7)$$

$\boldsymbol{\sigma} = p\mathbf{I} + \mathbf{S}$ is stress tensor; ρ is density; p is pressure; \mathbf{S} is deviator part of stress tensor,

$$p = K \left(\frac{V}{V_0} - 1 \right), \quad \mathbf{S} = G\mathbf{B}_D, \quad (8)$$

V and V_0 are actual and original volumes respectively; \mathbf{B}_D is the deviator part of the left Cauchy-Green tensor \mathbf{B} ; $\mathbf{B} = \mathbf{F} \cdot \mathbf{F}^T$; $\mathbf{F} = d\mathbf{x}/d\mathbf{X}$ is deformation gradient tensor; \mathbf{x} is the vector of actual location; \mathbf{X} is the vector of original location; K and G are bulk and shear modulus respectively.

The Von Mises yield criterion is used to describe the elastic limit:

$$-J_2(\mathbf{S}) \leq \frac{\sigma_y^2}{3}, \quad (9)$$

where σ_y is current plastic flow stress (depends on strain and strain rate).

The energy conservation law is employed in the following form:

$$\frac{d}{dt} \int_V c_V T dV = \int_V P dV + \oint_S \lambda \nabla T \cdot d\mathbf{s}, \quad (10)$$

where T is temperature; $P = \frac{\mathbf{j}^2}{\sigma}$ is power generated in the form of heat while an electric current is running through the coil and blank because of an active resistance of their materials. The System of equations (5)-(10) represents a full formulation of the problem. The electromagnetic forming machine serving as a generator of pulsed currents can be represented as R-L-C circuit. An electric current running into a coil-blank system as a boundary condition can be defined by the following equations using an explicit integration procedure.

$$\frac{d(LI)}{dt} + RI = U, \quad (11)$$

$$C \frac{dU}{dt} = -I, \quad (12)$$

At every time step we solved equations (11) and (12) and, based upon the defined value of current I , calculated its density in the coil $\mathbf{j} = I/S$ at the boundary cross-sections

where S is square of the cross-section of the coil. Boundary conditions for \mathbf{H} were calculated based upon the electric current I employing the following equation:

$$\oint_{\mathbf{l}} \mathbf{H} \cdot d\mathbf{l} = I. \quad (13)$$

where \mathbf{l} is a contour around the lead cross-section. Assuming that \mathbf{H} is directed tangential to the cross-sections of the incoming and outgoing leads and uniform along their contours, \mathbf{H} can be defined by (13) as

$$H = I/L, \quad (14)$$

where L is the perimeter of the lead of incoming or outgoing cross-sections.

In this formulation the propagation of an electromagnetic field in the coil, blank, die, and surrounding air was analyzed using the same set of equations applying a corresponding set of parameters for each media. Since there is a number of metallic parts in close vicinity to the system (coil bandage, die, clamping system, etc.) we believed that an external screen would be an appropriate boundary condition. According to this assumption, the following boundary condition can be applied to the surface of the screen:

$$\mathbf{H} = 0. \quad (15)$$

This system was solved numerically using the finite volume method, based on a non-orthogonal regular Lagrangian mesh which consists of 8 node cells, shown in Figure 1a. Each cell consists of 24 tetrahedrons. An example of tetrahedron "abcd" is shown in Figure 1. Vertex "b" is in the center of the cell's face, while vertex "c" is in the center of the cell. A control volume V is linked to every node of the mesh. According to the described discretization, each cell contributes to the control volume [2], as shown in Figure 1b.

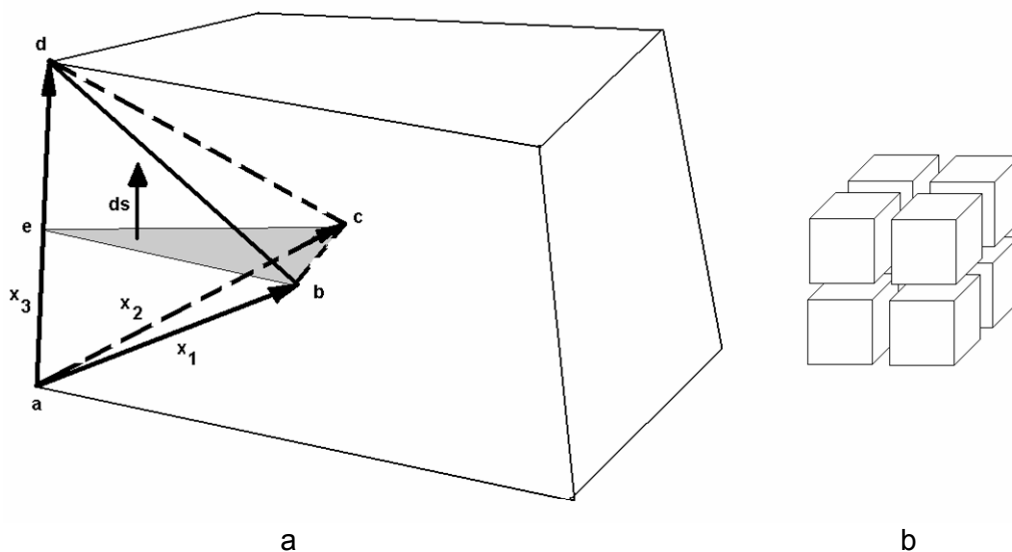


Figure 1: Numerical mesh in the control volume method

Equation (5) was solved by integrating the first term in its left side by time:

$$\mu_a V \frac{\mathbf{H}^{n+1} - \mathbf{H}^n}{\Delta t} = \mu_a \oint_S \mathbf{vH}^{n+1} \cdot d\mathbf{s} + \oint_S \frac{1}{\sigma} d\mathbf{s} \times (\nabla \times \mathbf{H}^{n+1}), \quad (16)$$

where V is the volume restricted by the surface S ; $d\mathbf{s} = \mathbf{n}dS$; \mathbf{n} is the external normal to S . Surface integrals in other terms of (5) are being defined as a sum of surface integrals along the k surfaces of the control volume surrounding this node, as shown in Figure 1.

$$\mu_a \oint_S \mathbf{vH}^{n+1} \cdot d\mathbf{s} + \oint_S \frac{1}{\sigma} d\mathbf{s} \times (\nabla \times \mathbf{H}^{n+1}) = \sum_{(k)} \left(\mu_a \oint_S \mathbf{vH}^{n+1} \cdot d\mathbf{s} + \frac{1}{\sigma} d\mathbf{s} \times (\nabla \times \mathbf{H}^{n+1}) \right), \quad (17)$$

The values of $(\nabla \times \mathbf{H})$ and \mathbf{vH} are considered to be constant for each element of the mesh. The increments of \mathbf{H} in each node of the mesh depend on the values of \mathbf{H} in the elements surrounding the node under consideration. In three-dimensional formulations we have a 27 point pattern. The actual position of the vertices of the tetrahedral element at time t was denoted by \mathbf{x}_a , \mathbf{x}_b , \mathbf{x}_c and \mathbf{x}_d . Let \mathbf{x}_i ($i = 1,2,3$) be the right-hand set of vectors directed along any three different ribs of the tetrahedron (Fig. 2a). Vector \mathbf{H} was assumed to be a linear function from radius-vector \mathbf{x} in the element:

$$\mathbf{H} = \mathbf{A} \cdot \mathbf{x} + \mathbf{b} \quad (18)$$

\mathbf{A} was defined by the following system

$$\begin{aligned} \mathbf{H}_1 &= \mathbf{A} \cdot \mathbf{x}_1 \\ \mathbf{H}_2 &= \mathbf{A} \cdot \mathbf{x}_2 \\ \mathbf{H}_3 &= \mathbf{A} \cdot \mathbf{x}_3 \end{aligned} \quad (19)$$

Then we obtained

$$\mathbf{A} = \mathbf{H}_i \mathbf{e}_i \cdot (\mathbf{x}_m \mathbf{e}_m)^{-1}. \quad (20)$$

Using the transformation (20), we defined the approximation of $\nabla \times \mathbf{H}$ in the element

$$\nabla \times \mathbf{H} = \frac{\partial}{\partial \mathbf{x}} \times (\mathbf{A} \cdot \mathbf{x} + \mathbf{b}) = \frac{\partial}{\partial x_k} \mathbf{e}_k \times \mathbf{H}_i \mathbf{e}_i \cdot (\mathbf{x}_m \mathbf{e}_m)^{-1} = \mathbf{x}^k \times \mathbf{H}_k, \quad (21)$$

where

$$\mathbf{x}^1 = \frac{\mathbf{x}_2 \times \mathbf{x}_3}{\mathbf{x}_1 \cdot (\mathbf{x}_2 \times \mathbf{x}_3)}, \quad \mathbf{x}^2 = \frac{\mathbf{x}_3 \times \mathbf{x}_1}{\mathbf{x}_1 \cdot (\mathbf{x}_2 \times \mathbf{x}_3)}, \quad \mathbf{x}^3 = \frac{\mathbf{x}_1 \times \mathbf{x}_2}{\mathbf{x}_1 \cdot (\mathbf{x}_2 \times \mathbf{x}_3)}. \quad (22)$$

A numerical procedure of integration (6)-(8) simulating the elastic-plastic deformation of the blank was discussed in [1,2]. An explicit integration procedure was considered to be

suitable to simulate a high-rate deformation process. The electromagnetic part of the problem was solved using an implicit integration procedure. In order to reduce computational time for practical three-dimensional problems, the integration step in the EM problem was n times larger than in the elastic-plastic problem. The parameter n was defined for each practical case in order to represent the changes in the distribution of the electromagnetic field appropriately. The clearance between the coil and the blank was expanding due to the acceleration of the blank driven by repelling electromagnetic forces. Therefore, the mentioned clearance was re-meshed periodically.

3 Results of the numerical simulation

The objective of a numerical simulation was to assist the development of the efficient coil for the restrike operation of a preformed aluminum blank. Preliminary experimental results indicated that sometimes electromagnetic pressure is applied in the area where plastic deformation was not expected. Therefore, specific attention was paid to the distribution of electromagnetic pressure and the formation of the blank. Parameters of the discharge were taken from the experimental results produced using a commercial EMF machine and a single turn coil made of aluminum alloy 6061-T6. The maximum energy of the machine was 22.5 kJ with a maximum charging voltage of 15 kV. Two cases were simulated: $C=0.0002F$ and $C=0.00025F$. Results of the numerical simulation are shown in Figure 2.

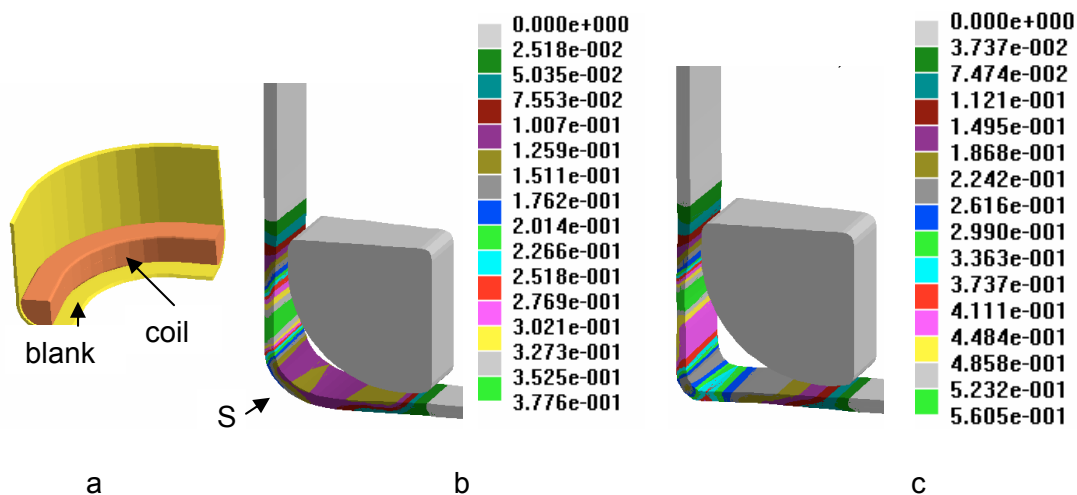


Figure 2: Results of the numerical simulation of EMF restrike of preformed aluminum blank 1mm thick made of AA6111-T4: a) initial position of the blank and coil; b) position of the blank and distribution of plastic strains in it after the EMF process with the following parameters $C=0.0002 F$, $U=15 kV$; c) similar results for the bank of capacitors $C=0.00025 F$

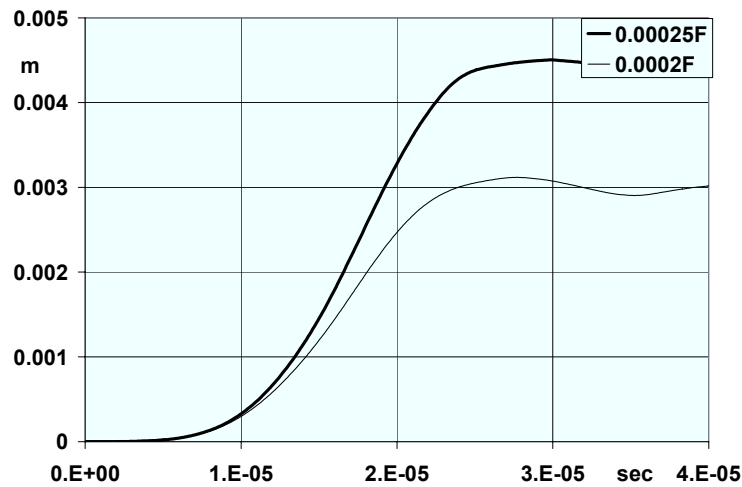


Figure 3: Radial displacements of the point S vs time for $C=0.0002F$ and $C=0.00025F$

Analyzing the strain distribution for two cases, we can conclude that for the case of $C=0.00025F$ maximum plastic strains were at the formability limit. A displacement of the point S of the blank, located on the external surface of the blank, facing the die and belonging to the bisecting line of the angle being formed, is shown in Figure 3.

As it was mentioned before, special attention was paid to the distribution of density of electric currents and pressure applied to the blank. For the single turn coil described above these distributions are shown in Figure 4.

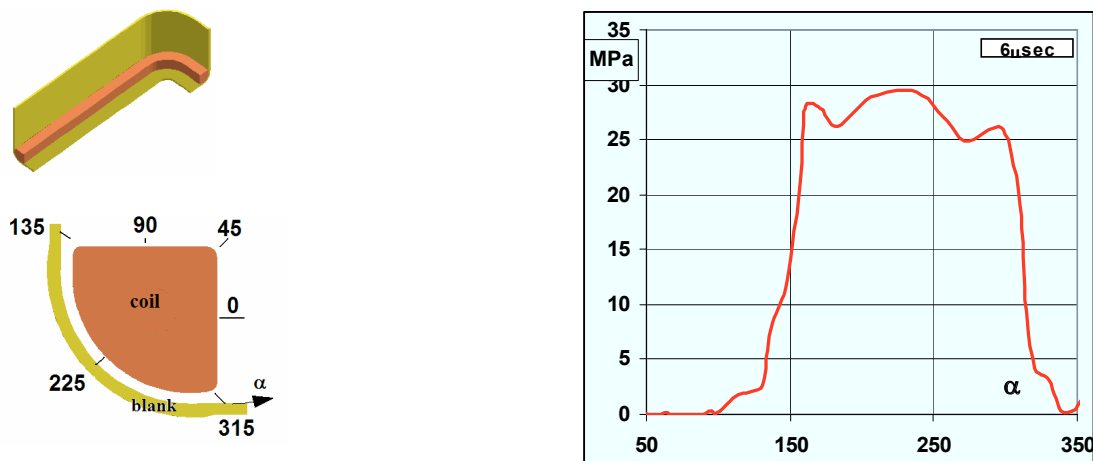


Figure 4: The coordinate system of a cross-section of the coil (left) and the distribution of EMF pressure at the time moment $t=6 \mu\text{sec}$ after the beginning of the process (right)

An attempt was made to simulate a composite coil which consists of two parts – a copper layer facing the blank and a steel layer reinforcing the coil against electromagnetic pressure. As a result (Figure 5), the density of electric currents in the area of the cross-section facing the blank can be significantly increased. Even though a composite coil is expected to

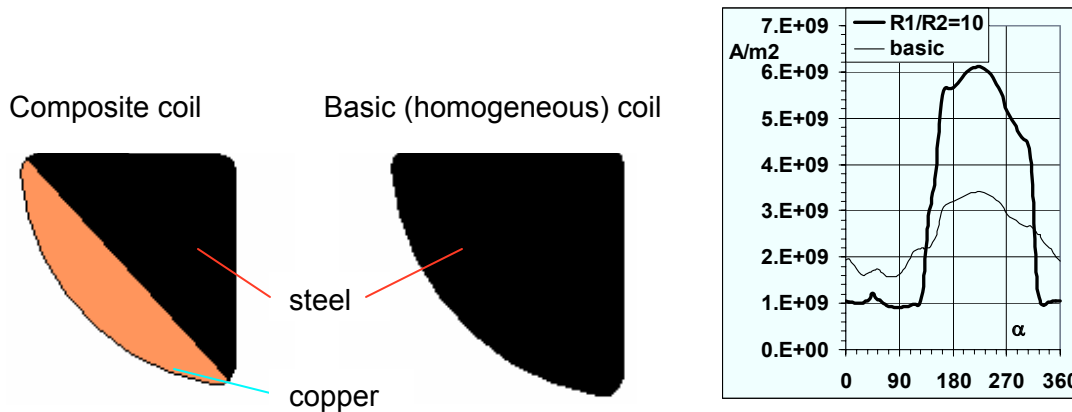


Figure 5: Results of the numerical analysis of the composite (copper-steel) coil compared to the basic coil fabricated from steel

be more expensive due to the necessity of the layers joining, it may provide better efficiency, higher strength, and less heat accumulation compared to the coils made of a homogeneous material. Special attention should also be paid to the accumulation of heat in the coil in high-volume EMF processes. As in well-known induction heating processes, electric currents in EMF processes tend to run within a relatively thin layer due to the “skin” effect. Later, the heat is redistributed due to the material thermal conductivity. After every new discharge of the machine additional heat is being generated in the skin layer. This heat generation process can be considered to be adiabatic. To define the amount of heat, electric current density was integrated over the duration of the process and produced the distribution of heat due to the active resistance of the coil material (Figure 6). Further heat flow and temperature redistribution happens within a much longer period of time between pulses of the EMF machine. In production conditions unloading of the stamped blank and loading of the next blank would take place between two discharges.

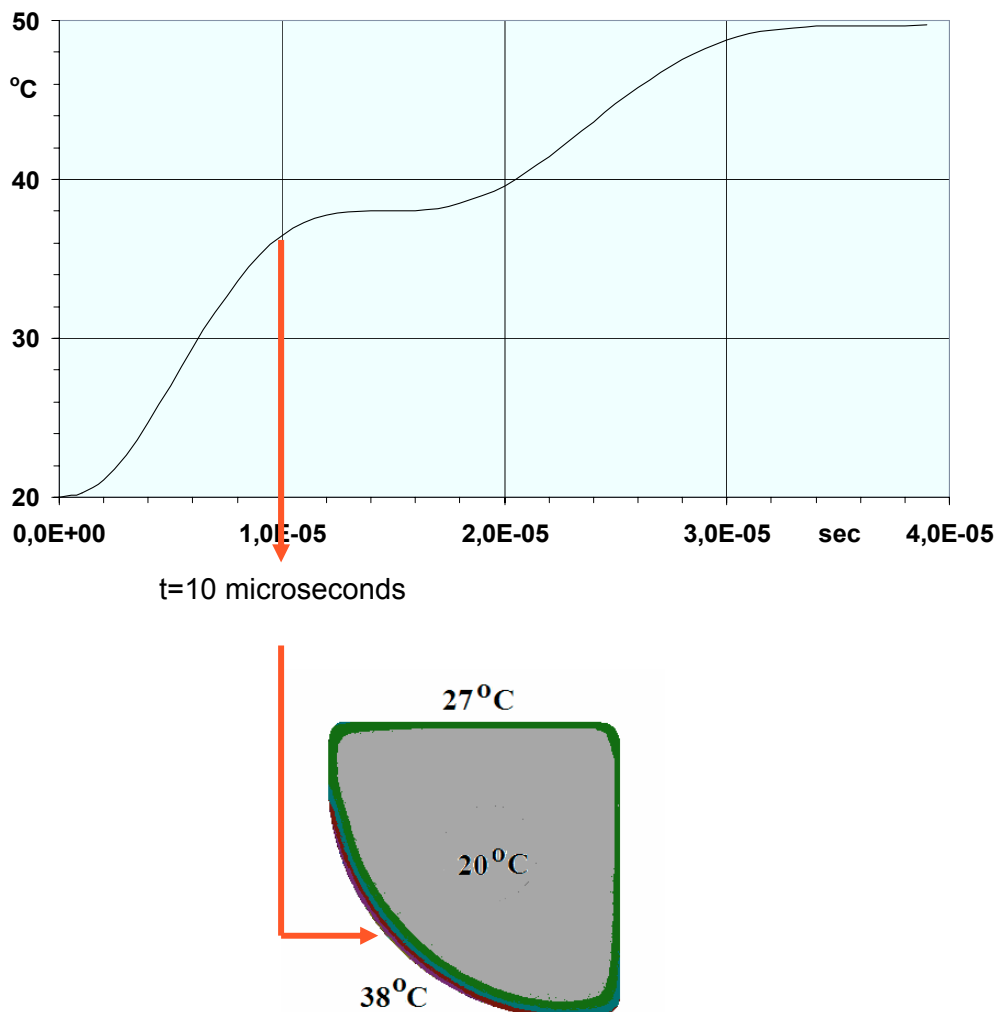


Figure 6: Distribution of maximum temperature vs time (upper graph) and distribution of temperature in the coil cross-section (lower graph) during one discharge of the EMF machine

In order to develop an efficient cooling system of the coil, a numerical model of the heat transfer through the coil was developed. This model took into account the air-cooling system which provided the air flow along the coil surface. The parameter which was expected to drive the cooling process was the velocity of air flow. According to the results of numerical simulation shown in Figure 7, the air flow with the speed of 20 m/sec could accomplish a satisfactory result since it provides a stabilization of the temperature of the coil. Slower air flows of 15 and 10 m/sec provide a stabilization at higher temperatures, which may not be appropriate for the insulation material and may reduce the durability of the coil.

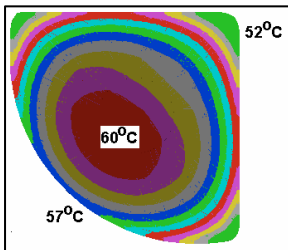
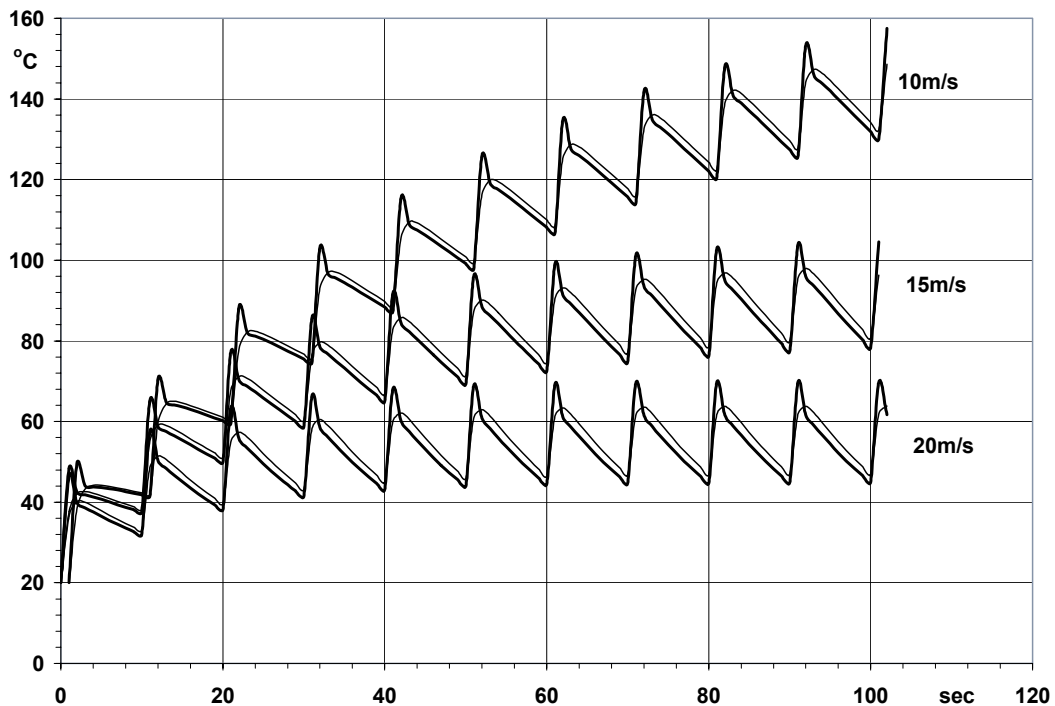


Figure 7: Maximum (thin lines) and average (thick lines) temperatures of the coil vs. time for production rate of 360 parts/hour with velocity of air flow of 10, 15, and 20 m/sec

An experimental study of the cooling process was conducted using the flat coil made of steel and micarta insulation plates, illustrated in Figure 8. Air flow was delivered through the slots between the micarta plates in the corners of the coil. The spiral surface was insulated from the blank by a thin plate of insulation material. The air flow was directed between the spiral surface and insulation plate so it would provide cooling of the working surface of the coil where a maximum amount of heat is generated. In this experimental study the energy of the process was specified based upon the energy allowing to form cones made of 1 mm thick aluminum sheet into the die with open round windows 76 mm in diameter, shown in Figure 8. In a durability study the aluminum blank was replaced by an aluminum plate which was clamped to the coil with four bolts, as indicated in Figure 8. An experimental study showed that after 5000 discharges the coil did not have any signs of damage and, therefore, has the potential to be used in high volume production conditions.

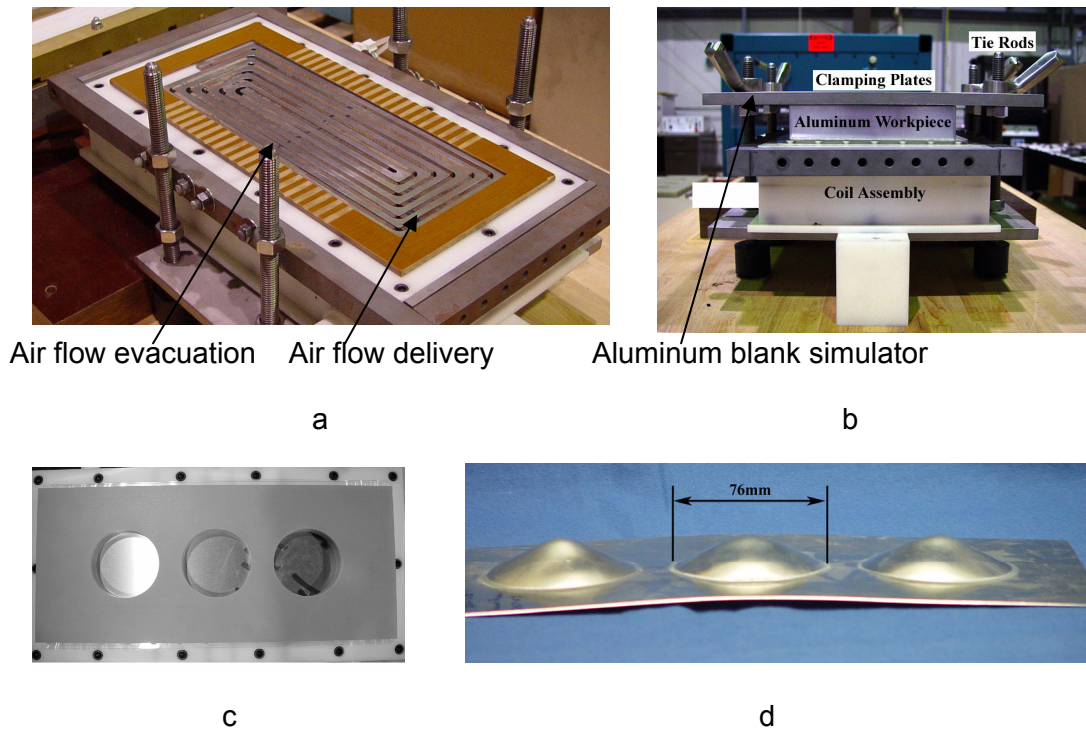


Figure 8: Experimental fixture employed for an experimental study of coil durability and heat accumulation: a – flat coil with air cooling system; b – assembled fixture for testing coil durability; c - experimental die for estimating the energy of the coil testing procedure; d – formed blank

4 Conclusions

This work developed numerical models that describe three critical elements of the EMF process: 1) propagation of an electromagnetic field through the coil-blank system and generation of pulsed electromagnetic pressure in specified areas, 2) high-rate deformation of the blank, and 3) heat accumulation and transfer through the coil with an air-cooling system. The process models provide the capability to analyze EMF restrike processes from the perspective of coil design, blank deformation, and cooling systems for the coil.

References

- [1] Bessonov, N.; Golovashchenko S.: Numerical Simulation of Pulsed Electromagnetic Stamping Processes. Proceedings of the 1st International Conference on High Speed Forming , Dortmund, Germany, 2004, p.83-91.
- [2] Bessonov, N.; Song, D.: Application of vector calculus to numerical simulation of continuum mechanics problems. Journal of Computational Physics.167/1,1999, p.22-38.

Electromagnetic Springback Reshaping

E. Iriondo¹, B. Gonzalez¹, M. Gutierrez¹, V. Vonhout², G. Daehn²,
B. Hayes³

¹ LABEIN Technological Research Center, Automotive Unit. Derio, Spain

² Department of Materials Science & Engineering. The Ohio State University.
Columbus, OH. USA

³ Aerojet. Sacramento, CA. USA.

Abstract

Electromagnetic forming is an impulse-based forming technique where high dynamic pressure is distributed to conductive materials by pure electromagnetic interaction. The aim of this paper is to present how springback can be controlled when the EMF technique is used as a second corrective step; bringing formed parts to the desired final shape by means of magnetic impulses in critical areas of the formed components. This analysis is based on the results of two experimental studies. In the first, the selected preformed specimen shape is the L-shape bent part of HSS DP600, in 0.8 and 1.95 mm thickness, and Aluminium Alloy 5754, in 1 and 2 mm thickness. The second geometries are two rocket nozzle panels made of a thick but soft copper alloy. While the geometry and the material are the similar, the first approach of this work was developed using smaller panels (about 30 cm long) and the full size (about 1 m long), in order to study the behaviour of the material and the approximate energy levels required to scale up the full size panels. Overall this study shows EM forming can have a potent effect in controlling springback.

Keywords:

Springback, Residual stress, Electromagnetic forming

1 Introduction

In sheet metal forming, control of elastic recovery of springback is a key in achieving the desired shape. Since all materials have a finite modulus of elasticity, plastic deformation is always accompanied by some elastic recovery when the load is removed. If the stress distribution is non-uniform, distortion will occur in load removal. The amount of springback is defined as the deviation between the final shape at the end of the loading stage and the shape after the part is removed from the forming die. The effect of unloading is equivalent

to adding elastic strain distribution to the fully plastic stress state. After unloading, the tension side of the bend has a significant compressive residual stress at the surface and there is residual tensile stress on the inner surface, as shown in Figure 1 [1].

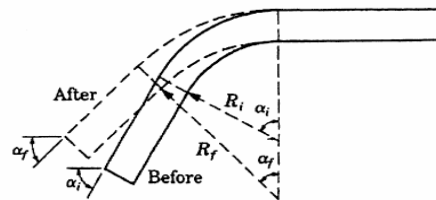


Figure 1: Schematic of loaded and unloaded stages of a bending process.

The focus was to analyze the behavior of springback when EM pulse or pulses are applied in an area with residual stresses. The first study selected the optimum energy levels to correct and quantified the deviations from the target geometry. The second study made a comparison between the hot sizing and the EM sizing of the panels.

The basic idea here is that electromagnetic forming can place an impulse in a desired location (set by coil configuration) and of a given energy (set by bank charging). This can be used to put a controlled and reproducible amount (small) of plastic deformation in the part. Either with a single or multiple shots, this can be used to correct for springback.

2 Springback on L-shape bent parts of AA 5754 and DP 600.

The process and materials were chosen based on the use of the AA and HSS in the automotive industry. The most basic operation of its structural components is based on the L-shape section. The objective is to understand the basic behavior of residual stresses under the impulse loading.

2.1 Experiment layout

The experiments have been carried out using electromagnetic impulses as a corrective step after the parts have been shaped by traditional metal forming. The selected specimen shape is the L-shape. The experimental part of the study started with the bending of DP-600 (0.8 and 1.95 mm thickness) and AA-5754 (1 and 2 mm thickness) of 170x100mm blank dimensions. After the bending stage, the springback angle of all L-shape parts was measured.

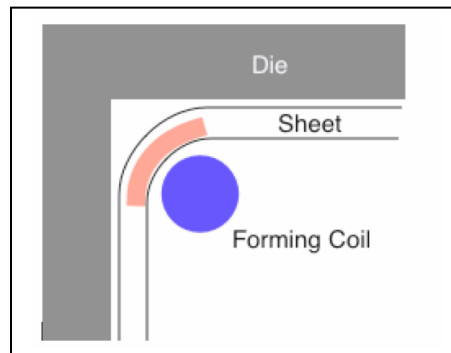


Figure 2: Schematic diagram of the use of an EM actuator in the corner section.

The capacitor bank used for discharging the energy through the coil has been the standard 16 kJ Maxwell-Magneform [2] (8.3 kV @ 16kJ), capacitance of 426 μ F and inductance of 140 nH. A single turn copper coil, positioned in the bending radius area, has been used for the development of these experiments. The specimen is positioned between the coil and the 90° steel die. After the EM pulse, the 90° die was removed and the final angle of the specimen was measured with an angle gauge. The return path was located below the forming coil to induce a return current in the sheet. This gives reasonable efficiency because there is a full eddy current path.

Input parameter of the process is the energy level discharged by the capacitor bank to each specimen and the output is the final angle between bent part's walls after the EM impulse.

2.2 Springback behaviour. Results

Springback has been corrected in both materials and thickness. The minimum energy discharged, in order to reach 90° between parts walls, was 0.8kJ for the 1mm thickness AA5754 and the maximum, 14.4 kJ, for the 1.95mm DP600.

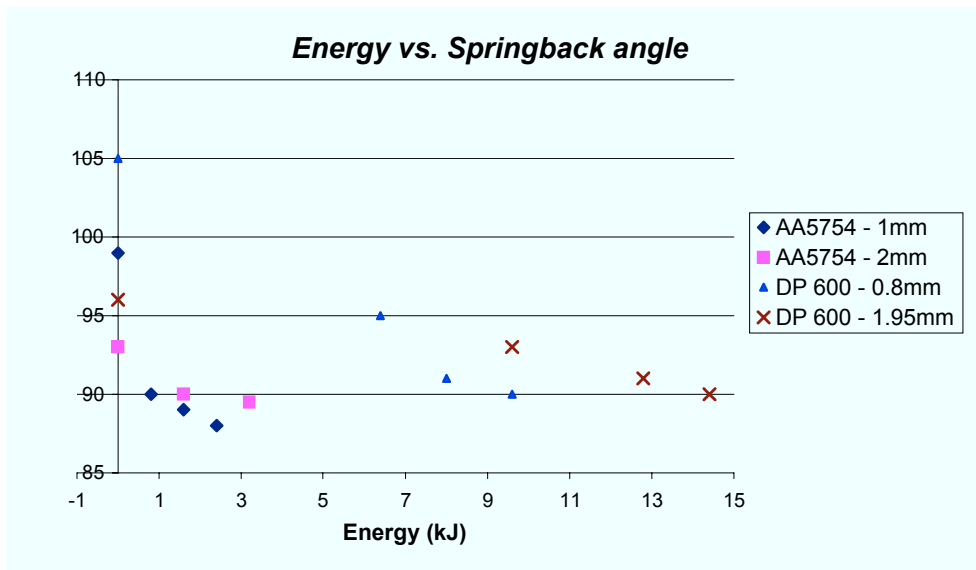


Figure 3: Springback angles vs. different input energy levels.

As shown in Fig 3, when we increased the impulse energy to AA5754 specimens of both thickness, from the optimum threshold level quoted before, we found over bending of the specimens as result. The method provides good control on springback angles. Details from the summary in Figure 3 are shown in Figures 4-6.

Some parameters involved are crucial for determining the efficiency of the process and a very important one in the EMF technique, uncommon for the rest of forming processes, is the electrical conductivity of the specimen material. In our case, the conductivity of AA5754 is higher than the DP600. The higher the conductivity of the material, the lower is the inductance resulting in higher EM force and better material forming. Other important factors affecting the final results are usual in sheet metal forming: the strength of the material (4 times higher for the DP-600) and the thickness.

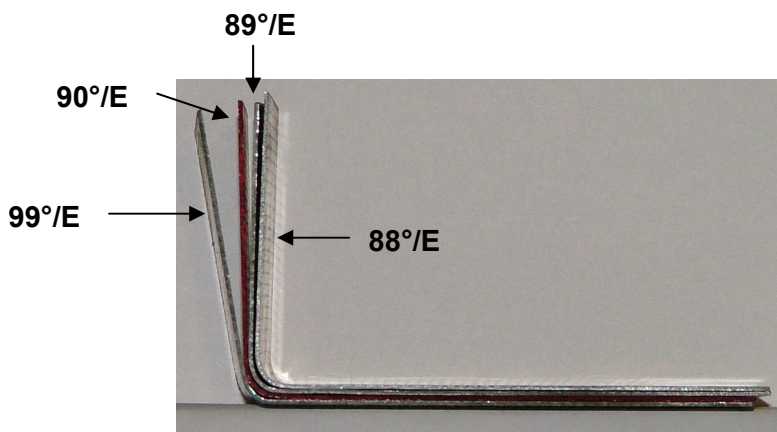


Figure 4: Springback angle changes, with different energy levels, of AA5754 of 1mm thickness.

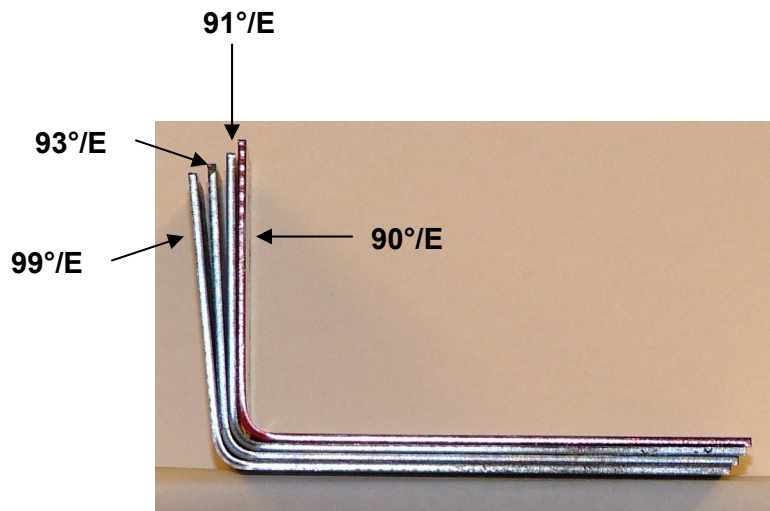


Figure 5: Springback angle changes, with different energy levels, of DP600 of 1.95mm thickness.

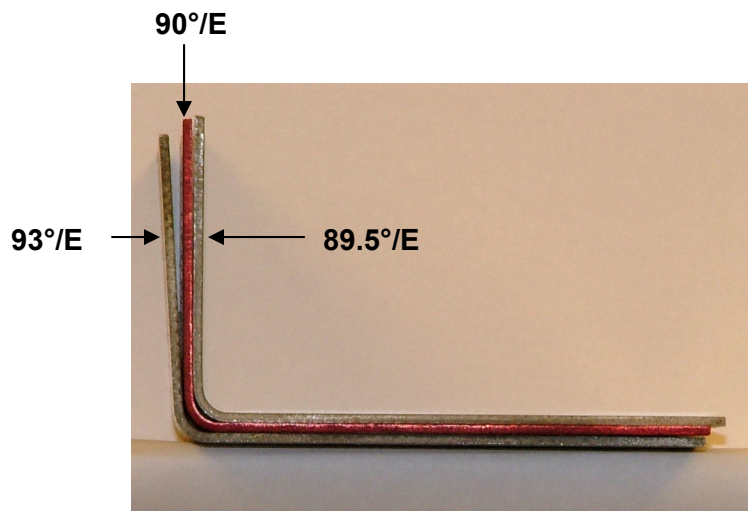


Figure 6: Springback angle changes, with different energy levels, of AA5754 of 2mm thickness. 90°.

3 Reshaping of a Rocket Nozzle Panel

This second experimental study follows to a real industrial problem of dimensional accuracy. Aerojet has developed process for stamping and assembling soft copper alloy rocket nozzle segments and springback leads to unacceptable final dimensions without

hot sizing, which causes internal microcracking. The final aim of this study is to compare the geometrical accuracy obtained by the hot sizing and the electromagnetic pulses.

EM reshaping was carried out with first a sub-sized panel and second a full-size panel. The same capacitor bank and protocol were used for both the subsize and full size panels.

3.1 Experimental Layout



Figure 7: Photograph of the coil used to reshape the full-sized liner.

The capacitor bank used for discharging the energy through the coil has been the 48 kJ Maxwell-Magneform [2] (10 kV @ 48kJ). A multi turn copper coil has been used for the development of these experiments. The specimen, with blue impression on the die surface to impact, is positioned between the coil and the target geometry die, which are simulating the work press on the close stage. After the EM pulse, the panel was removed from the tooling, and the specimen was positioned on a mold with target dimension. The impression blue marks on the panel, which indicate the pressure distribution, and the dimensional error assessed by feeler gauge, are the output.

3.2 Small nozzle

The corrective impulses applied, by a multi turn coil to this component of about 300mm long, 6mm thickness and 1.6 kg in weight, had a different character at this experimental development. If in the previous works the objective was to find the minimum energy level for correcting the deviation in one shot, in this case multiple shots of the same energy were carry out.

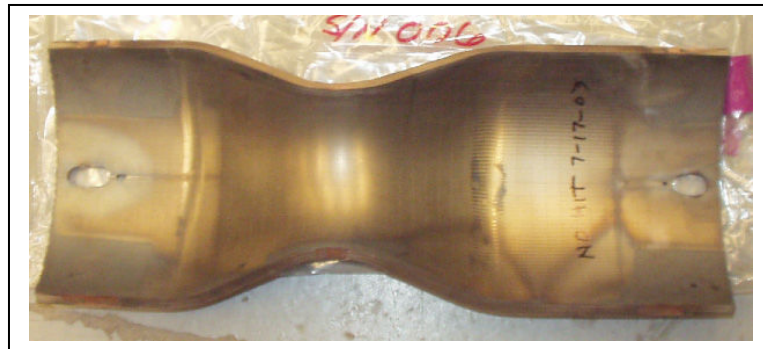


Figure 8: Small rocket nozzle panel.

Input parameters of this work are the energy level discharged by the capacitor bank and the standoff distance between the panel and the die to impact. The output is the dimensional deviation from the target geometry.

The best result was obtained by 10 repetitions of 4.8kJ and the standoff factor isn't going to be an input on the full size experiments because equivalent shape registry has been available with and without it.

3.3 Full size nozzle reshaping

During this phase of the study, a multi turn coil was applying EM pulses to the full size rocket nozzles of 1m length, 10mm thickness and 19 kg in weight. Equal to the previous phase, at this case multiple shots of the same energy were carry out

Energy levels required for improving the results of the hot sizing are below 15 kJ applied in multiple forming discharges between 3 and 10.

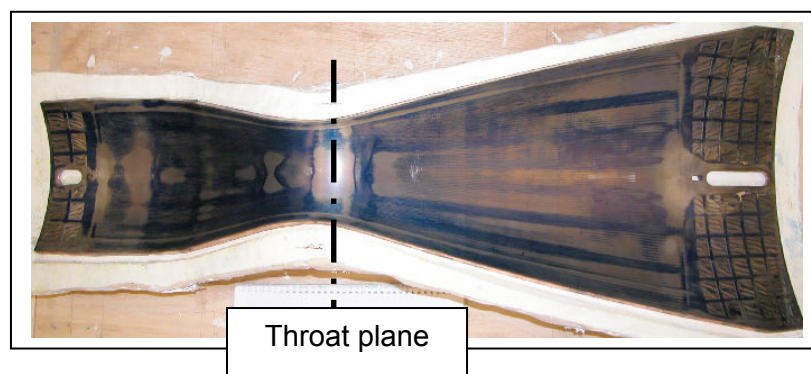


Figure 9: Full size rocket nozzle panel. Showing impression blue imprint after forming

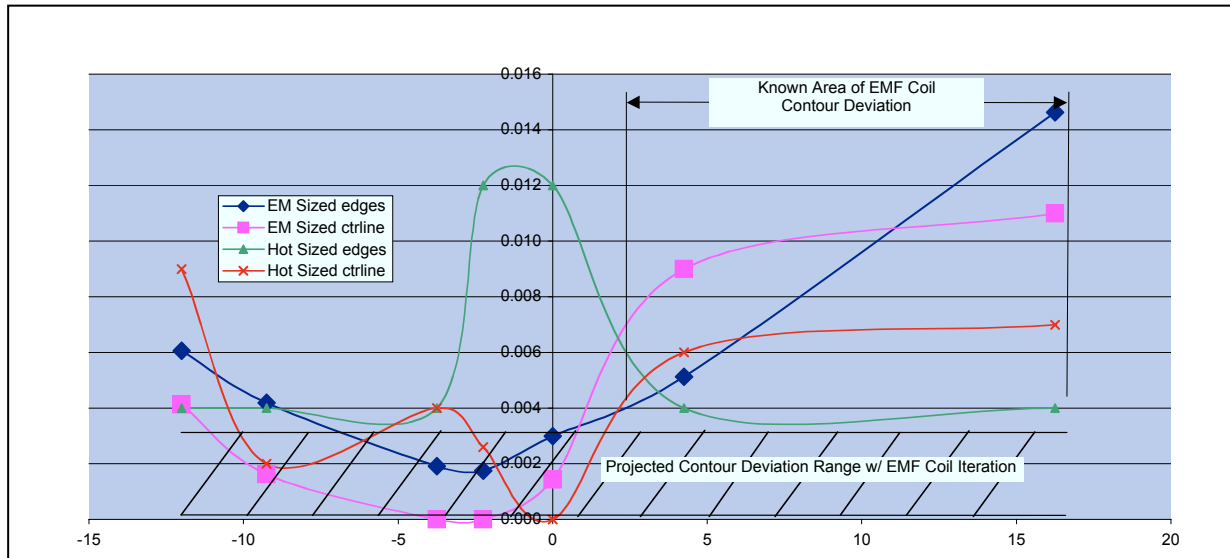


Figure 10: Comparison of EM and hot sizing results.

The comparison plotted in Fig 9 as a dimensional summary of this study, shows the geometrical improvement reached using EM pulses: eliminating the undesired effect of microcracking and obtaining a more uniform surface.

4 Conclusions

The analysis of our experimental results confirms that Electromagnetic forming is an effective technique for eliminating the springback.

- The most important “new” parameter to take into account on this process is the conductivity of the material
- This innovative technique opens an alternative to the springback correction
- The tooling for this method is relatively simple and very flexible even to couple it into an industrial configuration.

References

- [1] *Hu, J.; Marciniak, Z.; Duncan, J.:* Mechanics of Sheet Metal Forming, Butterworth Heinemann. 2002
- [2] www.magneform.com

Process Investigation of Tube Expansion by Gas Detonation*

M. Weber¹, M. Hermes², A. Brosius², C. Beerwald², G. Gershteyn³,
H. Olivier¹, M. Kleiner², F.-W. Bach³

¹ Shock Wave Laboratory, Aachen University, Germany

² Institute of Forming Technology and Lightweight Construction, University of Dortmund,
Germany

³ Institute of Material Science, University of Hanover, Germany

Abstract

The present paper deals with the expansion of tubes by direct application of gas detonation waves, i.e. the gas is both pressure medium and energy source. After an introduction to gas detonation forming, measurements of the motion process and the internal pressures are presented. Results of free expansion and of forming into a die are thoroughly studied and compared to the results of quasi-static burst tests and hydroforming. Using pure aluminum Al99.5 and a medium strength alloy AlMgSi1, expansions by 25 % and 20 % respectively are obtained. A simulation delivers details on the deformation process and specially prepared probes of high-speed tension tests give new insight into metallographic material behavior at different strain rates.

Keywords:

Forming, Tube, Shock wave

1 Introduction

Gas detonations have already been applied to sheet metal forming processes and their use in tube forming has also been suggested in the past [17-18], but their potential for the latter purpose and the interactions between the medium, the workpiece, and the tool system have not yet been studied in detail. Besides the well-known advantages of high-speed forming processes, which are higher degrees of formability for various materials and the reduction of press forces due to mass inertia of the tool system [16], the application of gas detonation offers a clean combustion, an easy automation, and less safety regulations compared to the use of solid explosives. Additionally, little need for external apparatuses, high flexibility, and a significant potential for steel forming compared

to electromagnetic forming, have to be mentioned as advantageous attributes. This opens up new possibilities, especially for the expansion of tubes in a die with a great variation of the cross section geometry over the longitudinal axis.

The process of gas detonation and the development of shock waves are theoretically and experimentally explored as far as possible. But the process of expanding tubes by gas detonation causes additional interactions where the constitutive effects influencing the deformation process are still unknown. Therefore, fundamental investigations are necessary in order to offer the possibility for a target-oriented process design in the future. Nowadays, numerical simulation by means of Finite-Element-Simulation (FEA) is an established tool for such tasks. But due to the coupled field problem, containing a mechanical, fluid mechanical, and a chemical part, the simulation and optimization by FEA is not as easy as for conventional forming operations. Therefore, it is important to analyze the process by observing the effects of the detonation on the workpiece with a combined strategy of complementary experimental work and numerical simulation. Thereby, the identification of essential process parameters to achieve a satisfying forming result is a major objective. First results of this fundamental research work are shown in the following.

2 Process principle of gas detonation

The process principle is shown in figure 1. A detonation wave, which is one of the macroscopic manifestations of an explosion, propagates axially through the tube at a stable velocity exceeding multiple sound velocity. Using a pre-compressed stoichiometric mixture of oxygen and hydrogen, the wave speed is about 3,000 m/s, the wave thickness is less than a millimeter, and the pressure immediately behind it exceeds approx. 20 times the initial pressure p_0 of the gas mixture.

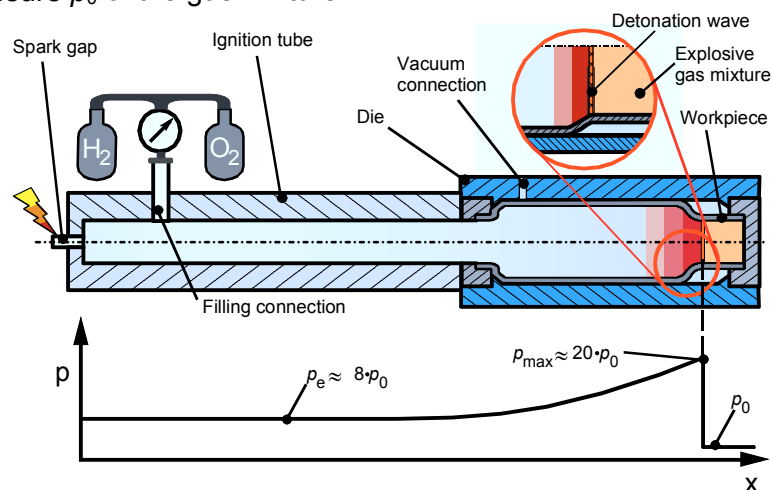


Figure 1: Process principle and experimental set-up

A detonation wave is a joint complex of shock waves and reaction zones, implying shock waves that are strong enough to induce an immediate chemical reaction. The shock compression of the gas is sufficient to cause an instantaneous reaction of the mixture, which quickly leads to a chemical equilibrium. The released heat sustains the wave. The wave is followed by an expansion wave – called Taylor-Expansion – implying a pressure

drop to a value that is approximately 8 times larger than the initial pressure when the gas settles again. The rate of this pressure drop is inversely proportional to the time that has passed since the initiation of the wave. In cylindrical cavities like in tubes this expansion takes about the same time that the wave has already propagated as from its position of initiation. So, the shape of the pressure pulse can be influenced by the length of the whole system, including the ignition tube. The initiation of a detonation wave requires a powerful igniter or a long tube for the transition of the initial deflagration through various states of turbulent combustion. In this work, exploding wires are used for the initiation. When the wave is reflected at the end of a tube it returns as a shock wave without any chemical reaction, leading to an additional pressure jump in the proximity of the reflecting wall. The amplitude of this wave diminishes rapidly, but it reflects several times between the tube ends before its energy is fully dissipated.

3 Experimental set-up and measurement techniques

The set-up for the experimental investigation of free forming processes is shown in figure 2.

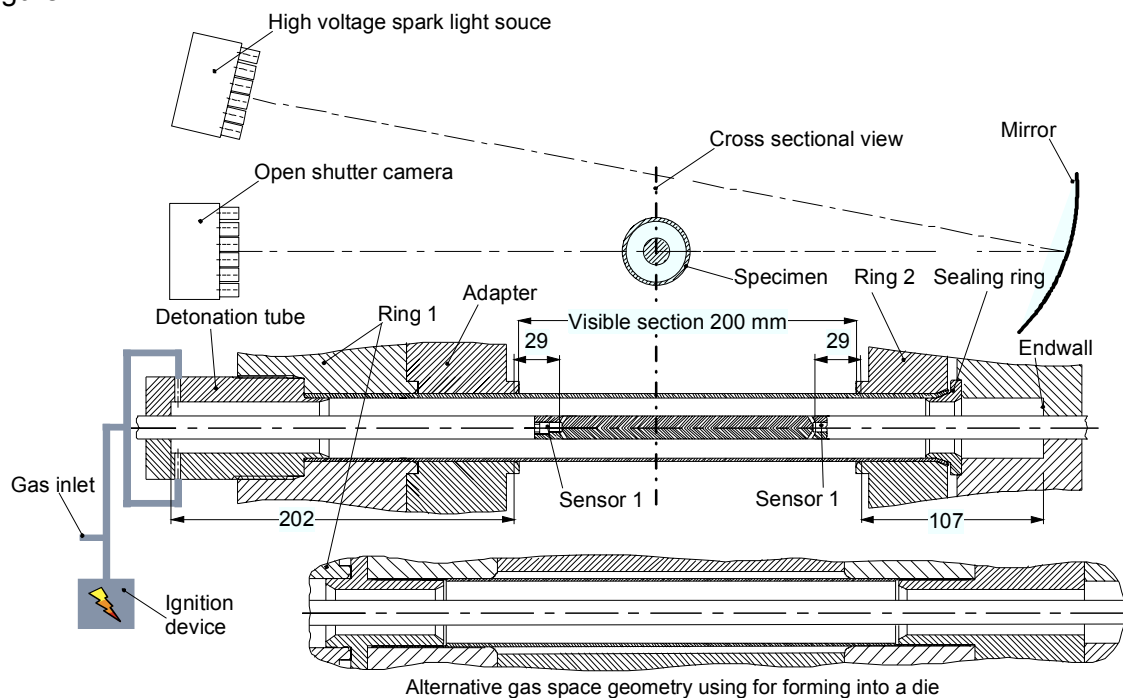


Figure 2: Experimental set-up for the measurement of acting pressure and workpiece deformation in the case of free tube expansion as well as forming into a die

The whole apparatus is filled with gas mixture, which was prepared using mass flow controllers, mixed in a pipe connection, and filled into the evacuated apparatus. The gas detonation is initiated externally by a capacitor discharge through an exploding constantan wire. It enters the detonation tube through the gas inlet and rapidly spreads over the whole cross-section. For an estimation of the pressure pulse width it can be assumed that the wave was initiated at the left end wall. The reason for igniting externally and keeping the detonation tube short was to enable the installation of a coaxial pressure probe that is

fixed in both end walls. It contains two piezo-electric sensors (type Kistler 603B for pressures up to 20 MPa and type Kistler 601H for higher pressures), oriented coaxially and connected to the gasspace by radial bores. The specimen is a tube with 40 mm diameter, 2 mm wall thickness, and with a length of approx. 380 mm. It is internally sealed at both ends. At the right end the tube is clamped while at the left end the tube is capable to deform in axial direction. Ring 2, which consists of two halves, is fixed to Ring 1 by means of rigid frame (not shown in Fig.2), so that the clamping force does not press the specimen axially. The adapter is only a ring to ensure the length of the forming section.

The specimen can be replaced by a thickwalled rigid tube with the same inner diameter to obtain pressure profiles at prevented expanding for comparison. For forming experiments a die (described in Section 6) was installed in the position of the visible section as well as its two neighbouring rings, the sensors being positioned again at 179 and 29 mm upstream of the forming section's end.

The used high speed camera type DRELLO is a 24-axis open shutter system capable of framing frequencies up to 10 MHz, using a conventional still film. The series of high-voltage sparks is triggered by the first pressure sensor. Images were scanned and processed to obtain contour plots of the specimen. As free forming only allows for relatively low initial pressures and forming rates, walls can be installed optionally around the specimen to prevent the motion and, thus, enable the observation of the start phase of faster motion processes. During the operation they are fixed in the above mentioned frame.

3.1 Measurement of acting pressure profile

The pressure records shown in Figure 3 are obtained for free expansion of Al99.5 specimens as well as for prevented deformation at similar initial conditions. Time zero is defined by the original signal at sensor 1, which triggers the camera.

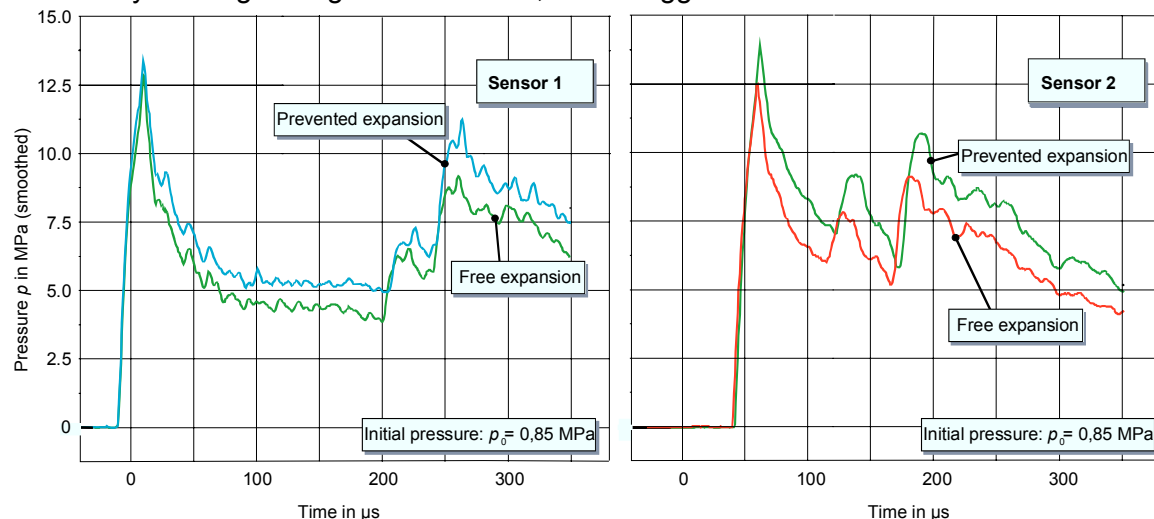


Figure 3: Smoothed pressure records at sensor 1 (left) and 2 (right) from experiments with prevented and free forming of an Al99.5 tube at 0.85 MPa initial pressures. Time zero is defined by the original signal at sensor 1, which triggers the camera

For the prevented deformation experiment the aluminum specimen has been replaced by a thick-walled rigid tube with the same inner diameter. The measured signals have been

smoothed with a half-width of 10 μs to eliminate extreme oscillations. Therefore, the true detonation pressure peak, whose theoretical value is 17 MPa, can not be fully resolved. The second pressure rise is caused by a partial reflection of the detonation wave at the right sealing ring (compare figure 2) and the third one is caused by the reflection at the end wall. Obviously, the expansion of the tube leads to a faster and further pressure drop following the detonation wave because of the increasing volume.

3.2 Measurement of the tube expansion process

Examples of the free expansion process of an Al99.5 specimen are shown in Figure 4. Figures 4a and b show an original high-resolution photograph and the generated contour plots for an initial pressure of 0.85 MPa. The plot that corresponds to the time of 121 μs after passage of the detonation wave at the first sensor almost shows the final shape. In the diagram also the wave front positions at 21 μs and 41 μs are marked. The highest radial velocity of 45 m/s is reached at the end of the free section, shortly before the second sensor shows a second pressure rise (Figure 3), which corresponds to the reflected wave.

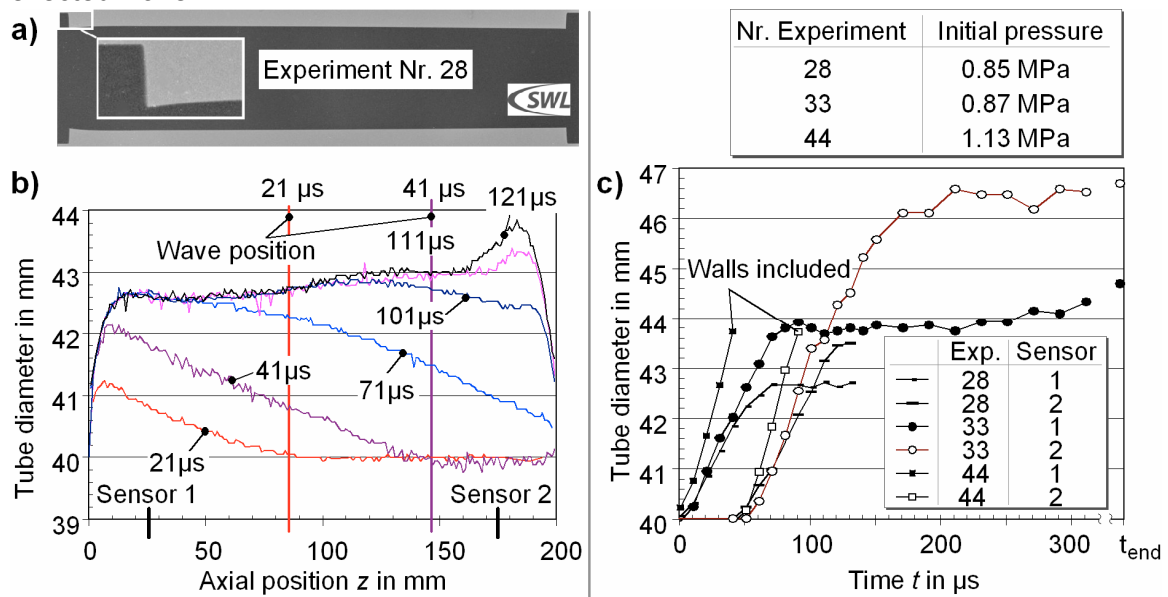


Figure 4: Expansion process of Al99.5 specimens (a) photograph and quad enlargement showing image quality, (b) contour plots and corresponding wave positions, (c) local course of expansion at the axial positions of both pressure sensors

An increase of the pressure to 0.87 MPa led to a much larger expansion, which did not stop within the observation time (see Figure 4c, Exp. 33); the finally reached diameters are given at the right ordinate. This plot shows the maximum achievable diameter of the free expansion of Al99.5 specimens because attempts to increase the initial pressure to 0.9 MPa or more lead to workpiece failure. At the axial position of the first sensor the expansion practically stops at a time of approx. 80 μs . At the second sensor position the expansion is faster. It starts to decelerate when a similar magnitude of expansion as at the first position is reached (at 100 μs), but one frame later it accelerates again due to the currently passing reflected shock wave.

Additionally, Figure 4c shows the start phase of the motion for an initial pressure of 1.13 MPa, where further motion was hindered by the optional supporting walls. A maximum radial velocity of 65 m/s corresponding to a strain rate of 3000 s^{-1} was reached at the position of pressure sensor 2. In these experiments a maximum strain of about 25 % has been achieved. In order to investigate the deformation process numerically, finite element simulations are done, described in the following.

4 Simulation of deformation

As mentioned above, the simulation of this high speed forming process deals with several physical problems which are strongly coupled. Since the consideration of the fluid mechanical field with the usually used Euler formulation will cause numerous numerical problems due to moving boundaries (tube wall) the simulation is uncoupled in a first step. To calculate the pressure time history, a one-dimensional shock tube simulation tool, called KASIMIR developed by the SWL, is used. This tool solves the thermodynamic equilibrium of a shock wave in combination with the chemical reaction using a Riemann solver [3]. The achieved results from this code are applied as time-dependent input in a mechanical simulation using the Finite-Element-Code MSC.MARC in combination with several user-subroutines developed at the IUL. In order to consider the mass inertia effect, the implicit NEWMARK time integration schema is used [3]. To apply the time- and location-dependent force boundary, an ALE-strategy was implemented using a second finite element mesh only for an interpolation of the input data. Fig. 5 shows the two meshes and the relevant boundary conditions.

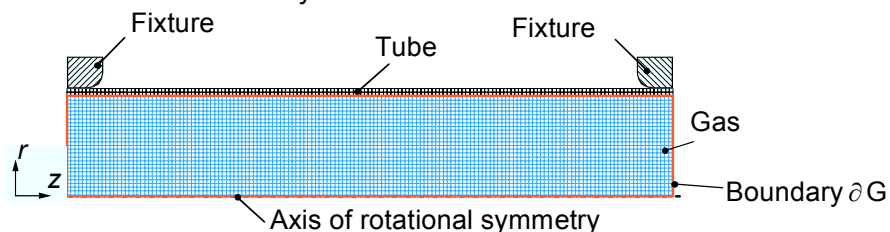


Figure 5: FE-Model using an ALE strategy

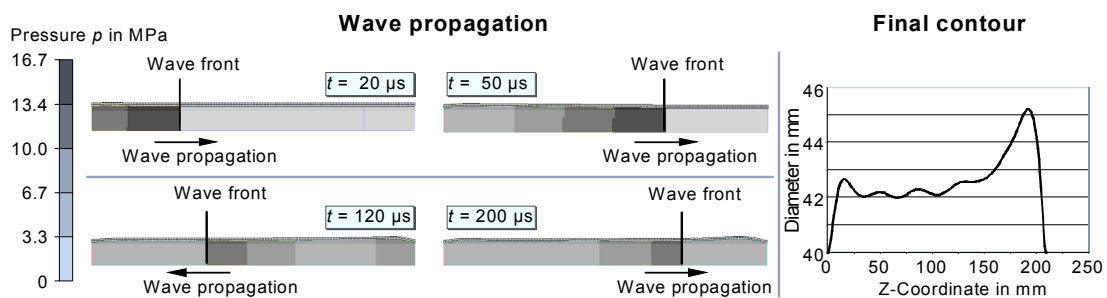


Figure 6: Simulation results of a free forming operation

Fig. 6 shows a result of this simulation strategy by means of a free forming operation. An aluminum tube (Al99.5) with a length of 210 mm, an initial diameter of 40 mm, and a wall thickness of 2 mm was considered. The initial pressure was chosen to $p_0 = 0.85 \text{ MPa}$. Starting with the initiation of the detonation wave, the left end of the tube wall remains for

several microseconds in the initial position until the deformation begins because of its mass inertia. The elastic-plastic deformation process of this initially accelerated tube region is finished when the detonation wave reaches the end of the tube. The time delay between the detonation wave and the movement of the tube wall is also obvious in the measurement data of the free forming operation (Fig. 4, time of 21 μ s and 41 μ s).

The wave is being reflected at the end of the tube and pressurizes the already accelerated tube again. The final geometry is achieved after the second reflection of the wave. The whole deformation process has a duration of approximately 200 μ s, which depends on the starting parameters, e.g. the initial pressure and wave speed, of course. The accordance between this simulation and the experiment can be seen by a comparison of the final contour of the tube (compare Fig. 6b and Fig. 11).

Obviously, the qualitative contour is fitted very well, but from a quantitative point of view large deviations are present. Regarding, this it has to be mentioned that the used simulation strategy is only a first approximation of the real procedure because the pressure drop due to forming and the subsequent volume increase is neglected and the material behavior is unknown. Due to the high strain rate the material behavior differs significantly from the one in quasi-static deformation processes [7, 15]. To overcome this deficit, high speed tensile tests are realized by the Institute of Material Science at the University Hanover (IW) in order to identify the relevant effects.

4.1 Investigation of material behavior

The micro-structural changes as a result of deformation can be described by a multiplicity of structure-relevant parameters. Dislocations and grain boundaries have a substantial influence on the dynamics of the forming process [9, 11]. For example, dislocations within a grain show a different behavior as at or near grain boundaries. These differences are caused by the structure and type of the dislocations [10].

Previous analyses of the dislocation movement and the dislocation density changes as well as the analyses of grain boundary migration took place under thermal activation or at low strain and strain rates. The present results of the conducted analyses can serve as basis for the description of the plastic deformation mechanisms at high strain rates in the finite element simulation. The structural changes were examined using aluminum samples. The processes during plastic deformation are related to different dislocation-drag mechanisms [15]. These are influenced by the following factors:

- thermally activated dislocation movement
- energy of dislocation drag
- impurity viscosity
- phonon viscosity
- electron viscosity.

The first three mechanisms are particularly relevant in static tensile tests with the conventional universal testing machines (tension speed of 2 μ m/s to 1,000 mm/min). It is well-known from literature that the mechanism of phonon viscosity is very important at tension speeds of 1 m/s to 1,500 m/s [1].

The processes at the grain boundaries are extraordinarily important as well as the dislocation drag in grains. The grain boundary mobility and its driving strength are the fundamental parameters of the grain boundary slip [13]. The origin of this driving strength has different causes. For most cases the strength results from the differences in the free

energy of the adjacent grains. This difference can be caused by the different surface energies, permeabilities, and disorientations of the adjacent grains or by different dislocation densities on both sides of the grain boundary [6]. By a grain boundary slip the deformation energy stored in the dislocations is set free and the energy of the complete system is minimized. One of the most important procedures for the analysis of the dislocation and the grain boundary structure is the light-microscope etching pit method. Numerous methods were already suggested for the determination of the defect structure in aluminum. At the Institute of Material Sciences a new etching agent as well as a special procedure were developed on the basis of an etching agent, recommended by Barret and Levenson [3]. Using this procedure, the dissolution speed does not depend on the crystallographic orientation so that the etching speed is evenly distributed on specific crystal faces. This procedure can be used for the determination of changes in the defect structure after the deformation of polycrystalline aluminum. A further application is that it is possible to simultaneously corrode grain boundaries, inner-grain dislocation pits, and grain boundary dislocation pits, using the described etching agent in combination with a certain parameter set for electrolytic polishing. The reproducibility of the metallographically determined etching pit density can be determined by comparison with trans-electron-microscopy (TEM) measurements of the dislocation density. The sample material was commercially pure polycrystalline aluminum (99.5%), which was tested in the form of rolled strips of 1 to 4 mm thickness and 70 mm width and of cast slabs of 7 mm thickness and 70 mm width. The tension test samples were prepared from strips and slabs, homogenized for 72 hours at the temperature of 580°C, and were cooled down along with the furnace.

After the tension tests with different test speeds the samples were examined by light-microscopy, parallel to the tension direction (longitudinal axis). The samples for the etching pit method were electrically polished in electrolytes (20% perchloric acid, 10% butylglycol, and 70% ethyl alcohol) with a voltage of 25 V and a flow rate 5 for a duration of 10 s. An etching agent was used for the corrosion (Content: 10% HF, 30% H₂O, 45% HCl and 15% HNO₃). In the following figures examples of the etched microstructure with testing speeds of 2 μm/s (Fig. 7), 1 m/s (Fig. 8) , and 6.5 m/s (Fig. 9) are shown. Figure 8a shows that the etching pit arrangement corresponds to a dislocation structure after deformation, whereas the original grain boundaries are marked by pit-free seams. At lower strain rates the dislocation density inside the grain is higher than at increased strain rates, whereas at increased strain rates the dislocations gather at the grain boundaries. (Fig. 8a).

At the test speed of 6.5 m/s (Fig. 9a) particularly many dislocation seams have been formed at or moved to the grain boundaries and the grain boundaries are stretched significantly in tensile direction. The grain boundary slip mechanism and the dislocation movement are both strongly dependent on different strain rates. The changes of the dislocation structure are stronger at increased forming speeds.

The highest tension rate occurs near the fracture zone of the samples and, accordingly, in these areas both aspects of the changed plastic deformation mechanism can be observed best. Here, the following effects can clearly be seen:

- increased dislocation density inside the grains (Fig. 8b)
- increase and redistribution of grain boundary dislocations (Fig. 9b)
- formation of dislocation seams at the grain boundaries (Fig. 9b).

It can be summarized that the analysis shows a strong influence of the strain rate onto the deformation mechanism, causing a different hardening behavior. Therefore, a strain rate dependent material law has to be applied during the finite element simulation in order to improve the quality of simulation. Another important aspect regarding the material behavior during the forming process using gas detonation is the sudden temperature rise. During the process several hundred degrees of Celsius are present at the surface of the deformable structure, but only for a very short duration. To give an advice whether this effect has to be incorporated into the hardening law or not, additional experimental investigations have to be done using an infrared camera measuring system with high-speed option.

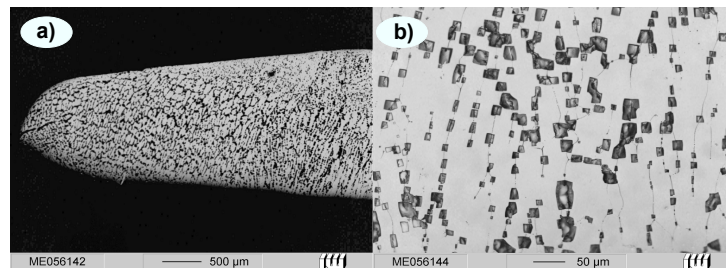


Figure 7: Micrograph of tensile specimen from tensile test with a speed of 2 μm/s

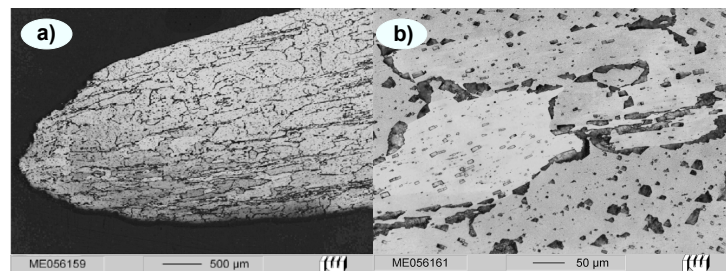


Figure 8: Micrograph of tensile specimen from tensile test with a speed of 1 m/s

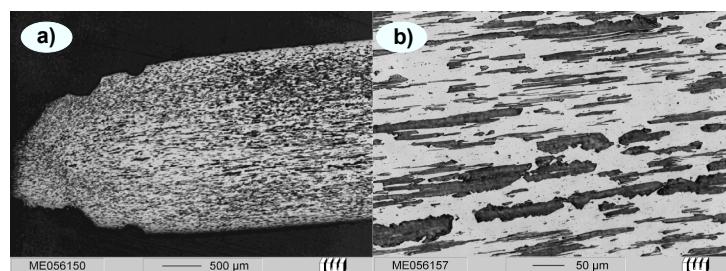


Figure 9: Micrograph of tensile specimen from tensile test with a speed of 6.5 m/s

5 Gas detonation and quasi-static burst tests in die-less forming

Investigations of the free forming process with Al99.5 tubes are necessary to understand the process coherences and to have e.g. the option of optical measurements. The application of the industrial less significant material Al99.5 is interesting for the material investigation to avoid the influence of added alloys.

5.1 Roundness and wall thickness

Before it is possible to use roundness and wall thickness measurements to identify the differences between the two processes the initial state of the specimens is determined. Roundness and wall thickness tests show a good quality of the cross-section geometry of the Al99.5 tube material. The tests were carried out on a CMM and showed that the wall thickness variation is less than 0.2 % and the roundness deviation comes to 0.1 %.

The gas detonation specimens under investigation were made at an initial pressure of 0.85 MPa. The static burst tests were made for the contour measuring at water pressure of approx. 6 MPa to obtain nearly the same diameter as in the measured areas of the gas detonation experiments.

To locate essential properties of the process, e.g. the influence of the higher strain rates on the material, a comparison between expansions by static pressure is essential. A special device was realized at the IUL in order to implement burst tests under static pressure conditions. By the application of a pressure sensor and inductive linear transducers it is possible to indicate the maximum pressure and the according diameter of the expanded tube.

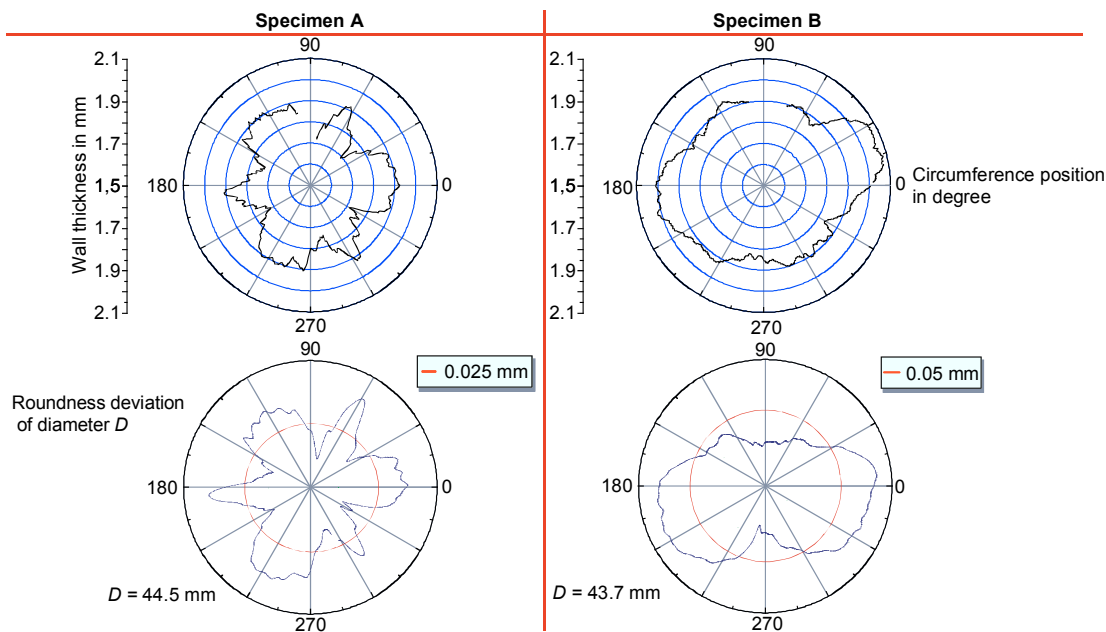


Figure 10: Wall thickness and roundness of the Al99.5 tubes after the gas detonation expansion (specimen A) and water pressure expansion (specimen B)

The specimen A in Figure 10 shows exemplarily the symmetric arrangement of the thicker locations of the wall thickness in the tube formed by gas detonation. They are also present in the roundness diagram because of the same striking peaks on the circumference. This shows that the final deviation from a circular tube cross-section can be partially ascribed to the local thinning of the wall thickness. This means that the good roundness quality of the tubes before the process remains the same. This aspect is caused by the mass inertia forces of the tube walls during the process that stabilize the process in a way that necking is shifted to later deformation states.

The cross-sections of the static burst test specimens (example specimen B) have unsymmetrical and inhomogeneous properties. A reason is the starting necking-in of weak areas along the circumference. The wall thickness of specimen B is, on the average, thicker than of specimen A after the test with static pressure. This is caused by the fact that the material flows in axial direction during expansion. Contrary, the expansion of specimen A is caused by steady material flow out of the wall thickness. The maximum reachable diameter is the same in both processes. Using Al99.5, a diameter of 47 mm die-less is obtainable.

5.2 Lengthwise contour and hardness measurement

The scanning plot in Figure 11 shows the geometry of a specimen made in the gas detonation device without using a die. The maximum at the right end of the curves in the diagram is caused by the reflection of the detonation wave at the end of the device and its interaction with itself, resulting in a sudden pressure rise (see chap. 3).

As expected, the hardness values in Figure 11 rise proportionally to the diameter of the specimen. The hardness at the non-formed ends of the specimen show an average hardness of 22 HV 5. This correlates with the statistic measuring of the bar stock material. The second period of the process that is generated by the reflection of the detonation wave can be seen as a second forming process, which causes additional strain hardening (see chapter 3). A dependency between strain hardening level (or hardness respectively) and high strain rates could not be observed [14].

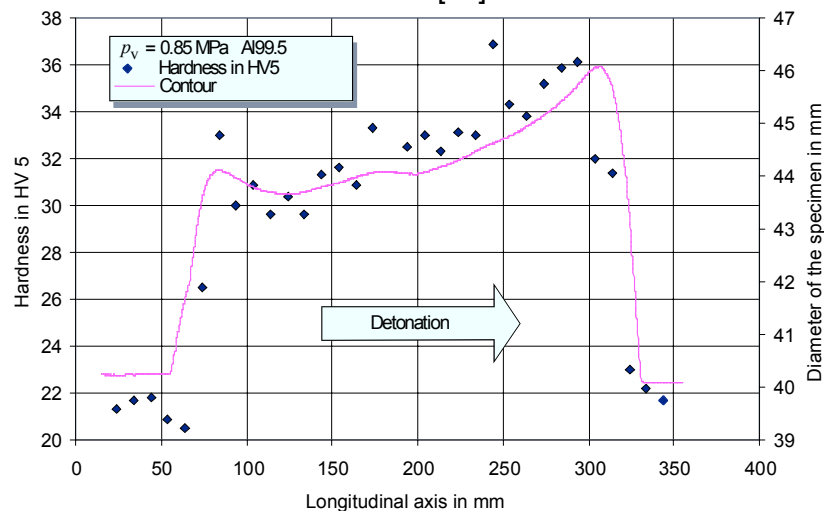


Figure 11: Left: hardness of the Al99.5 tubes versus rising diameters
Right: measurement of the lengthwise contour

6 Gas detonation experiments with die

For an industrial application it is necessary to use a die to realize reproducible workpiece contours. Furthermore, it is important to use more industrial-relevant materials like steel alloys and aluminum with higher strengths which were investigated here in a first approach.

6.1 Realized die construction

For the experiments a contour was used, which is a uniform enlargement of the tube diameter on a length of 300 mm. The cavity is changeable in its diameter by using changeable inserts (Figure 12). With this method it is possible to enlarge the diameter stepwise to find the biggest possible expansion without material failure. The workpiece is positioned between the upper and lower die and the axial sealing is realized on both sides by connexion nozzles. A possibility to generate a vacuum between cavity and workpiece was also realized to avoid negative effects caused by compressed air.

The shortness of the pressure shock in combination with the mass inertia of the tool system makes it possible to realize a forming of tubes with good calibration of details, e.g. small radii without high-performance presses, as they are needed in hydroforming processes [16].

Flexible tool systems were investigated during the experiments to enable an easy change of the dimensions of the workpiece. One example is using dies made of high-strength concrete. The manufacturing of these dies is similar to sandcast, using a turned polymer model. In this paper the experiments only included dies made of tool steel.

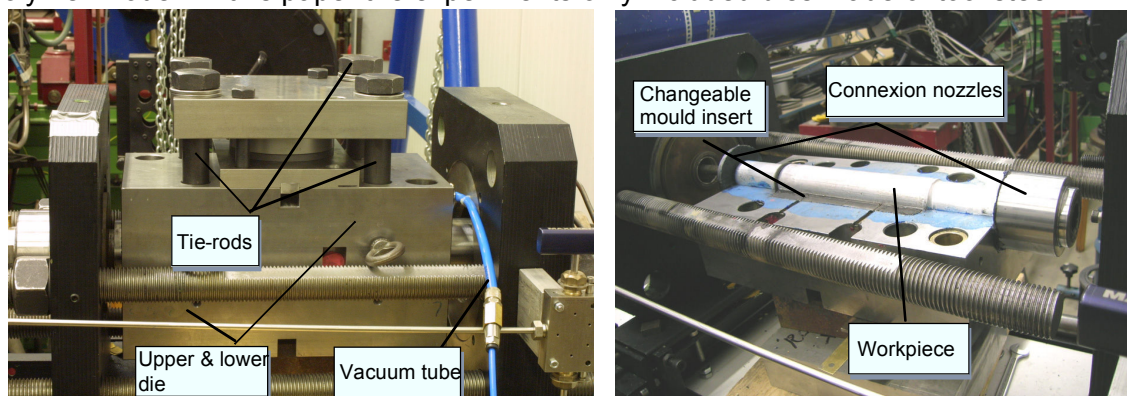


Figure 12: Experimental set-up with die

6.2 Experiments

As workpiece material the medium strength aluminum alloy AlMgSi1 (AA6082) was used. The material was precipitation-hardened at room temperature, resulting in a yield stress of $R_{p 0,2} = 110$ MPa and a tensile strength of $R_m = 205$ MPa. The theoretical elongation at break is 12 % [12]. In the static burst test without a die strain rates of approx. 8 % were achievable.

The experiments show that there is an according minimum pressure essential to realize an acceptable surface during forming operations in different diameters. This was demonstrated by a test made in an insert with a diameter of 47 mm. This is equivalent to 17.5 % tangential strain. At an initial pressure of 3 MPa no failure caused by crack formation was observed, but there were visible characteristic welding seams caused by the extrusion die. Using a higher initial pressure of the gas mixture of 3.5 MPa, the seams were not detectable any more. The high velocity impact of the tube walls levers the surface of the second workpiece. The surface details of the inserts can be found in the surface of the specimens. A strain rate influence of the material caused by the higher

initial pressure, and therefore a higher value of the expansion speed, is shown during the experiments, too (see chap. 3). An indication for this aspect is the noticeable diameter of 47 mm. In the static burst test without die only strains of approx. 8 % were achievable.

The behavior in the insert is shown in Figure 13. This contour measuring shows that a spring back effect can be located in the middle of the workpiece. The higher initial pressure of 3.5 MPa already shows a better calibration.

The maximum possible diameter up to now is 48 mm (Figure 13). This diameter was achieved at a test with an initial pressure of 4 MPa. This implies a tangential strain of 20 %. Here, it needs to be mentioned that there is only a small change in the total length of the workpiece. Before the experiments the length was defined by facing on a turning machine to be 358 mm. After the experiments the length was 357,5mm. So, the deformation is mainly realized by a reduction of the tube wall thickness. The static hydroforming test with the same die construction does not result in a successful workpiece with an insert with a diameter of 45 mm.

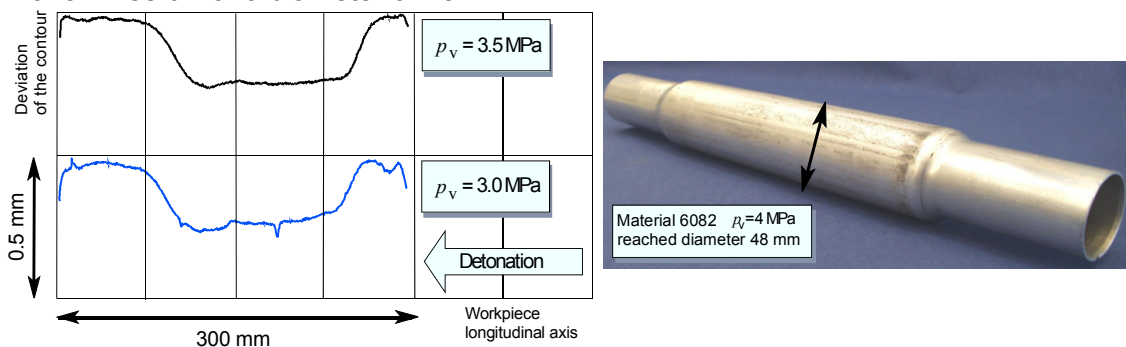


Figure 13: Left: moulding behavior; right: experiment with biggest diameter

To verify the influence of the special conditions in the process of gas detonation, reference experiments using hydroforming are done. A special hydroforming test tool was mounted on the 10MN press M+W BZE 1000-30.1.1 of the IUL.

The die has the same geometric features as in the gas detonation process. Thus, a direct comparison of the two processes is possible. During the experiments it was not possible to expand the AlMgSi1 tubes to a bigger diameter than 44 mm. The failure was caused by crack formation in the bulging of weak areas, mostly near the extrusion seams. It was possible to form Al99.5 workpieces calibrated at 60 MPa by an insert with a diameter of 47 mm.

7 Conclusion and Outlook

The experimental investigations of forming by gas detonation in combination with the numerical results, obtained by the developed simulation tool, have shown an enlargement of formability for the investigated types of aluminum. The accomplished material investigations confirmed this in general and identified the occurring high strain rates during the process as a major reason. Further investigations will focus on the detailed identification of process limits, adaptation of tool construction, application of different alloys, and complementary material analyses for a better understanding of this process combination. Thus, the long-term objective of a process design can be realized.

References

- [1] *Alshitz, V. I.; Indenbom V. L.:* Dynamic dragging of dislocations, Soviet Physics Uspekhi, Volume 18, Number 1, 1975
- [2] *Bartlmä, F.:* Gasdynamik der Verbrennung. Springer, Wien, Austria, 1975.
- [3] *Barrett, C.S.; Levenson, L.H.:* Formation of Etch Pits in Aluminium, Trans. Amer. Inst. Min. Met. Eng., Volume 137, S.112, 1940
- [4] *Bathe, K.-J.:* Finite Elemente Methoden, Springer-Verlag, 2. Auflage, 2002.
- [5] *Burden, R.; Snowden, L.; Hasegawa, K.; Newman, D.; Bauer, D.:* Elektromagnetisches Umformen. In: K. Siegert (Hrsg.), Tagungsband der Tagung „Neuere Entwicklungen in der Blechumformung“ 2000, 24. - 25. Mai 2000 in Fellbach, S. 331–354. Frankfurt, 2000.
- [6] *Czubayko, M.:* Korngrenzenbewegung in Aluminium und Zink, Aachen, RWTH, Diss., Shaker Verlag, 1998
- [7] *El-Magd, E.:* Fließkurvenermittlung im Hochgeschwindigkeitsbereich durch Versuch und numerische Simulation. Tagungsband zur Tagung „Werkstoffprüfung 1991“, 5. - 6. Dezember 1991, Bad Nauheim, S. 305-312.
- [8] *Esser, B.:* Die Zustandsgrößen im Stoßwellenkanal als Ergebnisse eines exakten Riemannlösers. Dissertation, RWTH Aachen, Germany, 1991.
- [9] *Gottstein, G., Shvindlerman, L.S.:* Grain boundary migration in metals: thermodynamics, kinetics, applications. Boca Raton, FL: CRC Press, 385 S., 1999
- [10] *Gottstein, G.:* Physik. Grundlagen der Materialkunde, Berlin Springer, 472 S., 2001
- [11] *Johnston W.G.; Gilman J.J.:* Dislocation Velocities, Dislocation Densities and Plastic Flow in Lithium Fluoride Crystals, Journal of Applied Physics, Volume 30, Number 2, S.129—144,1959
- [12] *Lehnert, W.:* Aluminium Taschenbuch Band 2. Aluminium-Verlag GmbH, Düsseldorf, 1996, p.96-100.
- [13] *Mattissen, D.:* In-situ Untersuchung des Einflusses der Tripelpunkte auf die Korngrenzenbewegung in Aluminium, Aachen, RWTH, Diss., Shaker Verlag, 2004
- [14] *Psyk, V.; Beerwald, C.; Homberg, W.; Kleiner, M.:* Electromagnetic Compression as Preforming Operation for Tubular Hydroforming Parts. Proceedings of the 1st International Conference on High Speed Forming (ICHSF) 2004, S. 171-180
- [15] *Roos, A.:* Fast-moving dislocations in high strain rate deformation, Groningen University Press, S. 29-58, 1999
- [16] *Thomas, W.:* Maschinenphysikalische Grundlagen patronenbetriebener trägheitsverriegelter Pressen zur Hochgeschwindigkeitsumformung, VDI-Verlag GmbH, Düsseldorf, p. 12-13, 1972
- [17] *Vohnout, V. J.:* A Hybrid Quasi-Static/Dynamic Process for Forming large Sheet Metal Parts From Aluminum Alloys. Ph.D. Dissertation of Vincent J. Ohio State University, Columbus, Ohio, USA, 1998.
- [18] *Vovk, V. T.:* Gasexplosion als "Werkzeug" in der Fertigungstechnik. Magdeburg, Univ., Habilitation, 1999.

Efficiency Improvement and Analysis of Changes in Microstructure Associated to a Uniform Pressure Actuator

P. Jimbert¹, A. Arroyo¹, I. Eguia¹, J.I. Fernandez¹, E. Silveira², I. Garuz², G.S. Daehn³

¹ LABEIN -Tecnalia Research Center, Automotive Unit. Derio, Spain

² INASMET-Tecnalia Research Center, Donosti, Spain

³ Department of Materials Science & Engineering, The Ohio State University Columbus, OH, USA

Abstract

During the 1st international Conference on HIGH SPEED FORMING held in Dortmund in 2004 a new forming coil giving significant advantages was presented in the framework of ongoing R&D programs at OSU (The Ohio State University). It established the improvement provided by the return path for currents induced in the workpiece.

To quantify the mentioned improvement, Labein has performed classical cone forming experiments with both configurations and analyzed energetic efficiency using well known alloys, more precisely AA 6016 and 1050. Both deformation mechanisms and contour analysis of the specimens were studied. General purpose multi-turn coils provide pressure distributions not extended to the whole forming area, resulting in zones undergoing significant delay as die the deformation sequence is referred.

As a result, varied deformation patterns can be found along the contour of a cone specimen formed in such way. Firstly, a macroscopic survey of the specimens shows that uniform pressure distributes deformation over the entire formed area during the deformation process. Secondly, the effect on efficiency provided by this new coil concept is focuses not only on the ability for distributing deformation, but on the energy required to create such deformation.

Finally, to validate the whole simulation, the predicted strain level, shape, and internal energy of the workpiece are compared with the experimental specimens. A key point in the validation process is checking the internal energy. It is known that the ratio of stored energy to deformation energy ranges in the order of 30 %. The procedure for the experiments follows this methodology.

Keywords:

Uniform pressure coil, High velocity forming, Pressure distribution.

1 Introduction

The results of a global analysis of the behavior of several magnetic actuator coils are presented here. For this purpose, two coil configurations were proposed as working inductors within the scope of a comprehensive sheet metal forming operation, as it is the cone forming experiment. Basically, when dealing with sheet metal workpieces, solenoid based solutions are the basic options [2], [3], [4], known as flat multi-turn coils like those presented in Figure 1. The main advantages of such coils can be summarized by its ease of fabrication while maintaining a good distribution of magnetic properties along its surface. On the other hand, the so called uniform pressure actuator is presented as an alternative working concept in the field. The strength of this kind of configuration lies in the uniform magnetic pressure field provided within close proximity of the conductor filled surface.

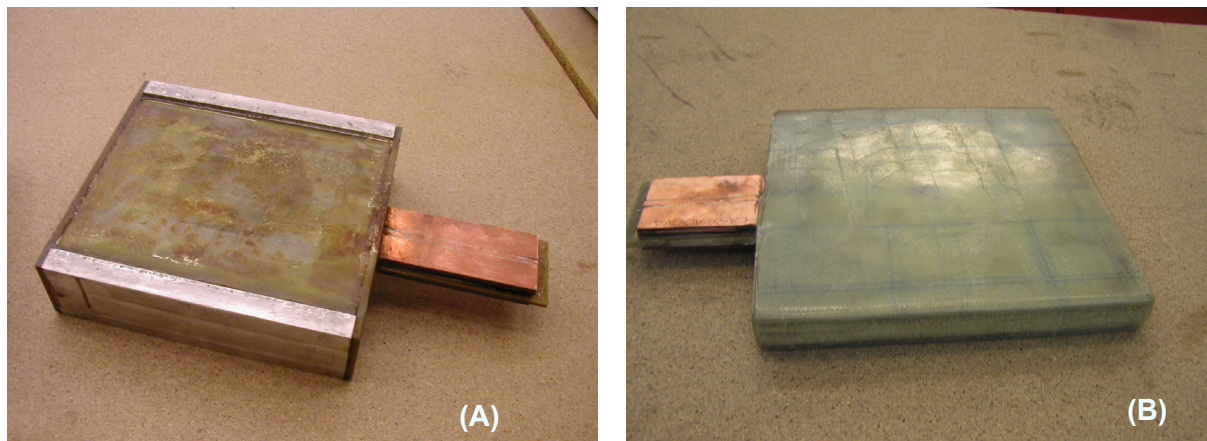


Figure 1: Uniform pressure coil (A) and multiturn coil (B)

1.1 Uniform pressure coil. Basic principles.

The working principle of the uniform pressure coil is presented in Figure 2. An outer conducting channel, electrically insulated with respect to the central core where the primary winding is placed, is incorporated, allowing for an extended circulating track for induced currents.

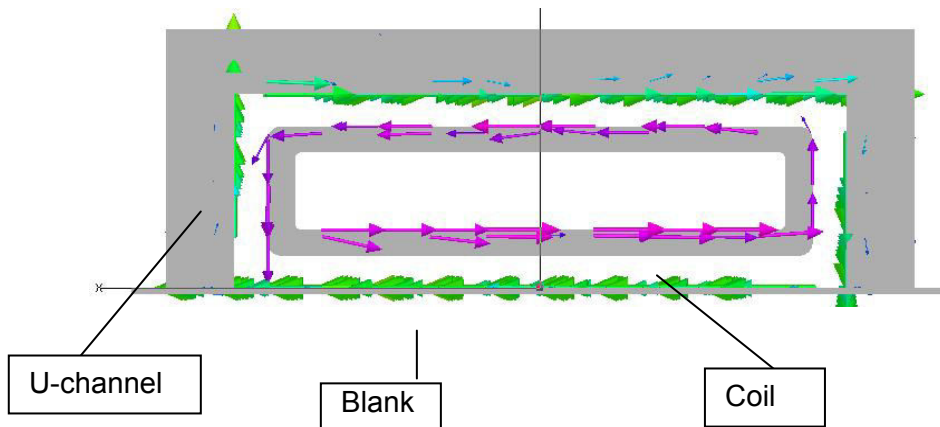


Figure 2: Primary and induced currents in the uniform coil, from Maxwell 3D

In Figure 3 the effect of the addition of an outer channel in terms of the induced magnetic field in the surrounding space can be seen. The uniform pressure coil gives rise to a higher field while redirecting current circulation, provided that rust free and clear contacts are achieved as contact surface. The contact surface is paramount to account for undesired arcing effects.

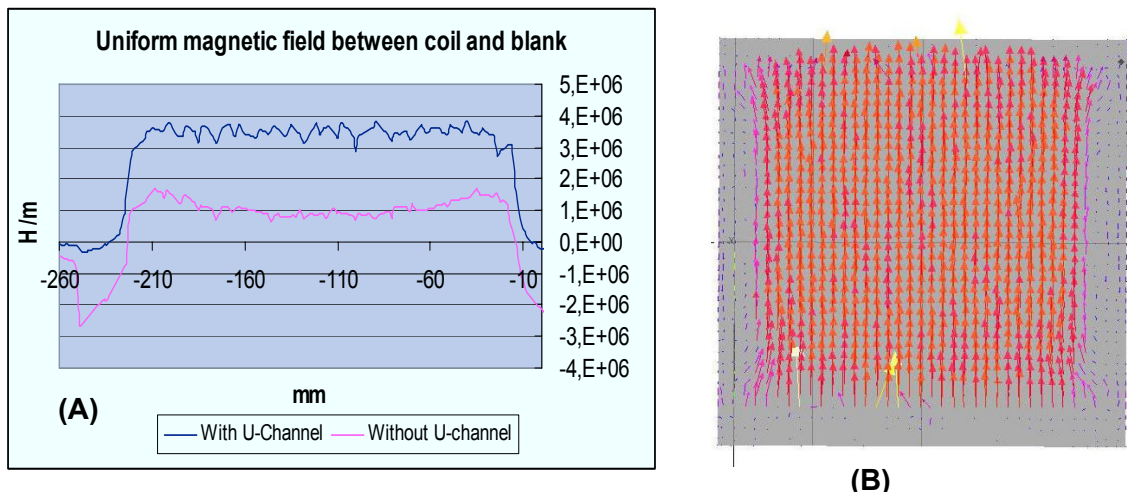


Figure 3: Magnetic field(A) and induced currents on the blank(B) for the uniform coil

The magnetic field provided by a conventional multi-turn coil is non homogeneous in the radial direction, and it takes several winding thicknesses until it builds up with full strength. An example of this is shown by the results of magnetic field distribution analysis performed with a 22 turn spiral coil. (Figure 4)

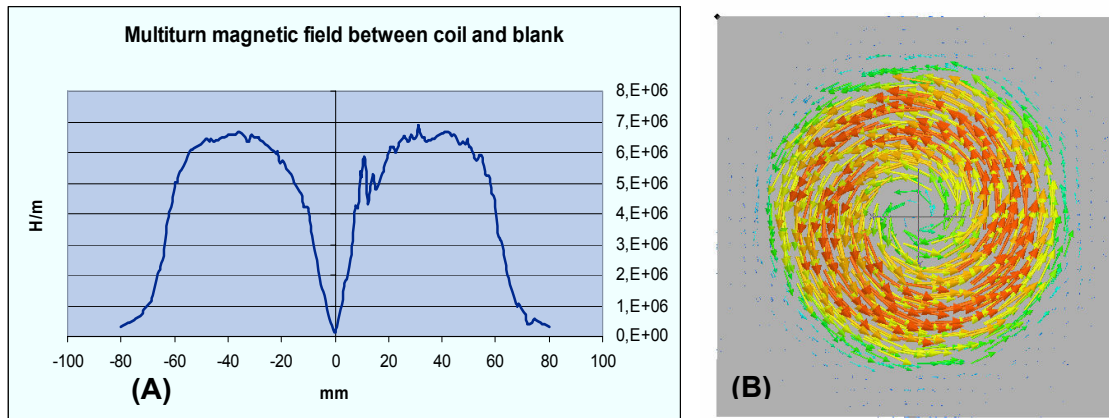


Figure 4: Magnetic field (A) and induced currents on the blank (B) for the multi-turn coil for a running current of 60 000 A in steady state regime

Regarding the forming stage, this results in zones undergoing significant delay as to the deformation sequence.

As a result, varied deformation patterns can be found along the contour of a cone specimen formed in such way, provided in part by the encounter between die wall and workpiece and the mentioned velocity gradient in the initial instants.

2 Experimental procedure

The aim of this paper is to determine the improvement achieved by using the uniform pressure coil with respect to the multi turn coil; hence, the experimental possible real improvements were established as follows; more uniform strain distribution on the workpiece, less microstructural changes. Afterwards, FEM process simulation would be used as tool to explain the differences achieved between different coil samples.

In this study, a 60 KJ Energy Storage and Control Unit Magneform machine was used for the experiments. The main characteristics of this machine are listed in Table 1:

Maximum energy (Kj)	60
Capacity (μF)	1800
Electric resistance ($\mu\Omega$)	956
Inductance (nH)	10,3

Table 1: Capacitor bank parameters

Two different aluminum alloys with dissimilar mechanical characteristics were chosen: Firstly, AA 1050, a low alloyed material in O temper state, AA1050, and 6016 T-4 aluminum, widely spread in the automotive industry for deep drawing of body panels. Their mechanical characteristics are listed in Table 2.

	AA 1050	AA 6016
Tensile strength, ultimate, MPa	76	230
Tensile strength, yield, MPa	28	120
Elongation at break, %	39	27
Poissons ratio	0.33	0.25
Thickness, mm	1	1

Table 2: Mechanical properties of AA 1050-0 and AA 6016-T4

2.1 Experimental set-up

The experimental set up is shown in Figure 5 and Figure 6.

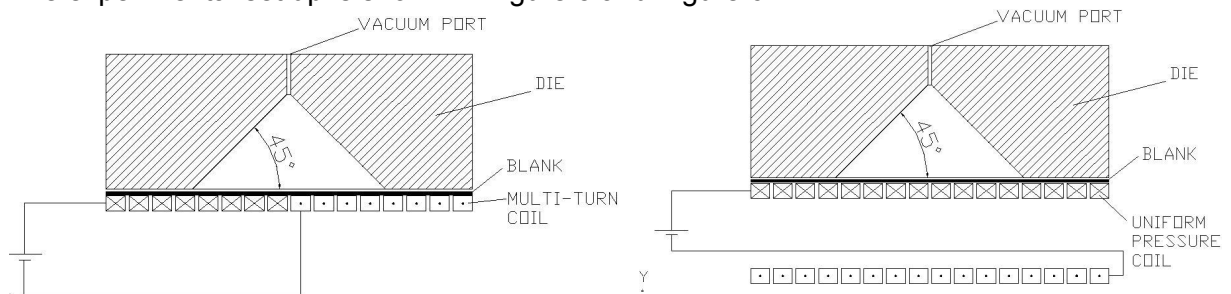


Figure 5: Experimental setup for multi-turn and uniform coil

A cone-shaped die with a 90 ° apex angle was chosen where the radius in die entrance was machined down to 3 mm. Material samples were squared to 240 mm side dimension and to fully account for reaction of the coil as a result of the exerted magnetic pressure, the entire assembly (coil, sheet metal and die) was clamped using a 100 ton hydraulic MTS machine. Reaction force value present during each discharge was recorded. Clamping force was gradually increased to avoid non-desired arcing in contact surfaces when using the uniform pressure coil. During the experiments charging energy was gradually increased until failure or localized necking occurred in the sample. Current pulse values were stored using a 192 –B Fluke Series Oscilloscope to serve as input for the simulation iteration.

2.2 FEM simulation

Based on practical considerations, an uncouple scheme was selected to estimate the forming mechanism of samples, the FEM procedure was stated as follows:

Maxwell 3D was initially used to simulate the electromagnetic aspect of the problem without consideration of the mechanical aspect. This part of the simulation starts with the electric pulse introduced as input for the coil for every experiment performed. As said, the pulse was firstly obtained with a 192 B Fluke series Oscilloscope by means of the Rogowski coil present in the ESCU 60 Kj Series Magneform machine used for the experiments. Afterwards, Maxwell 3D will perform the calculation of the electric current distribution running in the coil as well as the induced currents obtained in the workpieces

located nearby assuming a steady state regime. Associated with induced currents, the software obtains the magnetic field between the coil and the blank as well as the average force value exerted in the workpiece.

With this iterative process the estimation of the total average force applied on the sheet metal part is calculated and subsequently brought as an input load for the simulation of the deformation process, which is done by means of PAM-STAMP2G, a specific code devoted to sheet metal forming simulation.

A quantitative match of the mentioned force parameter is pursued by adjusting the peak value of the pressure or force pulse that serves as an input in Pam –Stamp. In this context, the need for such adjustment is justified if we consider the nature of the magnetic simulation:

- 1) A steady state regime of current circulation is assumed in the electromagnetic computation.
- 2) The computation time is restricted to a full cycle of a running current having a ringing frequency and amplitude equal to the ones present in the experimentally obtained current trace.
- 3) Relative movement between sample and coil is not taken into account.
- 4) The computed values correspond to mean values associated to a full current cycle.

The critical point is focuses on how to transfer this force value into the deformation code as an input load, i.e. the force vs. time curve. As such, the set of experiments proposed is not envisioned as a benchmark problem to asses the feasibility of the iteration scheme, but to obtain coarse trends as to the studied variables is referred:

- a) Global shape of formed samples.
- b) Evolution of deformation pattern.
- c) Strain levels present in the samples.
- d) Contour microstructure analysis.



Figure 6: Experimental setup

3 Results and discussion

3.1 Energy considerations, maximum vertex height

For each of the materials tested the following procedure was followed:

Initially, a maximum energy was determined for each alloy. In a sequence of experiments, energy was increased until fracture occurred either on the vicinity of the cone tip or near the die entrance. For each coil configuration a maximum energy was determined, resulting in 4 energy limits.

In case no rupture took place, as observed with the 1050-O alloy, the maximum energy was determined by geometrical considerations where the proximity to the desired final shape was the decisive factor. On the contrary, for the 6016 alloy fracture took place with both coil configurations.

Subsequently, four intermediate energies were chosen in a way that a significant difference in final shape would take place with each one. Three repetitions were made for every case.

Afterwards, the profile of the formed samples was captured for the sake of comparison with the desired final shape. In following figures (Figure 7, Figure 8), a comparison of the profiles can be observed.

The profiles obtained with the uniform pressure actuator show a smoother contour as a result of the initial energy distribution. The profiles with the spiral coil are the classical ones, exhibiting zones with different curvatures denoting distinct strain distribution.

The energy necessary for the uniform pressure coil is higher than the one needed for the spiral coil. A higher cone height is achieved with the uniform pressure coil as a result of the optimization in strain distribution. The maximum heights achieved are listed in the Table 3.

	AA 1050	AA 6016
Multi-turn coil	41 mm	30,6 mm
Uniform coil	43,3 mm	31,4 mm

Table 3: Maximum height obtained for the different configurations

The height obtained with the AA 1050 aluminum is close to the final. The uniform coil gives us a higher height due to the more uniform distribution of the deformation. This uniform distribution of the deformation allows the blank to have a final bigger elongation in terms of total distance (Figure 7).

3.2 Profile measurement

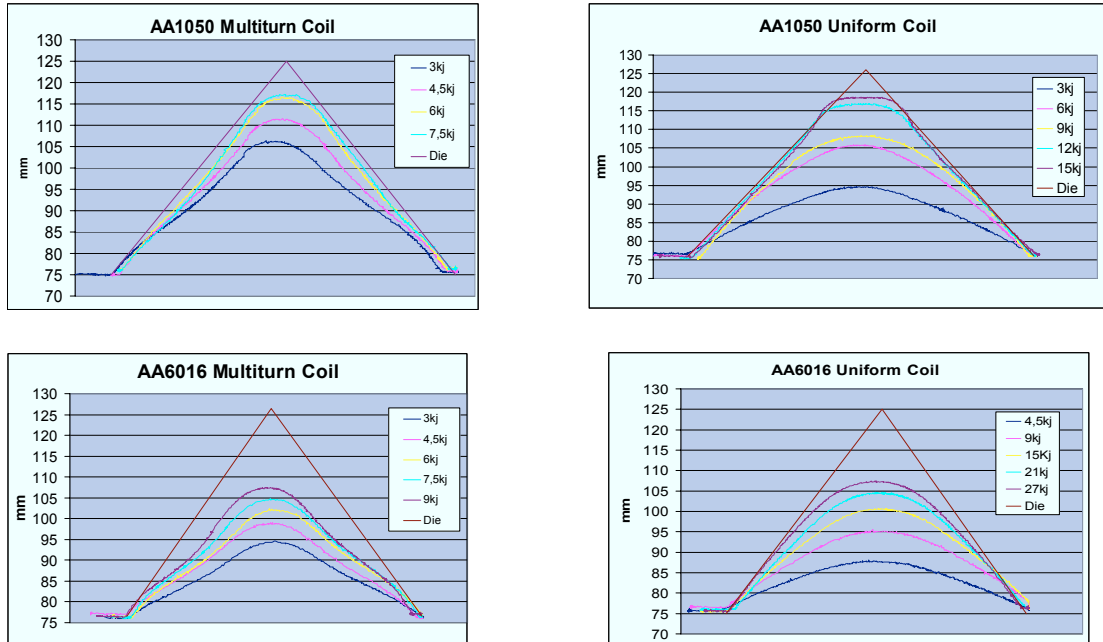


Figure 7: Cone profile progression for AA1050 and AA6016 formed with the uniform pressure coil (right) and multi-turn coil (left)

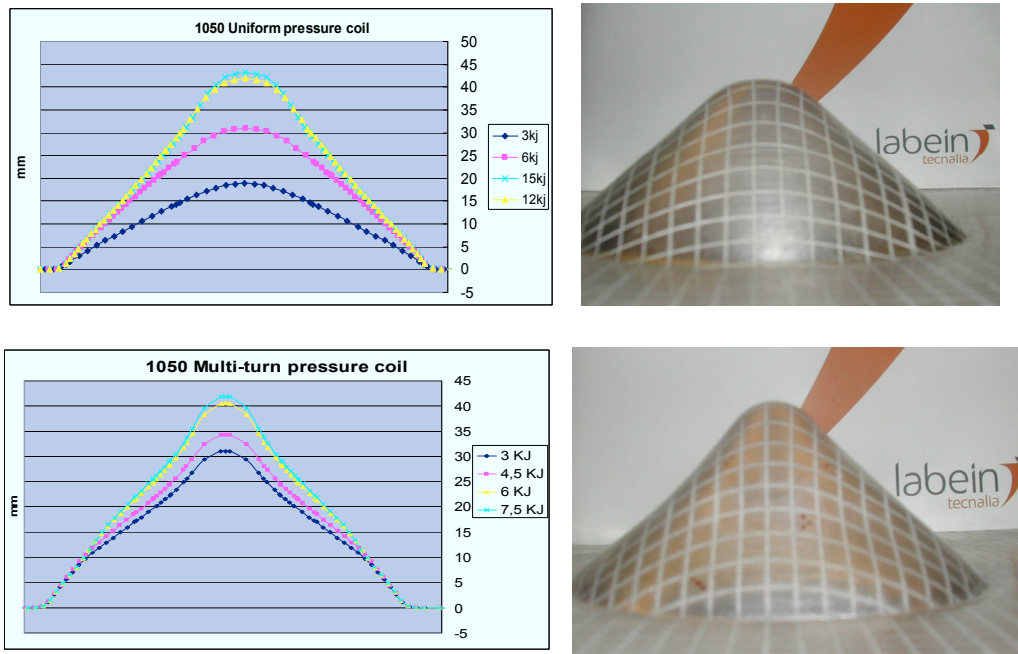


Figure 8: Results of simulations with final shapes of AA1050 samples formed at different energies (left) and AA1050 sample formed at 12 kj (right) using a uniform pressure coil (bottom) and a multi-turn coil (top)

3.3 Strain and thickness distribution along the contour of the specimen

The well-known measurement environment system ASAME of CamSys was used to monitorize the evolution profile of the major, the minor, and the thickness strain distribution over the specimen. Bellow, some plots are depicted.

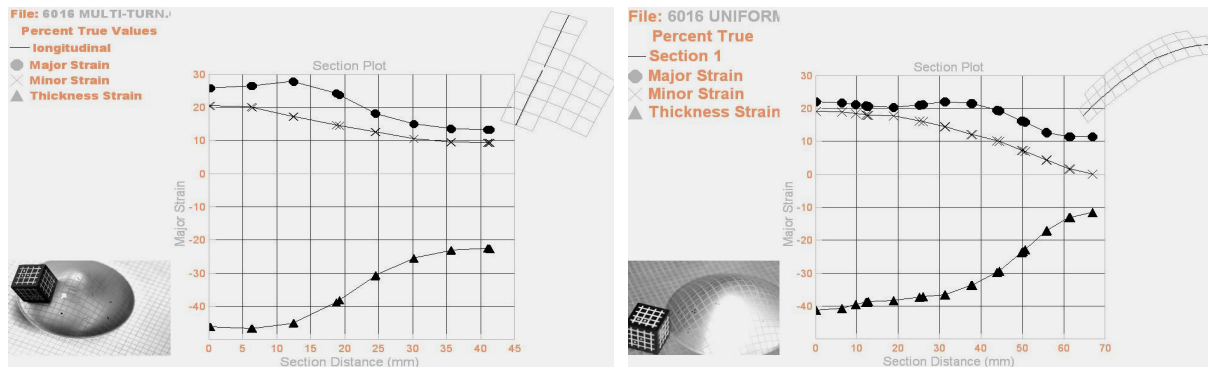


Figure 9: Major, minor and thickness strain distribution for the AA 6016 aluminum with the multi-turn coil (left) and the uniform pressure coil (right)

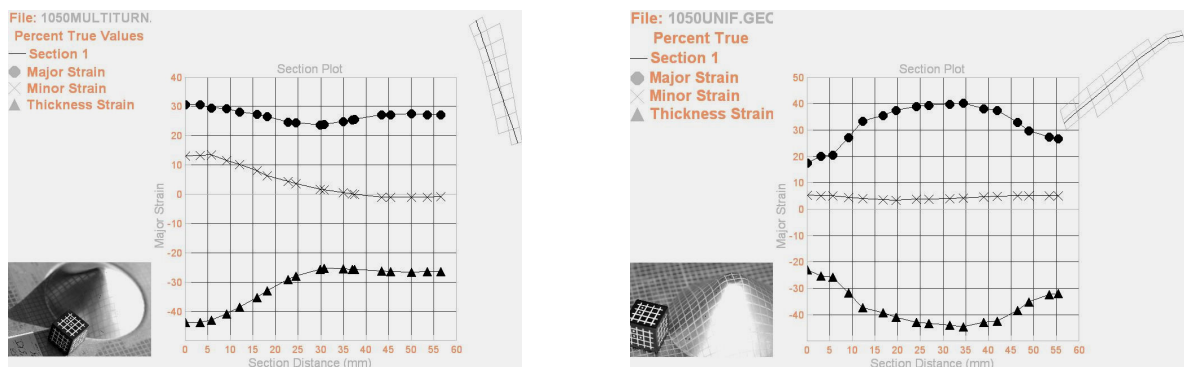


Figure 10: Major, minor and thickness strain distribution for the AA 1050 aluminum with the multi-turn coil (left) and the uniform pressure coil (right)

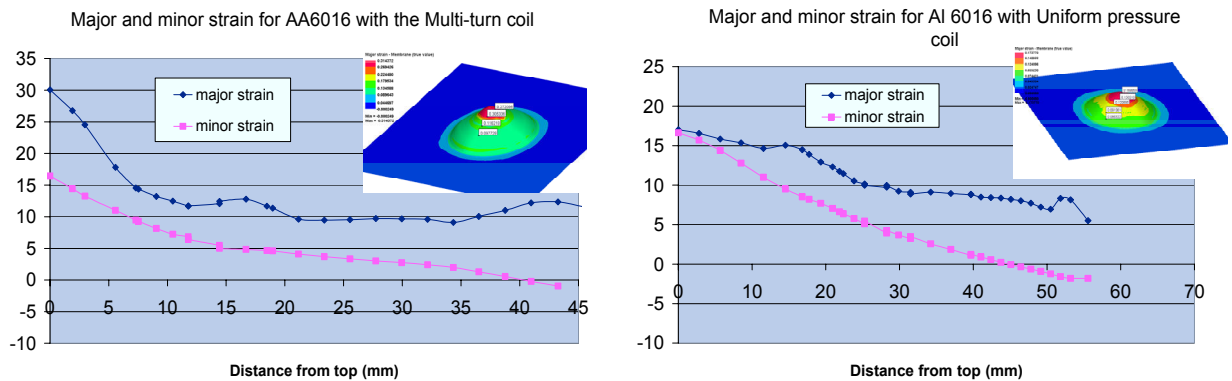


Figure 11: Major and minor strain distribution for the AA6016 alloy simulation with the multi-turn coil (left) and the uniform pressure coil (right)

As it can be seen from the plots, AA6016 comparison in Figure 9 and AA1050 in Figure 10, and supported by FEM predictions of strain distributions Figure 11, the following conclusions can be stated:

- The thickness distribution obtained with the uniform pressure coil is more uniform along the part, less ratio % strain variation / section distance. This means that, the thickness reduction is more uniformly distributed over the whole sample, hence larger forces than in the multi-turn coil would be withstood by the sample with failure
- Accordingly, with the previous statement the major and minor strain distributions are also more uniform along the part for the uniform pressure coil case. Furthermore, the strain field on the uniform pressure samples tends to be an equiaxial strain distribution. According to quasi-static FLC's, it is well-known that these strain states delay the failure predicted by the uniaxial equivalent strain criteria.
- Due to the uniform pressure distribution of the first coil the forming process looks like, in some aspects, a bulge free hydroforming process. So, a uniform distribution of strain is achieved. On the other hand, the multi-turn coil concentrates the pressure over some specific areas of the workpiece at the initial stage and, hence deformations achieved are also non-uniform.
- The major strain obtained in the electromagnetically formed parts is slightly higher than the one obtained by conventional mechanical characterization methods. Furthermore, the AA 1050 gives a higher elongation without failure.

3.4 Contour microstructure analysis

A microstructural analysis of the parts was carried out. Samples of both alloys from each of the coils were analyzed. A cone section containing the vertex was cut off for the analysis using a SEM. Special emphasis was put on the fracture zone. Figure 11 shows the fracture zone for an AA6016 alloy formed with the uniform pressure coil (left) and the multi-turn coil (right).

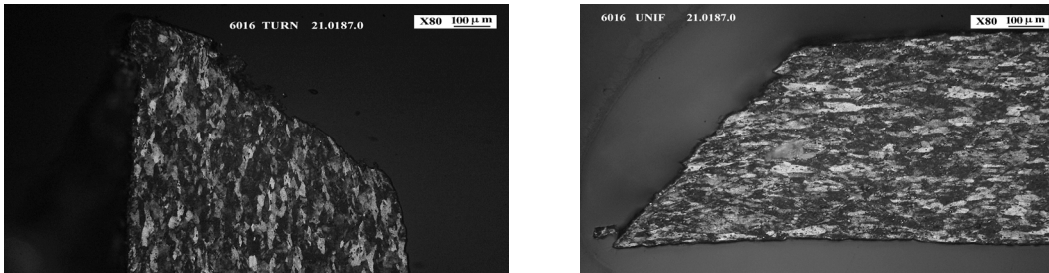


Figure 12: Microstructures observed for the AA6016 alloy with the multi-turn coil (left) and the uniform pressure coil (right)

The analysis of the microstructural study reveals that the main difference between both configurations lies in the elongation distribution. According to grain size, uniform coil samples exhibited a homogeneous elongation distribution along the cone generatrix whilst multi-turn samples have a non-homogeneous one, having isolated areas with highest elongation values.

A thickness distribution measurement was also made along the section with the microscope. The results are shown in Figure 12.

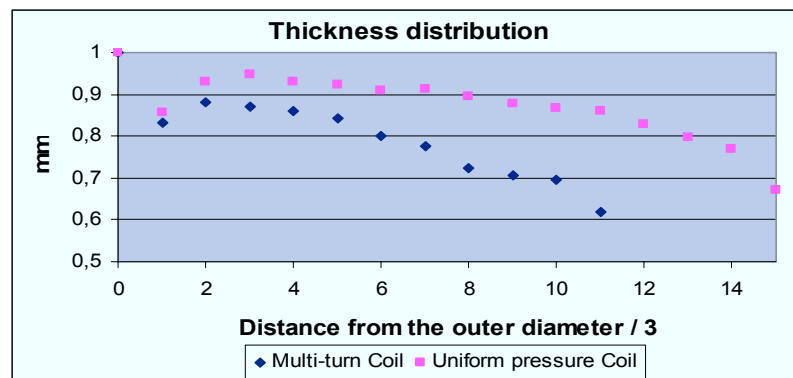


Figure 13: Thickness distribution for the AA 6016 with both coils

4 Summary

The improvements achieved by using the uniform pressure coil with respect to the multiturn coil have been proved. Samples of AA 6016 and 1050 have been tested in comparison with a conical shaped die. The following concluding remarks can be stated:

- More uniform strain distribution on the workpiece has been achieved
- A better fit to die walls was obtained
- Less microstructure changes along the generatrix of specimens were observed
- FEM process simulation has been used to assess the empirical evidences
- A reasonably good agreement between experimental samples and prediction with the uncoupled scheme of simulation was achieved

References

- [1] *Manish Kama, M.S.:* A uniform pressure electromagnetic actuator for forming flat sheets, Dissertation, The Ohio State University, 2005
- [2] *Risch, D.; Beerwald, C.; Brosius, A.; Kleiner, M.:* On the significance of the die design for electromagnetic sheet metal forming. Proc. of the 1st International Conference On High Speed Forming, March 31/April 1, 2004, Dortmund, Germany.
- [3] *Imbert, J. M.; Winkler, S. L.; Worswick, M. J.; Golovashenko, S.:* Formability and damage in electromagnetically formed AA5754 and AA6111. Proc. of the 1st International Conference On High Speed Forming, March 31/April 1, 2004, Dortmund, Germany.
- [4] *Livshitz, Y.; Shribman, V.; Izhar, A.; Gafri, O.:* Pulsed power forming. Proc. of the 1st International Conference On High Speed Forming, March 31/April 1, 2004, Dortmund, Germany.

SESSION 4
TOOLS & EQUIPMENT

Aspects of Die Design for the Electromagnetic Sheet Metal Forming Process*

D. Risch¹, E. Vogli², I. Baumann², A. Brosius¹, C. Beerwald¹,
W. Tillmann², M. Kleiner¹

¹ Institute of Forming Technology and Lightweight Construction (IUL), University of Dortmund, Germany

² Institute of Materials Engineering (LWT), University of Dortmund, Germany

Abstract

Within the electromagnetic sheet metal forming process, workpiece velocities of more than 300m/s can occur, causing typical effects when forming into a die, which will be described and discussed in the present paper. These effects make numerous demands regarding the die design. In order to analyze these requirements, experimental as well as numerical investigations have been carried out. Thereby, special focus is put on the possibilities to accomplish these requirements, which are discussed in the following.

Keywords:

Electromagnetic sheet metal forming, Tool design, Physical Vapor Deposition (PVD)

1 Introduction

The electromagnetic forming process (EMF) is a highly dynamic process using pulsed magnetic fields to form metals with high electrical conductivity such as aluminum. The process principle as well as the forming behavior of the workpiece is described in detail in [1]. When forming into a cavity, there are several requirements concerning the design of the dies. On the one hand, the feasibility of different geometrical forming elements is essential and on the other hand, the lifetime of the stressed parts of the die as well as the resulting workpiece quality is important.

Due to the process principle local workpiece velocities of more than 300 m/s are achievable within the EMF process, whereby a high contact force between the workpiece

* This work is based on the results of the research unit FOR 443; the authors would like to thank the German Research Foundation (DFG) for its financial support

and the die occurs during the impact (compare Figure 1). This causes typical effects when forming into a die:

- Rebound effect (described in [1]) due to high kinetic energy
- Wear, friction as well as fretting due to high normal contact forces combined with tangential movement of the workpiece

The kinetic energy of the workpiece, which strongly depends on the velocity as well as its distribution, is an important aspect regarding the die design for the EM sheet metal forming process. The velocity and its distribution can be strongly influenced by pressure distribution, the pressure over time curve, and the die design, e.g. by using geometrical inserts. The first mentioned parameters have already been analyzed in [1, 2], whereas the present investigations concentrate among other thing on the variation of the geometrical inserts in order to identify geometrical influencing parameters on the rebound effect.

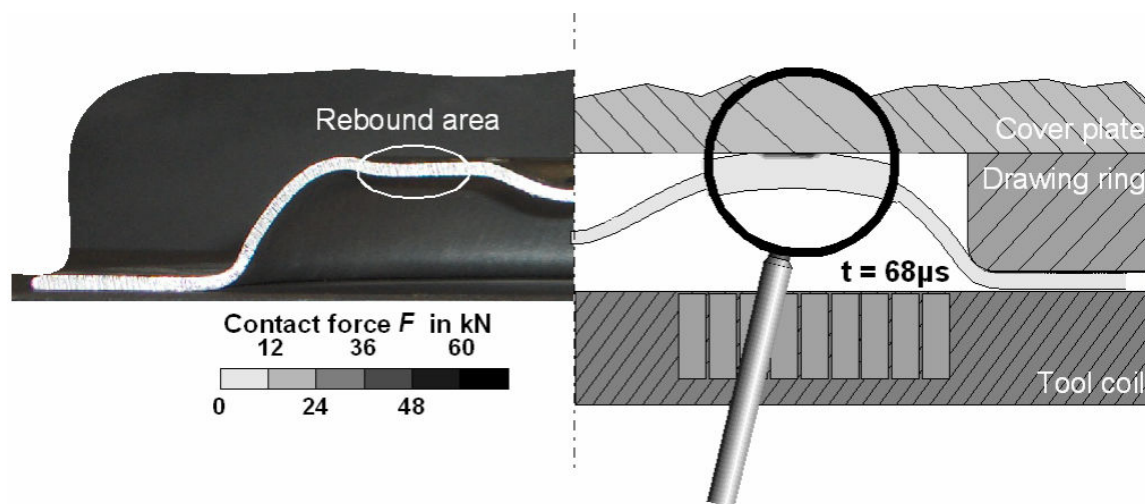


Figure 1: Rebound area and contact zone

The strongest loads have been detected in the zone of the first impact between workpiece and die, compare Figure 1. Here, an intermediate forming state in the place where the first contact on the cover plate occurs is highlighted in **Figure 1**. This contact zone is exposed to high stresses resulting from extensive surface wear and friction caused by high normal contact forces combined with tangential movement of the workpiece. At present, lubricants are used to reduce these undesired effects but an accumulation of the lubricants causes geometrical deviations of the workpiece. In order to reduce these effects, especially the occurring surface defects caused by fretting, the most stressed part of the die, namely the cover plate, will be deposited with different thin Physical Vapor Deposition (PVD) layers.

PVD is a well-established technology used to enhance the properties of tools and precision components as well as to improve their behavior and performance. Within the process the coating material is transferred from solid to vapour phase by means of different energy sources [4]. The advantages of this technology are already utilized to extend the lifetime of forming and machining tools and, therefore, to reduce costs. For this purpose, various kinds of thin layers with different morphologies have been deposited on forming tools to reduce friction and wear. In this way fretting on tools can be prevented. The selection of the individual hard layer system strongly depends on the material to be processed and the forming conditions such as temperature, pressure, forming velocity,

etc. [5]. The most common wear protection layers applied on forming tools and plates are TiC-, TiCN-, TiN-, TiAlN, and CrC-layers [6]. In addition, carbon layers like DLC (diamond like carbon) with a high wear and corrosion resistance [8] as well as solid lubricant coatings with a low friction coefficient have proved to be particularly favorable systems [9].

Both die concepts concerning the geometrical inserts as well as the coating strategy, will be described and discussed in the following chapters. Initially, the influence of the geometrical stiffness on the forming process will be investigated. In order to enhance the resistance of the cover plate against wear and impact, an innovative concept concerning the tool surface modification has been developed within the scope of this research work and will be described in the following.

2 Description and discussion of the experiments

2.1 Experimental setups

The experimental setup for the analysis regarding the geometrical inserts (case A), shown in **Figure 2**, consists of a spirally wound tool coil, a sheet workpiece, a drawing ring, a cover plate as well as different forming elements which can be adapted to the cover plate. Due to the modular die system an easy change of the forming elements is possible. A vacuum port is attached to the cover plate as well as to the inserts to ensure a vacuum inside the die and to avoid pressurized air which acts against the magnetic pressure. The used workpiece material was aluminum (Al 99.5) with a thickness of 1.5 mm, which was formed with a charging energy of 1,260 J.

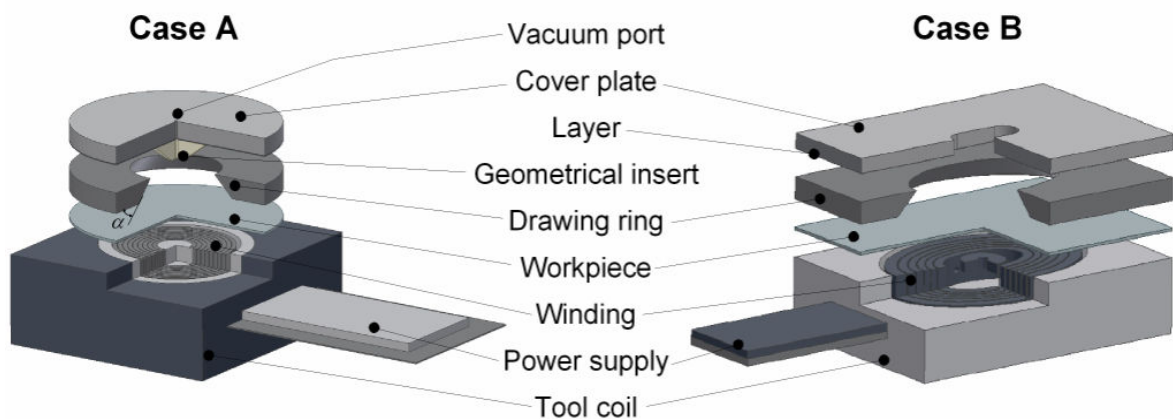


Figure 2: Experimental setups

With the purpose to investigate the behavior of different coatings in high dynamic processes (case B), an oval tool coil was used. The change towards the oval coil was done because a larger area of the coated cover plate is stressed which simplifies the analysis. To characterize the behavior of the layers during a small batch production, the experiments are repeated 40 times. The charging energy was kept constant at 2,560 J throughout the entire sequence of experiments. The used workpiece material was aluminum (Al 99.5) with a thickness of 2.0 mm. The setup, consisting of an oval tool coil, a workpiece, an oval drawing ring as well as a coated cover plate, is shown in **Figure 2**. Due to the hole in the center of the cover plate no evacuation is necessary. All

experiments are done with a Maxwell pulse generator with following properties: Inductance L of 44 nH, capacity C of 960 μ F and, an eigenfrequency f of 23 kHz.

In order to enhance the wear resistance of the cover plate against the impact and to reduce the friction between the aluminum workpiece and the cover plate, three different types of layer systems have been deposited. In this context, hard layers (DLC with and without H-doping), soft layers (MoS_2) and multilayer systems (Ti / TiAlN, TiAl / TiAlN) containing six individual layers have been deposited. To improve the adhesion between the surface layer and the substrate Cr-adhesion layers have been applied [13, 14]. The deposition has been carried out in PVD-Device (CemeCon, Deutschland), using the MF magnetron sputtering with a balanced magnetic field. The coating parameter values are summarized in Table 1.

Parameter	Values
Electric power	9.5 kW (Ti-, TiAl-cathodes) 2.5 kW (Cr-cathodes) 2 kW (MoS_2 -cathodes)
MF-voltage / Frequency	25 V / 350 kHz
Plasma gas	argon, krypton
Reactive gas	nitrogen (CrN), acetylene (H-doped DLC)
Dimension of the cathodes	Ti (500 x 88 mm) TiAl (500 x 88 mm) Cr (500 x 88 mm) MoS_2 (200 x 88 mm) C (500 x 88 mm)

Table 1: Coating parameters

The layer systems have been deposited on three different samples geometries: rectangular specimens (29 x 19 x 12 mm in size), cylindrical specimens (with a diameter of 40 mm, and a thickness of 12 mm) and the cover plates (200 x 140 x 12 mm in size), while tempered steel (1.2067) has been employed as substrate material. The rectangular specimens have been used to test the layers concerning their adhesion, their thickness, and hardness, while the cylindrical ones have been utilized to measure the sliding wear resistance. In order to characterize the layer systems during and after electromagnetic forming coated cover plates have been employed. The layer thickness has been determined by means of calowear tests with a 100Cr6 ball (20 mm diameter). The layer adhesion has been analyzed by means of scratch tests with a maximum load of 200 N, while the critical load has been determined by light optical microscope and acoustic emission. A pin-on-disc tribometer has been employed to test the friction and sliding wear characteristics of the layer systems in dry media. The tests have been performed using a 100Cr6 ball with 6 mm diameter and a load of 5 N. Three wear tracks with a diameter of 10 mm, 14 mm, and 18 mm and a constant track speed of 0.4 m/s have been adjusted. During the test the samples have been continuously monitored with regard to their wear behavior. The material loss is determined by weighing and/or measuring the profile of the resulting wear track. The layer hardness has been acquired by microhardness tests using a precision diamond indenter with a load of 50 N.

Scanning Electron Microscopy (SEM) and Light Microscopy (LM) have been employed to investigate the relationship between the different kinds of layers and the appropriate tribological properties of the coated cover plates after electromagnetic forming application. In addition, the surface topology was optically scrutinized with a confocal microscope.

2.2 Influence of the geometrical stiffness on the forming process

In [1], the so-called rebound effect was indicated as a negative influence on the workpiece geometry when forming into a cylindrical cup (see Figure 1). In order to identify geometrical influencing parameters on this rebound effect, an investigation concerning the die design has been carried out. The material, the sheet thickness, the depth as well as the tool coil geometry were chosen to be constant.

The die has been modified regarding the applied ring-shaped pressure distribution: the used cavity consists of flat bottoms and conical elements. In order to be able to vary the local stiffness of the workpiece, geometrical inserts which have been adapted to the cover plate are used. The results of this investigation will be explained exemplarily on the basis of selected geometrical elements, shown in **Figure 3**.

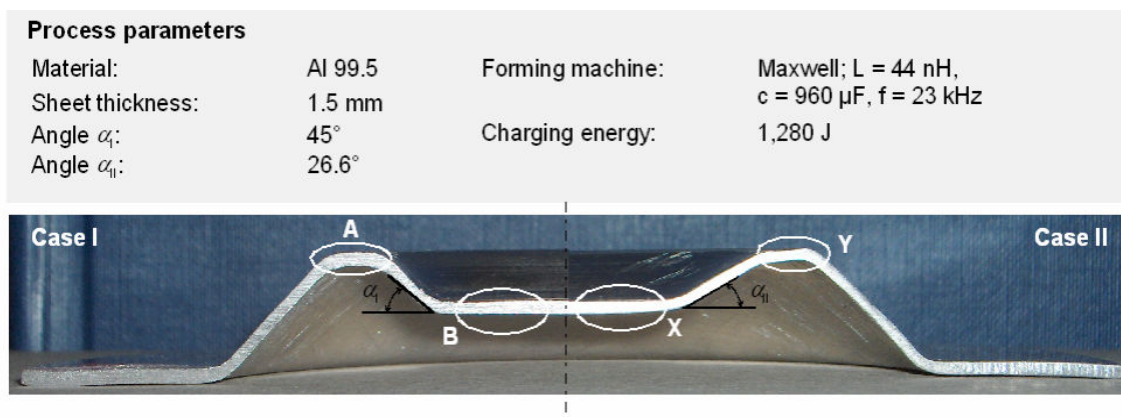


Figure 3: Exemplary results by using different geometrical inserts as forming elements

In order to keep as many parameters as possible constant, only the angle α has been varied (compare Figure 3). The photo shows that, in general, a good form filling is achieved in both cases. Here, it is remarkable that the flat areas marked as B in case I and X in case II are achieved in good order. The main difference of the two realized workpiece geometries is the geometrical stiffness, although the added geometrical inserts look quite similar. Regarding the achieved form filling in case II, a geometrical deviation can be observed in the ring-shaped area Y. The comparison with case I shows that by increasing the geometrical stiffness of the workpiece this effect on the workpiece could be significantly reduced. The desired contour could be achieved and no measurable geometrical deflection was detected, compare Figure 3.

In order to compare different geometries in a simple way, the significant value K is introduced to define the geometrical stiffness of the desired workpiece geometry. The geometrical stiffness K of the workpiece can be roughly estimated with the knowledge of the first eigenfrequency via the following formula [10].

$$K = (2\pi * f)^2 * m \quad (1)$$

Thereby, the eigenfrequency f as well as the mass of the workpiece m were calculated with a modal analysis in MSC.Mentat. The used method to determine the eigenfrequencies was Lanczos. In doing so, the ideal geometry concerning the design drawings is assumed and the undeformed flange area is neglected in the modeling of the workpiece because the flange increases the stiffness of the different geometries in the same manner. Furthermore, rigid body movements of the workpiece are allowed. This means that the first six eigenfrequencies are zero so that the seventh one, which is the real first eigenfrequency, is used. The calculated results for this eigenfrequency as well as the appropriate mode shape are summarized in Figure 4. A comparison of the different inserts has shown that the first eigenfrequency characterizes the bending mode shape in all regarded cases, whereas the corresponding eigenfrequency is quite different.

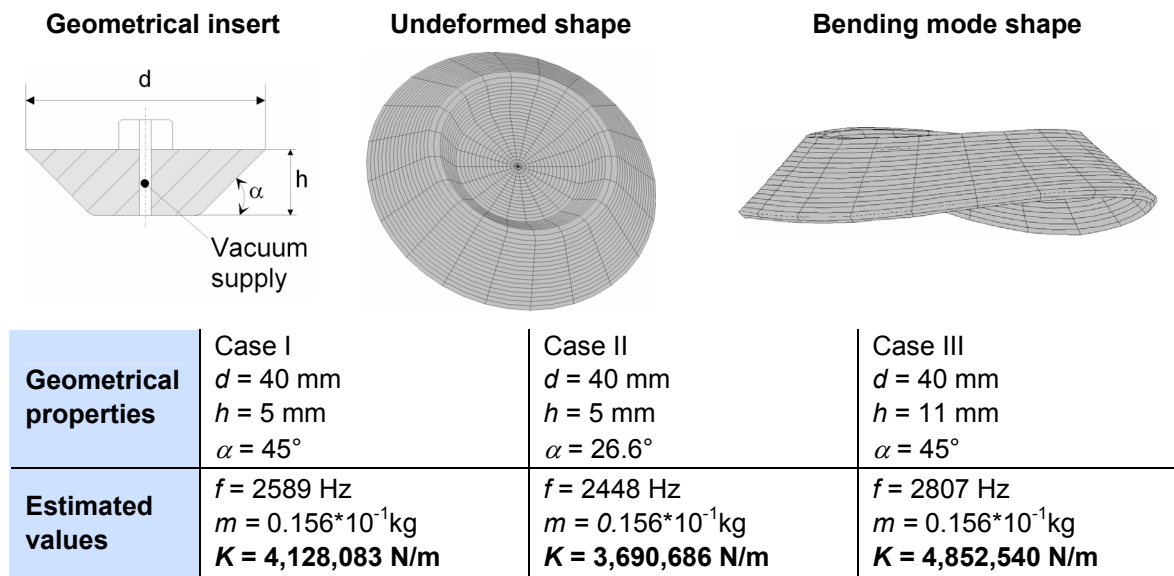


Figure 4: Results determined by a modal analysis in MSC.Mentat

The results of this analysis substantiate that by increasing the geometrical stiffness the rebound effect and the geometrical deviations respectively, as shown in **Figure 3**, could be reduced.

The long-term goal of this proposed design method using a modal analysis is to evaluate the feasibility of geometrical elements by means of electromagnetic forming. On this basis, a catalogue will be established listing different geometrical elements that could be assembled in order to estimate the total stiffness of the desired geometry. Thus, the feasibility of complex shapes can be appraised. Here, it is important to find balance between the required geometrical stiffness to realize a component and the maximum formability of the used material (e.g. thinning), which is acceptable regarding technical as well as functional requirements. This requires the improvement of the proposed method to realize the described approach.

Further effects concerning the die and the workpiece quality as well have been observed during these experiments. On the one hand, surface defects at the workpiece have been detected due to the accumulated lubricant and, on the other hand, fretting

occurs between the aluminum sheet and the die made of tempered steel (1.2067). In order to improve the workpiece surface and to avoid the occurred fretting, the die, especially the cover plate in the present investigation, should be coated with different methods. The approach and the results of this strategy are described and discussed in the following.

2.3 Characterization of the different layers

In order to develop an appropriate layer system for the electromagnetic forming processes with high wear and impact resistance, the layer systems have firstly been empirically investigated (Table 2). Based on the attained results a selection of layer systems has been conducted.

	Ti/TiAlN-multilayer	TiAl/TiAlN-multilayer	DLC	DLC (H-doped)	MoS ₂
Critical load [N]	125	73	72	108	80
Microhardness [HV]	638	935	1506	2338	979
Thickness [μm]	7,55	4,8	4,8	6,36	3,59
Wear coefficient	$18,5 \times 10^{-3}$	$9,54 \times 10^{-3}$	4×10^{-4}	$2,1 \times 10^{-4}$	No weight loss determined

Table 2: Results of the layer characterization

The results of the scratch test show a variation of the critical scratch load between 72 and 125 N, which demonstrate a high adhesion for all layer systems. All deposited layer systems exhibited thicknesses between 4 and 7 μm. In **Figure 5** it can be seen that the metallic layer is three times thicker than the TiAlN nitride layers in the Ti/TiAlN layer systems. In the TiAl/TiAlN multilayers the ratio between TiAl metallic layer thicknesses and TiAlN layers is about 2. This causes, on the one hand, a higher ductility of the layers and, on the other hand, this is associated with a low hardness as well as a low wear resistance (Table 2). Therefore, further layer and process optimization is needed as well to improve the properties of these layer systems and to adapt them to the demands of the electromagnetic sheet metal forming process.

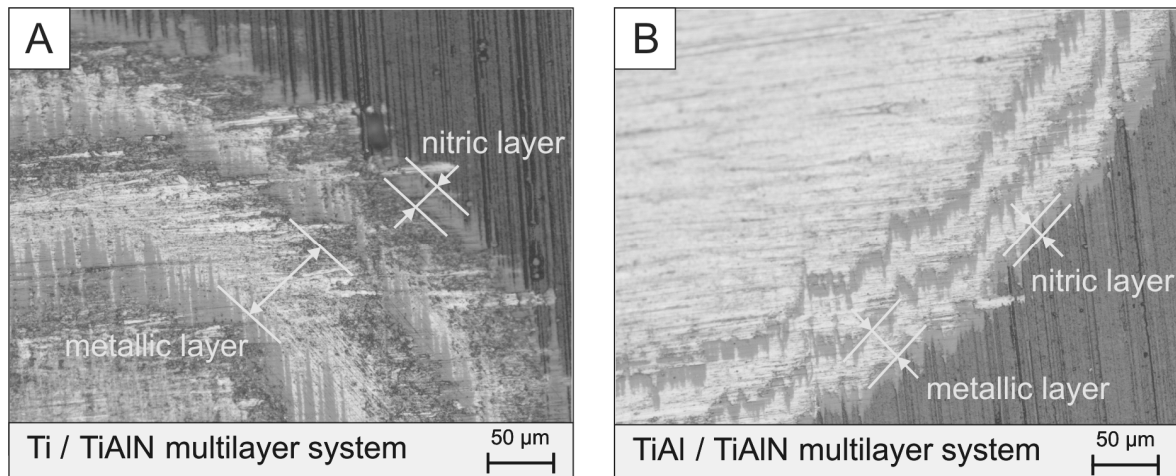


Figure 5: Light microscopy analysis of multilayers after calowear test

The wear coefficients increase from Ti/TiAlN layer system to H-doped DLC layer system, which correspond to the hardness of the layers. An exception has been shown in case of MoS₂-layers, although their low hardness exhibits a high wear resistance. This is caused by the solid lubricant effect of MoS₂ layer [12]. The measurements of the wear resistance show neither a weight loss of the layer nor a significant layer abrasion, even at a wear distance of 4,500 m. Based on the layer system's properties it can be established that H-doped DLC and MoS₂ layer systems, too, show the best performance. Therefore, they can be evaluated as appropriate layer systems for the EMF process.

2.4 Comparison and discussion of the coatings

Cover plates coated with H-doped DLC and MoS₂ layer systems have been investigated during electromagnetic forming of aluminum sheets and after 40 impacts. The results have been compared with uncoated cover plates, whereas the sheet has been lubricated before each forming process. Furthermore, special emphasis was put on the aluminum sheet quality throughout the investigation.

After the electromagnetic forming process a characteristic oval surface groove has been observed on the surface of all cover plates. This groove consists of two tracks: one on the long axis side and one track on the short axis side (see Figure 6). To evaluate the relationship between layer systems and tribological properties of the coated cover plates after electromagnetic forming, the cover plates and the formed Al-sheets have been examined in the Scanning Electron Microscopy (compare Figure 6C - G). Additionally, the surface topology has been scrutinized in a confocal light microscopy (shown in Figure 6A and B). The results of the reference examinations attained from the uncoated plate are presented in Figure 7.

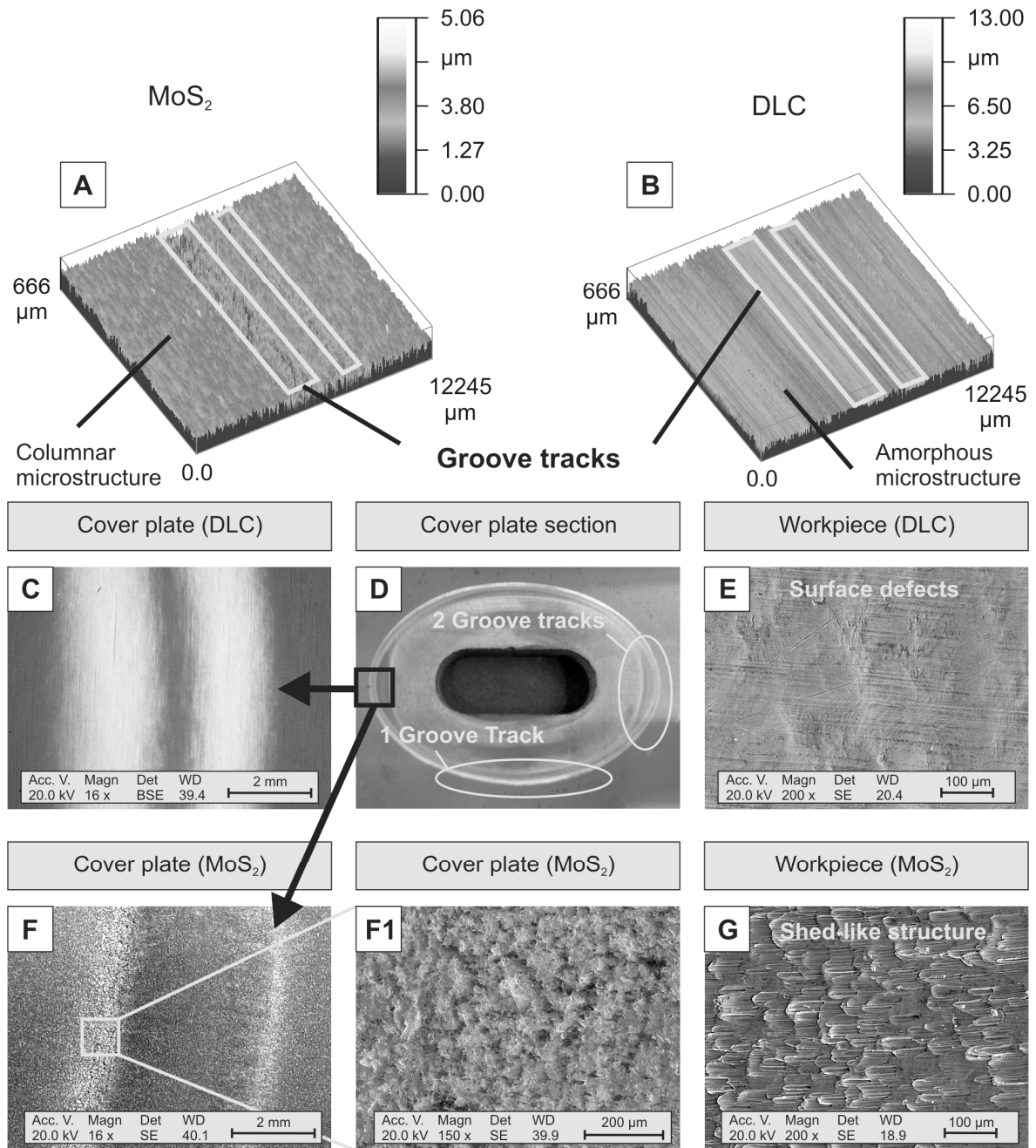


Figure 6: Cover plate and workpiece surface taken by SEM and confocal microscopy for DLC and MoS₂ layer systems

It can be seen that the forming process has different influences on the cover plate as well as on the formed workpiece surface depending on the layer system. The topology of the MoS₂ coated cover plates demonstrates a columnar microstructure of the layer (Figure 6A). The workpiece formed by using a cover plate coated with MoS₂ indicates a shed-like structure on the surface, which reflects the microstructure of the MoS₂ coated cover plate surface (Figure 6G). A reduction of the MoS₂ layer thickness promises for a smoother surface by a high wear resistance [11]. The analysis of the DLC layer topology presents a smooth surface (Figure 6B), which corresponds to the amorphous

microstructure of this layer [13]. Moderate surface defects by the impact have been observed on the workpiece surface after the EMF by using DLC coated cover plates (Figure 6E). The groove on the DLC coated cover plates presents a width of approximately 2 mm; whereas a width of only 0.5 mm can be detected on the MoS₂ coated cover plates (compare Figure 6C and F). Due to the low friction coefficient and the lubrication effect as well the MoS₂ layer [12] presents a higher resistance against the impact forces occurring by the electromagnetic sheet metal forming process.

A poor wear resistance can be observed on the uncoated cover plate compared to the coated ones. In case of the uncoated cover plate the groove width is approximately 3 mm, even using lubricants (Figure 7).

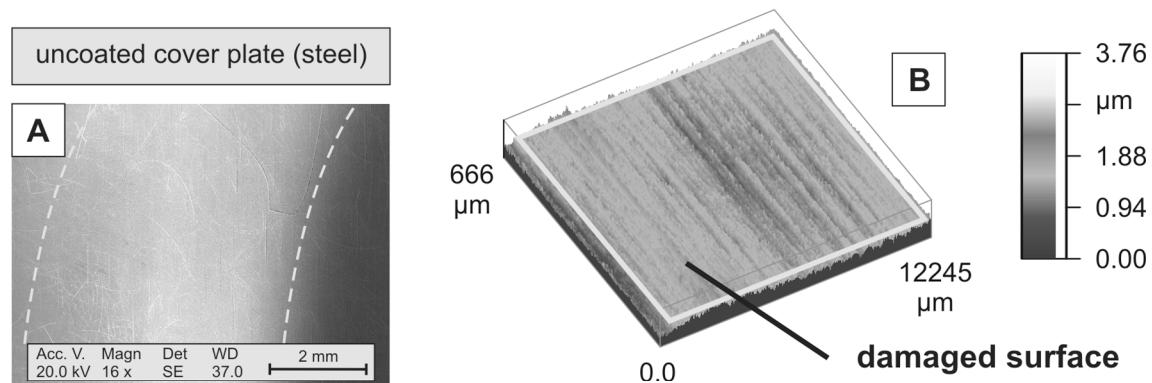


Figure 7: SEM-image and a 3D-profile of the uncoated cover plate surface

Based on the attained results the coated cover plates present a better protection potential against the impact forces occurring during the electromagnetic forming than the uncoated cover plates.

3 Summary & outlook

Two promising die concepts for the electromagnetic sheet metal forming process are pointed out in the present paper. One possibility regarding the die design is the target-oriented modification of local stiffness realized in the present investigation by use of geometrical inserts. It could be observed that the occurring geometrical deviations are reduced by increasing the stiffness of the workpiece. Here, it is important to find a balance between the required geometrical stiffness to realize a component and the maximum formability of the used material (e.g. thinning), which are acceptable regarding technical as well as functional requirements. A method to evaluate the feasibility of geometrical details is introduced, which needs to be developed in detail in the future.

The second possibility presented in this paper is the use of coated cover plates in order to increase the lifetime of the stressed parts of the die as well as to prevent the use of lubricants by the electromagnetic forming, which could cause geometrical deviations of the workpiece. For this purpose the different coating systems have been characterized. Based on this, two layers, namely the DLC-layer and the MoS₂-layer, have been chosen for further investigation regarding to their behavior during the electromagnetic sheet metal forming. Although the workpiece was not lubricated during the experiment, no fretting between aluminum workpiece and the coated cover plate could be observed. Moreover,

all coated cover plates have shown a better wear and friction resistance compared with the uncoated ones. Further layer optimization will be associated with a significant decline of the wear and impact resistance for high speed forming conditions which are present during electromagnetic forming.

References

- [1] *Risch, D.; Beerwald, C.; Brosius, A.; Kleiner, M.*: On the Significance of the Die Design for Electromagnetic Sheet Metal Forming, Proc. of the ICHSF 2004 - 1st Int. Conference on High Speed Forming, 31.3.-1.4.2004, p.191-200, Dortmund, 2004 ISBN 3-00-012970-7
- [2] *Beerwald, C.*: Fundamentals for Process Dimensioning and Design of Electromagnetic Forming (in German), PhD Thesis, Dortmund, 2004
- [3] *Kleiner, M.; Risch, D.; Beerwald, C.; Brosius A.*: Influence of the Velocity Distribution during the Process of Electromagnetic Sheet Metal Forming into Dies, Production Engineering - Annals of the German Academic Sociation for Production Engineering (WGP), vol. XII/2, p. 95-98, 2005
- [4] *Mertz, K.W.; Jehn, H.A.*: Paxishandbuch moderne Beschichtungen, Advanced Surface Coatings, Hanser Verlag München Wien, 2001, ISBN 3-446-21677-7
- [5] *Matthews, A.; Leyland, A.*: Developments and applications. In "Total tribology: towards an integrated approach" e. by I. Sherrington, W. B. Rowe R.J.K Wood, PEP Ltd, UK, pp. 39, 2003
- [6] *Eversberg, K.R.*: Produktivitätsgewinn durch CVD- und PVD-Hartstoffschichten bei großen Umformwerkzeugen, Konferenz-Einzelbericht: Beschichtete Werkzeuge - höhere Wirtschaftlichkeit in der Ur- und Umformtechnik, Workshop, 2002, EuroMold, 2002, p. 1-11
- [7] *Eversberg, K.R.*: CVD und PVD-Beschichtung von Werkzeugen und Bauteilen. CVD- and PVD-coating of tools and parts. In "Blech, Rohre, Profile, Band 39, Heft 7/8, p. 544-549, 1992
- [8] *Klose, K. ; Bräunlich, H.*: Werkzeugbeschichtung - Anforderungen aus der Sicht der Umform- und Schneidtechnik, insbesondere für das Innenhochdruck-Umformen, Konferenz-Einzelbericht: Beschichtete Werkzeuge - höhere Wirtschaftlichkeit in der Umformtechnik, Workshop, 2002, p. 1-14
- [9] *Janoss, B.*: PVD/CVD tool coatings & forming of stainless. PVD- und CVD-Beschichtungen der Umformwerkzeuge erhöhen die Leistung beim Stanzen und Umformen nichtrostender Stähle, Zeitschriftenaufsatz: Metal Forming, Band 33 Heft 3, p. 110-116, 1999
- [10] *Grote, K.-H. ; Feldhusen, J.*: Dubbel Taschenbuch für den Maschinenbau, Springer-Verlag, 19. Auflage, ISBN 3540221425
- [11] *Pflüger, E.; Savan, A.*: Vakkum in Forschung und Praxis Band 11, heft 4, S. 236-240, pp. 1999
- [12] *Coldwell, H.L.; Henderson, A.; Dewes, R.C.; Aspinwall, D.K.*: The use of a soft/lubricating coating for dry turning of aluminium alloy BS L168 Konferenz-Einzelbericht: NCMR, National Conf. on Manufacturing Research, 18 *, 2002, p. 355-360, ury St Edmunds, London: Professional Engineering Publ. Ltd.

- [13] *Gassner, G.; Mayhofer, P.-H.; Mitterer, C.; Kiefer, J.:* Structure property relations in Cr-C/a-C:H coatings deposited by reactive magnetron sputtering, *Surface and Coating Technology*, 200 [1-4], p. 1147-1150, 2005
- [14] *Tillmann, W.; Vogli, E.:* TiAlN/CrN deposited by arc-PVD. *Proc. Of THECoatings-Conference*, April 2004, Erlangen/Deutschland, 2004, S. 227-235 ISBN 3-87525-201-2

Electromagnetic Forming and Joining for Automotive Applications

S. Golovashchenko¹

¹ Manufacturing & Processes Department, Ford Research & Advanced Engineering, Dearborn, USA

Abstract

In this paper some options of how electromagnetic forming (EMF) can assist to expand the capabilities of conventional forming and joining technologies are discussed. Three different areas where EMF has the potential for a significant expansion of capabilities of traditional technologies are reviewed: 1) restrike operation to fill sharp corners of automotive panels; 2) low energy method of springback calibration; 3) joining of closed frames with an openable coil. Each of these applications was demonstrated in laboratory conditions and the description of the tooling is provided in the paper. Suggested design of a flat concentrator collecting induced electric currents from a flat coil was demonstrated for a corner filling operation and a springback calibration. An efficient technique of fabricating the flat coil from a flat plate by using water jetting technology enables a cost effective coil design, which can be reinforced by a system of non-conductive bars. The insulation of the coil is produced from the flat sheet of insulation material. Suggested design allows the coil to be repaired if a shortcut or fracture of insulation strips happens. A technology of low-energy calibration of stamped parts provides an option of working with a wider variety of materials including aluminum alloys, mild steels, and advanced high-strength steels. This technology is demonstrated for calibration of U-channels.

Keywords:

Forming, Joining, Tooling, Springback

1 Introduction

In pulsed electromagnetic forming and joining a coil can be described as a tooling replacing a punch in conventional forming operations. Depending upon the coil configuration, various stamping processes can be carried out, such as tube expansion, tube compression, and flat sheet forming [1]. However, due to a number of issues including coil durability, maximum stamping rate, safety implications etc., electromagnetic stamping technologies have not been able to compete with conventional stamping on the

press if conventional processes provided the desired result. Therefore, our strategy is to use electromagnetic forming (EMF) to expand the capabilities of conventional forming and joining technologies. In this paper, we will discuss three different areas where EMF has the potential for a significant expansion of capabilities of traditional technologies: 1) restrike operation to fill sharp corners of automotive panels; 2) low energy method of springback calibration; 3) joining of closed frames with an openable coil.

2 Restrike operation of parts preformed using conventional stamping technology

Due to the tendency that electromagnetic pressure is usually rapidly decreasing as soon as the blank moves away from the coil, deep drawing operations are not feasible for EMF unless some special arrangements are made to move the coil close to an already deformed blank. Another option is to use several steps of EMF with coil configuration at the following step, corresponding to the blank shape after the previous step. This approach may be acceptable for low-volume production. However, for high-volume production it may not be appropriate. More attractive is the combination of conventional forming and EMF when EMF is applied as a restrike operation for difficult-to-form areas. It has been proven experimentally [2] that for corner filling operations EMF can produce a significant improvement in formability due to a number of effects described in [3], including high strain rate, bending-unbending, significant hydrostatic pressure, and coining effect. Some complications of EMF employment for restrike operations are dictated by limited space for the coil. Typically, to have a high-efficiency EMF process, the ratio of the inductance of the coil with blank related to the total inductance of the EMF machine-coil-blank system should be approximately 0.8...0.9 [1]:

$$K_1 = \frac{L_{coil+blank}}{L_{mach} + L_{connection} + L_{coil+blank}} \approx 0.8...0.9. \quad (1)$$

In other words, the inductance of the coil should dominate over the inductance of the EMF machine and its connection to the coil. To satisfy this requirement, the coil should have multiple turns since the inductance of the coil can be described in a following way

$$L_{coil+blank} \sim n^2, \quad (2)$$

where n is the number of turns in the coil. Multiple turns are difficult to accommodate in limited space for restrike operations and also may not be feasible from the coil strength and durability point of view. Evidently, the cross-section of the turn dictates its stiffness against torsion moments developed as a result of interaction of adjacent turns of the coil and also due to the skin effect. Usage of a single turn coil usually leads to low efficiency of the process. The suggested solution is in a system including a flat coil and a concentrator [4], combining high efficiency of the multi turn coil and structural strength of a single-turn coil. The schematic of the discussed coil system is shown in Figure 1. The important feature of the flat coil is that its spiral is relatively easy to fabricate: the spiral can be manufactured from a flat plate [5] using water jetting technology, which provides a significant cost reduction compared to end milling technology. Compared to a winding

technique, the water jetting technology provides a more accurate shape of the surface and allows maintaining a uniform and rather small clearance between the coil and the blank since during the winding procedure an originally straight bar gets curved as a result of plastic bending, producing distortion of the original cross-section. Also, in the suggested new design the coil should be reinforced to balance significant forces in between the turns of the coil. This can be accomplished by employing non-conductive rods, as it is indicated in Figure 2. An expansion of the coil can be prevented by putting the coil into a metallic bandage [5].

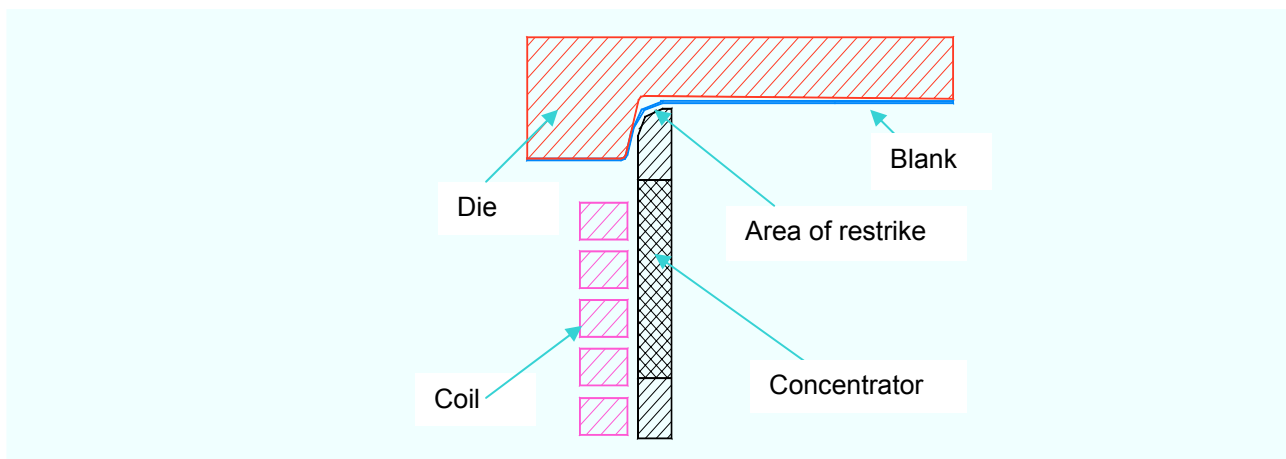


Figure 1: Schematic of a restrike operation using a flat coil with flat concentrator

The design of such a reinforced coil was developed based upon the analysis of failure modes of the coils in our laboratory practice. The insulation between the turns was fabricated from a micarta sheet. The thickness of the sheet was specified to be equal to the clearance between the turns of the coil produced by water jetting technology.

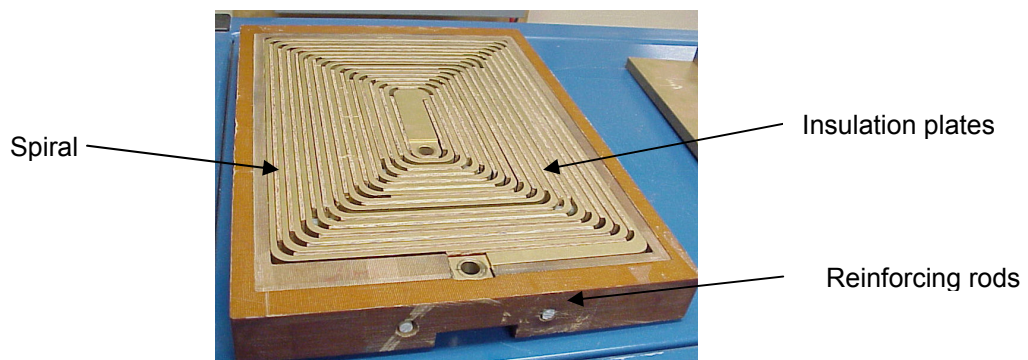


Figure 2: Flat multi turn coil employed for laboratory experiments

The design of the laboratory flat concentrator was applied to a corner filling operation. A flat blank of aluminum alloy 6111-T4 was used as a sample. It was positioned on the surface of a die fabricated to demonstrate the process in laboratory conditions.

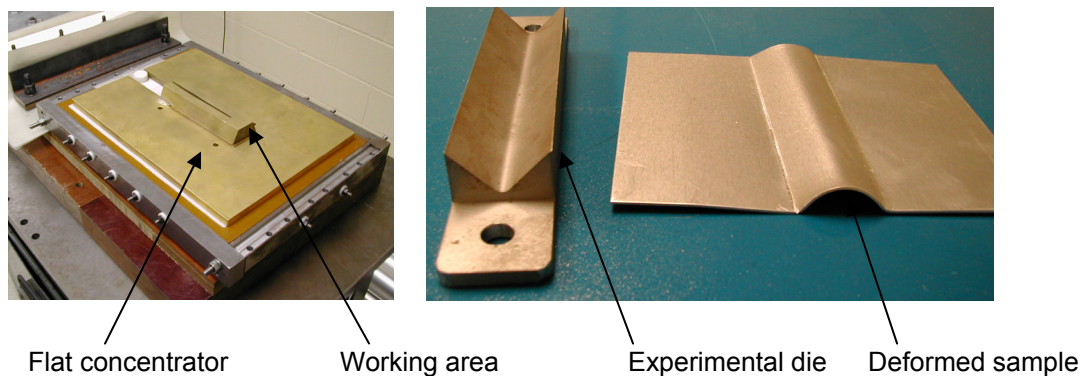


Figure 3: Flat coil with flat concentrator employed for laboratory experiments of corner filling operation

3 Springback calibration

The idea of springback calibration using high-speed forming technologies has been known for several decades. In many cases it was applied for calibration of cylindrical shells bent and welded from a flat sheet. Typically, the calibration effect was accomplished due to radial stresses, generated during a high-rate impact of the blank with the die. Any source of pulsed pressure, such as EMF, electrohydraulic or explosive forming, would be appropriate to provide a such calibration mechanism. In many cases it is essential to accelerate the blank up to the speed of 100-200 m/sec. In our recent development we suggested another calibration process based upon the elimination of internal stresses in the blank during the propagation of induced electric currents [5]. The blank can be calibrated after a conventional stamping operation and springback by deforming the blank elastically back to the desired shape and then by running a high voltage discharge through the coil positioned in close vicinity to the blank areas with significant internal stresses. Such process requires significantly less energy compared to traditional pulsed calibration technology. It was discussed in detail for a simple test of flattening pre-bent sheet in [7]. A similar technology was demonstrated for calibration of U-channels with a flat coil-flat concentrator system. The suggested process was verified for aluminum alloys AA6111-T4 and AA5754 and also for steels BH210, DP500, and DP600. The laboratory tooling is shown in Figure 4. The electromagnetic field was applied using a similar flat coil and a flat concentrator, which produced an electromagnetic field in the area of curved areas at the bottom of a U-channel.

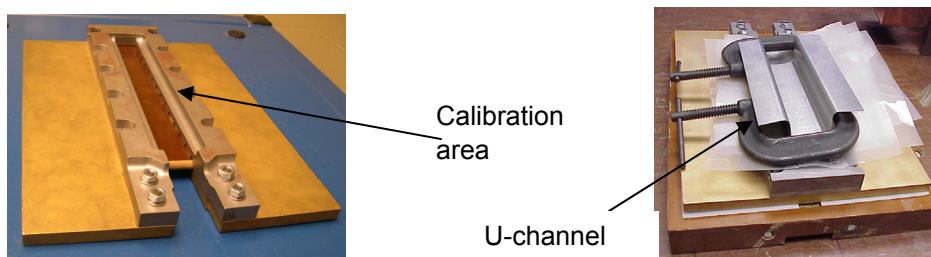


Figure 4: Flat coil with flat concentrator employed for U-channel calibration



Figure 5: Comparison of U-channels before and after calibration

4 Joining of parts with an openable coil

Finally, the third application which we discuss in this paper is joining with an openable coil. Evidently, the requirements for joints of structural parts are very high in terms of both strength and durability. Therefore, the desired joint should include a high strength crimp or cold weld, which can be produced using EMF. In this paper, we describe the design of an openable coil, which consists of two independent multi turn coils connected in series [6], each of which is mounted in its own shell. The shell was made of electrical insulation material with electrical connections to an EMF machine. On the side surface of each coil there is a concave work zone with the shape of a tubular component. The coils are located in such a way that their work zones are located opposite each other. Together both work zones form a closed-loop work cavity for the tubular component. The coils are connected in series by electrically conductive wire. The first turn of the first coil is connected to one pole of the EMF machine and the last turn of the other coil is connected to the other pole of the EMF machine. In this case, two coils act independently, but their combination is equivalent to a single cylindrical coil. The design of one half of the openable coil is illustrated in Figure 6. The pictures of the actual coil validated in laboratory conditions are shown in Figure 7. This coil was employed for joining a cylindrical tube to a cylindrical mandrel and also a rectangular tube to an inner rectangular mandrel, both shown in Figure 8. In the second case an openable concentrator was involved in the joining process [6]. In both cases the cylindrical and rectangular mandrels had grooves which were filled with tube material.

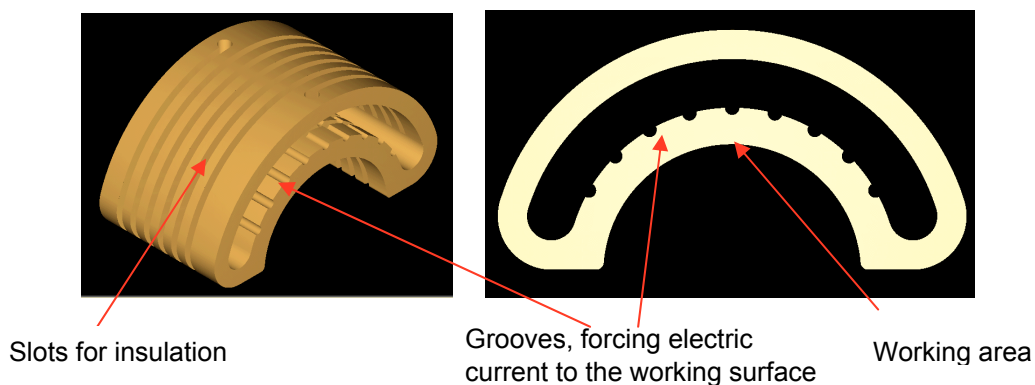
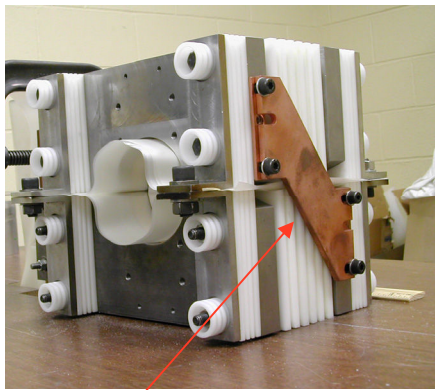
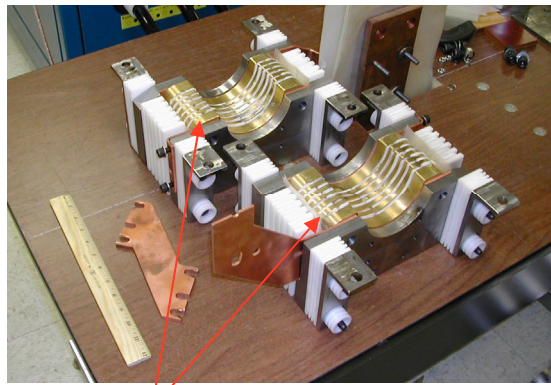


Figure 6: A spiral of the half of an openable coil



Electric connection between the halves of the coil



Assembled halves of the coil

Figure 7: An openable coil in assembled (left) and disassembled (right) position

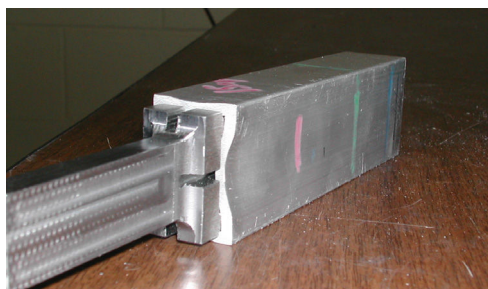


Figure 8: Examples of joints assembled using the openable coil

References

- [1] *Beliy, I.; Fertik, S; Khimenko, L:* Electromagnetic Metal Forming Handbook . Kharkov, USSR:Visha Shkola, 1977, p.62.
- [2] *Golovashchenko, S.; Mamutov, V.; Dmitriev, V.; Sherman, A.:* Formability of sheet metal with pulsed electromagnetic and electrohydraulic technologies. Proceedings of TMS symposium "Aluminum-2003," San-Diego, 2003, p.99-110.
- [3] *Imbert, J.; Winkler, S.; Worswick, M.; Olivera, D.; Golovashchenko, S.:* The effect of tool/sheet interaction in damage evolution of electromagnetic forming of aluminum alloy sheet. Transactions ASME. Journal of Engineering Materials and Technology, 2005, N1, p.145-153.
- [4] *Golovashchenko, S.:* Apparatus for Electromagnetic Forming a Workpiece, US Patent Application # 11/163411. October 18, 2005.
- [5] *Golovashchenko, S.; Dmitriev, V.; Krause, A.; Canfield, P.; Maranville, C.:* Apparatus for Electromagnetic Forming with Durability and Efficiency Enhancements, US Patent Application # 10/967978, October 19, 2004.
- [6] *Golovashchenko, S.; Dmitriev, V.; Sherman A.:* An Apparatus for Electromagnetic Forming, Joining and Welding. US Patent 6,875,964 B2, April 5, 2005.
- [7] *Golovashchenko, S.:* Springback calibration using pulsed electromagnetic field, Proceedings of NUMISHEET'2005, Detroit, 2005, p.284-285.

Purposive Design of a Magnetic Sheet Metal Forming Facility

P. Werdelmann¹, D. Peier¹

¹ Institute of High Voltage Engineering and EMC, University of Dortmund, Germany

Abstract

This paper is about the identification of lumped elements within an electric circuit diagram in the context of electromagnetic sheet metal forming. Based on fundamental physical considerations the forming coil and its workpiece can be modeled as a transformer, which is loaded on its secondary side by a resistor. A systematic oriented design process relating to an aimed at purpose is introduced in order to avoid time extensive trial-and-error methods. Based upon the theory of electromagnetic field equations, the complex impedance of the sheet metal is analytically identified as a function of the radial component. Based on the introduction of a force equivalent quantity, ways of designing and optimizing the remaining free parameters are presented. Thus, a design process for a forming facility is possible as the desired electromagnetic force can be characterized by the currents running through the forming coil and the sheet metal.

Keywords:

Network synthesis, Analytic modeling, Electromagnetic coupling

1 Introduction

A purposive design of a magnetic sheet metal forming facility determines the properties of the needed elements, apart from already existing realizations, under the aspect of efficiency and robustness. To assess the result of such a design process, it is important to know the principal restrictions, which are given by the forming mechanism itself and various boundary conditions. The following chapters examine the general behaviour of the magnetic forming process by use of an electric network model. The objective which is to be examined is the temporal distribution of the electromagnetic force the workpiece is exposed to. Therefore, a description of the aerielly distributed force density is captured by means of an equivalent quantity, which is expressed by integral values within the electric circuit structure.

2 Equivalent circuit structure

The main principle of an electromagnetic sheet metal forming process is the interaction between a generated magnetic field and induced eddy currents resulting in electromagnetic force. Figure 1 shows the arrangement consisting of a flat spiral coil beneath a conducting plate. A pulsed current $i_1(t)$ through the forming coil causes a temporally changing magnetic flux Φ_1 , which affects the sheet metal diffusely and induces an eddy current $i_2(t)$ within the workpiece. Obviously, this coupling of two currents by a magnetic field shows analogy to a transformer concerning the ability of being modeled by an electric circuit diagram.

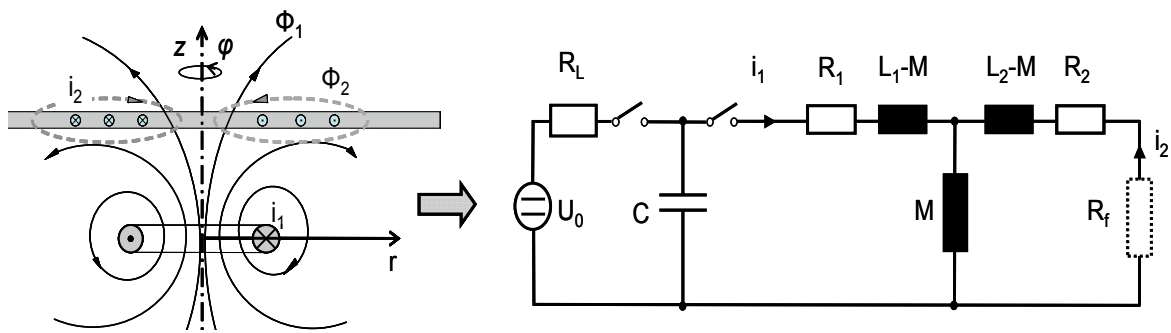


Figure 1: Principal structure of an electromagnetic sheet metal forming facility. The setup consisting of a flat spiral coil beneath the workpiece is modeled by the equivalent circuit diagram of a transformer

The primary side of this electric network model describes the forming tool with its self-inductance L_1 in series with an ohmic resistance R_1 . By means of the mutual inductance M the coil current is coupled with the workpiece current density, which is aurally distributed within the sheet metal. Its network elements R_2 and L_2 depend on the material's conductivity as well as on the frequency. The secondary side of this transformer is loaded by another resistive element R_f , which dissipates the forming energy being transferred to the workpiece. This energy is part of the initially stored energy provided by the capacitive energy storage C . Further research activities, which have not been published yet, reveal that the current through the workpiece is barely affected by the resistance R_f so that the resistance R_2 is assumed to be much larger than R_f . This assumption is valid for a fixed sheet metal or if the workpiece is activated by a short initial impulse of force.

The transition from aurally distributed quantities to concentrated network elements has to keep a physical reasonability as the magnetic flux is modeled by the network structure's inductivities relating to the respective flux causing current. These, of course, are integral values; hence, the electric circuit diagram in figure 1 can not directly consider any densities or spatial electromagnetic field distributions.

3 The sheet metal's network elements

The equivalent lumped elements R_2 and L_2 of the workpiece are determined by a given local distribution of the current i_2 , which is based on the induction of an eddy current density $J_2(t)$ at a certain frequency. The complex impedance of a metallic conductor is generally given as the quotient of the electric voltage and the current. In case of presence of the skin effect there is no homogeneous current density within the conductor's cross section. Thus, with regard to figure 2, the resulting complex impedance is being expressed with respect to the causing field quantities [1, 2]. In case of a rotationally symmetric conducting plate the impedance is formed by the circumferential electric field strength E_0 at the plate's surface in relation to the entire current flowing through the workpiece.

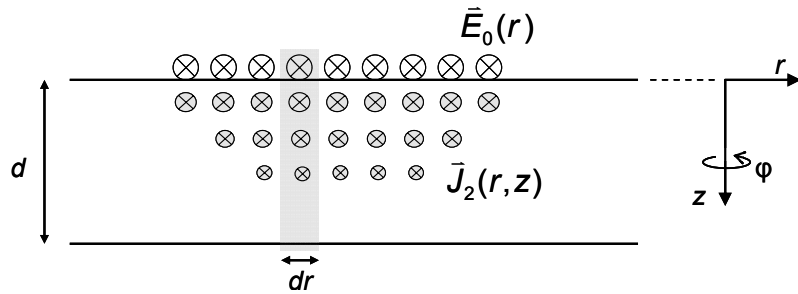


Figure 2: Simplified illustration for the determination of the sheet metal's complex impedance. Within an infinitesimal cross section the field distribution is homogeneous

$$\underline{Z} = \frac{\underline{U}}{\underline{I}} = \frac{\oint \bar{E}_0(r) dl}{\iint \bar{J}_2(r, z) dr dz} \quad (1)$$

This equation is valid for homogenous field distribution among the radius. However, $E_0(r)$ and $J_2(r, z)$ are functions depending on the r - and z -component. The z -dependence is known and can be separated as a factor, which is not possible for the radial dependence. Thus, impedance per unit length remains instead of a discrete value from equation (1) when integrating the current density among the plates thickness d . The resulting impedance per unit length can thereby be written as a function of the radius and depends on the frequency, as considered by the skin penetration depth δ [3].

$$\underline{Z}'(r) = \frac{2\pi r \cdot \bar{J}_0(r)}{\kappa \cdot \bar{J}_0(r) \cdot \int_0^d e^{-\frac{(1+j)z}{\delta}} dz} = \frac{2\pi r \cdot (1+j)}{\kappa \cdot \delta \cdot \left[1 - e^{-\frac{(1+j)d}{\delta}} \right]} \quad (2)$$

To get an expression for concentrated network elements, the complex apparent power \underline{S}_2 can be calculated as an integral value. The real part of this expression represents the real power, which is dissipated by the ohmic resistance R_2 , whereas the imaginary part

corresponds with the idle power and the plate's inductance L_2 . For an assumed current distribution these quantities are presented in figure 3 as functions of the frequency. When relating the real part of the sheet metal's impedance R_2 to the imaginary part ωL_2 it can be seen that there is a global minimum of the impedance relation, depending on a certain frequency.

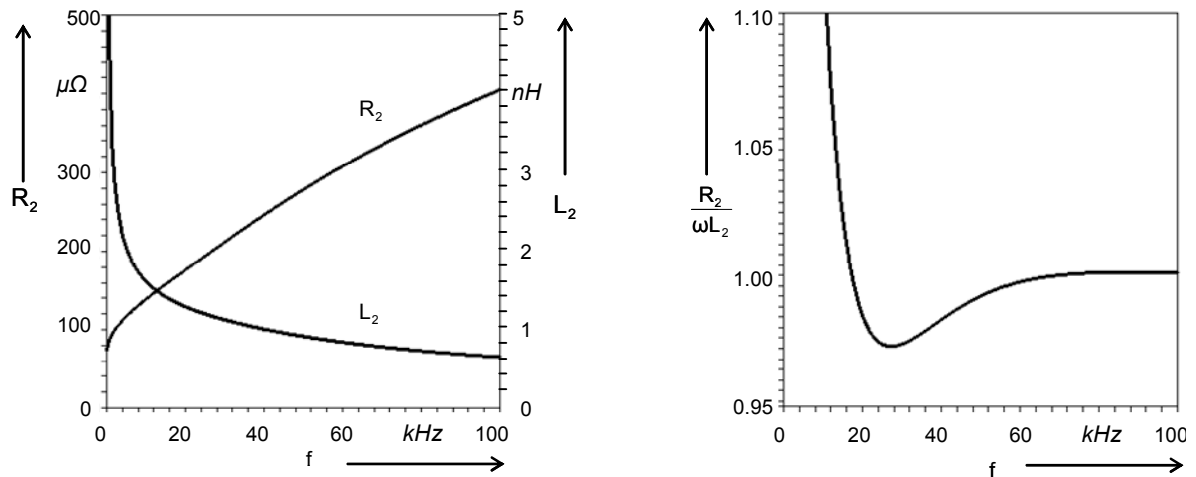


Figure 3: Course of the sheet metal's resistance R_2 and inductance L_2 and the relation of both as a function of the eddy current's frequency (material: aluminium, $d=2\text{mm}$)

4 Calculation of the electromagnetic force

By means of field quantities the resulting electromagnetic force between forming coil and workpiece is obtained by the vector product of the coil's magnetic flux density B_1 and the eddy current density J_2 within the workpiece [4]:

$$\vec{F} = \vec{J}_2 \times \vec{B}_1 \quad (3)$$

Regarding the electric circuit structure from figure 1, J_2 is expressed by the integral quantity $i_2(t)$, whereas B_1 is represented by the product of the coil's self inductance L_1 and the flux causing current $i_1(t)$. Therefore, a substitutive quantity as an equivalent $F^*(t)$ for the magnetic force $F(t)$ is given by equation (4).

$$F(t) \sim L_1 \cdot i_1(t) \cdot i_2(t) = F^*(t) \quad (4)$$

By this expression it is evident that the whole information about the temporal development of the electromagnetic force can be obtained from the electric equivalent circuit diagram.

For a further discussion the elements from the circuit structure in figure 1 are lumped to substitutive elements, which provide the ability of the transition to a RLC series resonant circuit. These elements are determined by rules of network calculation and are carried over to a substitutive network topology, as shown in figure 4.

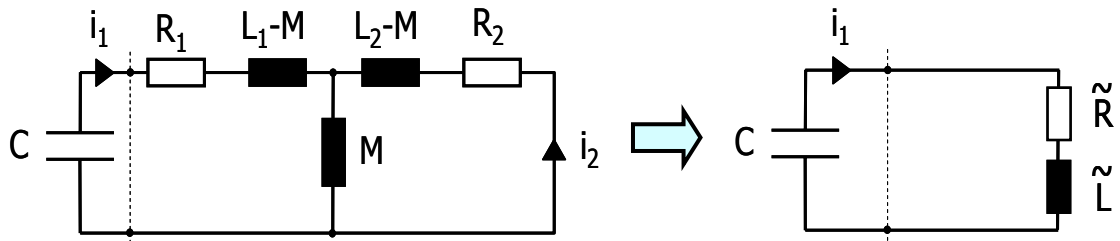


Figure 4: Transition from a transformer equivalent circuit to a RLC series oscillating circuit

$$\tilde{R} = R_1 + \frac{R_2 \cdot \frac{M^2}{L_2^2}}{1 + \left(\frac{R_2}{\omega L_2}\right)^2} \quad \text{and} \quad \tilde{L} = L_1 - \frac{L_2 \cdot \frac{M^2}{L_2^2}}{1 + \left(\frac{R_2}{\omega L_2}\right)^2} \quad (5)$$

The new circuit diagram's damped oscillation is characterized by the resonant angular frequency ω_0 and the quality factor Q [5,6], as expressed by equation (6).

$$\omega_0 = \frac{1}{\sqrt{\tilde{L}C}} \quad \text{and} \quad Q = \frac{\sqrt{\tilde{L}C}}{\tilde{R}} \quad (6)$$

For the RLC series oscillation circuit an ordinary second order differential equation for the capacitor's voltage is obtained due to the fact that there are two different types of energy stores in this network. The corresponding solution for the coil current is found to be:

$$i_1(t) = -\omega \cdot C \cdot U_0 \cdot \frac{4Q^2}{4Q^2 - 1} \cdot e^{\left(-\sqrt{\frac{1}{4Q^2 - 1}} \cdot \omega t\right)} \cdot \sin(\omega t) \quad (7)$$

The identified coil current is subsequently used to determine a mathematical expression for the load current $i_2(t)$ flowing through the sheet metal. Within the electric circuit diagram in figure 4, the load branch is parallel to the mutual inductivity so that the voltages may be equated, resulting in a first order differential equation for the coil current $i_2(t)$, for which the solution is given in equation (8). Within this expression, a phase shift ψ occurs, which is mainly caused by the sheet metal's parameters R_2 and L_2 , as expressed by equation (9).

$$i_2(t) = -C \cdot U_0 \cdot \frac{M}{L_2} \cdot \frac{\sqrt[3]{\frac{4Q^2}{4Q^2 - 1}}}{\left(1 + \left(\frac{1}{\sqrt{4Q^2 - 1}} - \frac{R_2}{\omega L_2}\right)^2\right)} \cdot \left[\sqrt{1 + \left(\frac{1}{\sqrt{4Q^2 - 1}} - \frac{R_2}{\omega L_2}\right)^2} \cdot e^{\left(\frac{\omega t}{\sqrt{4Q^2 - 1}}\right)} \cdot \sin(\omega t + \psi) - \frac{R_2}{\omega L_2} \cdot e^{\left(\frac{R_2 \cdot \omega t}{\omega L_2}\right)} \right] \quad (8)$$

$$\psi = \arctan \left(\frac{\frac{R_2}{\omega L_2}}{1 - \frac{1}{1-4Q^2} - \frac{1}{\sqrt{1-4Q^2}} \cdot \frac{R_2}{\omega L_2}} \right) \quad (9)$$

The expression for the workpiece current $i_2(t)$ shows the same exponentially damped, sinusoidal temporal development as the coil current $i_1(t)$. In addition, the sheet metal's network parameters cause a volatile current component, which causes an extra damping of the current's first amplitude peaks. Because of the phase shift ψ the product of both currents is not always positive, which leads to a possible change of the force's direction. Figure 5 shows the run of the force equivalent quantity F^* for a workpiece constant of $R_2/\omega L_2=1$ as a function of time and the quality factor Q .

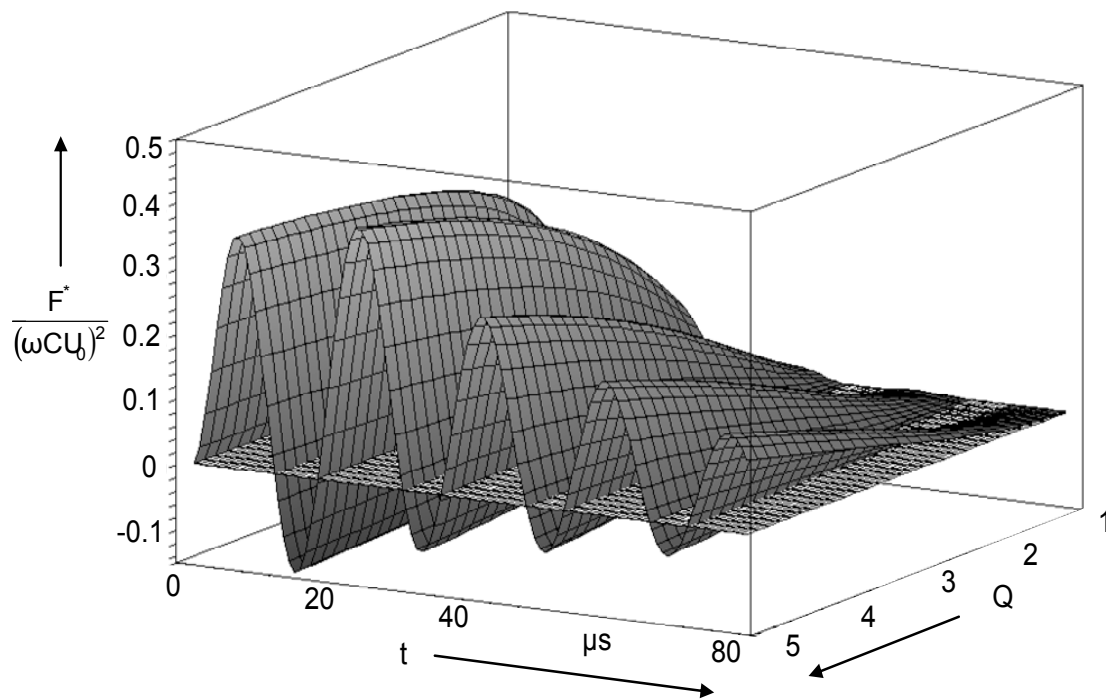


Figure 5: Normalized temporal development of the force equivalent quantity F^* , depending on the facility's quality factor. For a certain workpiece constant ($R_2/\omega L_2=1$) a negative force is possible due to the phase shift between the participated currents, and thus, decreasing the efficiency

5 Assessment of the forming process

For the best temporal course of an initial electromagnetic force, trying to get near a desired unipolar temporal course, the argument of the arctan function in equation (9) has to be minimized. This is achieved for a high quality factor Q as well as for a small workpiece constant $R_2/\omega L_2$. For a purposive analytical design strategy the challenge is to determine the free parameters of an existing forming facility in order to match the required demands. For typical applications and types of workpiece materials the workpiece parameter $R_2/\omega L_2$ is almost equal to 1, as figure 3 reveals. With this constant, expressions (5) can be simplified and put into the quality factor's equation (6). By introducing the magnetic leakage factor σ a conditional equation for the overall Q -factor is obtained in equation (10).

$$Q = Q_A \cdot \frac{\sqrt{\frac{\sigma+1}{2}}}{1 + \frac{1}{2} \cdot \frac{L_1}{R_1} \cdot \frac{R_2}{L_2} \cdot (1-\sigma)} \quad \text{with } \sigma = 1 - \frac{M^2}{L_1 \cdot L_2} \quad (10)$$

Q_A is the quality factor and ω_{0A} the resonant angular frequency of the facility in non-load operation, e.g. without the workpiece.

$$Q_A = \frac{1}{R_1 \cdot C \cdot \omega_{0A}} \quad \text{with } \omega_{0A} = \omega_0 \cdot \sqrt{\frac{\sigma+1}{2}} \quad (11)$$

The proportion R_1/L_1 in equation (10) is obtained by the combination of (5), (6), and the magnetic leakage factor σ .

$$\frac{R_1}{L_1} = \frac{1}{2} \left(\frac{\omega_0}{Q} (\sigma+1) + \frac{R_2}{L_2} (\sigma-1) \right) \quad (12)$$

These general expressions imply the needed information for the application of a design process. From section 3 the sheet metal's impedance is received for the postulation that the skin penetration depth δ matches a quarter of the plate's thickness d , which implies a required frequency f . This assumption is made on the condition that, the magnetic field should be properly shielded by the workpiece. Generally, the skin penetration depth is user-defined and can be chosen. The quality factor is determined to be a value for which there is no more gain of the force equivalent's magnitude to be expected for an increasing Q . The according parameters are listed in table 1.

d [mm]	δ [mm]	f [kHz]	R_2 [$\mu\Omega$]	L_2 [nH]	$R_2/\omega L_2$	Q
2.0	0.5	28.14	209	1.22	0.973	3.5

Table 1: Design specifications and the resulting sheet metal parameters for a chosen skin penetration depth of $\delta=d/4$

To show the interrelation of the respective quantities, a graphic interpretation is presented in the form of a nomogram. Figure 6 pictures the nomogram of equations (10)-(12) for a specific workpiece parameter $R_2/\omega L_2=0.973$.

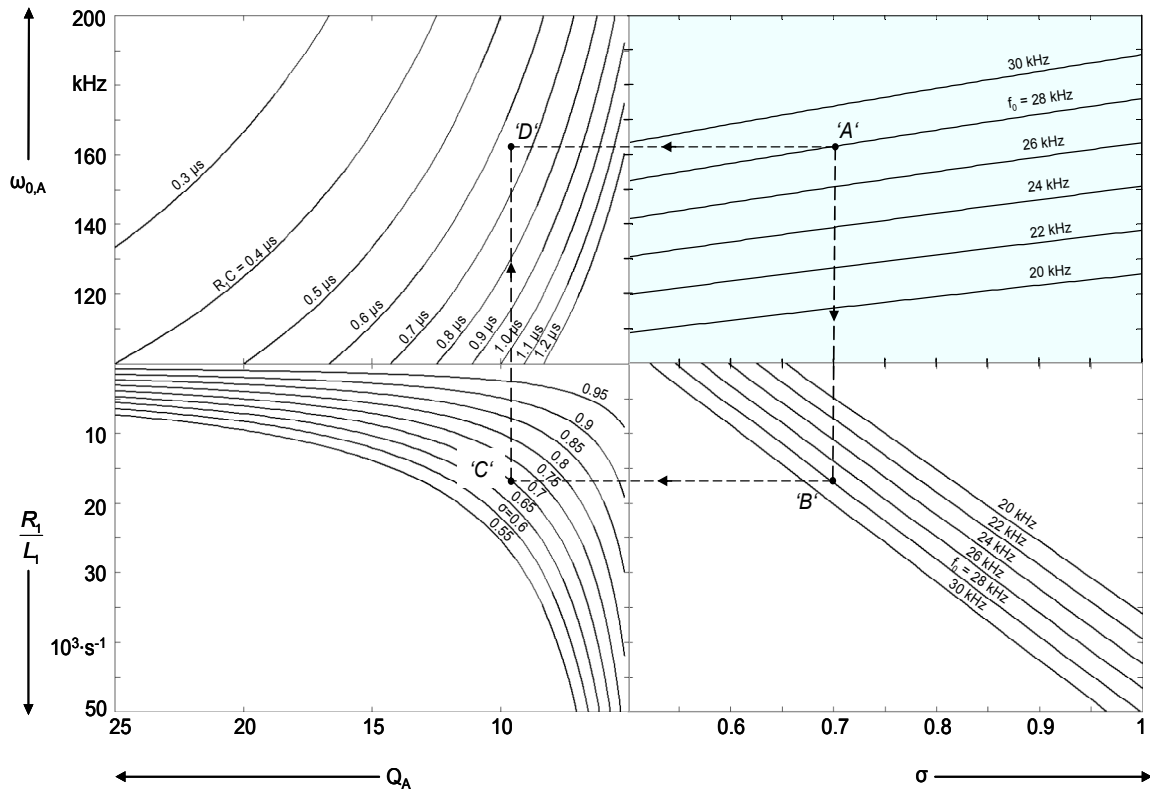


Figure 6: Nomogram chart of the mathematical relation of the participated quantities to identify the optimal combination of the facility's parameters

Each equation has its own pair of axes, implicating that particularly two quadrants share one common axis. The first quadrant shows the resonant angular frequency ω_{0A} over the leakage factor σ of the non-loaded facility with the frequency f_0 of the entire set, acting as the parameter for the array of curves. The second quadrant pictures the curves of the facility's quality factor Q_A as a function of its resonant frequency ω_{0A} . The parameter for these curves is the capacitor's time constant R_1C . Additionally, this quality factor is shown as a function of the reciprocal coil's time constant R_1/L_1 . According to equation (12), the fourth quadrant shows the quantity R_1/L_1 , depending on the magnetic leakage factor σ with the resonant frequency f_0 as parameter. The leakage factor σ is a rate for the magnetic coupling between forming coil and workpiece. It should be mentioned that all scales within this chart are suppressed-zero scales. So it is evident that there are definite restrictions concerning a technical feasibility.

With the parameters from table 1, which act as input data for the optimization, an example design process is performed with the objective to identify the optimal coil parameters regarding to a given energy store. For this arrangement the influence of a different leakage factor as a rate for a changing mutual inductance is parametrically

examined. The starting information is the leakage factor σ for which, in combination with the given frequency $\omega \approx \omega_0$, the point 'A' is determined. A projection into the fourth quadrant delivers the point of intersection with the same parameter's curve in 'B'. Keeping in mind the start information σ , the only curve to be depicted out of the array in quadrant three is the one for the same leakage factor as parameter. Point 'C' is projected into the second quadrant where the intersection with the determined resonant frequency ω_{0A} reveals the conditional value for the time constant R_1C . In combination with equations (10) to (12) the unknown elements can be identified. In table 2 the identified network elements of the forming coil are listed for three different cases of an initial leakage factor, from which the third case's path ('A-B-C-D') is pictured exemplarily in the nomogram chart. The boundary condition for this example is formed by the capacity, which is set to $C = 10 \mu\text{F}$.

	R_1/L_1	Q_A	ω_{0A} [kHz]	f_{0A} [kHz]	R_1C [μs]	R_1 [m Ω]	L_1 [μH]	M [nH]
$\sigma=0.60$	6 500	25.0	157	25.0	0.27	27	0.42	15.5
$\sigma=0.65$	12 000	13.5	160	25.5	0.46	46	3.84	43.7
$\sigma=0.70$	17 000	9.5	162	25.8	0.65	65	3.82	40.34

Table 2: Solution of the forming coil's optimized parameters for the load parameters given in table 1

For different values of the leakage factor the quality factor of the facility gets smaller, whereas the relation between ohmic resistance and self-inductance R_1/L_1 of the forming coil has to be increased in order to keep the main quality factor Q high and the phase shift ψ low.

6 Conclusion and outlook

Within this work, ways of identifying and optimizing unknown network elements of an electromagnetic forming facility's components are presented. In order to set up conditional equations for the examined quantities, the temporal behaviour of the entire facility is investigated by means of electric network analysis. Thus, the coil current as well as the workpiece current are obtained as solutions of the system's particular ordinary differential equations. As the one-dimensional network model can not consider any aerial distributions of electromagnetic field terms, a substitutive quantity for the electromagnetic force as an integral value is introduced. Therefore, the product of the coil's self-inductance with both the coil's current and the work piece's current, is examined and treated as the objective function, for which an optimal time course is aimed at.

Due to a phase shift between coil and workpiece current the resulting force changes its direction momentarily, which is dependent on the workpiece characteristic.

The sheet metal's concentrated network elements are obtained by treating the apparent power within the sheet metal as an integral value, which is caused by the aerielly distributed eddy current density and the radial impedance per unit length. The influence of different materials acting as the workpiece regarding the efficiency of electromagnetic sheet metal forming can be examined in terms of the system's network performance. The mentioned phase shift is treated to be minimized, but the time-based analysis of the electric network model reveals that this phase angle will only disappear if the workpiece's resistive part tends to zero. This implies that an entirely unipolar temporal development of the electromagnetic force can not be achieved.

The quality factor of the entire system has been shown to be a useful criterion for optimizing the process' efficiency. Therefore, the mathematical interrelations between the participating quantities is figured out and used to determine the system's free parameters. The presentation of the individual functions, which are affecting the quality factor, is useful to get an overview of the respective coherences. This chart also shows restrictions for the range of the optimized quantities, according to a technical feasibility.

The presented design process can also be applied backwards with only little change in operation for different demands. For example, this will be useful to determine the optimal set of parameters for diverse types of energy stores, whether it is a capacitive or inductive one. Having determined a set of optimized electrical network parameters, the next step should be to apply this information to a geometric design process concerning the magnetic field distribution with regards to geometry.

References

- [1] *Simonyi, K.:* Theoretische Elektrotechnik. Barth Verlagsgesellschaft, Bad Langensalza
- [2] *Schunk, H.:* Stromverdrängung. Dr. Alfred Hüthig Verlag, Heidelberg, p. 104-108, 1973
- [3] *Binns, K.J.; Lawrenson, P.J.; Trowbridge, C.W.:* The Analytical and Numerical Solution of Electric and Magnetic Fields. John Wiley & Sons Ltd, Chichester, p 97-99, 1992
- [4] *Schmidt, V.:* Untersuchung der magnetischen Induktion, Stromdichte und Kraftwirkung bei der Magnetumformung. Verlag W. Girardet, Essen, p. 35, 1976
- [5] *Philippow, E.:* Taschenbuch der Elektrotechnik, Band 1. Carl Hanser Verlag, München, 1976
- [6] *Leonhardt, W.:* Wechselströme und Netzwerke. Vieweg Akademische Verlagsgesellschaft, Braunschweig, 1968

Design, Construction, and Applications of the Uniform Pressure Electromagnetic Actuator*

M. Kamal¹, V. Cheng², J. Bradley³, S. Hatkevich⁴, G. S. Daehn^{1*}

¹ Department of Mat. Sci. and Eng., The Ohio State University, Columbus, OH, USA

² Metals Industry Research and Development Center, Kaoshung, Taiwan

³ General Motors R&D, Detroit, Michigan, USA

⁴ American Trim Corporation, Lima, OH, USA

*Corresponding Author: Daehn.1@osu.edu, 614-292-6779

Abstract

High velocity forming can lead to better formability along with additional benefits. The spatial distribution of forming pressure in electromagnetic forming can be controlled by the configuration of the actuator. A new type of actuator is discussed which gives a uniform pressure distribution in forming. It also provides a mechanically robust design and has a high efficiency for flat sheet forming. Key quantitative concepts are presented that help in the design of the system. Examples of uses of the actuator are then presented, specifically with regard to forming shapes and surface embossing. This paper emphasizes the approaches and engineering calculations required to effectively use this actuator.

Keywords:

Sheet metal forming, High velocity forming

1 Introduction

Electromagnetic forming (EMF) is a non-contact forming technique where large forces can be imparted to a conductive metallic workpiece by pure electromagnetic interaction [1]. When properly applied, this can accelerate the sheet to velocities on the order of 200 m/s over a distance of a few millimeters. This high velocity forming can be quite beneficial. It can provide: improved formability, improved strain distribution, reduction in wrinkling, active control of springback, and the possibility of local coining and embossing [1, 2].

* This work is largely based on the Ph.D. Thesis of Manish Kamal. It can be accessed at <http://www.ohiolink.edu/etd/view.cgi?osu1127230699>.

If one is to use conventional electromagnetic forming actuators to form directly, it is important that the EM pressure distribution is appropriate for the part that one would wish to form. It has been found that the velocity distribution within the sheet metal during forming significantly influences the result [3]. Risch et al. [3] have shown that puckers can form when the launch velocity is not uniform.

The spatial distribution of forming pressure can be controlled by the configuration of the actuator [4-6]. Traditionally, EM actuators have been used to form axisymmetric parts as in tube expansion and compression. Sheets have been formed with flat spirals. One issue with spiral actuators of any configuration is that the pressure distribution is not uniform. Figure 1 shows the typical example where a flat spiral actuator was used to accelerate a circular disk. Here, the magnetic pressure is zero at the center of the part and the edges and reaches a maximum midway between them.

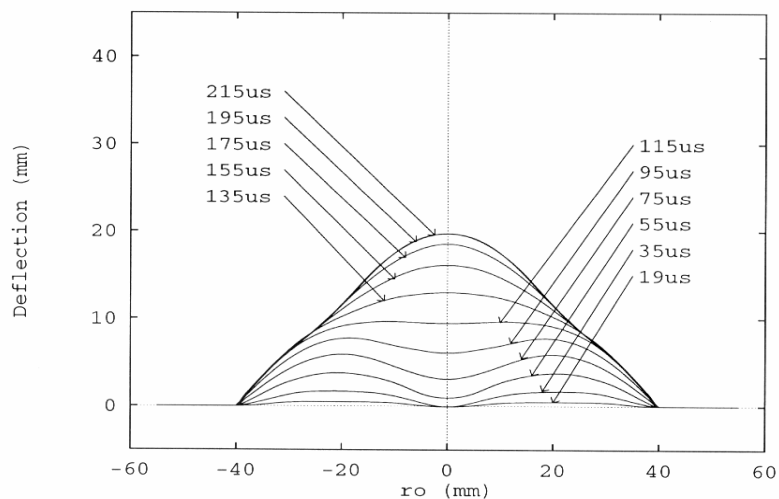


Figure 1: CALE calculated displacement profiles of Takatsu disk [7] during deformation with a flat spiral actuator [8]. The sheet is secured at its circumference.

The early literature (from the first wave of electromagnetic forming research) seems to have only one reference to a non-axisymmetric actuator [6]. It consists of an elongated actuator and that work also discusses the non-uniform pressure distribution developed. Work on actuators for flat forming of sheet has been limited and it appears that an actuator that gives a uniform pressure distribution has not been available until now.

Uniform pressures can be developed if the current in the actuator and sheet are both uniform and the gap between them is roughly constant. It can be achieved in two ways: (i) a section along one perimeter of a flat spiral actuator (which might be elongated). Although the pressure varies along the radius of the coil, if one takes a small section, the pressure distribution at that section is close to uniform. An appropriate eddy current distribution must be considered if this approach is to have useful efficiency. (ii) By using a linear actuator, like taking a section in a three bar coil. Along any particular bar the pressure is close to being uniform so long as the sheet to coil gap is small relative to the bar width. The efficiency of this single-turn approach may be poor, however.

Process efficiency is of paramount importance. The cost of electrical energy in EMF is rather trivial, but if one is to use especially large energies or charging voltages, these cause problems with electrical interconnects and insulation, this puts large

mechanical forces on the actuators that can damage the electromagnetic actuators. The approaches mentioned above can create a uniform pressure distribution, but the efficiency of such systems is poor.

This paper presents a new approach, which offers a uniform pressure distribution as well as high efficiency for flat sheet forming.

2 Experimental procedure

Figure 2 shows a schematic of a section through the uniform pressure actuator. When the capacitor bank is discharged the primary current flows through the primary coil. The primary coil is well insulated from the outer conductive channel. The outer channel and the sheet metal form a closed circuit and the induced current flows through it. Repulsive Lorentz forces develop between the opposed primary and induced currents, causing sheet metal to be thrown at the die with potentially high velocity. Since the induced current path completely encircles the actuator there is little loss of the magnetic flux energy and hence better efficiency. Also, since the primary coil repels from both the sheet and channel it is forced onto a mandrel and this can provide a robust actuator design.

Three different actuators were used in this study. The first (Actuator 1) was based on winding 15 turns of copper magnet wire with a 9.0 mm² round cross section over a machined G-10 laminated phenolic composite block. The wound core was then placed inside an aluminum channel (7.5 x 2.5 x 9.375 cm and 0.3125 cm thick), which has Kapton[®] insulation on its interior. Urethane potting was then used to provide insulation and structural support. The actuator with the metal sheet is then clamped using an arrangement of eight nuts and bolts with a typical total clamping force of 80 kN. Actuator 2 was similar in construction, except it used 23 turns of rectangular copper wire (11.5 mm² cross section), presented a larger active area (15 x 15 cm), and used a machined, contoured aluminium return path. The third generation actuator (Actuator 3) featured an 11 turn primary coil machined from copper with a much larger cross section. It presents pressure over an area of (5 x 8 cm).

All actuators were driven using a commercial Maxwell-Magneform capacitor bank. The bank has a maximum stored energy of 16 kJ. The energy is stored in 8 capacitors, each with a capacitance of 53.25 µF. The system has a maximum working voltage of 8.66 kV. Both the number of capacitors and charging voltage are changed to control the discharged energy and voltage. Primary and induced currents are measured by active Rogowski flexible coils from Rocoil [8].

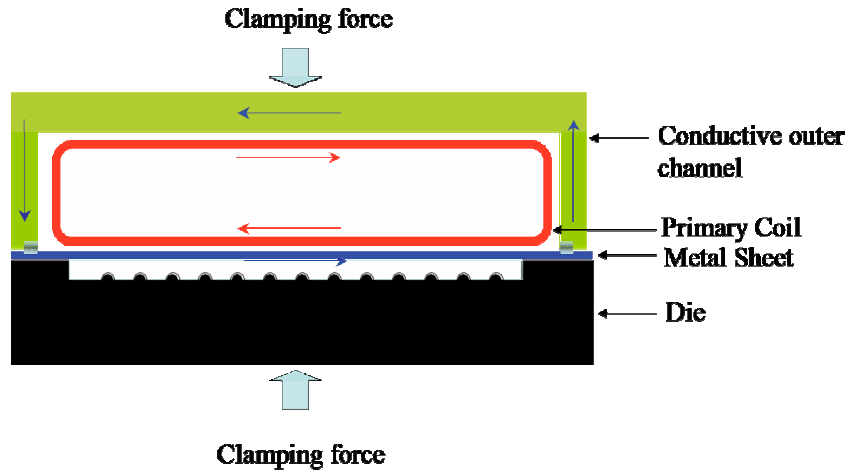


Figure 2: Schematic of a uniform pressure coil. The primary coil has many turns going into the depth of the paper

3 Key design concepts

In essence, the coil shown in Figure 2 acts as a simple LRC circuit. The variation in primary current with time is easily described in this manner. The most difficult part of a design calculation is determining the inductance of the actuator-workpiece system. Simple upper and lower bounds can be easily calculated based on assuming the inductance of an unshielded solenoid for the upper bound, and assuming the magnetic flux is completely contained in the volume between the outside of the coil and inside of the return channel and workpiece. These can be represented as:

$$L_s^{low} = \frac{\mu_0 A_s n^2}{l_s} \quad (\text{Low frequency upper bound}) \quad (1)$$

$$L_s^{high} = \frac{\mu_0 A_{gap} n^2}{l_s} \quad (\text{High frequency lower bound}) \quad (2)$$

Here, L represents inductance, n is number of coil turns, l is length A_s represents that area inside the solenoid and A_{gap} represents the area between the coil and return path. These equations are shown along with experimental data in Figure 3. Based on this, usual procedures can be used to estimate peak currents, rise times, and so forth. The pressure that acts on the workpiece can be calculated as:

$$P_m = \frac{\mu_0 H_p H_i}{2} \quad (3)$$

Here, P_m is magnetic pressure, and H_p and H_i respectively represent the current densities expressed in current per length (width) in the primary and induced circuits respectively. Relative to metal yield strengths, the generated pressures generated in electromagnetic forming are generally small. It is the impact with the die that generally generates the high pressure that can produce deep embosses and other phenomena that require high pressure.

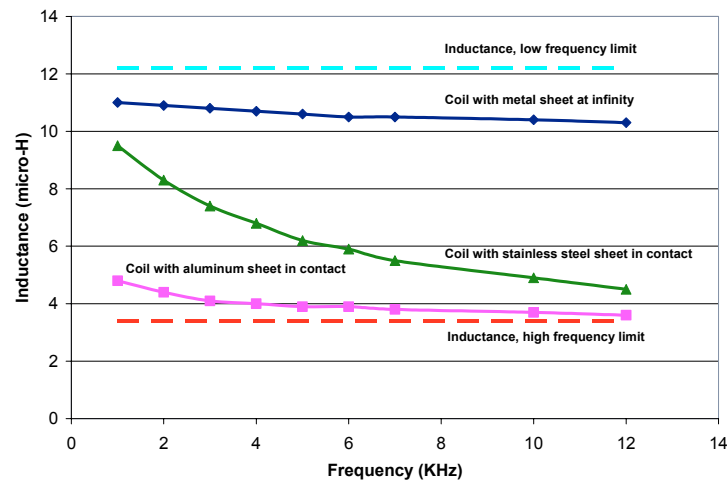


Figure 3: Variation of actuator inductance with frequency, measured with LCR Bridge (Actuator 2)

The pressure can accelerate a thin metal sheet towards a die in accord with Newton's first law. Because the pressures are substantial and the sheets are thin, over the space of just a few millimeters, the workpiece can be accelerated to significant velocities. This is demonstrated in Figure 4, which shows the predicted velocities of two aluminum sheets (both roughly 1mm in thickness) accelerated by two different coils. Very significant velocities can be reached using less than 2mm space for acceleration and only modest stored electrical energies are needed for launch.

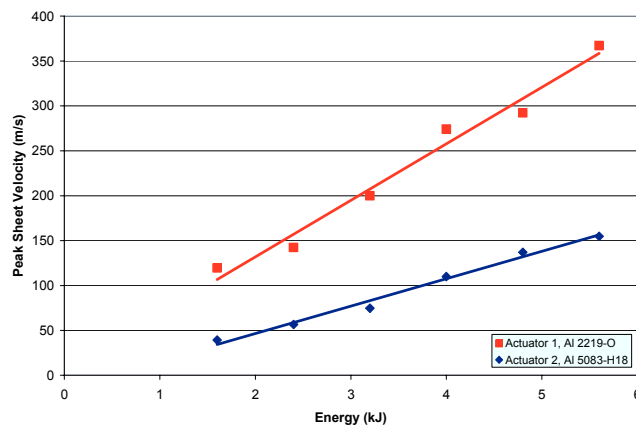


Figure 4: Predicted variation of peak sheet velocity with energy with actuators 1 and 2. Key assumptions are that plastic work is not done on acceleration and the sheet is only accelerated over the first quarter-cycle. The 2219 and 5083 sheets have thicknesses of 0.8 and 1.1 mm, respectively

4 Example operations with the UP actuator

The Uniform Pressure (UP) actuator provides capabilities that have not been available in a manufacturing tool. In short, it allows one to accelerate sheet metal to high velocities

very uniformly and robustly and in a manner that is extremely repeatable. The closest competitor to this is the flat spiral coil that has been used in electromagnetic forming. This coil has a well-known spatial distribution of pressure that is problematic in that the pressure vanishes in the center. Also, these coils can not survive long life service at high pressures. Plum quotes as this coil being able to only sustain 35 MPa [9], which is much less than more traditional tube compression coils can sustain (up to 340 MPa [9]). The UP actuator has repeatedly robustly produced pressures exceeding 100 MPa. In addition, the pressure distribution is uniform over the area of the sheet and the UP actuator uses the electrical energy from the capacitor bank in a more efficient way.

Figure 5 shows some examples of the kinds of operations that can be performed with the UP actuator. In addition, the actuator is well suited for complex punchless shearing operations. This shows that the coil can be used for large-scale forming operations, such as cell phone cases. Lastly, areas that require modest forming over large areas, like fuel cell bipolar plates, can be formed. There are two very important practical implications to this. First, because pressure is spatially uniform the same energy will appropriately shear or form ridges on the workpiece, regardless of location. Second, all these operations are done where only one side of the workpiece makes contact with any tool and the only moving part is the sheet itself. This has obvious advantages if one would like to shear or blank complicated shapes. Further, it means that coated or decorated materials can be formed without any contact on one side of the sheet.

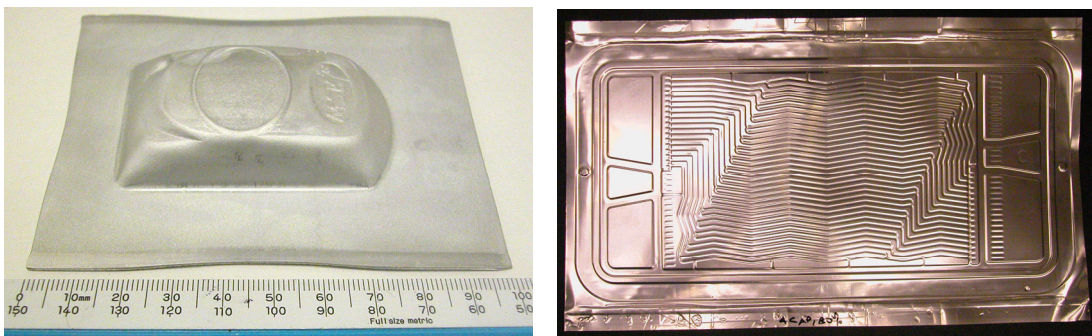


Figure 5: Examples of operations formed with the UP actuator at Ohio State. From left: an example of forming into an aggressive cellphone die. This example used 0.8mm thick 2219-0 and two shots were used to aid shape forming. Right shows a prototype fuel cell bipolar plate (22.5 cm x 35 cm) that was formed from 0.13mm thick 301 stainless steel. This plate was formed in three vertical sections using a 0.13mm thick copper driver and 19 kJ per forming operation

There is voluminous literature on the impact of solids and the effects of this in terms of both wave propagation and microstructure changes. Much of this literature is concerned with ballistic events that have velocities of 750 m/s and beyond. At or beyond these impact velocities materials suffer severe plastic deformation, spalling, and/or other forms of damage upon impact and this work is often concerned with penetration mechanics. At lower velocities the impact may be fully elastic, using linear elasticity; The impact pressure, P_i , that is developed when two semi-infinite elastic bodies labeled 1 and 2 collide at an impact velocity V_i is given as:

$$P_i = \frac{\rho_1 \rho_2 C_1 C_2}{\rho_1 C_1 + \rho_2 C_2} V_i \quad (4)$$

Here, for each material, 1 and 2, ρ represents density and C is the longitudinal wave speed. Longitudinal wave speeds are on the order of 7,000 m/s for most structural metals. For aluminum-steel and steel-steel impact pressures of about 2 GPa and 5.6 GPa are generated for a 200 m/s impact. Higher pressures are available by modifying the strike material or by increasing the impact velocity. Also, at these pressures there are significant deviations from linear elastic behavior. The required equations of state are well known (Example, these are included in the libraries for impact codes such as AUTODYN) and these deviations cause higher pressures than estimated from the elastic equation and for planar impact events the shock wave is not dissipated terribly rapidly by plastic deformation.

This impact pressure can be useful in several aspects of surface engineering. First, pressures high enough to produce significant microstructural changes, such as those produced by techniques as e.g. laser-shock-peening. Second, as shown by Prandtl's 1920 analysis of the hardness test, if a deformable material is pressed over a rigid surface with a pressure that is some factor (about 3 times) greater than the flow stress of the deformable material it will flow and conform to the surface of the rigid material. This is the basic theory behind hardness testing. The pressures generated by Equation 4, thus, can exceed the flow stress of common engineering metals by many times. So, if features are significantly thinner than material thickness simple impact can be used to reproduce them. Figure 6 shows an example of this. Here, aluminum sheets are impact embossed into a decorative optical diffraction grating made from electroless nickel (much harder than aluminium or copper). Optically, the grating pattern is transferred to the metal sheet and SEM shows that there is very good reproduction of the submicron features. This manner of surface reproduction may be suitable for many problems in micro manufacturing.

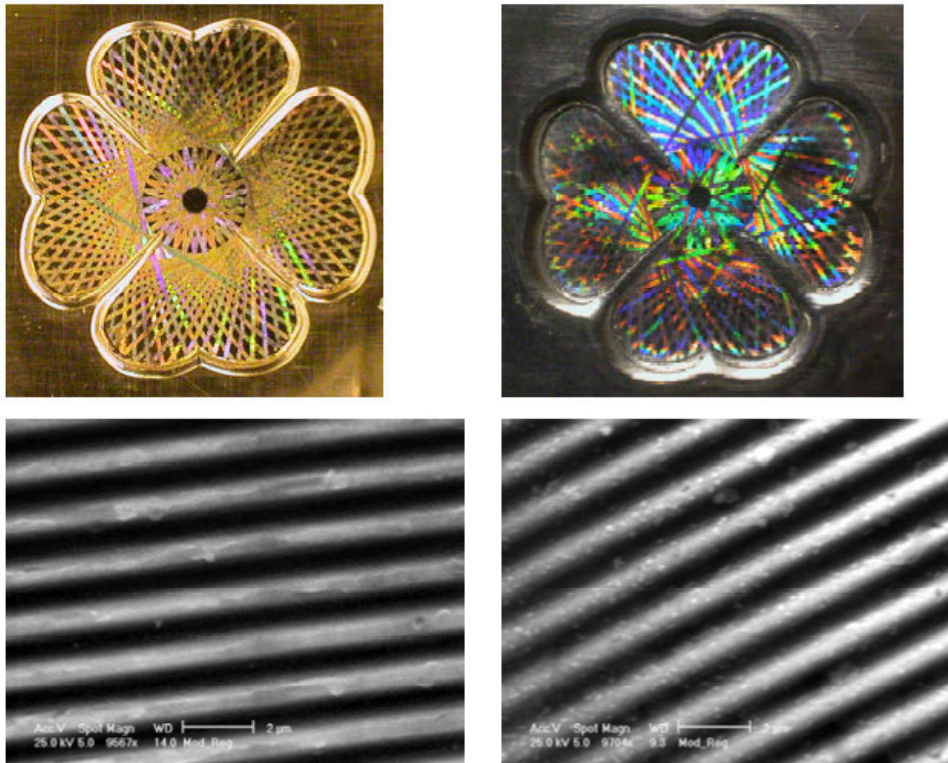


Figure 6: Examples of embossing onto sheet from a coin with a holographic image (about 2.5 cm across) into 0.13 mm thick soft copper sheet (left) and 0.25mm thick 5052-H32 sheet. Both experiments had rough vacuum on both sides of the sheet and a standoff of 2.32 mm. The copper was formed at 2.4 kJ; the aluminum was formed at 4.0 kJ. SEM images compare the original holographic surface (electroformed nickel) and the pattern embossed in the copper (right). In both cases the entire area formed was about 100 x 75 mm

5 Conclusions

A new type of electromagnetic actuator that can produce pressure relatively uniformly over sheet structures is presented. The actuator is mechanically robust and electrically efficient. It can develop sheet velocities in excess of 200 m/s over short acceleration distances. This can make it appropriate for many embossing and/or micro manufacturing applications.

References

- [1] Daehn, G.S.: High Velocity Metal Forming. Draft for publication in ASM Handbook (2003/2004), "Forming and Forging", (2003)
- [2] Daehn, G.S.: Electromagnetically Assisted Stamping-A vision of a future for Metal Forming. www.hyperplasticity.com, April, (2005)
- [3] Risch, D.; Beerwald, C.; Brosius, A.; Kleiner, M.: On the Significance of the Die Design for Electromagnetic Sheet Metal Forming. Proceedings of the First International Conference on High Speed Forming. pp. 191-200, (2004)

- [4] *Belyy, L. V.; Fertik S. M.; Khimenko, L. T.:* Electromagnetic Metal Forming Handbook. (A Translation of the Russian Book: Sprvochnik Po Magnitno-impul' Snoy Obrabotke Metallov), Translated by M. M. Altynova and Glenn S. Daehn, Columbus, OH, (1996)
- [5] *Batygin, Y. V.; Daehn, G. S.:* The Pulse Magnetic Fields for Progressive Technologies. Kharkov, Columbus, (1999)
- [6] *Hassani, S.T.S.A.; Duncan J. L.; Johnson, W.:* Techniques for Designing Electromagnetic Forming Coils, Proc. Second International Conference on High Rate Forming, Colorado, USA, pp. 5.1.2 -5.1.16, (1969)
- [7] *Takatsu; Kato; Soto; Tobe:* High-Speed Forming of Metal Sheets by Electromagnetic Force. JSME International Journal, Series III, Vol. 31, No. 1, pp. 142-148, (1988).
- [8] <http://www.rocoil.cwc.net>, April 2005
- [9] *Plum, M.:* Electromagnetic forming. ASM Handbook, vol. 14, 9 ed: ASM, 1995.

A 100 kJ Pulse Unit for Electromagnetic Forming of Large Area Sheet Metals*

W. Hartmann¹, M. Römheld¹, A. Donner²

¹ Siemens AG, Corporate Technology, CT PS 5, Erlangen, Germany

² Siemens AG, Automation and Drives, A&D MC RD 8, Chemnitz, Germany

Abstract

Magnetoforming of tube or sheet metal parts can significantly extend the range of geometries conceivable with state-of-the-art forming methods. A major advantage is the considerably higher forming speed of the process achievable by using a magnetic piston without inertia. Key for this technology is the development of reliable, long-lifetime, high current pulse power generators able to deliver tens to hundreds of kiloamps of peak current to a mainly inductive load which is highly variable in time during the forming process. A high-current, high energy pulse generator for electromagnetic forming of large area sheet metal has been developed and was taken into operation.

Design criteria were reliability and safety for all possible load cases, including short circuits and short-circuiting loads under operation, at nominal peak currents of up to 200 kA and peak pulse energies of up to 100 kJ. In order to comply with the safety requirements, an all-solid-state design has been chosen using high power semiconductor switches for pulse forming instead of ignitrons or spark gaps. Due to constraints concerning space and manageability, the coupling between the load and the pulse forming unit is achieved via a semi-rigid bundle of high voltage cables, allowing an adjustment of the carrier of the forming coil while being electrically connected to each other.

We report on the development of a pulse generator for peak currents of 50 kA to up to 200 kA at a pulse width of typically around 100 μ s, depending on the load parameters. In order to meet lifetime requirements suitable for industrial applications, the short circuit handling capability of peak currents of up to 450 kA is a major issue in the pulse generator design.

A modular 3-branch design of parallel capacitor banks has been adopted to achieve the requirements concerning reliability, lifetime, and short circuit handling. The prototype pulse generator is based upon off-the-shelf devices, including high-current semiconductor switches. First operating results of the commissioning phase of the installation are reported.

¹ This work was supported by the "Sächsische Aufbaubank" within the framework of a joined project between IWU (Chemnitz), Siemens AG (Erlangen, Chemnitz), H&T (Zwickau), and Volkswagen AG (Wolfsburg)

Keywords:

Pulse generator, Magnetoforming, Solid-state switch

1 Introduction

Magnetoforming is a well-known metal forming process which has been in industrial use for decades. Up to now, however, the major range of applications is limited to coaxial forming of tube-like parts, whereas sheet metal forming has been developed to larger cross-sectional areas only recently [1]. The main reason for this limitation is that sheet metal forming requires considerably higher pulse energies than coaxial forming due to the large cross-sectional areas usually involved in flat workpieces. For an appropriate acceleration of sheet metal parts to velocities on the order of > 200 m/s sufficient for impact forming in a suitable matrix [2] peak pressures on the order of >200 bars are needed at risetimes of a few tens of microseconds only. Peak currents on the order of > 50 kA up to 200 kA are therefore necessary in order to process large area workpieces.

In this work, we report on the feasibility of a fully solid-state pulse generator with corresponding high peak currents of up to 200 kA nominal current at a pulse width on the order of $100 \mu\text{s}$ FWHM (full width at half maximum). Due to the low inductance of the pulse generator the peak current in the system can reach more than 400 kA during a short circuit in the load or at the transmission line between pulse generator and the driving magnetic field coil. Such a system failure must be regarded as a regularly occurring phenomenon at least during the development and test phase of the generator and drive coil and, thus, must be safely handled by all system components. Care has therefore been taken to design a system which inherently tolerates such a failure by limiting the peak electrical stress to the safe operating areas of the specific components.

During normal operation the load inductance varies rapidly due to the moving workpiece which is accelerated by the magnetic force. The generator is therefore subjected to rapidly changing load impedance, from close to short circuit to an impedance which is large as compared with the generator internal impedance. The circuit design is chosen such as to tolerate this variation under all operating circumstances.

A modular design with three parallel sub-modules has been adopted to achieve the requirements concerning reliability, lifetime, and short circuit handling. The prototype design is based upon off-the-shelf devices, including high-current discharge switches based on semiconductor devices. The basic concept of the pulse generator is presented, including results from extensive circuit modeling concerning nominal performance as well as short circuit behavior.

2 Circuit design

The pulse generator is intended to be used under a broad variation of load parameters; to support this requirement, the nominal data of the pulse generator were chosen as follows:

Peak current	50 to > 200	kA typ.
Pulse duration	$80 \mu\text{s}$ typ.	FWHM

Load inductance	1 to >10	μH
Lifetime	> 10.000	pulses
Short circuit current	< 450	kA peak

The restrictions on switches, lifetime, and components are caused by the requirements of minimal maintenance and costs, maximum safety, and reliability under industrial constraints, while the electrical data are derived from a preliminary estimate of the necessary peak currents and current rates of rise.

A. Pulse generator design

A modular design of a capacitor bank with three parallel sub-modules has been described in [3] to achieve the requirements and is shown schematically in figure 1a. Each module accommodates its own combination of switch and crowbar diode S1/D1... S3/D3 in order to limit the peak stress of these components to be within their SOA (safe operating area). Each sub-module contains a multitude of parallel capacitors; modularity can be achieved by adding or removing individual capacitor banks, which opens up the possibility to vary the impedance of the pulse generator.

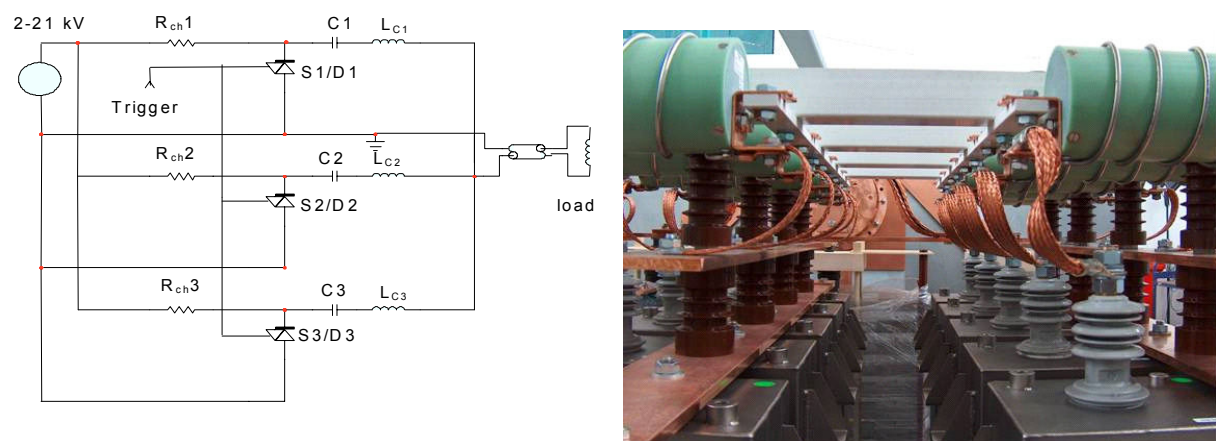


Figure 1: Equivalent circuit of the pulse generator circuit design 1a, (left) based on a capacitor bank with three parallel sub-modules, each equipped with its own switch S1 to S3 and crowbar diode D1 to D3 respectively. L_{Cx} : $\approx 1.5 \mu\text{H}$, series inductance of the individual capacitor banks. 1b, right: View into the pulse generator showing two of three rows of capacitors with busbars, current leads, and current limiting / balancing resistors

The low side of the three sub-modules C1...C3 is directly connected to the load inductance L_{load} by a busbar in a hard-wired fashion. Therefore, the output is nominally grounded by the series load inductance (drive coil) and is only exposed to high voltage during the current pulse. The high sides of the sub-modules are charged in parallel through a single high voltage power supply V1 and are de-coupled from each other during the pulse by series charging resistors R_{ch} . The pulse generator output is connected to the coil via a low impedance cable transmission line, which is also exposed to high voltage stress only briefly during the pulse. An end-on view into the pulse generator is shown in fig. 1b.

Semiconductor switches made from stacks of high power, and high voltage thyristors are used in this circuit design, with peak currents in the short circuit case of less than 150 kA per switch [4]. Such elements are commercially available by several companies, including ABB, DYNEX, EUPEC, NKG, and Westcode, in the form of individual components or even as

complete high-voltage stacks. The high voltage is limited to 21 kV for safety reasons and in order to stay within the SOA of the components for all working conditions.

B. Electrical characteristics

The electrical characteristics of the pulse generator according to figure 1 have been investigated with PSPICE simulations for the case of a maximum charging voltage of 20 kV and a total capacitance of 450 μF (i. e., 3x150 μF in parallel). Load inductance was varied between 1 and 10 μH . During nominal generator performance a peak current of ≈ 60 to 120 kA is generated in the load coil at a pulse duration of 130 μs (FWHM), as shown in figure 2.

For a load inductance of 1 μH and a load resistance of 40 milliohms a peak current of 220 kA is reached at a charging voltage of 20 kV. In this case, up to 60 kJ of electrical energy are discharged through the load coil (fig. 3).

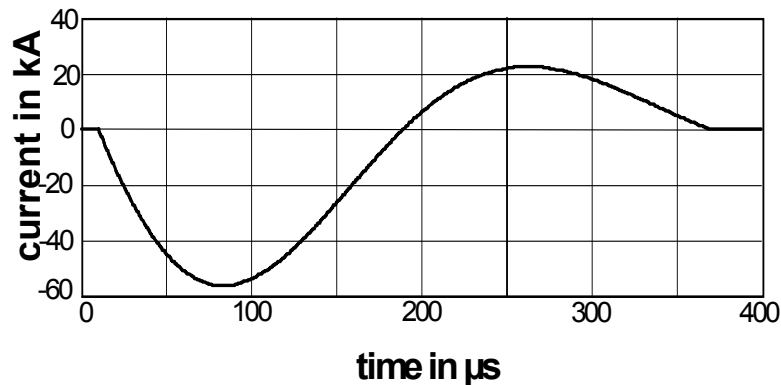


Figure 2: Simulated load current as a function of time for a load inductance of 10 μH . Charging voltage 15 kV; capacitance 300 μF

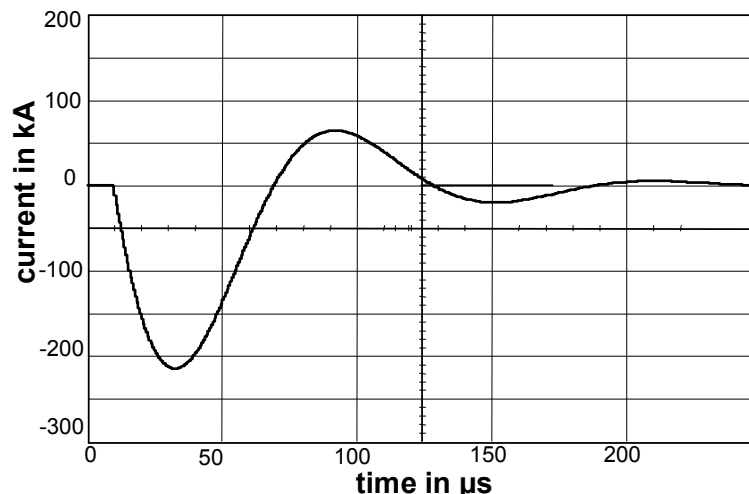


Figure 3: Simulated pulse current shape as a function of time for a fixed load inductance of 1 μH . Charging voltage 20 kV; capacitance 300 μF ; load resistance 40 milliohms

3 Component tolerances

A critical issue in the performance is a well balanced behavior of all parallel sub-modules. However, natural tolerances of components as well as jitter in switch timing lead to an imbalance of the current flow in the individual sections. Such an imbalance can lead to increased current and voltage stress in components of the individual sub-modules which, in turn, can lead to component failure. Intensive circuit simulations were therefore performed in order to investigate the behavior and tolerable working range of the pulse generator under realistic assumptions of component tolerances.

A. Switch timing jitter

A major reason for switch failure can be caused by poor switch timing among the sub-modules, which leads to high peak currents in individual sub-modules. An example for poor switch timing, assuming a timing error of 20 μs of one module as compared to the others, is shown in figure 4 as an example.

Although in the case shown in fig. 4 the individual maximum switch currents do not vary considerably (48.8 kA in S1 vs. 48.6 kA in S2,3), the lack of balance leads to a variation in the I^2t value, which is even more severe in the case of a low inductance load of 1 to 2 μH . The most restrictive case is that of a short circuit; assuming a short circuit inductance of only 200 nH, the maximum permissible jitter in switch timing is on the order of 5 μs for the circuit parameters of fig. 4, which, however, is much larger than that anticipated for high voltage thyristor stacks.

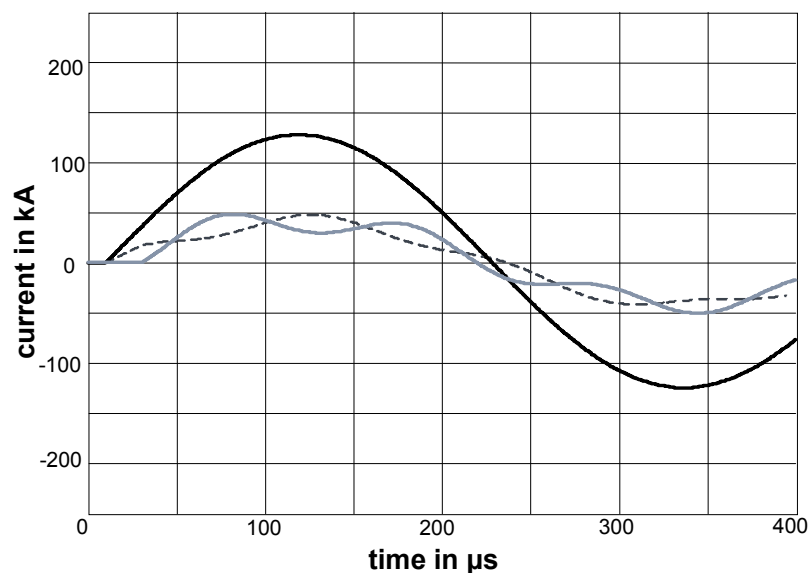


Figure 4: Simulated total load current (solid black line), switch 1 current (solid grey line), and currents through switches 2 and 3 (dashed line) for the case of a switching delay of 20 μs of switch 1 as compared to switches 2/3. Charging voltage 20 kV; load inductance 10 μH ; capacitance 450 μF

B. Capacitor tolerances

Although a switch timing error can be compensated for electronically, and is thus less severe in practical application, a more worrisome imbalance is produced by the tolerances of capacitors and inductances. In general, without preselection (which can be very costly for customized components), tolerances are usually in the range of 10 to 20 %, which can lead to an unacceptably high imbalance between the sub-modules. A current imbalance on the order of 25% occurs for a capacitance tolerance of 20% (figure 5). Particular attention must be paid to the decrease of the capacitance as a function of lifetime due to capacitor aging, as this effect can cause capacitor tolerances of the above mentioned magnitude. Almost up to 20% of imbalance in the branch capacitance is acceptable without sacrificing the SOA of the semiconductor components.

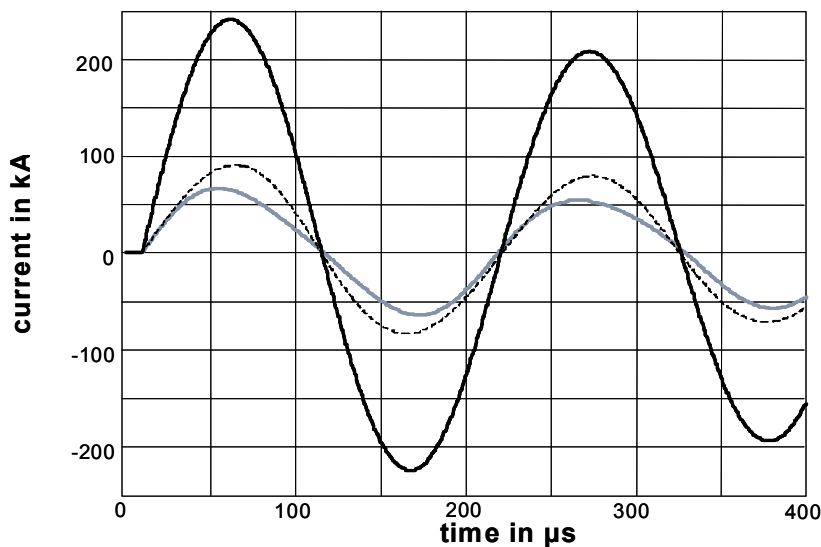


Figure 5: Pulse current into load (solid black line), switch 1 current (solid grey line), and currents through switches 2 and 3 (dashed line) for the case of a capacitance reduction of 20% of C_1 as compared to cap's 2,3. Charging voltage 20 kV; load inductance 2 μH ; total capacitance 420 μF ; pulse width 70 μs (FWHM)

C. Inductance tolerances

The system is considerably tolerant to a variance of the external inductance, mainly due to the fact that the load is predominantly inductive, with a total load inductance comparable to or even larger than the internal inductance of a single sub-module of the pulse generator – except in the case of a short circuit. This makes it particularly insensitive to the rapid inductance variation which is expected during operation as a result of the workpiece acceleration.

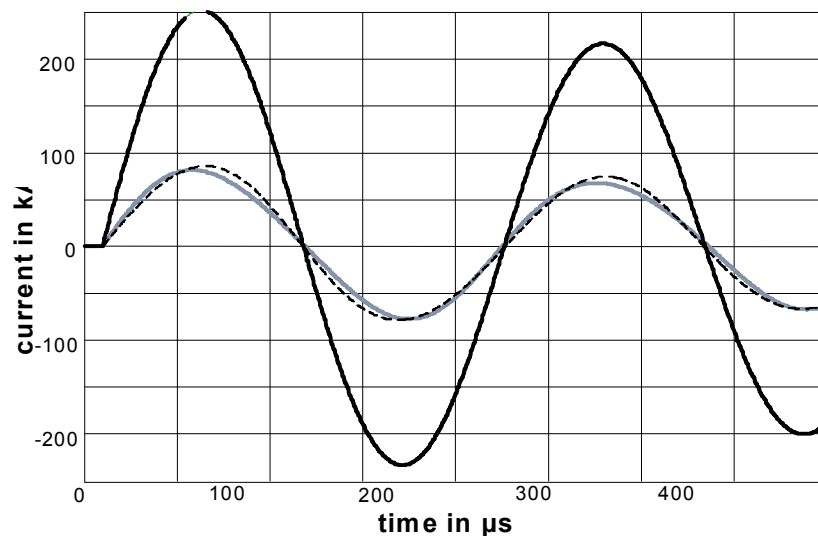


Figure 6: Pulse current into load (solid black line), switch 1 current (solid grey line), and currents through switches 2 and 3 (dashed line) for the case of an inductance reduction of 20% of LC1 as compared to the inductances of branches 2,3. Charging voltage 20 kV; load inductance 2 μ H; total capacitance 450 μ F; pulse width 72 μ s (FWHM)

For short-circuit currents, however, load sharing of the individual modules is strongly reduced and the acceptance range of tolerances of the internal inductance of a single branch relative to the others is reduced to the order of $\approx 10\%$ (fig. 6). Therefore, the short circuit case limits the working range of the pulse generator considerably, more than the use of highly inductive loads. The latter show a more pronounced impedance change than low-inductance driving coils. Hence, care has to be taken to thoroughly symmetrize the sub-modules in regard of their individual series inductance before adding the currents at the generator output.

4 Experimental results

During commissioning of the pulse generator, the build-in voltage and current diagnostics have been used to determine the generator parameters. Also the symmetry of the individual modules has been compared to each other. The output current is measured individually for each module by means of current transformers and added in an analogue adder to get the total generator current. An A/D converter – fibre optics coupler provides decoupling of the analogue signal and provides a connection to the data acquisition site. In addition, the output voltage at the generator interface of the high-current cable assembly (fig. 7) is also measured and transferred to the data acquisition system.

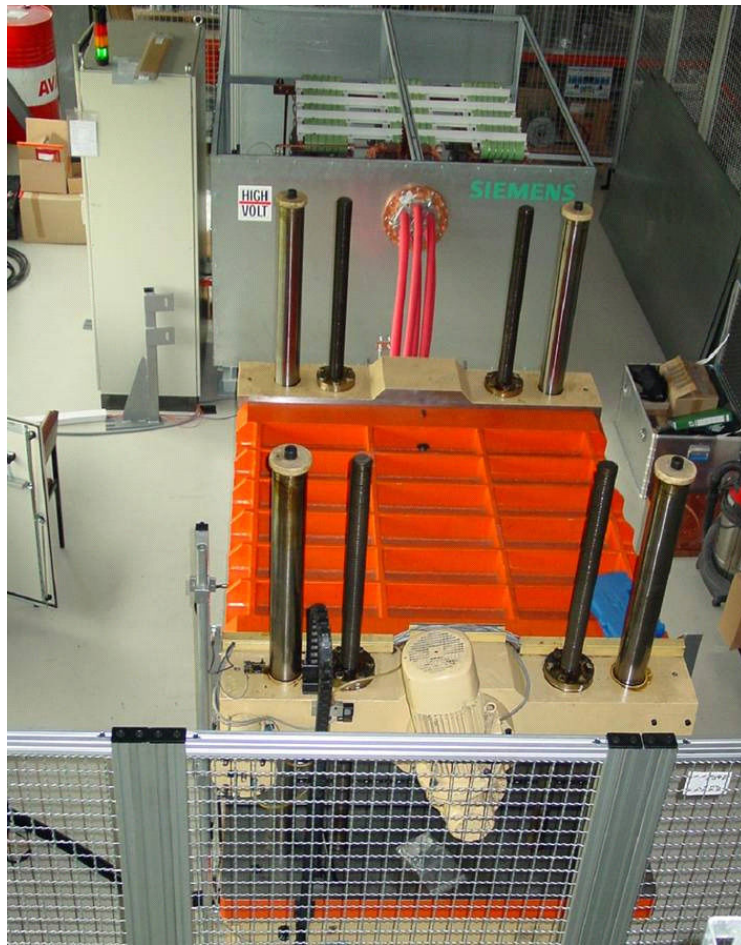


Figure 7: Front-end of the pulse generator with high-current cable connection to the load

From these measurements, the generator and cable parameters are determined by comparison with simulations. The generator current and voltage are shown for the case of a short-circuited coil in figure 8. The following parameters have been achieved:

Generator inductance	790 nH
Generator resistance	16 m Ω
Interface inductance	90 nH
Cable inductance	90 nH
Short-circuit inductance	50 nH

and correspond well with the design values.

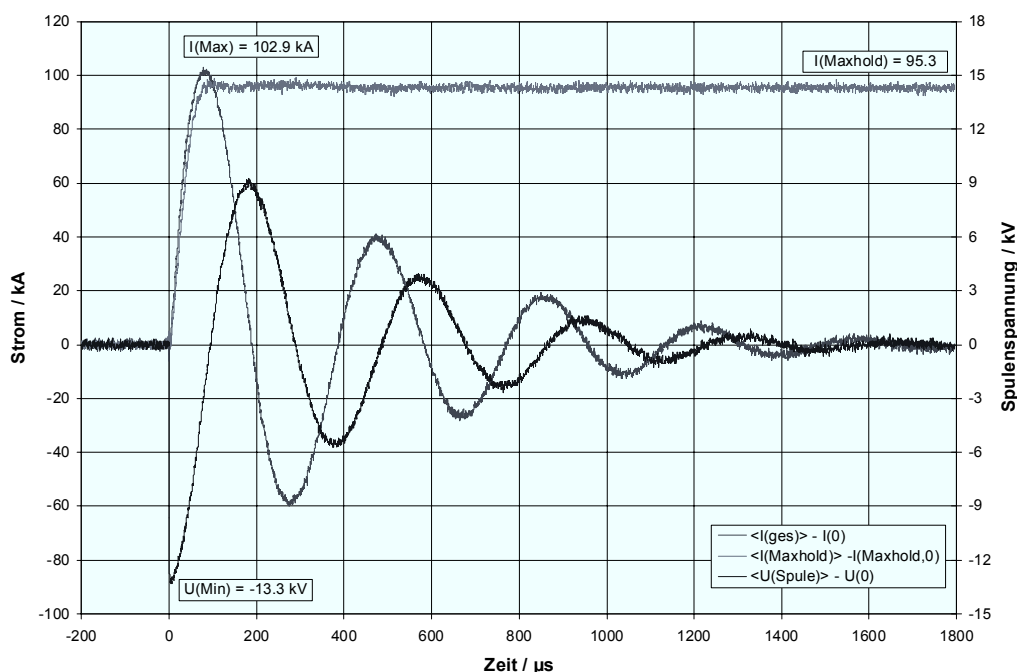


Figure 8: Generator current (positive-going sine, 20 kA/div) and voltage (negative, cosine, 3 kV/div) as a function of time (100 μ s/div) for the case of a short-circuited coil

The excellent symmetry of the three individual sub-modules is demonstrated in fig. 9, which is a superposition of the raw signals of the corresponding current transformers.

While the currents of the outer modules (C1, C3 of fig. 1) of the capacitor bank are indistinguishable from each other within the measurement accuracy, the inductance of the central module (C2) is slightly overcompensated, which can be seen from a minor reduction (<5%) of the amplitude of the current of the central module in respect to the outer modules. This deviation, however, is well within the permissible limits, as discussed in the previous sections.

The weakest component of the installation, i.e. the load coil, failed at this energy level late in the first current half wave (fig. 10). Due to this electrical breakdown between load coil and workpiece the reversing current sees a short circuit load, which led to the increase of the reverse current through the crowbar diodes to a level of 104 kA. No further damage occurred, the pulse generator works satisfactorily according to its specifications.

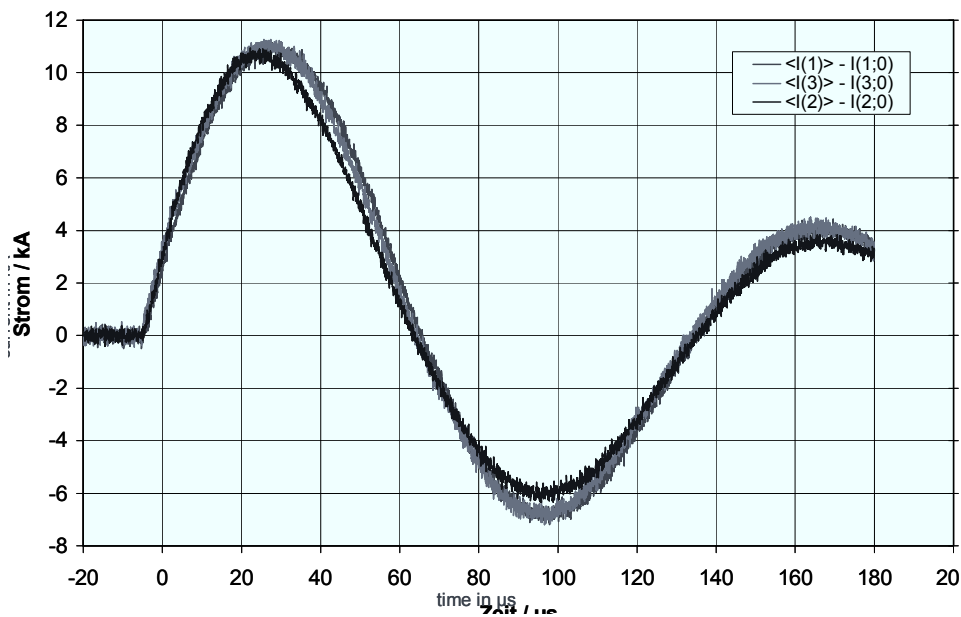


Figure 9: Superposition of the current transformer signals of the individual sub-modules into a short circuit load. Gray lines: outer modules; black line: centre module. 2 kA/div, 20 μs/div

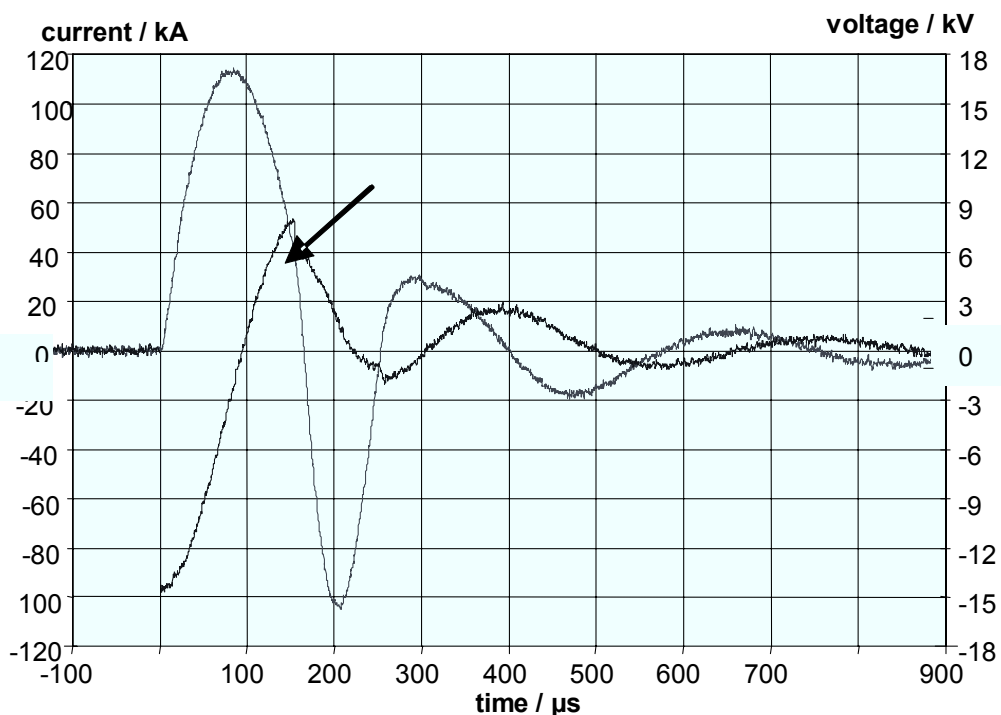


Figure 10: Generator current (20 kA/div) and voltage (3 kV/div) as a function of time (100 μs/div) for a charging voltage of 18 kV; shortly before current reversal (arrow), breakdown of the load coil occurs

5 Summary

A high current pulse generator for magnetofforming of sheet metal parts has successfully been developed and commissioned. The design is based on the use of commercial, off-the-shelf components and a modular architecture of the capacitor bank. The most critical design parameters are

- the ability to withstand short-circuit loads and the corresponding high peak currents,
- tolerances of switch timing jitter, and
- tolerances of the internal inductance of the parallel branches of the capacitor bank.

With careful design of the coupling section between the three sub-modules a sufficiently high symmetry between the sub-modules better than $\pm 5\%$ has been achieved for the case of a short circuit load. The pulse generator operates satisfactorily to its specifications, including the flexible high-current cable connection between pulse generator and load. High-power semiconductor switches are a key component of this generator.

References

- [1] *Daehn, G. S. et al.*: Improved Formability with Electromagnetic Forming: Fundamentals and a Practical Example. <http://www.er6.eng.ohio-state.edu/%7Edaehn/overview/index.htm>, (2003)
- [2] *Badelt, M.; Beerwald, C.; Brosius, A.; Kleiner, M.*: Process analysis of electromagnetic sheet metal forming by online-measurement and finite element simulation. 6th ESAFORM Conference on Material Forming, Salerno, Italy, April 28-30 (2003)
- [3] *Hartman, W.; Roemheld, M.*: Design of a high current pulse generator for Magnetofforming. Proceedings 26th IEEE Power Modulator Symposium, San Francisco, CA, USA (2004), pp. 310-313
- [4] *Welleman, A. et al.*: Semiconductor switches for single pulse and repetitive pulse applications. 4th Int. AECV Conference, The Netherlands, Sept. 24 – 26 (2001)

High Power Semiconductor Devices and Solid State Switches for Pulsed Discharge Applications

A. Welleman, W. Fleischmann

ABB Switzerland Ltd, Semiconductors, Fabrikstrasse 3, CH-5600 Lenzburg / Switzerland
(adriaan.welleman@ch.abb.com)

Abstract

Based on long term experience, collected mainly with military applications like Rail Guns and Active Armour, a range of optimized semiconductor devices for pulsed applications was developed by ABB Switzerland Ltd and described in this presentation. The presented devices are optimized for pulsed discharge and fit very well for switching the short but high electrical power demand used for magnetic forming. Devices are available in different versions with silicon wafer diameters up to 120 mm and blocking voltages of over 6500V. Because of the different application requirements a differentiation is made in device technology. Depending on the discharge circuit, devices for low, medium, or high di/dt can be selected and the difference in advantages and disadvantages between both technologies will be described. To minimize the inductance between switching device and freewheeling diode, ABB can integrate this diode monolithic on the switching wafer. These so called reverse conducting devices are very common for magnetic forming applications. Thyristor structures are commercially available up to 8500V with 120 mm silicon wafers and GTO-like structures are available up to 4500V with 91 mm silicon wafers. For higher voltages or higher currents a combination of devices in series and/or parallel connection is required. The presentation will also describe the evolution of complete discharge switching modules in the range of 10kV / 50 kJ, a large discharge system of 21kV / 200kA, and a newly designed high current switch in the range of 15kV / 3MJ. The solid state switch solutions offered today and those shown in the presentation are based on a standard platform of components existing already for several years. For reliability reasons it is of great importance that the switch assemblies for high current pulsed applications are designed in cooperation with the device manufacturer who has in-depth knowledge of the switching behavior of the semiconductor components under pulsed conditions. The advantage of a complete switch assembly is that the whole unit can be tested under application conditions. ABB has a test capability up to 65 kV and 85 kJ stored energy.

Keywords

Semiconductor device, Solid state switch, High current, High di/dt,

1 Introduction

Semiconductor devices have made dramatic progress in power handling over the last decade. Today's technology and production capabilities make it possible to produce devices with high blocking voltage combined with very high current handling. Depending on the design and the device structure, also very high current rise rates in the range of up to several tenth's of kA/ μ s are possible. Especially for single pulse or medium pulse repetition rates semiconductor devices are getting more and more competitive in comparison to conventional technologies like thyratrons, ignitrons, spark-gaps and mechanical switches. The main advantages are the reliability, lifetime, and almost no maintenance of the semiconductor switches if the characterization is done right. Main advantages like longer life-time, environmental friendliness (no mercury etc.), and flexible mounting position compensate the higher initial cost of a solid state design. The type of semiconductor used and the rating of the device are extremely important for a reliable operation and need an in-depth know-how of the application and the switching device. ABB has developed a specific range of semiconductor devices and adapted standard products over the years, which can fulfil the requirements for pulsed applications. Beside the semiconductor devices, ABB is also in the position to supply complete custom made ready-to-use solid state switch assemblies including clamping, triggering, cooling, and with application-oriented testing. The presentation describes both, the loose semiconductor components as well as some custom made solid state switches for single pulse or low repetition rate pulsing.

2 Device technology

Semiconductor devices for pulsed applications can be divided in turn-on and turn-off devices. Turn-on devices are thyristors (SCR's) and in the group of turn-off devices we find the GTO's (Gate Turn-Off Thyristor), IGCT's (Integrated Gate Controlled Thyristor) and IGBT's (Insulated Gate Bipolar Transistor). For high energy short pulse discharge applications like high speed forming, mostly thyristor technology is used. The table below gives a short overview of the different possibilities.

Device type	Max. forward blocking voltage	Max. peak pulse current capability	di/dt	Switch-on	Switch-on/off
Thyristor	≤ 8500 V	120 kA	1.5 kA/ μ s	Yes	No
GTO-like thyristor	4500 V	150 kA	50 kA/ μ s	Yes	No
Integrated GTO-like thyristor	4500 V	150 kA	50 kA/ μ s	Yes	No
GTO	4500 V	4 kA	3 kA/ μ s	4 kA	4 kA
IGCT	≤ 6000 V	4 kA	2 kA/ μ s	4 kA	4 kA
IGBT (Wire bonded module)	≤ 6500 V	1 kA	5 kA/ μ s	1 kA	1 kA

Table 1: Overview of different semiconductor device technologies

For high speed forming the use of capacitor discharge switching is very common because high energy has to be switched into a load in a very short time. The capacitor can be discharged completely and this means that devices with high switch-on capability are selected in the first place if no switch-off capability is needed. For this presentation we will concentrate on the switch-on devices in thyristor and GTO-like thyristor technology.

2.1 Thyristor technology

Thyristor (SCR) technology is a well proven solution which is used for high currents, relatively long pulses, and low current rise rates in capacitor discharge applications. Standard commercial off-the-shelf devices can be used, but it should be taken into consideration that the life-time of such devices is often reduced due to the fact that the manufacturer has not designed and not tested the device to be used outside the datasheet values. Therefore, it is of vital importance to check the capability and the corresponding device life-time with the manufacturer before. Depending on the application, the pulse current, current rise-time, pulse length, and pulse repetition rate, different wafer designs can be selected to fulfil the requirements. Figure 1 shows the evolution of Ø 51 mm thyristor wafers from 1975 till the year 2000. These designs are available in different diameters for different current capabilities. Blocking voltages can be from 1800V till up to 8500V per device for the thyristor designs and up to 6000V for the highly interdigitated designs (GTO-like structure). For higher voltage devices can be stacked in series connection.

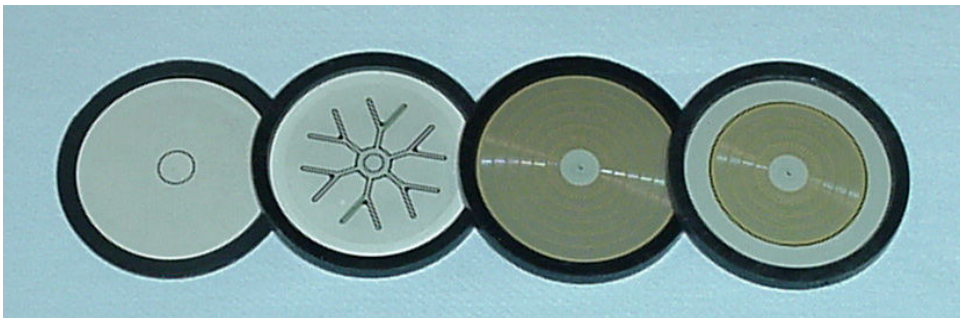


Figure 1: Si-wafers Ø51 mm for $di/dt < 0.1\text{ kA}/\mu\text{s}$, $1\text{ kA}/\mu\text{s}$, $18\text{ kA}/\mu\text{s}$, and $15\text{ kA}/\mu\text{s}$; the right one is with a monolithic integrated freewheeling diode

The first wafer shown in Figure 1 is not used for pulsed application because the plasma spread over the silicon area will be too slow. The second wafer design is commonly used for crowbar and dump switch applications with di/dt up to about 1 - 2 $\text{kA}/\mu\text{s}$. The two wafers on the right side of the picture represent the GTO-like wafer structure.

	Thyristor structure	GTO-like structure
Max. wafer size	≤ 120 mm	≤ 91 mm
Forward blocking	Up to 6500V	4500V
Reverse blocking	Up to 6500V	18V
Reverse conducting	Not possible	Possible
Max. current capability	120 kA @ 1000 μs	150 kA @ 100 μs
Current rise rate	< 1 $\text{kA}/\mu\text{s}$	Up to 50 $\text{kA}/\mu\text{s}$
Driver available	Yes, separate	Yes, integrated

Table 2: Comparison between Thyristor and GTO-Like gate structured devices

These GTO-like structures use a lot of small thyristor segments on one silicon wafer and have a very high di/dt capability.

2.2 GTO-like thyristor technology

Above the GTO-like technology is mentioned. This technology uses the same type of gate structure as GTO devices, but has no switch-off capability. Therefore, it benefits from a very fast switch-on capability of about 1 μs and can handle very high di/dt of up to 50 $\text{kA}/\mu\text{s}$ by using a 91 mm wafer diameter. Depending on the overall diameter, between 800 and 2600 small thyristor islands are located in parallel on the silicon wafer. The devices are available with 51mm, 68mm, and 91 mm wafer diameters and can be asymmetric blocking (Forward 4500V, Reverse 18V) or reverse conducting, with an integrated freewheeling diode. The advantage of the monolithic integrated freewheeling diode is that there is almost no induction between the switching component and the freewheeling diode, which is otherwise located in a separate stack assembly. The GTO-like devices are available as single devices without driver unit. Triggering can be done with a strong gate pulse in the range of about 500A and di/dt of about 1 $\text{kA}/\mu\text{s}$. These devices are mainly used for crowbar or dump switch applications [2] where triggering events are very limited. For those applications where switching is often required or where repetition rates are high the device can be delivered with an integrated driver unit reducing the inductive path between driver and device substantially. The driver units are specially made for use with series connected devices and are energized by a separate current source power supply using a HV cable through the input transformers of the driver units. The HV cable is the isolation between the device levels in the series connection. The current source has an output of 25 kHz and 4A and can drive up to 8 devices in series, depending on device size and pulse repetition frequency. Figure 2 shows the low inductive gate path in a GTO-like thyristor housing.

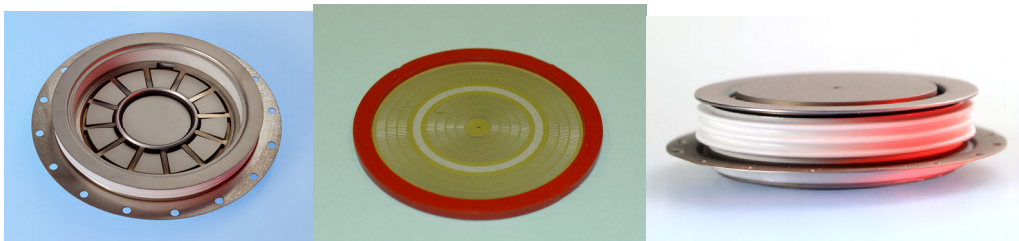


Figure 2: Low inductive housing, GTO-like wafer and complete device

By integrating the driver unit a so called IGCT (Integrated Gate Controlled Thyristor) will be the result. The IGCT is normally supplied in switch-on / switch-off version. For pulsed discharge applications ABB has a driver unit which is optimized for switch-on only. The combination of the optimized wafer and driver unit results in a product which is unique in this field. As mentioned above, these devices have blocking voltages up to 4500V and for higher voltages series connection is required. The driver unit is designed for easy series connection by means of an inductive coupling with a separate current source. The isolation between the device levels is given by the isolation voltage of a HV closed loop cable, which is sloped through the input transformers of the driver units (See Fig. 4 and 7). Because of the active powering of the driver units it is possible to reach pulse repetition rates of up to several hundred Hertz, the max. pulse rep. rate however depends on the thermal management of the device which can be increased by using air or water cooling. Further details about this will be described with the switch assemblies. Fig. 3 shows a

pulse discharge device with integrated driver unit, including a separate asymmetric and reverse conducting wafer 91 mm. [1]

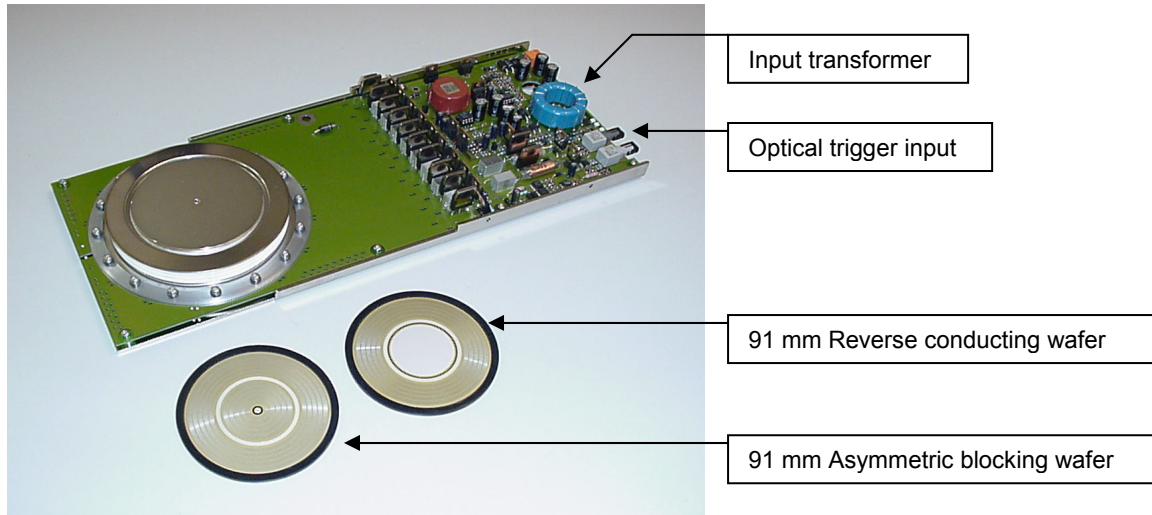


Figure 3: Discharge device p/n: 5SPY 36L4506, $V_{drm}=4500V$ complete with driver unit

By integrating the driver unit a so called IGCT (Integrated Gate Controlled Thyristor) will be the result. It has to be mentioned that standard IGCT devices have turn-on and turn-off capability; those devices designed for discharge applications have turn-on capability only and are optimized for very fast turn-on with high current rise rates.

3 Switches

3.1 Reverse conducting discharge switch 210 kA / 21 kVdc / 100 μ s

In 2005, a prototype switch for magnetic forming was designed and produced using reverse conducting devices ABB p/n 5SPR 26L4506. Table 3 shows the basic specification which had to be fulfilled.

Parameter	Normal condition	Short circuit condition
Max. charge voltage	21 kV	21 kV
Peak pulse current forward	210 kA	420 kA
Peak pulse current reverse	90 kA	150 kA
Current rise rate (di/dt)	3 kA/ μ s	9 kA/ μ s
Pulse duration	100 μ s	50 μ s
Pulse form	Damped sine wave	Damped sine wave
Pulse rep. rate	1 Shot / Min.	1 Shot / 10 mins
Lifetime	20.000 Shots	1.000 Shots

Table 3: Specification for reverse conducting 210 kA / 21 kV switch assembly

For the specification shown in Table 3 the reverse conducting 91 mm discharge device, 5SPR 26L4506, with integrated driver unit was selected. To withstand the 21 kVdc charge voltage, 8 devices of $V_{drm}=4500V$ / $V_{dc}=2800V$ have to be used in series connection. To fulfil the requirement of 210kA nominal current and 420kA short circuit

condition, three devices in parallel are needed. This means for the total switch $N_s=8$ and $N_p=3$ devices, in total 24 devices are used. The circuit diagram is shown in figure 4.

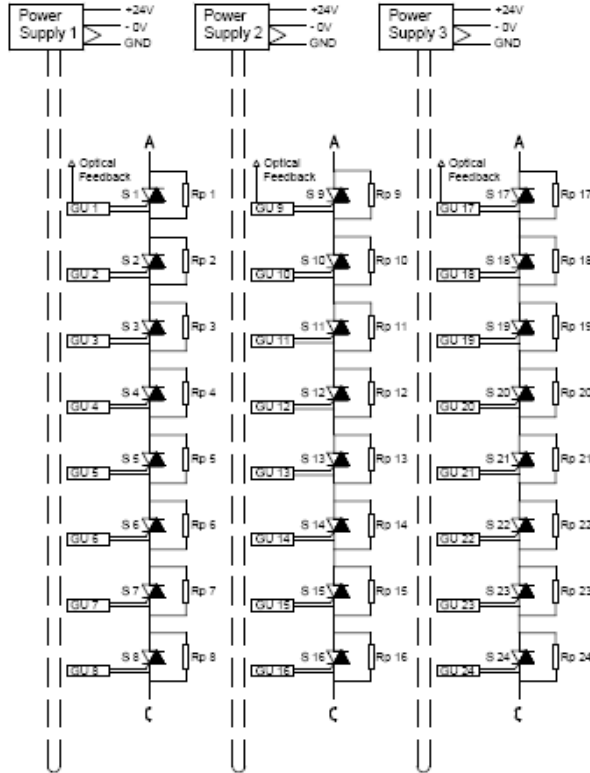


Figure 4: Circuit diagram 21 kV switch

Because reverse conducting devices are used and no switch-off is required no snubber circuit is needed, only voltage sharing resistors in parallel with each device level. Three independent stacks were used in parallel to avoid hard parallel connection of 3 devices. This configuration allows also the use of one single stack if less power is required. Every stack can handle the 70 kA nominal and the 140 kA short circuit condition. The driver units are optical triggered from a light distribution box and this box can be selected to fire 1, 2, or all 3 stacks simultaneously or sequential. The figures below show measurements on one of the stack assemblies.

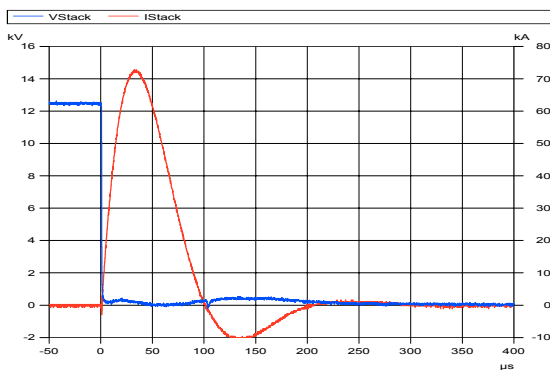


Figure 5: Single stack pulse test

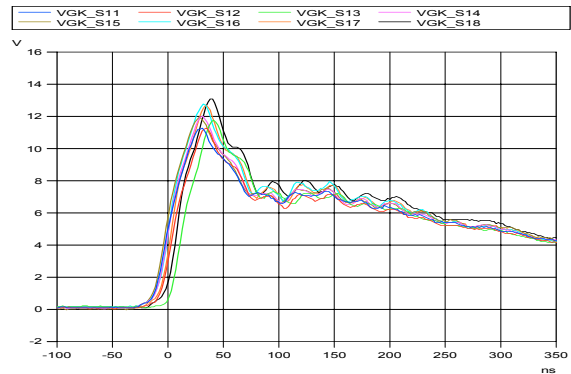


Figure 6: Gate signal delay at turn-on

Figure 5 shows a picture of one of the single stack assemblies (out of three) with the current source power supply. The current source power supply can feed all 8 driver units with 25kHz / 4A by means of an inductive coupling (input transformer). Air convection cooling can be used as the pulse repetition rate for this application is 1 shot per minute. For higher rep. rates forced air cooling or water cooling can be applied. In case of higher rep. rates, water cooling is preferred to keep the dimensions as compact as possible.

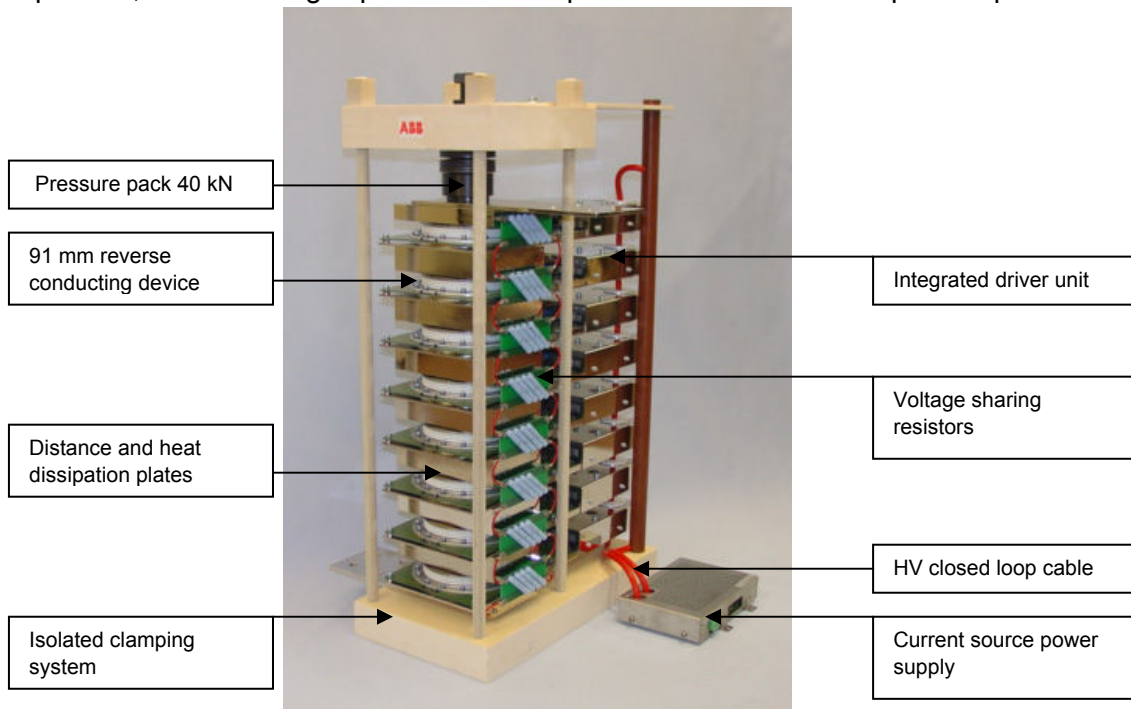


Figure 7: Discharge switch assembly 21 kVdc / forward 70 kA / reverse 30 kA

3.2 10 kV / 50 kJ Discharge switch device / module

The German-French Research Institute, I.S.L. Saint-Louis / France has developed a 50 kJ capacitor discharge module in 1995, which includes the 10.5 kV / 50 kJ capacitor, the semiconductor switch, the inductor, and a triggering system. A few hundred of such modules were made. 200 of them were used for a 10 MJ rail gun facility and some for other pulsed power supplies. Over the last 10 years, the design was optimized and miniaturized. This construction is also of interest for magnetic forming applications. The capacitor is a 50 kJ can with a multichip thyristor p/n 5STF 07Z1350 as switch and a freewheeling multichip diode p/n 5SDA 27Z1350. Both have a blocking voltage of 13.5kV.



Figure 8: Multichip diode 5SDA 27Z1350 and multichip thyristor 5STF 07Z1350

For active armour applications the current rise rate is higher as this type of thyristor can handle, and therefore a device with a GTO-like wafer structure was selected. The solution were 3 switching devices 91 mm and one diode 91 mm in series connection. The use of discrete devices resulted in a total height of 106 mm, an overall diameter of 120 mm, and a weight of 6.2 kg. Because for this single shot application cooling is not a serious issue, all 4 wafers were put into one special housing and by additionally reducing the thickness of the copper pole pieces a total height of 54 mm could be achieved. This height was reached by using standard production material such as standard Molybdenum discs, standard gate connections, and standard optimized wafers 91 mm.

5SPB 36Z1350	
Forward blocking	13.5 kV
Reverse blocking	4.5 kV
Max. charge voltage	10.0 kVdc
Peak pulse current	120 kA
Pulse duration	100 µs
Current rise rate	10 kA/µs
Overall dimensions	H=53 x Ø=120 mm
Clamping Force	40 kN
Weight	3.0 kg

Table 4: Target data of new multichip device 5SPB 36Z1350 / 13.5 kV

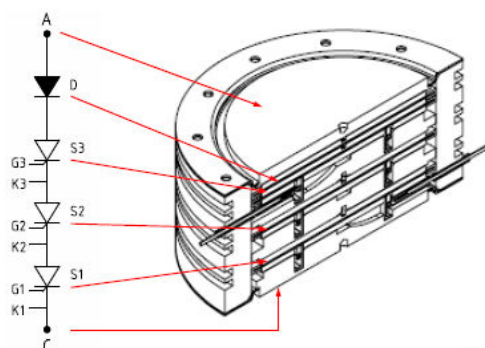


Figure 9: Built-up of multichip device



Figure 10: Device complete with 91mm wafers in front

ABB has done the testing on wafer level and voltage blocking tests on the device, the application oriented tests were done at ISL [3] in combination with the 50kJ / 10kV capacitor. In total, more than 300 discharges were made with the devices. All devices survived the tests based on the target specification. Table 5 shows test results on one device.

I-pulse (kA)	di/dt (kA/µs)	t-pulse (µs)	Shots
110	2.2	125	210
80	12.5	25	20
10.5	24	50	2

Table 5: Test results 5SPB 36Z1350

It has been detected that the pulse test with $24 \text{ kA}/\mu\text{s}$ is on the limit of the capability. The reason is that the gate connection is made with a one pin entrance through the housing, which limits the trigger di/dt . The originally used 26 mm thick discrete devices have annular gate connections and 12 entrances to the wafer, resulting in a much higher di/dt capability. By limiting the specification of the multichip construction to a maximum di/dt of $10 \text{ kA}/\mu\text{s}$ @ $100\text{kA} / 50\mu\text{s}$ it can comfortably fulfil the target specification for magnetic forming or other pulsed discharge applications. The thermal recovery time depends on the current value and pulse length. The picture below shows the evolution over the last 10 years of the 50 kJ capacitor discharge module by reducing the mechanical sizes of the capacitor and switches, resulting in a higher performance and 62% less size.

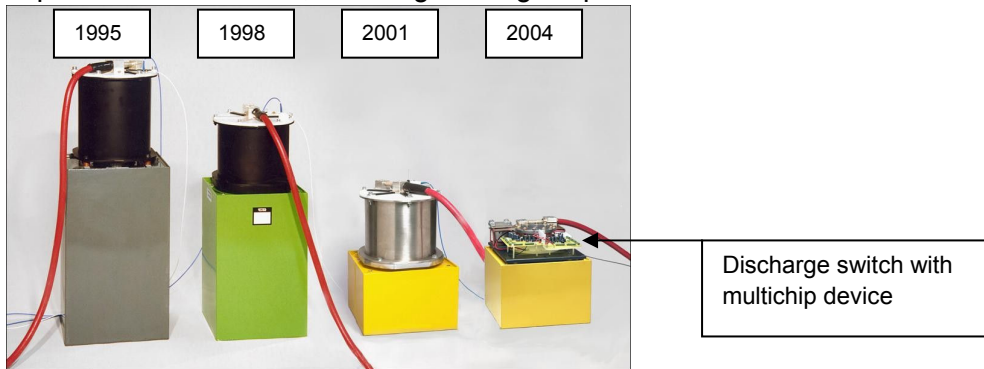


Figure 11: Evolution of 50 kJ discharge modules, the right one with $1.2 \text{ MJ}/\text{m}^3$

3.3 Low di/dt , long pulse, discharge switch for 260 kA / 15 kVdc

A design was made for a large 200MJ (Rail Gun) system using a series connection of $N_s=5$ and parallel connection of $N_p=3$ thyristors with 120 mm wafer size. The devices are rated for $V_{\text{drm}}=5200\text{V} / V_{\text{dc}}=3300\text{V}$ ABB p/n 5STP 52U5200. The requirement for the switching module in the application is for $I\text{-pulse}=260 \text{ kA} / V_{\text{dc}}=15 \text{ kV} / t\text{-pulse}=3 \text{ ms}$ pulse / $di/dt=165 \text{ A}/\mu\text{s} / \text{action}=113 \text{ MA}^2\text{s}$. To reach the 200 MJ, several switching modules will be used in parallel. Because of high reversal voltage after the pulse the thyristors needed a protection circuit, which is designed with $R_s / C_s / R_p$ and MOV. The triggering is done with a simple driver unit per device level, which is inductively coupled with a trigger generator. The isolation between the driver units is given by a HV isolated closed loop cable whose current will trigger all 15 thyristors simultaneously.

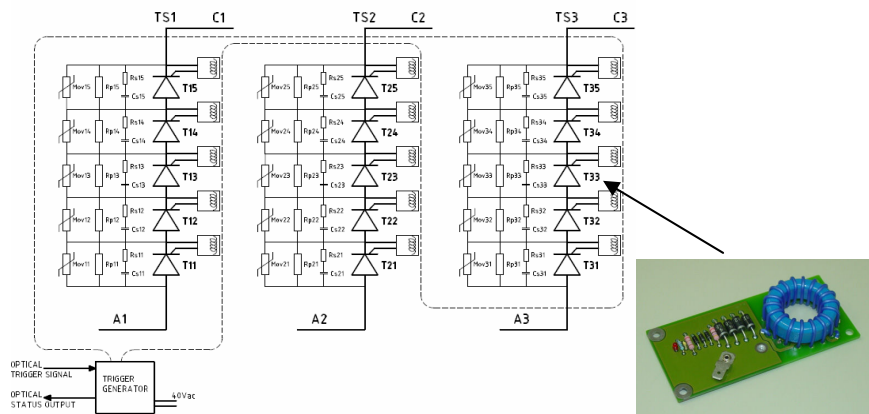


Figure 12: Circuit diagram 260 kA / 15kV / 3 MJ switch module and a picture of the inductive coupling for simultaneous triggering



Figure 13: Design drawing of 260kA 15kVdc thyristor module

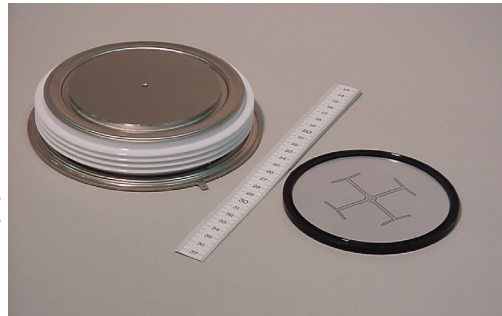


Figure 14: ABB thyristor p/n 5STP 52U5200.

The overall size of the thyristor module is $W=690 \times H=570 \times D=250$ mm. The thyristors are assembled with 135 kN clamps on a glass fiber epoxy base which has a thickness of 100 mm. The trigger generator is located under the base plate. The temperature increase of the thyristor wafer after the shot is about 110°C . Because the assembly is used at low rep. rates of some shots per minute large aluminum blocks between the devices will dissipate the heat with air convection. For higher pulse repetition rates active cooling or more devices with lower blocking voltage have to be used.

4 Conclusions

It has been shown that solid state switches are state of the art today. ABB produces a wide range of reliable semiconductor devices and switches, which are optimized for pulsed applications. Solid state switches successfully replace electronic tubes and other technologies in many applications. Due to deliveries in all kinds of systems and close connections to research institutes and governmental organisations, a wide practical experience has been built up. The initial higher cost of a semiconductor switch is compensated by the higher reliability and practically no needed maintenance.

References

- [1] Welleman, A.; Fleischmann, W.: Solid State Switches for Repetitive Pulse Applications. European Pulsed Power Symposium, EPPS2004, Hamburg, September 2004
- [2] Welleman, A.; Fleischmann, W.: High Voltage Solid State Crowbar and Low Rep. Rate Switches. IEE Pulse Power Symposium, Basingstoke UK, September 2005
- [3] Spahn, E.; Buderer, G.; Brommer, V.; Sterzelmeier, K.: Novel 13.5kV Fast Multichip Thyristor. Pulse Power Conference, PPC2005, Monterey CA, June 2005

ISBN 3-00-018432-5